UNIVERSITÀ DELLA CALABRIA

UNIVERSITA' DELLA CALABRIA
Dipartimento di Ingegneria Civile

Dottorato di Ricerca in
Scienze ed Ingegneria dell'Ambiente, delle Costruzioni e dell'Energia

CICLO
XXXI

CRACK PROPAGATION MODELLING IN LAYERED STRUCTURES BY USING MOVING MESH METHOD

Settore Scientifico Disciplinare: Scienza delle Costruzioni (ICAR/08)

Coordinatore: Ch.mo Prof. Salvatore Critelli
Firma

Supervisore/Tutor: Ch.mo Prof. Paolo Lonetti
Firma

Dottorando: Dott. Marco Francesco Funari
Firma

LIST OF FIGURES III

LIST OF TABLES X

ABSTRACT XI

ABSTRACT (ITALIAN VERSION) XIV

CHAPTER 1 INTRODUCTION 1

1.1 Thesis topics 2

1.2 Layered structures 2
  1.2.1 Modelling of interfacial delamination phenomena 3
  1.2.2 Modelling of interlaminar reinforcement systems 7
  1.2.3 Sandwich Structures 10

1.3 Aims and scope 15

CHAPTER 2 A COUPLED ALE-COHESIVE FORMULATION TO PREDICT INTERFACIAL DEBONDING EVOLUTION IN LAMINATE STRUCTURES ... 16

2.1 Theoretical Formulation 17
  2.1.1 ALE formulation and interface approach 17
  2.1.2 Governing equations 18

2.2 Numerical Implementation 23

2.3 Implementation of the interlaminar reinforcements 27

2.4 Results 28
  2.4.1 Single delamination in unidirectional laminates 28
  2.4.2 Multiple delaminations in unidirectional laminates 35
  2.4.3 Single delamination in unidirectional laminates reinforced with z-pins 41

CHAPTER 3 INITIATION AND COALESCENCE PHENOMENA 50

3.1 Theoretical Formulation 51
  3.1.1 Formulation of the crack onset modelling 51

3.1.2 Crack evolution mechanism 53

3.2 Numerical implementation 56

3.3 Results........ 62

3.3.1 Multi-layered structures, crack onset, propagation and coalescence: Static framework 63

3.3.2 Multi-layered structures, crack onset, propagation and coalescence: Dynamic framework...... 70

3.3.3 Multi-layered structures with inter-laminar reinforced with z-pins 79

CHAPTER 4 SANDWICH STRUCTURES 84

4.1 Generalization of the ALE interface model to describe skin core debonding 85

4.1.1 Results........ 88

4.2 Model based on ALE to describe crack propagation 2D solids 99

4.2.1 Theoretical formulation of the model........ 99

4.2.2 Numerical implementation of the model........ 103

4.2.3 Computational procedure and implementation algorithm 104

4.2.4 Results and validation 108

4.3 Experimental Campaign 123

4.3.1 Preliminary results 127

CHAPTER 5 CONCLUSIONS 133

5.1 Conclusions 134

REFERENCES........137

APPENDICES 144

Publications in international Peer-reviewed journals........ 144

Publications in national and international Conference Proceedings 145

List of Figures

Fig. 1.1: Composite materials, field of application. 3
Fig. 1.2: Effective traction-separation relationships: (a) cubic polynomial, (b) trapezoidal, (c) smoothed trapezoidal, (d) exponential, (e) linear softening, and (f) bilinear softening [9]. 6
Fig. 1.3: (a) Photograph showing the size of a typical z-pin and (b) z-pins inside a prepreg composite [27]. 8
Fig. 1.4: Schematic application process of z-pins[27]. 9
Fig. 1.5: Schematic representation of two failure mode of Sandwich Structures: Crack Kinking and Skin/Core interface de-choesion. 11
Fig. 2.1: Multilayered laminate structure: geometry and interfaces. 17
Fig. 2.2: ALE formulation: kinematic and referential configuration. 18
Fig. 2.3: Interface moving boundary: debonded and perfect adhesion regions. 21
Fig. 2.4:Synoptic representation of the mapping rule between moving coordinates and material points. 24
Fig. 2.5: Interface moving boundary: debonded and perfect adhesion regions. 26
Fig. 2.6: Multilayered laminate structure: representation of the geometry; interface TSL (a,b) and Z-pin pull-out model (c). 27
Fig. 2.7: Laminate configurations and loading schemes: Double Cantilever Beams (DCB) (a); Mixed Mode Bending test (MMB) (b). 29
Fig. 2.8: Mode I DCB configuration: comparisons in terms of loading curve (F-U_2/L) and crack tip position (X_T/L) with analytical [87] and XFEM [86] solutions. 31
Fig. 2.9: MMB configuration: comparisons in terms of loading curve (F-U_2/L) and crack tip position (X_T/L) with analytical [87] and XFEM [86] solutions. 31
Fig. 2.10: MMB configuration: influence of the mesh discretization on the loading curve (F-U_2/L) and dimensionless crack tip position (X_T/L). 32
Fig. 2.11: MMB configuration: influence of the debonding length parameter (Ω_{deb}) on the loading curve (F-U_2/L) and dimensionless crack tip position (X_T/L). 33
Fig. 2.12: MMB configuration: influence of the loading rate in terms of load-displacement curve. 34
Fig. 2.13: MMB configuration: influence of the loading rate in terms of crack tip speed. 35

Fig. 2.14: Laminate configuration and loading scheme: Multiple Delamination Scheme (MDS). 35

Fig. 2.15: MDS configuration: comparisons in terms of loading curve (F-U_2/L) with numerical results and experimental data 37

Fig. 2.16: MDS configuration: comparisons in terms of crack tip position (X_T/L) with others numerical data. 38

Fig. 2.17: MDS configuration: comparisons in terms of loading curve (F-U_2/L) with numerical results and experimental data. 39

Fig. 2.18: MDS configuration: influence of the loading rate in terms of load-displacement curve. 40

Fig. 2.19: MDS configuration: influence of the loading rate in terms of crack tip speed.40

Fig. 2.20: DBC scheme reinforced by z-pins. 42

Fig. 2.21: Comparisons in terms of loading curve with experimental data [93] and numerical results [33, 94]. 43

Fig. 2.22: Comparisons in terms of nominal crack tip position with experimental data [93] and numerical result [94]. 43

Fig. 2.23: Damage distribution in the z-pins and interlaminar fracture function at representative points of the loading curve. 45

Fig. 2.24: MMB scheme reinforced by z-pins. 45

Fig. 2.25: Comparisons in terms of loading curve (F/G_{IC} B-U_2/L) with experimental data [93] and numerical result [33]. 46

Fig. 2.26: Comparisons in terms of nominal crack tip position (X_T/L-U_2/L) with UP configuration. 47

Fig. 2.27: Influence of the loading rate in terms of loading curve (F/G_{IC} B-U_2/L)..........48

Fig. 2.28: Influence of the loading rate in terms of nominal crack tip speed 48

Fig. 3.1: Multilayered laminate structure: geometry, interfaces and TSL. 51

Fig. 3.2: Representation of the coordinate systems employed: Before crack initiation (a), After crack initiation, material and moving coordinates system are coincident (b), ALE formulation: referential and moving configuration introduced to describe debonding phenomena (c). 52

Fig. 3.3: Strategy to describe debonding phenomena by means ALE interface elements: description of the iterative procedure. 56

Fig. 3.4: Synoptic representation of the Numerical implementation: Searching of the crack onset condition and itself position (a), Process of changing geometry and mesh refinement (b), description of the debonding phenomena by means ALE elements (c). 58

Fig. 3.5: Schematic representation of the algorithm for layered structure, crack initiation and evolution. 61

Fig. 3.6: Layered configuration formed by six structural layers. 63

Fig. 3.7: Laminate structure: influence of the mesh discretization on the loading curve (F/G_{IC} B-U_2/L) and comparisons between proposed model (M1-M2-M3) with classical Cohesive approaches (PC1-PC2). 66

Fig. 3.8: Laminate structure: influence of the mesh discretization on the crack tip position (X_T/L-U_2/L) and comparisons between proposed model (M1-M2-M3) with classical Cohesive approaches (PC1-PC2). 66

Fig. 3.9: Number of the total DOFs and CPU time ratio for the numerical simulation performed by using proposed modelling (M1-M2-M3) and classical cohesive approach (PC1). 67

Fig. 3.10: Laminate structure: influence of the material discontinuity length on the loading curve (F/G_{IC} B-U_2/L). 67

Fig. 3.11: Layered configuration submitted to a four-point bending test. 68

Fig. 3.12: Four-point bending test scheme: (G_c=0.050) influence of the mesh discretization on the loading curve and crack tip displacement , comparisons with CZM [100] and FFM [100]. 69

Fig. 3.13: Four-point bending test scheme: (G_c=0.50) influence of the mesh discretization on the loading curve and crack tip displacement, comparisons with CZM [100] and FFM [100]. 70

Fig. 3.14: Layered configuration formed by two structural layers. 70

Fig. 3.15: Perfect interface debonding (P): comparison in terms of loading curve (F/G_{IC} B-U_2/L) between static and dynamic cases for different loading rate. 72

Fig. 3.16: Imperfect interface debonding (IP): comparison in terms of loading curve (F/G_{IC} B-U_2/L) between static and dynamic cases for different loading rate. 73

Fig. 3.17: Imperfect interface debonding (IP): evolution of the crack tip speed normalized to the shear wave speed of the material and kinetic to strain energy ratio as function of the normalized applied displacement. 73

Fig. 3.18: Steel beam configuration and loading scheme. 74

Fig. 3.19: Comparisons in terms of loading curve for different thickness of the FRP strip. 76
Fig. 3.20: Comparisons in terms of time histories of the debonding front speed for different thickness of the FRP strip. 76
Fig. 3.21: Comparisons in terms of loading curve for different thicknesses of the adhesive layer. 77
Fig. 3.22: Comparisons in terms of time histories of the debonding front speed for different thickness of the adhesive layer. 77
Fig. 3.23: Comparisons in terms of interfacial tractions across the two cohesive interfaces for different positions of debonding front. 79
Fig. 3.24: Layered configuration with two structural layers and two material discontinuities: UP configuration, C1 configuration, C2 - C3 configurations. 80
Fig. 3.25: Comparisons of the different pinned configurations in terms of loading curve (F/G_{IC} B-U_2/L) with the UP solution [101]. 81
Fig. 3.26: Influence of the inertial effects (v_0=10 [m/s]): comparisons of the different pinned configurations in terms of loading curve (F/G_{IC} B-U_2/L) with the UP solution [101]. 82
Fig. 3.27: Comparisons in terms of nominal crack tip speed: UP configuration [101] (a), C1 configuration (b), C2 configuration (c) and C3 configuration (d)...............................83
Fig. 4.1: Synoptic representation of the sandwich structure. 85
Fig. 4.2: Moving and referential coordinate systems in the ALE description. 86
Fig. 4.3: Moving mesh interface elements, process zone and crack onset.......................86
Fig. 4.4: Loading schemes and geometrical configuration for mode I analysis. Definition of the internal debonding geometry. 89
Fig. 4.5: Mode I analysis, normalized loading vs opening displacement: comparisons with numerical [103] and experimental [104] data in terms of normalized loading curve and opening displacement. 90
Fig. 4.6: Mode I analysis, normalized loading vs opening displacement: effect of the loading rate on the resistance curve: comparisons between static and dynamic loading curves. 91
Fig. 4.7: Mode I analysis, normalized loading vs opening displacement: Effect of the internal debonding length: comparisons between static and dynamic loading curves......92

Fig. 4.8: Mode I analyses: crack tip speed vs crack displacement as a function of the loading rate and the internal debonding length for C1 and C2 configurations. 93

Fig. 4.9: Mode I analyses: crack tip speed vs crack displacement as a function of the loading rate and the internal debonding length for C1 and C2 configurations. 93

Fig. 4.10: Loading schemes and geometrical configuration for Mode II analysis. Definition of the internal debonding geometry. 94

Fig. 4.11: Mode II analysis, normalized loading vs opening displacement: comparisons with numerical [103] in terms of normalized loading curve and opening displacement. 96

Fig. 4.12: Mode II analysis: comparisons with numerical data arising from [103] in terms of traction forces for lower and upper interfaces. 96

Fig. 4.13: Mode II analysis, normalized loading vs opening displacement: comparisons between static and dynamic loading curves for C1 configuration. 97

Fig. 4.14: Mode II analysis, normalized loading vs opening displacement: comparisons between static and dynamic loading curves for C2 configuration. 98

Fig. 4.15: Mode II analysis: comparisons in terms of traction forces for different position of the debonding front 98

Fig. 4.16: Mode II analysis: comparisons in terms of the crack tip speed for different internal debonding lengths. 99

Fig. 4.17: Schematic representation of a 2D problem including a macro-discontinuity. 100

Fig. 4.18: Referential and Moving coordinate systems for a 2D problem 102

Fig. 4.19: Schematic representation of the proposed algorithm: (a) crack onset condition satisfied, evaluation of θ; (b) crack propagation in θ direction until the angle variation predicted is lower than $toll_Q$; (c) tolerance condition is satisfied, new definition of the computational nodes (P3 and P4)..105

Fig. 4.20: Schematic representation of the algorithm for crack propagation in 2D solids. 107

Fig. 4.21: Geometrical, loading and mesh configuration: (a) Model A involving in pure mode I; (b) Model B involving in Mixed Mode. 109

Fig. 4.22: Influence of the loading condition in the J_2/J_1-X, comparisons between loading scheme A and B. 110

Fig. 4.23: Loading scheme: mode I SIF in terms of the crack propagation length, comparisons with numerical data arising from [111]. In the legend is reported the Pearson's correlation coefficient (R=0.998)...111

Fig. 4.24: Loading scheme: crack tip coordinates Y-X, comparison with numerical data arising from [110]. In the legend is reported the Pearson's correlation coefficient (R=0.999). 112

Fig. 4.25: Synoptic representation of the mesh motion during the crack propagation; (b) Von Mises stress maps for four crack propagation steps arising from[108]; (c) Von Mises stress maps for four crack propagation steps arising from the proposed model. 113

Fig. 4.26: Loading scheme Fig.5b: influence of the algorithm parameter $toll_Q$ in the prediction of the crack path. The symbols on the graph represent the remeshing events. On each curve the presence of the symbol denotes a remeshing event 114

Fig. 4.27: Loading scheme B: comparisons in term CPU time and number of remeshing for the numerical simulation performed by using different idealized value of $toll_Q$ (C1, C2, C3 and C4). 115

Fig. 4.28: Geometrical and loading configuration of the PMMA beam: (a) without holes, (b) with holes 116

Fig. 4.29: P1 configuration: Predicted crack path, comparisons between Experimental [114] and Numerical [113] data. 117

Fig. 4.30: P1-holes configuration: Predicted crack path, comparisons between experimental [114] and numerical [113] data. 118

Fig. 4.31: P2 configuration: predicted crack path, comparisons between experimental [114] and numerical [113] data. 118

Fig. 4.32: P2-holes configuration: predicted crack path, comparisons between experimental [114] and numerical [113] data. 119

Fig. 4.33: Mesh discretization detail around the crack tip for M1, M2 and M3 configurations. 120

Fig. 4.34: P2 configuration: influence of the mesh discretization on the prediction of the crack path. 121

Fig. 4.35: configuration: influence of the mesh discretization on the prediction of the ERR mode ratio 122

Fig. 4.36: P2 configuration: comparisons in term CPU time and number of elements for the numerical simulation performed by using different mesh discretizations (M1, M2 and M3). 122

Fig. 4.37: M1 configuration: synoptic representation of the mesh motion during the crack propagation. 123

Fig. 4.38: Experimental Setup: (a) SCB specimen; (b) ASCB specimen. 123

Fig. 4.39: Cutting samples by using Denford CNC router...124

Fig. 4.40: Experimental Setup: Load machine, digital camera and high speed led lights. 125

Fig. 4.41: Load – midspan vertical displacement relationship and DIC strain maps: (a) SCB specimen..126

Fig. 4.42: Load – midspan vertical displacement relationship and DIC strain maps: ASCB specimen (S_2=5.5 mm) 126

Fig. 4.43: (a) uniformly distributed opening force applied along the upper skin of the panel; (b) point opening force applied at the cracked edge of the panel (b); detail of the mesh discretization in the core (c)...128

Fig. 4.44: Load-displacement response: uniformly distributed opening force. 129

Fig. 4.45: Load-displacement response: point opening force. 130

Fig. 4.46: Uniformly distributed opening force: Von Mises contour plots and crack evolution for different loading steps. 130

Fig. 4.47: Point opening force: Von Mises contour plots and crack evolution for different loading steps...130

Fig. 4.48: Uniformly distributed opening force: interfacial stresses across the upper cohesive interfaces at different value of core’s crack tip positions. 131

Fig. 4.49: point opening force: interfacial stresses across the upper cohesive interfaces at different value of core’s crack tip positions...132

List of Tables

Tab. 2.1: Mechanical and geometrical properties of the laminates (single delamination). 29
Tab. 2.2: Interface properties of the laminates (single delamination)...............................29
Tab. 2.3: Mechanical and geometrical properties of the laminates (multiple delamination). 36
Tab. 2.4: Interface properties of the laminates (multiple delamination)...........................36
Tab. 2.5: Mechanical and Interface properties of the laminates (single delamination). ..41
Tab. 2.6: Properties of the single nonlinear spring (z-pin T300/BMI). 41
Tab. 3.1: Incremental-iterative procedure of the proposed algorithm. 62
Tab. 3.2: Mechanical and geometrical properties of the layered structures reported in Fig. 3.6...63
Tab. 3.3: interface properties of the layered structures reported in Fig. 3.6. 64
Tab. 3.4: Mechanical and geometrical properties of the layered structures reported in Fig. 3.11...68
Tab. 3.5: Interface properties of the layered structures reported in Fig. 3.11. 68
Tab. 3.6: Geometrical and mechanical properties of the steel beam [21]. 74
Tab. 3.7: Geometrical and mechanical properties of the adhesive layer. 74
Tab. 3.8: Geometrical and mechanical properties of the FRP strip [21]...........................74
Tab. 3.9: Interfaces parameters of the Adhesive-Steel interface and Adhesive-Frp interface [21]. 75
Tab. 4.1: Geometrical, mechanical and interface properties..90
Tab. 4.2: Geometrical, mechanical and interface properties..95
Tab. 4.3: Incremental-iterative procedure of the proposed algorithm. 108
Tab. 4.4: PMMA Beam simulated configurations. 117
Tab. 4.5: Experimental results in terms SIFs and maximum load reached. 127
Tab. 4.6: Mechanical and interface properties of the structures reported in Fig. 4.43. ..128

Abstract

The study presented in this PhD thesis is focused on development of advanced numerical models to describe crack propagation and interface decohesion phenomena in laminate and sandwich structures. The general idea is to simulate crack tip motion by using a moving mesh methodology to reproduce quasi-static and fast crack propagation phenomena in layered structures. Without going into too much details, the nodes are moved to predict changes of the geometry produced by the crack motion allowing to avoid several remeshing and saving computational time. The thesis presents a series of numerical investigations, which are performed in order to validate the introduced features in the numerical methodology along the development process.

The starting point of the research was the investigation of the interface crack propagation phenomena in multilayered structures simulated by using shear deformable beam elements. The theoretical formulation was based on Arbitrary Lagrangian and Eulerian (ALE) methodology and cohesive interface elements, in which weak based moving connections are implemented by using a finite element formulation. In this framework, only the nodes of the computational mesh of the interface region are moved on the basis of the predicted fracture variables, reducing mesh distortions by using continuous rezoning procedures. The use of moving mesh methodology in the proposed model allow us to introduce nonlinear interface elements in a small region containing the process zone, reducing the numerical complexities and efforts, typically involved in standard cohesive approach.

Furthermore, this numerical methodology was developed to investigate the strategy commonly adopted to improve the interlaminar strength of composite laminate. Basically, in order to simulate the z-pins reinforced area, a set of discrete nonlinear springs fixed to material domain was introduced.

As is well known, a very important feature that should have a numerical model is the capability to simulate both crack onset condition and coalescence phenomena in structures with initial perfect interfaces. To this end, proper script files were carried out to manage the steps involved in the procedure, regarding the geometry variation due to the crack onset, the debonding length definition and the mesh enrichment in the process zone. The numerical strategy could be solved in both static and dynamic frameworks, taking into account time dependent effects produced by the inertial characteristics of the structure and

the boundary motion involved by debonding phenomena. In both cases, the governing equations have been integrated by means of proper stop and restart conditions, to modify the computational mesh due to the onset of debonding phenomena. The ability of the proposed model has been verified by simulating several onset configurations, including the case, in which multiple debonding mechanisms with coalescence affect the interfaces.

The research project has been focused on the study of the sandwich structure failure modes. From physical and mathematical viewpoints, two main issues are demanding a detailed understanding of the mechanical behaviour of sandwich panels: the propagation of internal macro-cracks in the core and the delamination at skin/core interfaces. To concern the delamination between skin and core, previous numerical strategy, already used in the framework of composite laminate, was generalized simply by modifying the relative displacement between skin (shear deformable beam) and core (2D plane stress formulation).

In order to simulate the macro crack propagation in the core, the ALE approach has been generalized in two-dimensional framework. The approach has combined concepts arising from structural mechanics and moving mesh methodology, which was implemented in a unified framework to predict crack growth on the basis of Fracture Mechanics variables. In particular, moving computational nodes were modified starting from a fixed referential coordinate system on the basis of a crack growth criterion to predict directionality and displacement of the tip front. The use of rezoning mesh methods coupled with a proper advancing crack growth scheme has ensured the consistency of mesh motion with small distortions and an unaltered mesh typology. In addition, the moving grid was modified from the initial configuration in such a way that the recourse to remeshing procedures has been strongly reduced. Numerical formulation and its computational implementation have shown how the proposed approach can be easily embedded in classical finite element software. Numerical examples in presence of internal material discontinuities and comparisons with existing data obtained by advanced numerical approaches and experimental data have been proposed to check the validity of the formulation.

Furthermore, the crack propagation in the core of sandwich structures has been analysed on the basis of fracture parameters experimentally determined on commercially available foams.

The (summary) thesis comprises the following: Chapter 1 - Introduction (thesis topics, literature review, aims and scope); Chapter 2 and 3 - present theoretical formulation and numerical implementation followed by results of the numerical methodology to describe crack onset, propagation and coalescence respectively; Chapters 4 - reports the numerical investigation about sandwich structure failure modes and the generalization of the ALE approach to simulate crack propagation in 2D continuum (core); Chapters 5 -presents the conclusions and future works

Abstract (Italian version)

Lo studio presentato in questa tesi di dottorato è focalizzato sullo sviluppo di modelli numerici avanzati per la simulazione dei fenomeni di frattura e delaminazione interfacciale che posso avvenire nelle strutture multistrato e nei pannelli sandwich. L'idea generale è di simulare il movimento dell'apice della frattura usando la tecnica della *moving mesh*, che consente di riprodurre il fenomeno sia in ambito statico che dinamico. In particolare, la posizione dei nodi computazionali è modificata al fine di predire il cambiamento di geometria generato dall'avanzamento della frattura. Questo ha ripercussioni sulla riduzione degli eventi di *remeshing*, con conseguente riduzione della complessità computazionale. La tesi è corredata da una serie di investigazioni numeriche, le quali sono eseguite al fine di validare le peculiarità del modello numerico formulate ed introdotte durante le fasi di sviluppo.

Nella prima fase, il progetto di ricerca si è incentrato sull'analisi dei fenomeni di propagazione della delaminazione in strutture multistrato, le quali sono state simulate utilizzando elementi trave deformabili a taglio. La formulazione teorica è basata sull'approccio ALE (*Arbitrary Lagrangian and Eulerian*) e un modello di interfaccia coesiva, i quali sono stati accoppiati adoperando un codice agli elementi finiti. In questo contesto, solo i nodi computazionali che si trovano all'interfaccia sono modificati sulla base del soddisfacimento di un appropriato criterio di propagazione della frattura. L'uso della *moving mesh* ci ha permesso di introdurre le non linearità soltanto intorno la zona di processo. Questa scelta ha avuto importati ripercussioni sulla riduzione della complessità numerica e dell'onere computazione.

La metodologia numerica sopra descritta è stata adoperata anche per verificare il funzionamento delle tecniche oggi adoperate per migliorare la resistenza intralaminare dei laminati in composito. A tal fine i rinforzi intralaminari sono simulati utilizzando un set di molle non lineari fissate al dominio materiale. In questo contesto, il modello numerico è caratterizzato dalla presenza di due zone di interfaccia coesiva: la prima implementata nel dominio mobile (interfaccia), la seconda fissa al dominio materiale (z-pins).

Come è noto, una caratteristica molto importante che dovrebbero avere i modelli numerici, è la capacità di simulare sia le condizioni di innesco della delaminazione che il fenomeno della coalescenza. A tal fine, un codice Matlab® è stato sviluppato per gestire i passaggi

necessari per garantire l’efficienza del modello numerico proposto. Il codice Matlab®, ha avuto come obiettivo l’automatizzazione di alcuni passaggi come: la variazione di geometria causata dall’avanzamento della frattura, la definizione della zona di processo e l’infittimento della mesh in zone precise. La strategia numerica può essere risolta sia in ambito statico che dinamico, semplicemente tenendo in considerazione gli effetti prodotto dalle caratteristiche inerziali e dal movimento della zona di processo. Il modello numerico è stato validato attraverso molte simulazioni numeriche e confronti con risultati presenti in letteratura: casi di delaminazione multipla e fenomeni di debonding nei quali si verificano fenomeni di coalescenza.

Successivamente, il lavoro di ricercaha riguardato lo studio delle modalità di fallimento dei pannelli sandwich. Dal punto vista fisico e matematico, il modello numerico dovrebbe essere in grado di simulare le due principali modalità di fallimento dei pannelli sandwich: la propagazione della frattura nel *core* e la delaminazione all’interfaccia tra *skin* e *core*. Riguardo la delaminazione tra *skin* e *core*, la strategia già sviluppata nel contesto delle travi multistrato, è stata generalizzata modificando le equazioni per il calcolo dello spostamento relativo tra *skin* (simulata attraverso una trave deformabile a taglio) e *core* (simulato attraverso elementi 2D in stato piano di tensione).

Al fine di simulare la propagazione della macro-frattura nel *core*, l’approccio ALE è stato generalizzato in ambito bidimensionale. Il modello numerico combina la meccanica strutturale e la metodologia delle *moving mesh*, che sono accoppiate in un singolo modello per predire la propagazione della frattura sulla base di un criterio consistente con la teoria della Meccanica della Frattura.

I nodi computazionali vengono modificati da un sistema di riferimento referenziale sulla base di un criterio di avanzamento della frattura capace di rilevare la direzione e lo spostamento dell’apice della cricca. Al fine di garantire l’efficienza numerica del metodo, un ruolo fondamentale viene giocato dai metodi di *Smoothing* e *Rezoning*, che accoppiati con un appropriato schema di avanzamento della frattura evitano il ricorso ed onerosi eventi di *remeshing*. La formulazione numerica e la sua implementazione mostrano come l’approccio proposto sia facilmente implementabile in un codice agli elementi finiti. Numerosi esempi numerici in presenza di discontinuità interne e confronti con dati sperimentali sono stati eseguiti al fine di controllare e validare la formulazione proposta.

Infine, la propagazione della frattura nel *core* dei pannelli sandwich è stata analizzata sulla base di parametri sperimentali determinati testando *core* semi-rigidi comunemente adoperati per nella fabbricazione dei pannelli sandwich.

Il sommario della tesi comprende quanto segue: Capitolo 1 - Introduzione (argomenti trattati, revisione della letteratura, obiettivi e scopi); Capitoli 2 e 3 - presentano la formulazione teorica e l'implementazione numerica seguita da risultati numerici della metodologia numerica per descrivere i fenomeni di innesco, propagazione e coalescenza; Capitolo 4 - riporta le analisi numeriche riguardo i pannelli sandwich e la generalizzazione dell'approccio ALE per simulare la prolazione del crack in un continuo bidimensionale (core); Capitolo 5 - presenta le conclusioni ed i possibili sviluppi futuri.

Chapter 1 **Introduction**

In this chapter, a review of the state-of-the-art of numerical methodologies utilized to predict fracture phenomena in multi-layered structures is reported. In particular, numerical methods able to describe interfacial delamination phenomena in layered structures will be discussed. Moreover, theoretical and numerical approaches to simulate the effect of interlaminar reinforcements will be presented. Finally, some considerations about the failure modes and their numerical description in the framework of sandwich structures will be shown.

1.1 Thesis topics

Failure analysis of layer composite structures has attracted a great deal of interest in recent years due to the increased application of composite materials in a wide range of high performance structures (Fig. 1.1). Extensive experimental and theoretical studies have concentrated to report delamination toughness data of new composite materials; others dealt with various delamination test and numerical simulations. A particular class of layer structures are the sandwich panels. Throughout the 20th and 21st century, sandwich structures have received increasing attention, because of their excellent structural properties that pioneer the lightweight construction design. sandwich structures owe their exceptional structural performance is generated using two thin layers of a stiff and strong material (skins) separated and bonded together by a light and compliant material (core). Due to their layered nature, sandwich structures can experience a variety of different failure modes of which some are unique in that are unique to sandwich structures not encountered in more commonly used structural elements. The stiffness and thermal mismatch between the face-sheets and core material can lead to local stress states that in some cases can lead to damaging and premature failure. Further, the bonding of the face-sheets to the core material is crucial for the structural integrity of the sandwich, and this may be compromised due to the complexity of the manufacturing process. In the case where plies are separated by weak interfaces their layered nature may lead to separation of the layers. Sandwich structures are sensitive to localized damage in one or more of their constituents as well as the interfaces between the face-sheets and the core, and this may lead to initiation of damage and consequently loss of structural integrity.

1.2 Layered structures

Layer structures, such as composite laminates or reinforced concrete beams strengthened with FRP materials, typically exhibit a low resistance to damage with respect to interlaminar damage mechanisms. In particular, such materials are typically composed of layers connected through interfaces, in which material discontinuities due to production processes or high interlaminar stresses may be generated. In the following subsections, critical review about strategies to model interfacial delamination phenomena and interlaminar strength are reported.

Fig. 1.1: Composite materials, field of application.

1.2.1 Modelling of interfacial delamination phenomena

Debonding phenomena may affect several classes of structures ranging from thin film, layered materials, composite laminates or strengthened reinforced concrete beams. In any cases, damage phenomena strongly reduce the structural integrity, leading to catastrophic failure mechanics, which are essentially of dynamic nature. In literature, several approaches and formulations able to predict crack growth in layered structures ranging from micro-, meso- and macro- scales are proposed.

A distinction should be made concerning existing formulations available from literature, since explicit or implicit crack representations could be used to simulate interfacial defects [1]. Implicit crack formulations are essentially based on continuum models, in which constitutive relationships are introduced in the governing equations to predict stiffness reductions. However, such modelling does not provide any information about the length scale, which is much important to describe fracture phenomena; moreover, it is unable to capture the formation of few dominant cracks leading to failure mechanisms. In this framework, an accurate choice of the mesh discretization is required, which is typically adopted in such a way that the mesh spacing coincides with the internal length involved by the material discontinuities.

As a consequence, in the literature discrete or explicit models are preferred to continuum approaches. In the explicit representations, the internal discontinuities are considered as geometrical entities of the model, which should be updated as far as their shape is modified.

In this framework, constrained or arbitrary shape methods are well known in literature. In the former approach node-decoupling or node splitting techniques are easily endorsed in standard Finite Element Method (FEM) or Boundary Element Method (BEM) formulations, since the crack path is known in advance [2]. However, more advanced formulations are proposed in the case of arbitrary shape approaches, in which the initial discontinuities have no restrictions on both size and shape during their evolution. To this aim, meshless based methodologies, which do not require any spatial discretization or node connectivity, are proposed, since the local approximation is mainly governed by interpolation functions defined on a fixed mesh outline. Intrinsic complexities arise in order to reproduce essential boundary conditions for complex structures or to achieve the required local accuracy of the fracture variables at the near-tip level. Additional formulations, based on adaptive FEM/BEM methods, propose an explicit description of the micro-cracks in structures by updating the current mesh to the evolving cracked geometry [3]. Such models require an efficient treatment of both mesh functions and discretization processes, since, during the crack advance from the internal to boundary edges, the element topology of the structure must be guaranteed [4].

It is worth noting that previous models defined above, in order to simulate debonding phenomena in both initiation and evolution phases, require specific formulations and numerical tools to quantify the corresponding fracture parameters. To this end, the crack growth can be expressed as a function of Fracture Mechanics (FM) variables such as Stress Intensity Factor (SIF) or Strain Energy Release Rate (SERR), whose definition requires the existence of an initial cracked length and a small region in which separation phenomena take place [5]. As far as the crack length vanishes, the ERR is not defined and the stresses are not affected by the classical singularity behaviour. However the inability to reproduce crack initiation can be circumvented by proper crack criteria, that utilize coupled relationships described in terms of energy and stress variables and evaluate the applied loading, crack onset and evolution [6, 7].

Alternatively, cohesive models propose an easy way to simulate debonding phenomena including crack onset. The cohesive approach was firstly developed, alternatively, to FM, by introducing the possibility to mitigate stress singularity and to simulate large scale decohesion phenomena. To this end, distributed or discrete interface elements are introduced between continuum elements based on traction separation damage laws [8]. In terms of modelling, Cohesive Zone Method (CZM) is widely used to reproduce fracture phenomena, in which interface elements with a softening constitutive relationship are inserted in the finite element mesh [2]. In this framework, several models are proposed in the literature, which are mainly classified as either non-potential or potential-based models [9].

Non potential-based cohesive interaction models are relatively simple to develop, because a symmetric system is not required. However, these models do not guarantee consistency of the constitutive relationship for arbitrary mixed-mode conditions, because they do not account for all possible separation paths. For potential-based models, the traction-separation relationships across fracture surfaces are obtained from a potential function, which characterizes the fracture behaviour. Note that the existence of a potential for the cohesive constitutive relationship is addressed in conjunction with the non-negative work for closed processes. Due to the nature of a potential, the first derivative of the fracture energy potential provides the traction (cohesive interactions) over fracture surfaces, and its second derivative provides the constitutive relationship (material tangent modulus).

Several potential-based models are available in the literature; such as, models with specific polynomial orders, models with exponential expressions, and a model with general polynomials. Each model possesses advantages and limitations. There are generally required characteristics for cohesive constitutive relationships, which are summarized as follows:

- the traction separation relationship is independent of any superposed rigid body motion.
- the work to create a new surface is finite, and its value corresponds to the fracture energy, i.e., area under a traction separation curve.
- the mode I fracture energy is usually different from the mode II fracture energy.
- a finite characteristic length scale exists, which leads to a complete failure condition, i.e., no load-bearing capacity.
- the cohesive traction across the fracture surface generally decreases to zero while the separation increases under the softening condition, which results in the negative stiffness.
- a potential for the cohesive constitutive relationship may exist, and thus the energy dissipation associated with unloading/ reloading is independent of a potential.

As reported in [9], the Cohesive traction-separation relationships may be obtained by employing theoretical, experimental and computational techniques. For example, based on the J-integral approach, a traction-separation relation was obtained for double cantilever beam specimens [10]. Inverse analyses were employed to calibrate a traction-separation relationship so that the best predicted global load-displacement curve was achieved [11, 12]. Based on a measured local displacement field, digital image correlation techniques and inverse analysis were employed to estimate fracture parameters and determine traction-separation relationships [13, 14]. Additionally, macroscopic traction-separation relationships were also obtained by considering microstructure in conjunction with multiscale analysis [15]. Several constitutive relationships of the cohesive zone model have been developed on the basis of an effective displacement (Δ) and an effective traction ($T(\Delta)/\sigma_{\max}$). The effective displacement and traction easily define various cohesive relations such as cubic polynomial [16], trapezoidal [17], smoothed trapezoidal [18], exponential [19], linear softening [2] and bilinear softening [20] functions, as shown in Fig. 1.2.

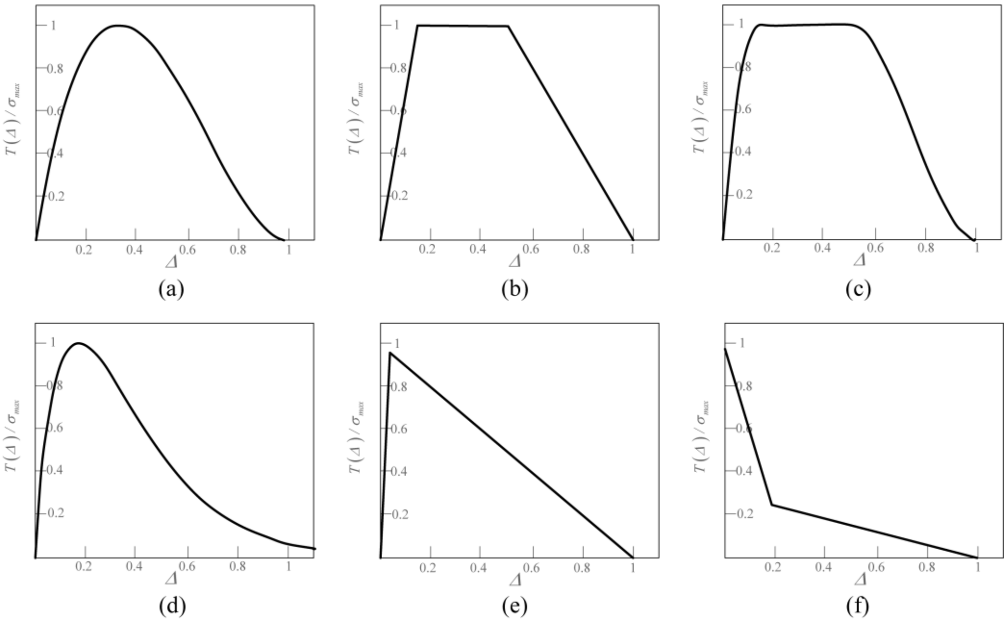

(a) (b) (c)

(d) (e) (f)

Fig. 1.2: Effective traction-separation relationships: (a) cubic polynomial, (b) trapezoidal, (c) smoothed trapezoidal, (d) exponential, (e) linear softening, and (f) bilinear softening [9].

However, the cohesive approach shows some numerical limitations. Such modelling is strictly dependent from the mesh discretization since the direction of crack propagation is restricted by the element size and orientation adopted by the user. Moreover, the presence of an initial finite stiffness may produce in brittle solids an excess of compliance and in those cases in which a high stiffness is introduced spurious traction oscillations [8]. Such problems may be partially circumvented by introducing a very fine discretization at the crack tip front to obtain a high resolution of the characteristic fracture length of the interface [21]. The resulting model is affected by computational complexities, because of the large number of variables and nonlinearities involved along the interfaces. To this end is needed combines the CZM modelling together a numerical scheme able to decrease the computational efforts by keeping the advantages earlier mentioned.

1.2.2 Modelling of interlaminar reinforcement systems

The structural systems in the form of laminates are typically affected by several kind of failure modes, such as debonding, interlaminar cracks, affecting matrix, fiber or fiber/matrix interfaces, which produce relevant loss of toughness and catastrophic collapse mechanisms [22]. In order to improve the performance against debonding or delamination failure modes, several techniques are proposed [23], in which FRP or advanced materials are utilized effectively in straight or arched structure [24-26]. Alternatively, Through-The-Thickness (TTT) elements, such as rods or z-pins, are introduced prior to resin infusion in textile laminates or in uncured pre-preg materials as shown in 3D weaving, stitching methods or Z-pinning techniques [27], leading to an improved debonding resistance. In particular Z-pinning approach is widely used in several structural applications ranging from aerospace to automotive. Pins may be used for the wide-area reinforcement of damage tolerant panels or used in selective areas requiring local reinforcement, such as structural bonds, stiffener attachments, stress concentrations and holes.

Z-pins act as fine nails that lock the laminate plies together by a combination of friction and adhesion (Fig. 1.3). Thin metal rods were first used to reinforce laminates in the 1970s, although the pins were inserted individually using a labour-intensive manual process that is not practical for large-scale production [27]. Various methods are used to manufacture z-pinned laminates, with the most common method being the process that involves inserting z-pins into an uncured prepreg stack using an ultrasonic tool. The process starts by placing a polymer foam carrier containing z-pins over the prepreg (Fig. 1.4). Z-Pins are made from extruded metal wire or fibrous composite produced by pulling a continuous fibre tow through a resin bath and then pultruding it through a circular die. The metal wire or composite strand is then cut to length and inserted into the foam carrier. The foam is used to ensure an even spacing between the z-pins and to provide them with lateral support during insertion. The foam carrier does not form part of the final composite product, and is discarded after the z-pins have been inserted. z-Pins are driven from the foam carrier into the prepreg using an ultrasonically actuated tool that can be operated in a manual hand-held mode by a trained operator or controlled using an automated system (Fig. 1.4b). The ultrasonic horn generates high frequency compressive waves that are transmitted into the foam carrier, which collapses under the pressure that drives the z-pins into the prepreg. The stress waves also cause moderate heating of the prepreg that softens the resin matrix which eases insertion of the pins. z-Pins are inserted progressively by moving the ultrasonic tool over the foam carrier several times until all the pins have penetrated the prepreg stack (Fig. 1.4c). The compressed foam carrier and any excess length of z-pin protruding the prepreg is shaved off using a blade to ensure a smooth surface finish (Fig. 1.4d) [27].

With the purpose to define they structural performance, the behaviour of z-pins was extensively investigated in the literature from both experimental and numerical points of view. Improvements provided by Through-The-Thickness (TTT) reinforcements are quite dependent from the geometry and their interaction with the host material [28]. Moreover, the benefits provided by the external reinforcements are observed only in those cases in which debonding phenomena are triggered and, consequently, pull-out or shear forces applied to TTT elements are activated [29].

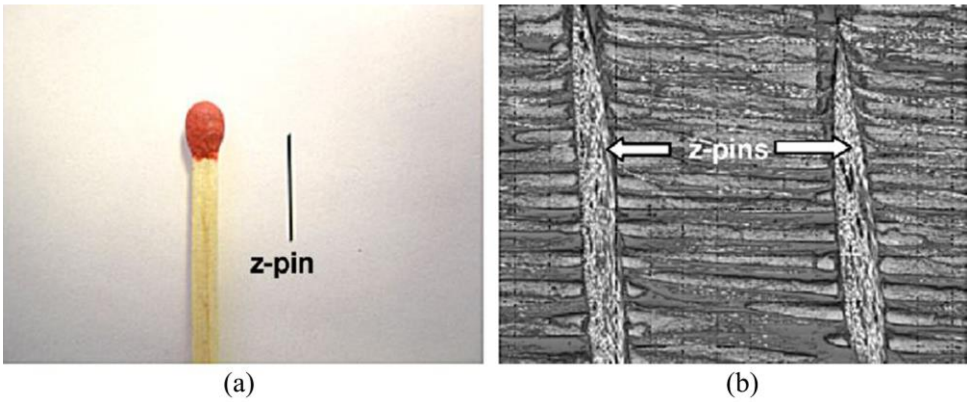

Fig. 1.3: (a) Photograph showing the size of a typical z-pin and (b) z-pins inside a prepreg composite [27].

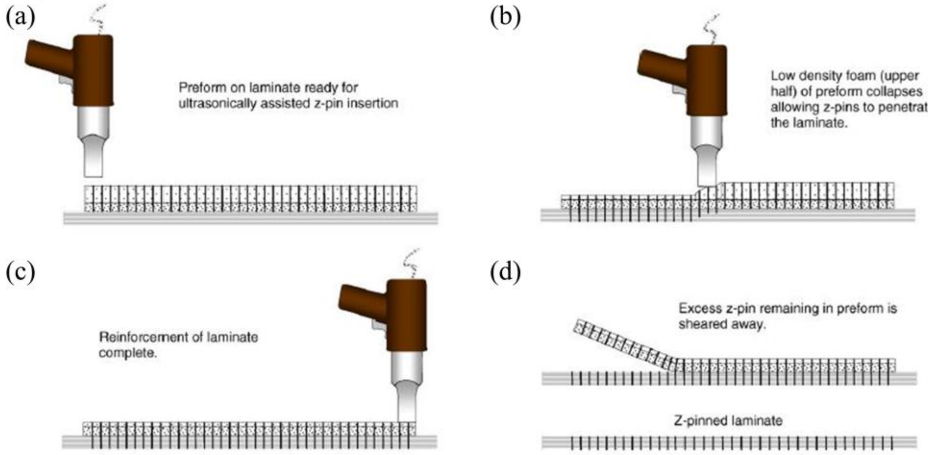

Fig. 1.4: Schematic application process of z-pins[27].

Therefore, crack initiation, growth and interlaminar strengthening effects should be described accurately by using coupled modelling to reproduce correctly the actual behaviour. In this framework there are two issues: the strategy adopted to simulate the effects of z-pins and the and the modelling of the interfacial delamination. To this end, distributed cohesive elements reproducing z-pins behaviour with averaging bridging forces over the whole interfacial areas have been proposed [30]. Such modelling provides good results mainly for low z-pin spacing step. To this end, discrete interface elements with nonlinear traction separation laws are developed in the literature to simulate the individual behaviour of a single z-pin. In both cases, under a mode I loading condition, the traction forces are quite dependent from the pull-out mechanism, which is influenced mainly by z-pin characteristics, i.e. matrix/host material frictional contact and strength [31]. Moreover, under a mode II loading case, the traction forces, in proximity of the crack surfaces, are dominated by local shear bond integrity [32]. The generalization of the above referred analyses to mixed mode cases requires the evaluation of coupled relationships, in which the traction separation laws based on equivalent sliding and normal stress-strain relationship should be introduced to identify accurately the z-pin bridging response. Refined models based on micromechanics analyse complex phenomena concerning frictional sliding at the interface, resin deformation and z-pin failure mechanisms on a RVE containing a single z-pin [33, 34].

In order to investigate the behaviour of z-pinned composite laminates, it is required to reproduce an accurate modelling not only in the definition of the z-pins but also to identify the interlaminar mechanisms arising from delamination or debonding phenomena. This point is of particular relevance, since the z-pin pullout mechanisms are triggered by the internal discontinuities which could be in the structure as pre-existing due to manufactory processes or produced, during the structural service life, due to stress-concentration effects. The prediction of the crack growth in laminates requires efficient methods, that are able to reduce computational costs involved in the solving procedure, which are typically observed under dynamic loading because of the wave material characteristics [35-41]. Actually, traditional FEM based analyses, typically require remeshing/re-modelling procedures to predict evolving and propagating cracks [39, 42, 43]. In order to overcome such difficulties, several techniques, developed in the framework of the FEM, are proposed. In particular, CZM method takes into account interfacial discontinuities by introducing cohesive separation laws along possible crack paths, in which debonding phenomena may affect the structure [8]. Moreover, in presence of interlaminar reinforcements, homogenized constitutive relationships should be defined to reproduce discrete pull-out mechanisms arising from the presence of z-pin and distributed Traction Separation Laws (TSL) to predict debonding phenomena [44]. The prediction of crack initiation and growth is intrinsically achieved by the computational strategy based on the CZM approach, but the model requires a refined mesh to correctly evaluate the interfacial variables as well as proper numerical procedures to overcome numerical complexities involved by nonlinear constitutive relationships [45]. Fracture Mechanics (FM) is able to reproduce crack growth on the basis of ERR or SIF, whose definition requires the existence of an initial cracked length and a small region, in which bridging phenomena may take place [46]. However, complexities may arise in the definition of the fracture variables during the transition of the crack tip to the region strengthened by the interlaminar reinforcements. Previous approaches require accuracy in the definition of the fracture variables by means of a proper mesh discretization in the region containing the process zone. The presence of interlaminar reinforcements introduces additional traction forces along the interfaces, which are triggered when material discontinuities reach z-pin elements. Moreover, interlaminar reinforcements introduce stress concentration effects, producing crack onset conditions along the interfaces, which should be accurately identified.

1.2.3 Sandwich Structures

Sandwich structures are a particular class of composites consisting of two thin face sheets made of stiff and strong materials such as metal or fiber reinforced composites bonded to a thick and deformable core with low density [47]. They are able to ensure a good resistance under bending/shear loading, offering a great variety of lightweight structural systems. Unfortunately, sandwich panels are affected by both macroscopic and microscopic damage phenomena, mainly produced by the heterogeneity of the layered systems, which reduce the integrity of the composite structure, leading to catastrophic failure mechanisms [48].

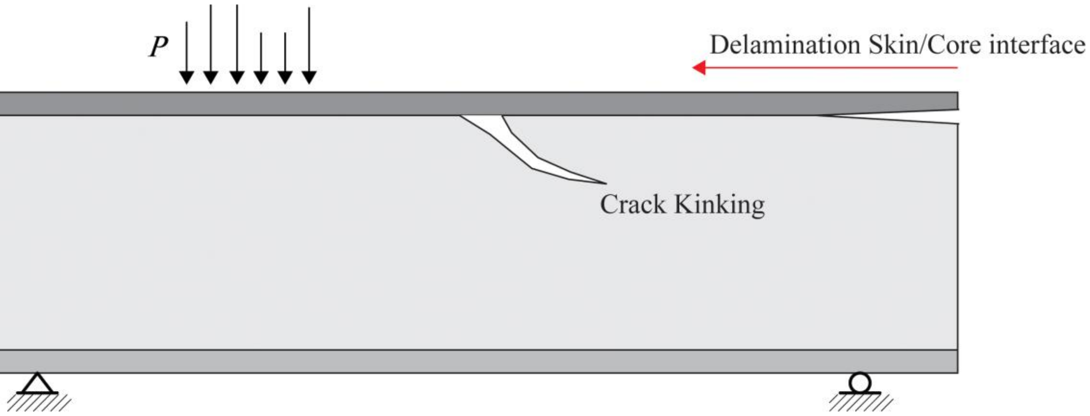

Fig. 1.5: Schematic representation of two failure mode of Sandwich Structures: Crack Kinking and Skin/Core interface de-choesion.

From physical and mathematical viewpoints, two main issues are demanding a detailed understanding of the mechanical behaviour of sandwich panels: the propagation of internal macro-cracks in the core [49] and the delamination at face/core interfaces [50]. In order to describe skin/core delamination (Fig. 1.5), several approaches have been proposed in literature. In particular, the analysis started by means of macroscale approaches, in which analytical and numerical formulations aimed to identify critical failure loads for design purpose were developed [51]. Specific modelling techniques are required to predict crack tip motion of internal material discontinuities. Interface elements based on Cohesive Zone Model (CZM) or Linear Elastic Fracture Mechanics (LEFM) are frequently used to predict crack tip evolution. Discrete or distributed interface elements can be easily incorporated into FEMs, by introducing constitutive traction forces between adherent internal surfaces [8]. These methodologies are frequently used in sandwich structures to predict the crack evolution at the core/skin interfaces, since the crack motion is expressed as a function of a linear positional variable coinciding typically with the interface coordinate. However, such modelling is affected by numerical problems due to mesh dependence, computing inefficiency, and sensitivity to the element aspect ratio. These issues may be partially addressed by adopting a very fine discretization at the crack tip front, but numerical complexity remains, due to the high number of computational points requested.

The considerations reported in the section 1.2.1, which are referred at the layered structures are valid also in the framework of the delamination at the skin/core interfaces of sandwich panels.

1.2.3.1 Modelling of crack propagation phenomena in 2D solids

Sandwich structures can be affected by macro-cracks in the core (Fig. 1.5). Quite complex scenarios are observed in presence of kinking phenomena of the crack, starting from the interfaces. In these cases, the crack growth requires more advanced numerical modelling techniques, since it needs to be expressed both in terms of angle of propagation and tip displacement. Computational fracture mechanics has been considered an active research area aimed to predict crack growth and failure scenarios in structural and mechanical systems. In particular, computational methods are frequently utilized to assess vulnerability and reliability of cracked structures, in terms of ultimate load capacity and evolution of pre-existing cracks. However, the arbitrariness of the crack path requires proper numerical procedures, since, numerical instability phenomena affect the structural system by means of stiffness reduction and fast crack propagation mechanisms.

Most of the models available from the literature are developed by using the FEM because of its ability to model complex structures, ensuring accuracy in the prediction of interfacial variables between dissimilar materials. To begin with, crack propagation was simulated for prescribed or constrained crack representations by means of node-release or node-decoupling techniques [52]. In this framework, CZMs were frequently utilized with large success, by introducing interface elements with a constitutive damage law, in the region affected by the crack evolution [8]. However, since the crack trajectory is not known “a priori”, interface elements require to be introduced in the whole structure or at least where the crack path is expected. Such problem produces a large increase of the computational costs and numerical complexities of the model [53, 54]. Moreover, due to the presence of nonlinearities involved in the constitutive laws, the governing equations are affected by ill-posed problems[2]. However, in those cases in which the crack path is arbitrary, FEM computational formulations require to modify the positions of the computational grid elements [55] to simulate the evolution of the crack advance. Such task was achieved by the use of adaptive mesh methods [56], which modify, according to the cracked geometry, the current computational points, ensuring consistency in the mesh element topology. Although, mesh refinement is enforced, locally, at the crack tip region, advanced numerical tools should be considered to avoid loss of accuracy during the mapping procedure. The recourse to remeshing procedures is quite cumbersome and typically produces high computation efforts during the transition procedure[57]. BEM could be utilized in Fracture Mechanics, in which only the boundaries of the structure are represented by using a mesh discretization and not the internal domains. Such hypothesis simplifies remeshing procedures, reducing the computational costs required to generate new elements. However, complexities still remain in the definition of singular integral [58]. Alternatively to FEM/BEM approaches, Meshfree methods are implemented with the purpose to eliminate the mesh discretization from the numerical model and to identify the solution in terms of nodal quantities [59]. The accuracy of the modelling is determined by the influence function and its dependence from the reference nodes. Meshfree methods avoid the use of remeshing procedure, since the current solution is expressed as a function of the nodal quantities only. However, such methodology is affected by intrinsic complexities in the definition of essential boundary conditions especially when Kronecker delta property is not verified, leading to high computational costs in the solving procedure [42].

Previous formulations are classified in the literature as “geometrical representation” approaches, since an explicit definition of the cracked surface is required by the numerical models to evaluate fracture variables and subsequent crack propagation. In addition, specific updating procedures are needed to simulate the evolution of internal material discontinuities. Alternatively, formulations based on an implicit definition of the crack area are developed, in which constitutive relationships with softening damage or kinematic laws able to predict strain localization effects [60, 61]. The former, known as smeared crack representations, simulates the presence of material discontinuities by constitutive degradation models, which are supposed to affect mesh elements, when damage activation conditions are satisfied. Such methodologies are typically affected by mesh-dependence phenomena as well as strain localization problems of the solution defined in terms of material internal length [62, 63]. In kinematic models, the current crack geometry is embedded in each mesh elements by modifying the strain-displacement relationship. In this framework, several approaches are proposed in the literature, known, for instance, as XFEM or GFEM [64] . The basic idea of such formulations is the use of nonconforming elements to model crack discontinuities by enriching shape functions of the mesh elements by discontinuity properties. Such formulations require further extension to predict fracture variables for nonlinear problems, especially in presence of frictional effects. Moreover, the methodology needs a different number of kinematic variables for each node and thus the total number of mesh points may vary with the crack growth [65].Others methodologies based on Discrete Element Method (DEM) [66-68]o or Meshfree Methods (MFMs) [69] have been formulated in the last decade, providing valid alternatives to study such problems. Methods based on Moving Mesh technique (MM) provide a feasible and sensible way to predict crack growth mechanisms in continuum media. Early studies were developed in [70], where MM was employed to predict energy release rate by using a virtual crack extension.

The literature review, referred to above, has shown that, currently, does not exist a unique and best approach, since each modelling presents negative and positive features.

1.2.3.2 Evaluation of the fracture parameters in cellular core material

The main aims of the core in a sandwich structure are to separate and support the face sheets, and transfer shear between the face sheets when the sandwich is subject to bending loads [47]. As described in [71], a foam material consists of a cellular structure having interconnected small solid struts and or plates forming on an open or closed cell foam. The spongy cancellous bone in animals and humans are two of many examples of foam structures occurring in nature. Substantial efforts are being made to exploit the cellular structure by using materials such as metals, ceramics and glasses. Most of the rigid polymeric foams have a linear – elastic behaviour in tension up to fracture, and a brittle failure behaviour. So, they can be treated using fracture criteria of Linear Elastic Fracture Mechanics (LEFM) [72].

In order to describe macro-crack propagation in the core region of sandwich panels, a fundamental task is to detect the fracture toughness of these materials. The evaluation of the fracture toughness and modes of such foams is important because cracks weaken the sandwich structures capacity of carrying load [73]. Many authors have developed experimental tests with the purpose to investigate fracture performance of different types of foams. There are several studies to determine mode I fracture toughness and to investigate the influence of density, loading speed and loading direction [74, 75]. A linear correlation between Mode I fracture toughness and relative density of the foam was observed by Danielsson [76] on PVC Divinycell foams, Viana and Carlsson on Diab H foams [74]. Brittle fracture without yielding produced in mode I was observed in these experiments. It is to be noted that a correlation between the static fracture toughness and relative density was proposed in [71] Kabir et al. [77] used the procedure described by ASTM D5045 [78] for determining the fracture toughness of polyvinyl chloride (PVC) and polyurethane (PUR) foams. Only few studies present the mixed mode fracture of polymeric foams, and only for PVC foams. Hallsttröm and Grenestedt [79] investigated mixed mode fracture of cracks and wedge shaped notches in expanded PVC foams. Different types of specimens made of Divinycell H100 were investigated and the non-singular T-stress was considered in formulation of fracture criteria. It was concluded that for predominantly mode II the use of T-stress improved the facture predictions. Marsavina et al. [72] presents several work about the evaluation of the fracture toughness in mixed mode. The experimental investigations were carried out on Asymmetric Semi-Circular Bend (ASCB) specimens [73, 80].

1.3 Aims and scope

The aim of this work is to develop numerical strategies consistent to moving mesh methodology and to reproduce quasi-static and fast crack propagation phenomena in layered structures. Starting from previous works, which were developed in the framework of moving mesh approach and FM, the proposed research project is targeted to couple ALE approach with cohesive methodology.

At first, the target of the proposed thesis is to develop a numerical strategy to simulate interface delamination. In this framework, interface cohesive elements and ALE formulation are coupled

Once validated the methodology earlier defined, the ALE approach is generalized in the framework of 2D structural systems. The numerical approach is aimed to reduce the recourse to remeshing events, which typically increase the computational costs.

Chapter 2 A coupled ALE-Cohesive formulation to predict interfacial debonding evolution in laminate structures

In this chapter theoretical and numerical model based on a coupled ALE-cohesive interface approach will be presented. The proposed approach is able to describe delamination phenomena of layered structures affected by a pre-existing interfacial defects. The theoretical formulation is quite general and provide the possibility to implement the effects of generalized interlaminar reinforcement such as z-pins. The outline of the chapter is as follows. Section 2.1 presents the formulation of the governing equations for the ALE and interface approaches, whereas in Section 2.2 the numerical implementation in FEM is reported. Then, in Section 2.3 the implementation of interlaminar reinforcement effects is reported. Finally, comparisons and parametric results to investigate static and dynamic behaviour of debonding phenomena are proposed in Section 2.4.

Part of analyses and results presented and discussed in this chapter were already published by the following papers:

- *Funari, M.F., Greco, F., Lonetti, P., A moving interface finite element formulation for layered structures, Composites Part B: Engineering, 2016, 96, 325-337.*
- *Funari, M.F., Greco, F., Lonetti, P., A cohesive finite element model based ALE formulation for z-pins reinforced multilayered composite beams, Structural Integrity Procedia, 2016, 2, 452-459.*
- *Funari, M.F., Lonetti, P., Pascuzzo, A., A Moving Cohesive Mesh Formulation to predict Debonding Phenomena in Layered Structures, CEPM Journal, 2018, 1(2), 16-26.*

2.1 Theoretical Formulation

The proposed model is presented in the framework laminate structures, in which thin layers are connected through adhesive elements. The theoretical formulation is based on a multilayered shear deformable beams and a moving interface approach (Fig. 2.1).

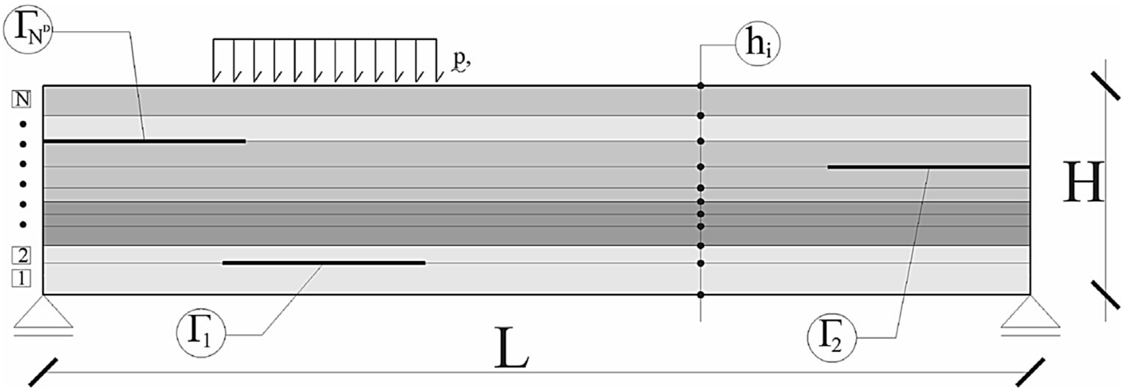

Fig. 2.1: Multilayered laminate structure: geometry and interfaces.

The former is able to reproduce 2D solution by introducing a low number of finite elements along the thickness of the structure, whereas the latter is able to simulate the crack tip motion on the basis of the adopted growth criterion [81]. The interfacial defects are assumed to propagate along the interfaces between the laminas, which are considered in this analysis as weak planes where the delaminations are able to growth. This assumption can be motivated from a physical point of view, since many experimental observations have shown that the evolution of such interfacial defects proceeds along a prescribed path almost fixed in the interface zones. Let us consider, a bounded domain $\Sigma \subset \mathbb{R}^2$ with $\Sigma = \sum_{i}^{N} \left[L \times h_i \right]$, which consists of N layers with total length L and thickness h_i. The laminate is affected by ND internal discontinuities $\left(\Gamma_{N^d}, \mathrm{i} = 1,..,N^D \right)$, which are supposed to be located along the interfaces, parallel to the longitudinal axis of the structure.

2.1.1 ALE formulation and interface approach

In order to predict the evolution of such internal discontinuities, a moving mesh methodology based on ALE approach is proposed, which is introduced only for the interface regions, leaving the governing equations of the structural model basically unaltered. To this end, fixed or material coordinates are introduced to describe structural formulation, whereas, for the interfaces affected by internal discontinuities, moving coordinates are supposed to describe the mesh motion on the basis of the predicted fracture parameter. In particular, ALE kinematic is based on the use of a fixed Referential frame (R) Ξ_R, which differs from the classical Spatial (S) or Material (M) domains, i.e. Ξ_S and Ξ_M respectively. In the spatial motion, the position $\underset{\sim}{X}$ of a physical particle in Ξ_S is described by $\underset{\sim}{X} = \Phi\left(\underset{\sim}{x}, t\right)$, with $\Phi : \Xi_M \rightarrow \Xi_S$. However, introducing the referential map $\zeta : \Xi_R \rightarrow \Xi_S$, it is possible to describe the mesh motion in terms of a fictitious referential position, namely $\underset{\sim}{\xi}$ (Fig. 2.2). Therefore, according to ALE description the following referential maps can be introduced which identify referential, material and spatial configurations:

$$\underset{\sim}{X} = \Phi\left(\underset{\sim}{x}, t\right) \qquad \underset{\sim}{x} = \Psi\left(\underset{\sim}{\xi}, t\right) \qquad \underset{\sim}{X} = \zeta\left(\underset{\sim}{\xi}, t\right) \tag{2.1}$$

where the transformation between material and referential configuration is described by the mapping Ψ with $\Psi : \Xi_R \rightarrow \Xi_M$ and $\Phi = \zeta \circ \Psi^{-1}$. Starting from Eq.(2.1) in the case of one dimensional problem, material and referential derivatives can be computed introducing the related deformation gradients:

$$\frac{d}{dX} f\left(X, t\right) = \frac{d}{d\xi} f\left(X, t\right) \frac{d\xi}{dX} = \frac{d}{d\xi} f\left(X, t\right) J^{-1} \tag{2.2}$$

where $J = dX/d\xi$ and $J^{-1} = d\xi/dX$ are the Jacobian and its inverse of the transformation, respectively.

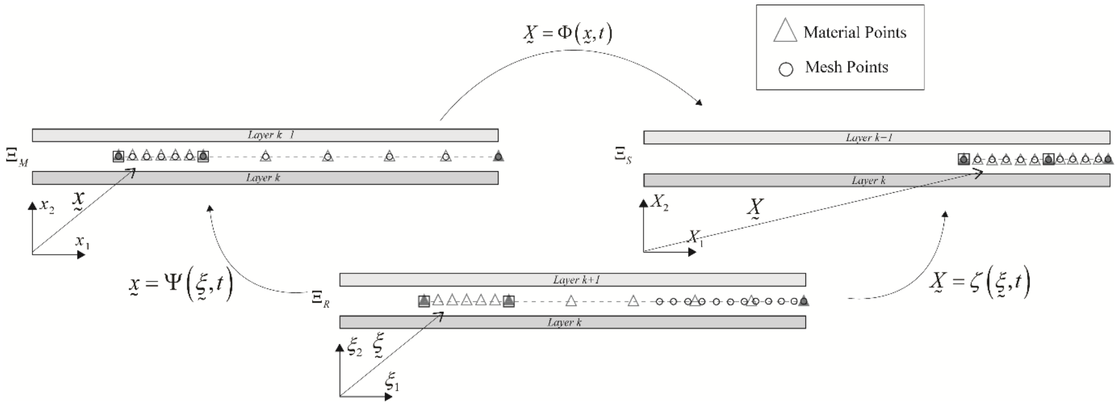

Fig. 2.2: ALE formulation: kinematic and referential configuration.

2.1.2 Governing equations

The derivation of the model is based on the principle of virtual works:

$$\delta T + \delta U + \delta W + \delta \Lambda + \delta C = 0 \tag{2.3}$$

where δT, δU, δW are the incremental works of inertial, internal and external forces, and $\delta \Lambda$ is the functional related to displacement continuity along the perfect interfaces. Moreover, δC is the work performed by the traction separation forces at those interfaces, affected by internal discontinuities. According to the first-order transverse shear deformable laminate theory and multilayered approach [82], the variational form of the governing equations can be expressed by means of the following expressions:

$$\begin{aligned}
\delta T &= \sum_{i=1}^{N} \int_{0}^{L_i} \left[\mu_i \left(\ddot{U}_{1i} \delta U_{1i} + \ddot{U}_{2i} \delta U_{2i} \right) + \mu_{0i} \left(\ddot{\Phi}_i \delta \Phi_i \right) \right] dx, \\
\delta U &= \sum_{i=1}^{N} \int_{0}^{L_i} \left[N_i \delta \varepsilon_i + M_i \delta \chi_i + T_i \delta \gamma_i \right] dx, \\
\delta W &= \sum_{i=1}^{N} \int_{0}^{L_i} \underset{\sim}{f}_i \cdot \delta \underset{\sim}{U}_i h_i dx + \sum_{i=1}^{N} \int_{0}^{L_i} \underset{\sim}{p}_i \cdot \delta \underset{\sim}{U}_i dx, \\
\delta \Lambda &= \sum_{i=1, i \neq k}^{N} \int_{0}^{L_i} \underset{\sim}{\lambda}_i \, \delta \Delta \overline{\underset{\sim}{U}}_i \, dx + \sum_{i=1, i \neq k}^{N} \int_{0}^{L_i} \underset{\sim}{\lambda}_i \, \delta \Delta \overline{\underset{\sim}{U}}_i \, dx
\end{aligned} \tag{2.4}$$

where the subscripts *i=1,..,N* and *k=1,..,N*^{D} indicate the numbering of the layers (*N*) and the interfaces (N^D) affected by debonding phenomena, $(\varepsilon, \gamma, \chi)$ $\left(\varepsilon = U_1' \ , \chi = \Phi', \gamma = \Phi + U_{2,x_1} \right)$ and $\bullet' = \dfrac{d(\bullet)}{dx}$ represent the generalized strains, (N, T, M) are the generalized stresses defined as a function of the classical extensional (A), bending (D), bending–extensional coupling (B) and the shear stiffness (H) variables, μ and μ_0 are the mass and polar mass per unit length of the layer, $\underset{\sim}{f}_i$ and $\underset{\sim}{p}_i$,with $\underset{\sim}{f}^T = \left[f_1 \quad f_2 \quad 0 \right]$ and $\underset{\sim}{p}^T = \left[p_1 \quad p_2 \quad m \right]$, are the per unit volume and area forces acting on the *i*-th layer, respectively. Moreover, virtual works performed by the cohesive elements, i.e. δC, are defined introducing a failure constitutive law along surface discontinuity, relating the displacement jump vector $\underset{\sim}{\Delta}^T = \left[\Delta_t \quad \Delta_n \right]$ and the cohesive traction vector $\underset{\sim}{T}^T = \left[T_t \quad T_n \right]$, by means of the following expression:

$$\delta C = \sum_{k=1}^{N^D} \int_{0}^{L_i} \underset{\sim}{T}^k \cdot \underset{\sim}{\Delta}^k \ dX = \sum_{k=1}^{N^D} \int_{\Omega^k} \left[T_n^k \left(X^k \right) \delta \Delta_n^k \left(X^k \right) + T_t^k \left(X^k \right) \delta \Delta_t^k \left(X^k \right) \right] dX \tag{2.5}$$

where X^k is the moving coordinates defined on the interface domain. It is worth noting that cohesive functional is related to the work performed by the traction forces, which are expressed in the moving coordinate system to simulate the crack tip motion. The evaluation of the traction forces as well as the moving discontinuities is achieved by means of a moving mesh method based on ALE formulation. In particular, the mesh motion is introduced in the process zone ahead of crack tip, by linear-decaying cohesive traction forces, which are moved as far as the growth criterion, defined by the fracture function g_f^k , is satisfied. However, in order to reproduce the crack motion, a small portion close to the crack tip, equal to the characteristics length of cohesive zone, is moved rigidly, in such a way to capture accurately the large scale cohesive effects arising from debonding phenomena. As a consequence, in Eq. (2.5), the interface region (Ω) is defined as the sum of a fixed portion Ω_{deb} and a variable one Ω_{ad}, with $\Omega = \Omega_{deb} \cup \Omega_{ad}$, in which debonding phenomena and perfect adhesion boundary conditions should be introduced:

$$\begin{aligned}\delta C = &\sum_{k=1}^{N^D} \int_{\Omega_{deb}^k} \left[T_n^k \left(X^k \right) \delta\Delta_n^k \left(X^k \right) + T_t^k \left(X^k \right) \delta\Delta_t^k \left(X^k \right) \right] dX \; + \\ &+ \sum_{k=1}^{N^D} \int_{\Omega_{ad}^k} \left[\left(k_n^k \Delta_n^k \left(X^k \right) \right) \delta\Delta_n^k \left(X^k \right) + \left(k_t^k \Delta_t^k \left(X^k \right) \right) \delta\Delta_t^k \left(X^k \right) \right] dX\end{aligned} \tag{2.6}$$

In the present study, the basic form of the cohesive law uses the formulation developed in [44], which was revised including a linear response prior the onset of fracture and the rate dependent effects [83]. As depicted in Fig. 2.3, for each mode components, the Traction Separation Law (TSL) depends on the choice of a critical cohesive stress, $\left(T_t^c, T_n^c\right)$, the critical and initial opening or transverse relative displacements, namely $\left(\Delta_n^0, \Delta_n^c\right)$ and $\left(\Delta_t^0, \Delta_t^c\right)$ by means of the following expression:

$$T\left(\Delta\right) = \begin{cases} \dfrac{T^c}{\Delta^0} \Delta & \Delta \le \Delta^0 \\ T^c \left(\dfrac{\Delta - \Delta^c}{\Delta^0 - \Delta^c} \right) & \Delta > \Delta^0 \; and \;\; \Delta < \Delta^c \end{cases} \tag{2.7}$$

where $\left(\Delta,\ T^c,\Delta^0,\Delta^c\right)$ is equal to $\left(\Delta_n,\ T_n^c,\Delta_n^0,\Delta_n^c\right)$ or $\left(\Delta_n,\ T_n^c,\Delta_n^0,\Delta_n^c\right)$ in the case of the TSL for tangential or opening modes, respectively. In order to reproduced the fracture behavior of mixed-mode cases, a mode-dependent cohesive-zone model is introduced.

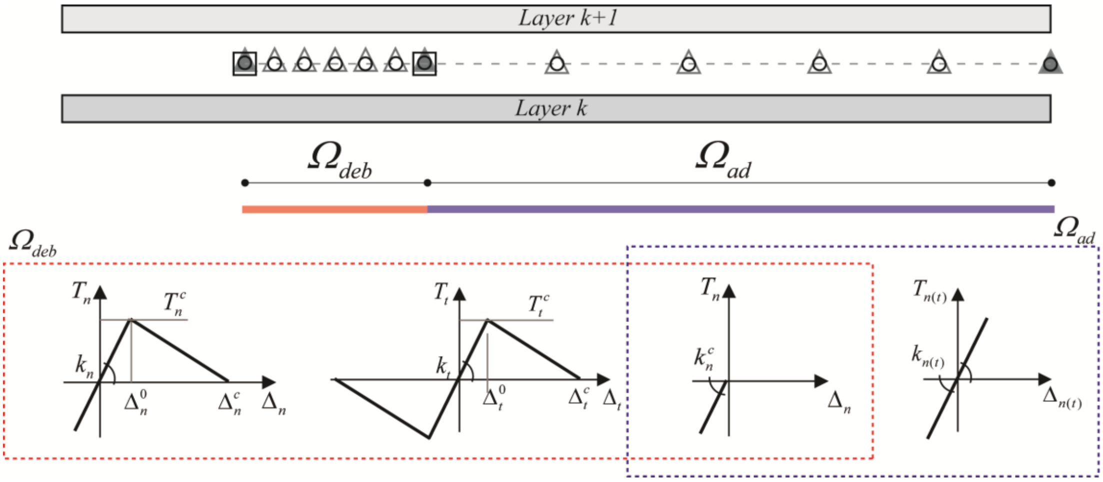

Fig. 2.3: Interface moving boundary: debonded and perfect adhesion regions.

In particular, opening and shear traction separation laws are coupled by means of simple failure criterion, which is satisfied as far as the crack growth function g_T^k reaches the zero value, as follows:

$$g_f^k = \left(\frac{G_I}{G_{IC}}\right)^{\frac{f}{2}} + \left(\frac{G_{II}}{G_{IIC}}\right)^{\frac{f}{2}} - 1 \tag{2.8}$$

where f is the constant utilized to describe fracture in different material and $\left(G_{IC},G_{IIC}\right)$ are the total area under the traction separation law, whereas $\left(G_I,G_{II}\right)$ are the individual energy release rate calculated as $G_I = \int_0^{\Delta_n^c} T_n\left(\Delta_n\right)d\Delta_n$ and $G_{II} = \int_0^{\Delta_t^c} T_t\left(\Delta_t\right)d\Delta_t$.

In order to include the rate dependence effects of the TSL, a modification of Eq.(2.7) should be achieved. According to experimental evidences, it is supposed that the critical stress T_n^c or T_t^c of the material is constant and the critical crack opening or sliding displacements increase with the corresponding speed $\dot{\Delta}_n$ or $\dot{\Delta}_t$, producing an amplification of the dynamic fracture toughness mainly produced by the multi-micro-cracking mechanisms, defined as follows:

$$\Delta_{n,t}^{c(dyn)} = \Delta_{n,t}^{c(st)} \left[1 + \left(\frac{\dot{\Delta}_{n,t}^{c}}{\bar{\dot{\Delta}}_{n,t}^{c}} \right)^{m} \right] \tag{2.9}$$

It is worth noting that despite existing models available from the literature, the proposed formulation restricts the use of cohesive element to a small portion containing the process zone, in which, typically, an accurate description of the stress and displacement fields is required. Moreover, for the remaining region of the interface, perfect adhesion, based on linear interface elements, is achieved, whose stiffness is proportional to the penalty parameter, introduced to impose displacement continuity. As far as the crack tip region is concerned, the computational effects and complexities of the mesh are strongly reduced, since nonlinearities involved in the TSL are restricted to the debonding length only. The mesh motion is described as the difference between spatial and the referential coordinates:

$$\Delta X_1^k = X_1(t) - \xi^k(t) = \zeta^k(r,t) - \xi^k(t) \qquad on \quad \Omega^k = \Omega_{deb}^k \cup \Omega_{ad}^k \tag{2.10}$$

where ξ and ζ represent fixed or referential and moving coordinates, respectively. In order to reduce mesh distortions, produced by the mesh movements, rezoning or smoothing equations are introduced to simulate the grid motion. In particular, Laplace or Winslow Smoothing Method, i.e. LSM or WSM, can be utilized, which are, in the case of one dimensional domain for both Static (S) and Dynamic (D) cases, defined on the basis of the following relationships:

LSM

$$\Delta X_{,\xi\xi}^{k} = \zeta,_{\xi\xi}^{k} \quad \text{(S)} \qquad \Delta \dot{X}_{,\xi\xi}^{k} = \dot{\zeta},_{\xi\xi}^{k} \quad \text{(D)} \tag{2.11}$$

WSM

$$\Delta X_{,X_1X_1}^{k} = J^{-2}\zeta,_{\xi\xi} \quad \text{(S)} \qquad \Delta \dot{X}_{,X_1X_1}^{k} = J^{-2}\dot{\zeta},_{\xi\xi}^{k} \quad \text{(D)} \tag{2.12}$$

where J is defined by the Jacobian of the transformation defined according to Eq. (2.2). Eqs.(2.11)-(2.12) should be completed by means following boundary equations, with the purpose to reproduce the crack tip motion on the basis of the assumed crack growth criterions, namely g_f^k. To this end the following boundary conditions should be introduced, which are completed by the Kuhn–Tucker optimality conditions:

$$\Delta \dot{X}_T^k \geq 0 \qquad g_f^k \leq 0 \quad \text{with} \quad \Delta \dot{X}_T^k g_f^k = \Delta \dot{X}_T^k \dot{g}_f^k = 0, \quad \text{at} \quad X = X_T^k \tag{2.13}$$

$$\Delta X_T^k = 0, \quad \text{at} \quad X = L, \quad \Delta X^k\left(X_T\right) = \Delta X^k\left(X_T + \Omega_{deb}\right) \tag{2.14}$$

where X_T^k indicates the position of the crack tip front of the *k*-th debonded interface. The boundary value problem, given by the set of Eqs.(2.11)-(2.14) is solved by using a variational approach. In particular, taking into account the transformation rules defined by Eqs. (2.1)-(2.2) and introducing mesh displacement conditions on internal and external boundaries, the following expressions for LSM or WSM in weak form, defined in the referential configuration, are obtained for the static case:

$$\begin{gathered}
\delta M_1 = \int_{\Omega^k} \zeta^k_{,\xi} \delta\zeta^k_{,\xi} d\xi, \quad \left(LSM\right), \quad \delta M_1 = \int_{\Omega^k} \left(J^{-1}\zeta^k_{,\xi}\right)\left(J^{-1}\delta\zeta^k_{,\xi}\right) d\xi \quad \left(WSM\right) \\
\delta\Lambda_M = \left\{ \left[\lambda^k_{1T}\delta\zeta^k + \delta\lambda^k_{1T}\left(\zeta^k - \zeta^k_{1T} - \Delta X^k_T\right)\right]\Big|_{\zeta=\zeta^k_{1T}} + \left[\lambda^k_{2T}\delta\zeta^k + \delta\lambda^k_{2T}\left(\zeta^k - \zeta^k_{2T} - \Delta X^k_T\right)\right]\Big|_{\zeta=\zeta^k_{2T}} \right\}
\end{gathered} \tag{2.15}$$

where ζ^k_{1T} and ζ^k_{2T} are the positions in the referential system of the debonding length extremities. Similar expressions can be obtained of the dynamic case, which are not reported for the sake of brevity. Therefore, starting from Eq.(2.15), the governing equations for the ALE problem are defined by the following expressions:

$$\begin{gathered}
\int_{\Omega^k} \zeta_{,\xi}\delta\zeta_{,\xi} d\xi + \sum_{\mathrm{j}=1}^{2} \left\{ \left[\lambda^k_{jT}\delta\zeta^k + \delta\lambda^k_{jT}\left(\zeta^k - \zeta^k_{jT} - \Delta X^k_T\right)\right]\Big|_{\zeta=\zeta^k_{jT}} \right\} = 0 \quad (LSM) \\
\int_{\Omega^k} \left(J^{-1}\zeta_{,\xi}\right)\left(J^{-1}\delta\zeta_{,\xi}\right) d\xi + \sum_{\mathrm{j}=1}^{2} \left\{ \left[\lambda^k_{jT}\delta\zeta^k + \delta\lambda^k_{jT}\left(\zeta^k - \zeta^k_{jT} - \Delta X^k_T\right)\right]\Big|_{\zeta=\zeta^k_{jT}} \right\} = 0 \quad (WSM)
\end{gathered} \tag{2.16}$$

It is worth noting that structural problem is coupled with the ALE approach only by the interface traction forces and the fracture criterion, since they are defined in the referential coordinate system. Moreover, the mesh motion of the *k*-th crack tip front, is taken into account in the variational from, by introducing weak terms as a function the Lagrange multiplied method, which basically correspond to internal constrain conditions which modify the mesh position.

2.2 Numerical Implementation

Governing equations introduced in previous section are formulated by means of a numerical formulation based on the Finite Element (FE) approach. In particular, the derivation of the FE starts from the principle of virtual works in terms of displacements, integrating the equations on the volume of the elements. A Lagrange cubic approximation is adopted to describe both displacement and rotation fields, whereas linear interpolation functions are adopted for the axial displacements. Moreover, for the variables concerning moving mesh equations, quadratic interpolation functions are assumed to describe the mesh position. The discrete equations are derived introducing the conventional interpolation functions:

$$\underset{\sim}{\eta}(x,t)=\underset{\sim}{N}\ \overline{\underset{\sim}{\eta}},\ \underset{\sim}{X}(\xi,t)=\underset{\sim}{H}\,\overline{\underset{\sim}{X}}\ ,\underset{\sim}{\Lambda}(\xi,t)=\underset{\sim}{N}\overline{\underset{\sim}{\Lambda}},\ \underset{\sim}{\Gamma}(\xi,t)=\underset{\sim}{N}\overline{\underset{\sim}{\Gamma}}, \tag{2.17}$$

where $\underset{\sim}{N}$ or $\underset{\sim}{H}$ represent shape function matrixes of Timoshenko or ALE variables, $\underset{\sim}{\Lambda}$ and $\underset{\sim}{\Gamma}$ are the Lagrange's multipliers vectors concerning perfect adhesion interfaces and moving constrains at the process zone, $\left(\overline{\underset{\sim}{\eta}},\overline{\underset{\sim}{X}},\overline{\underset{\sim}{\Lambda}},\overline{\underset{\sim}{\Gamma}}\right)$ are the vectors containing the nodal variables of displacements, mesh position and Lagrange's multipliers, respectively. The structural problem is formulated by using spatial coordinates, except for the cohesive functional, which is implemented in terms of a moving coordinate system. In order to evaluate the TSL at those material points identified by the moving mesh points, a projection operator $\underset{\sim}{Q}$, with $Q:\Xi_S \rightarrow \Xi_M$ and $\underset{\sim}{X} = \underset{\sim}{Q}\underset{\sim}{x}$, is introduced. As shown in Fig. 2.4, such operator characterizes the mapping between moving coordinates and material points on the basis of a geometrical projection, which connects the interface domain and the corresponding material point. The projection is achieved vertically along the thickness direction.

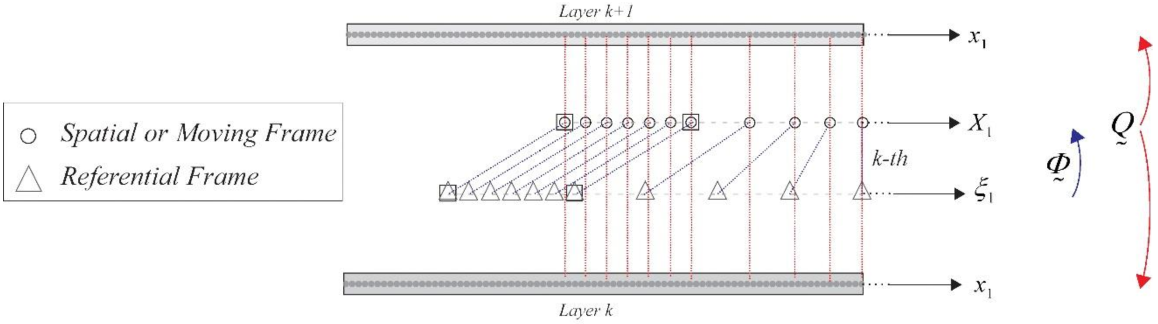

Fig. 2.4:Synoptic representation of the mapping rule between moving coordinates and material points.

Therefore, the cohesive traction forces on both debonded or undebonded regions are assumed to be defined as a function of the moving mesh variables taking into account the transformation rule between referential and moving coordinate systems, by means of the following equation:

$$\begin{aligned}\delta C = & \sum_{k=1}^{N^D} \int_{\Omega_{deb}^k} \left[T_n^k \left(X_d^k \right) \delta\Delta_n^k \left(X_d^k \right) + T_t^k \left(X_d^k \right) \delta\Delta_t^k \left(X_d^k \right) \right] dX + \\ & + \sum_{k=1}^{N^D} \int_{\Omega_{ad}^k} \left[\left(k_n^k \Delta_n^k \left(X_d^k \right) \right) \delta\Delta_n^k \left(X_d^k \right) + \left(k_t^k \Delta_t^k \left(X_d^k \right) \right) \delta\Delta_t^k \left(X_d^k \right) \right] dX = \\ & = \sum_{k=1}^{N^D} \left[\underset{\sim}{D}_1 \underset{\sim}{Q} \overline{\underset{\sim}{\eta}} \cdot \underset{\sim}{Q} \delta \overline{\underset{\sim}{\eta}} \right]_{\Omega_{deb}^k} \quad + \sum_{k=1}^{N^D} \left[\underset{\sim}{D}_2 \underset{\sim}{Q} \overline{\underset{\sim}{\eta}} \cdot \underset{\sim}{Q} \delta \overline{\underset{\sim}{\eta}} \right]_{\Omega_{ad}^k}\end{aligned} \tag{2.18}$$

where $\underset{\sim}{D}_1$ and $\underset{\sim}{D}_2$ are the stiffness matrixes concerning debonded (cohesive) or perfect adhesion regions, respectively. The discrete equations can be derived from the principle of virtual works substituting Eq.(2.17), into Eq.(2.3), taking into account of Eqs.(2.4)-(2.5) and Eq.(2.15)-(2.18), which yield the following set of ordinary differential equations in time:

STRUCTURAL

$$\begin{aligned}& \sum_{i=1}^{n} \underset{\sim}{M}_i \overline{\underset{\sim}{\eta}''}_i + \sum_{i=1}^{n} \underset{\sim}{K}_i \overline{\underset{\sim}{\eta}}_i + \sum_{i=1}^{n} \underset{\sim}{L}_i \overline{\underset{\sim}{\Lambda}}_i + \sum_{i=1}^{n_{deb}} Q_i^T D_{1i} Q_i \overline{\underset{\sim}{\eta}}_i + \sum_{i=1}^{n_{ad}} Q_i^T D_{2i} Q_i \overline{\underset{\sim}{\eta}}_i = \sum_{i=1}^{n} \underset{\sim}{P}_i \ , \\ & \sum_{i=1}^{n_{ad}} \left(L_i^k \overline{\underset{\sim}{\eta}}_i^k + L_i^{k+1} \overline{\underset{\sim}{\eta}}_i^{k+1} \right) = 0\end{aligned} \tag{2.19}$$

ALE INTERFACE (k)

$$\sum_{i=1}^{n_{ad}+n_{deb}} \underset{\sim}{W}_i \cdot \overline{\zeta}_i + \sum_{i=1}^{n_{ad}+n_{deb}} \underset{\sim}{N}_i \overline{\underset{\sim}{\Gamma}} = 0, \quad \sum_{i=1}^{n_{ad}+n_{deb}} \underset{\sim}{N}_{ii} \left(\overline{\underset{\sim}{\zeta}} - \overline{\underset{\sim}{\zeta}}_0 - \Delta \underset{\sim}{X}_T \right) = 0 \tag{2.20}$$

where $\underset{\sim}{M}_i$ and $\underset{\sim}{K}_i$ are classical consistent mass and stiffness matrixes, $\underset{\sim}{P}_i$ is the external load vector and $\overline{\Lambda}$ is the Lagrange functional constraint for adhesion between undamaged layers, $\underset{\sim}{W}$ is the ALE discretization matrix $\overline{\underset{\sim}{\Gamma}}$ is the Lagrange multiplier vector concerning the ALE formulation and $\left(n, n_{deb}, n_{ad} \right)$ defined the total number of finite elements, those in the debonding and perfect adhesion regions, respectively. It is worth noting that in order to avoid numerical oscillations due mesh distortions in the cohesive region, the debonding length is moved, enforcing the same displacements at the corresponding nodal point extremities. Moreover, in order to evaluate the mesh displacements, which verify consistency conditions concerning the crack advance, i.e. Eq.(2.13)-(2.14), an iterative procedure is implemented, which is able to identify the position of the crack tip on the debonding portion. In particular, at the current time step, the crack position of the *k*-th crack tip $\underset{\sim}{X}_T^k$ is defined by searching, the incremental displacement of the crack tip, which corresponds to the zero-solution of the function g_f^k along the debonding region. Such task is performed by using a simple procedure based on the predicted values of the fracture function g_f^k at the extremities of the debonding length. In particular, as depicted in Fig. 2.5, the current increment of the crack position ΔX^k is determined by searching the value which sets to zero on the debonding length the function g_f^k. Such quantity can be easily obtained by means the following linearized expression on the basis of the values assumed by the fracture function g_f^k at the extremities of the debonding length:

$$\Delta X_T^k = 0 \quad g_f^k \leq 0, \;\; \Delta X_T^k = \frac{g_f^k\left(X_T^k\right) + toll}{g_f^k\left(X_T^k\right) + toll - g_f^k\left(X_T^k + \Omega_{deb}^k\right)} \Omega_{deb}^k \;\; g_f^k > 0 \qquad (2.21)$$

It is worth noting that, the initial length of the debonding region, which characterizes the dimension of the process zone, can be estimated in several ways. A discussion of the characteristic length and its relationship with the mechanical and fracture properties of the laminate can be recovered in [84]. However, an analysis on the choice and influence of such parameter will be presented in section of the results.

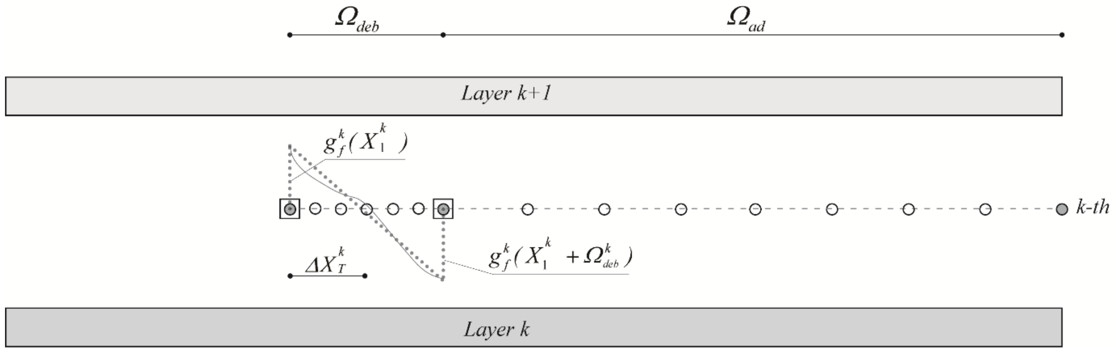

Fig. 2.5: Interface moving boundary: debonded and perfect adhesion regions.

The proposed approach takes the form of a set of nonlinear differential equations, whose solution is obtained by using a customized version of the finite element package Comsol Multiphysics [85]. The model can be solved in both static and dynamic framework, taking into account the time dependent effects produced by the inertial characteristics of the structure and the boundary motion involved by debonding phenomena. In both cases, since the governing equations are essentially nonlinear, an incremental-iterative procedure is needed to evaluate the solution. In the case of static analysis, the resulting equations are solved by using a nonlinear methodology based on Newton-Raphson or Arch length integration procedures. In the framework of a dynamic analysis, the algebraic equations are solved by using an implicit time integration scheme based on a variable step-size backward differentiation formula (BDF).

2.3 Implementation of the interlaminar reinforcements

Introducing the effects of the z-pins, the governing equations, previously introduced, remain essentially the same. As described in the previous subsection, a moving weak discontinuity approach based on ALE formulation is implemented to describe moving traction forces acting on the interface region of the laminate. Instead, in order to simulate the effects of the z-pins a set of nonlinear springs fixed to material frame is introduced. Furthermore, the proposed model has two cohesive zone, the first defined in the moving or spatial domain, while the second fixed to material domain. In Fig. 2.6 a synoptic representation of the model is reported.

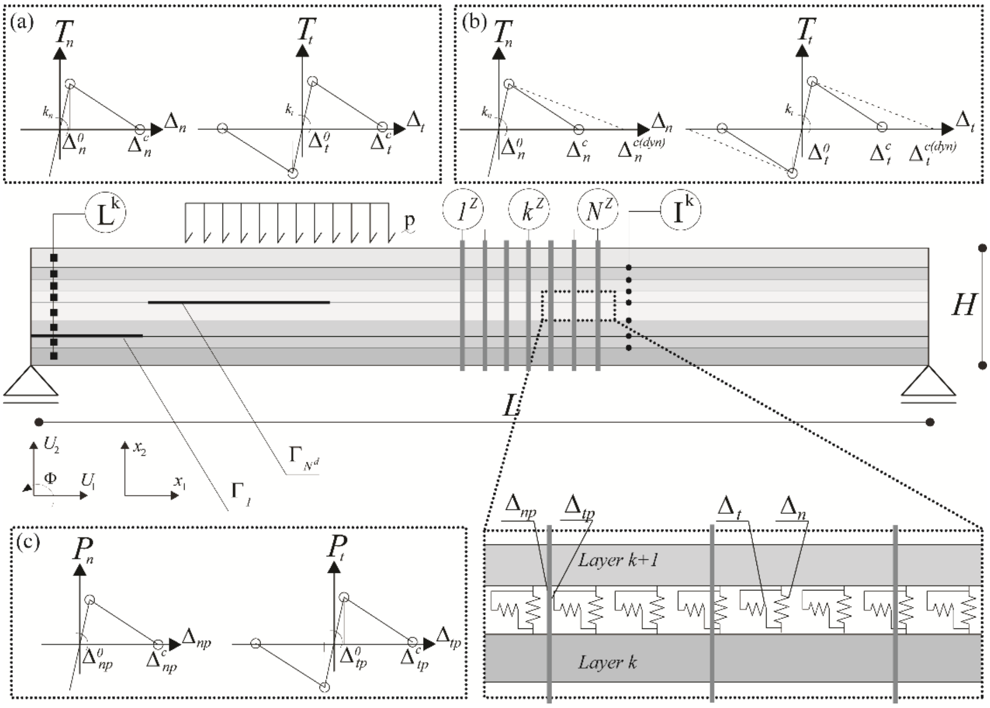

Fig. 2.6: Multilayered laminate structure: representation of the geometry; interface TSL (a,b) and Z-pin pull-out model (c).

From a numerical point of view, in order to describe the behaviour of a laminate reinforced by interlaminar reinforcements, z-pin traction potential is introduced in the principle of virtual works, modifying Eq. (2.3) as follows:

$$\delta T + \delta U + \delta W + \delta \Lambda + \delta C + \delta Z = 0 \tag{2.22}$$

where δZ is defined by means of the following expression:

$$\delta Z = \sum_{k=1}^{N^Z} \left[T_n^k \left(x^k \right) \delta \Delta_{np}^k \left(x^k \right) + T_t^k \left(x^k \right) \delta \Delta_{tp}^k \left(x^k \right) \right] \tag{2.23}$$

where N^Z represents the number of z-pin elements introduced in the laminated structure, $\left(T_{np}^c, T_{tp}^c \right)$ are the critical cohesive stress, $\left(\Delta_{np}^0, \Delta_{np}^c \right)$ and $\left(\Delta_{tp}^0, \Delta_{tp}^c \right)$ are critical and initial opening or transverse relative displacements. The traction forces are assumed by means of bilinear constitutive laws, which reproduce the initial elastic phase, until interfacial strengths are reached, and the subsequent pulling out and sliding mechanisms by means of damage constitutive laws Fig. 2.6.

Fracture function is introduced as energy criterion to estimate the complete failure of z-pins in terms of fracture toughness $\left(G_{IC}^{pin}, G_{IIC}^{pin} \right)$ and individual energy release rates $\left(G_I^{pin}, G_{II}^{pin} \right)$:

$$g_f^{pin} = \left(\frac{G_I^{pin}}{G_{IC}^{pin}} \right) + \left(\frac{G_{II}^{pin}}{G_{IIC}^{pin}} \right) - 1 \tag{2.24}$$

The individual ERRs are determined on the basis of constitutive relationships for normal and sliding tractions on the bridging area at the *k*-th interface as follows:

$$G_I^{pin} = \int_0^{\Delta_{np}^c} P_{np} \left(\Delta_{np} \right) \delta \Delta_{np} \qquad G_{II}^{pin} = \int_0^{\Delta_{tp}^c} P_{tp} \left(\Delta_{tp} \right) \delta \Delta_{tp} \tag{2.25}$$

2.4 Results

In this section, results are developed with the purpose to verify the consistency and the reliability proposed methodology. At first, the debonding behaviour is investigated for laminated composites with a single or multiple delaminations. Finally, numerical simulations to verify the influence of interlaminar reinforcement are presented.

2.4.1 Single delamination in unidirectional laminates

At first, the analysis is developed with reference to loading schemes based on classical Double Cantilever Beam scheme (DCB) and Mixed Mode Bending scheme (MMB), in which pure mode I and mixed I/II with a mode-mixity ratio of 0.5, respectively, are investigated [86]. The loading, the boundary conditions and the geometry are illustrated in Fig. 2.7, whereas the mechanical properties assumed for the laminate and the interfaces as well as the ones required by the cohesive zone model are reported in Tab. 2.1 and Tab. 2.2. In the follow subsections are presented the results obtained from both static and dynamic simulations.

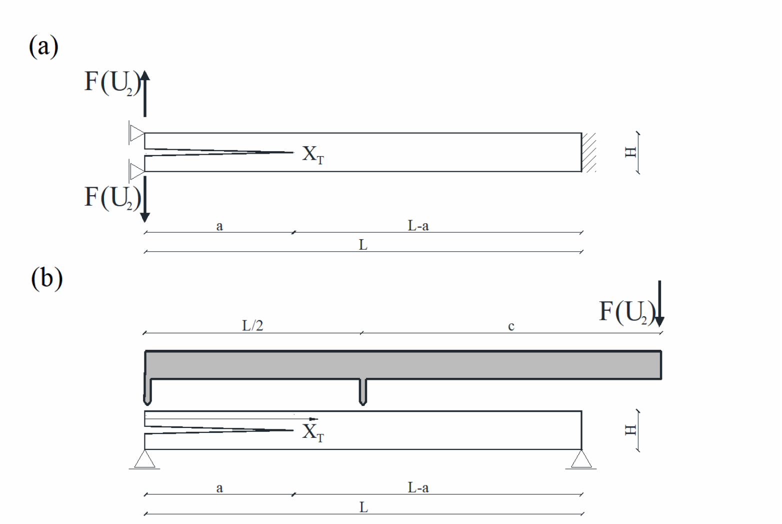

Fig. 2.7: Laminate configurations and loading schemes: Double Cantilever Beams (DCB) (a); Mixed Mode Bending test (MMB) (b).

$E_1\left[\text{GPa}\right]$	$E_2 = E_3\left[\text{GPa}\right]$	$G_{12}\left[\text{GPa}\right]$	ν	$\rho\left[\text{kg m}^{-1}\right]$
120	10.5	5.25	0.3	1500
$L\left[\text{mm}\right]$	$B\left[\text{mm}\right]$	$a\left[\text{mm}\right]$	$H\left[\text{mm}\right]$	-
150	20	35	3.1	-

Tab. 2.1: Mechanical and geometrical properties of the laminates (single delamination).

$T_n^c\left[\text{MPa}\right]$	$\Delta_n^0\left[\text{mm}\right]$	$\Delta_n^c\left[\text{mm}\right]$	$\bar{\dot{\Delta}}_n^c\left[\text{m s}^{-1}\right]$	-
30	0.0057	0.0173	2.5	-
$T_t^c\left[\text{MPa}\right]$	$\Delta_t^0\left[\text{mm}\right]$	$\Delta_t^c\left[\text{mm}\right]$	$\bar{\dot{\Delta}}_t^c\left[\text{m s}^{-1}\right]$	m
60	0.00334	0.0334	2.5	1

Tab. 2.2: Interface properties of the laminates (single delamination).

2.4.1.1 Static framework

In this Section, numerical investigation obtained from static framework are presented. The numerical discretization utilized for the comparisons is assumed to be uniform and with a length equal $\Delta D / L = 0.2/150$, with ΔD the element length. The dimension of the debonded region is adopted on the basis of formulas available from the literature, which identify, for classical cohesive zone models, the characteristic length parameter. Such value, in relationship to the geometrical and mechanical properties of the laminate, is assumed to be equal to a small fraction of the total length of the laminate, i.e. to $\Omega_{deb} \approx 0.05L$. In all cases, along the thickness direction, only two elements located up and down of the interface plane are considered in the analysis. To obtain a stable crack propagation the samples are loaded under a displacement control mode. Fig. 2.8 and Fig. 2.9, the relationships between the loads, crack propagation and applied displacement for mode I and mixed mode schemes, reported in Fig. 2.7a-b respectively, are presented. In both cases, results obtained by the proposed model are in agreement with the ones obtained by a refined X-FEM modelling [86] or the analytical solution obtained according to corrected beam theory [87]. However, small differences are observed in the case of mixed mode loading condition, in which the solution obtained by the proposed formulation is between the prediction obtained from the literature. It is worth noting that the numerical model arising from [86] is based on the use of 4-node bilinear plane strain quadrilateral elements, in which an uniform mesh size equal to 0.1 mm was chosen to satisfy the solution accuracy. As a consequence, the total number of elements is approximately equal to 45000 involving 46469 DOF. Moreover, the modelling developed in the framework of XFEM approach is based on an enrichment of the interpolation functions of the elements affected by debonding phenomena, leading to more complexities in the solution. Contrarily, by using the proposed approach, the number of FE variables is strongly reduced, since a uniform discretization the mesh element length equal to 0.2 mm utilized. In this configuration, the total number of elements is equal to 2075 involving 6234 DOF.

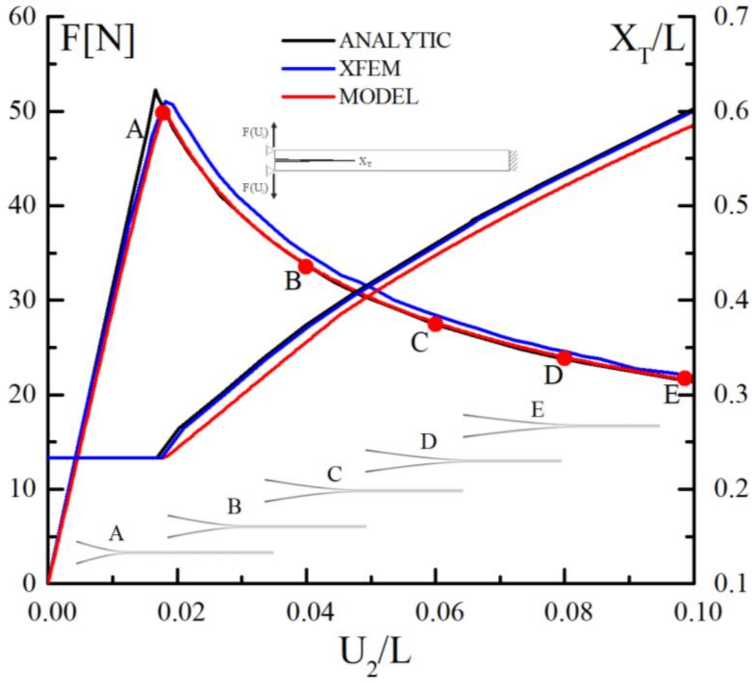

Fig. 2.8: Mode I DCB configuration: comparisons in terms of loading curve (F-U_2/L) and crack tip position (X_T/L) with analytical [87] and XFEM [86] solutions.

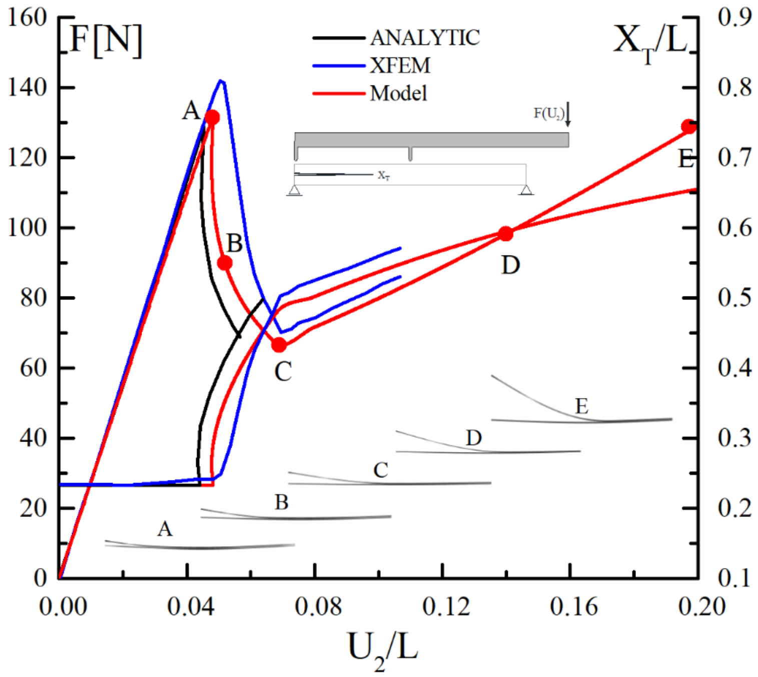

Fig. 2.9: MMB configuration: comparisons in terms of loading curve (F-U_2/L) and crack tip position (X_T/L) with analytical [87] and XFEM [86] solutions.

2.4.1.1.1 Influence of the mesh discretization

In order to verify the influence of the mesh discretization on the accuracy of the solution, parametric results in terms mesh characteristics are proposed. To this end, comparisons expressed as a function of loading curve and crack tip position are proposed for several mesh sizes, ranging from coarse to refined discretizations. In particular, two different numeric models, namely M1 and M2, in which mesh uniform lengths for the layer and interface with value equal $\Delta D / L = 1/150$ and $\Delta D / L = 2/150$ are adopted except for the debonding length, where at least five elements are introduced. The analyses reported in Fig. 2.10 denote that, as far as, the mesh size is increased the solution oscillates around the refined one. Moreover, the results show how the use of a coarse mesh produces jumps in the predicted values with false instabilities are observed. However, when the mesh in the structure is enriched, an asymptotically convergence of the solution, asymptotically, is observed.

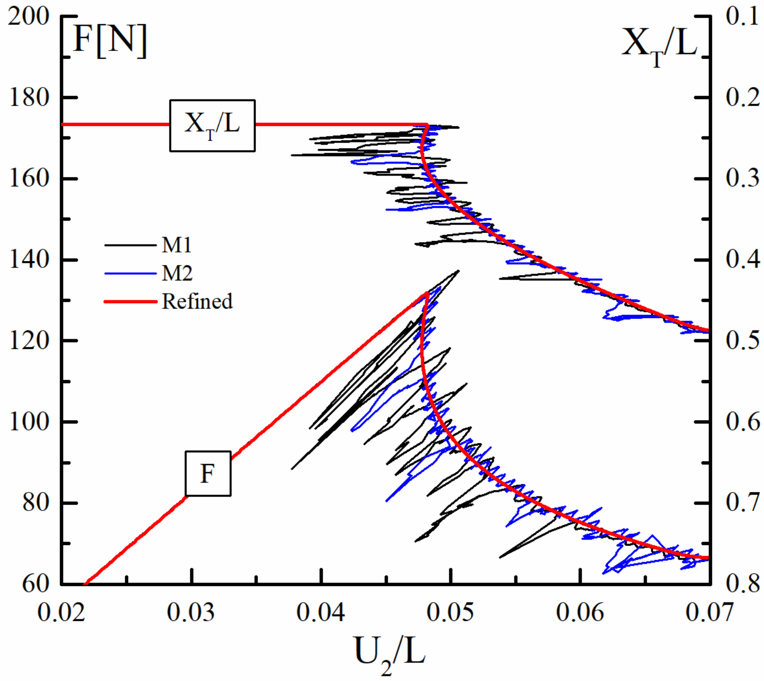

Fig. 2.10: MMB configuration: influence of the mesh discretization on the loading curve (F-U_2/L) and dimensionless crack tip position (X_T/L).

2.4.1.1.2 Influence of the length of deboning region

The prediction of the proposed formulation and the stability of crack propagation were verified by means of a parametric study in terms of the length of the debonding region. The results reported in Fig. 2.1 denote that the choice of the length which describes the process zone is able to strongly influence the debonding mechanisms, since different predictions of the first debonding load are observed. This behaviour can be explained by the distribution of the fracture function along the debonding region, which was reported for all the investigated cases also in the Fig. 2.11. In particular, although the values at the crack tip are basically the same, different evaluations are observed at the internal extremity of the debonding length, in which the fracture function assumes larger values as far as the debonding length decreases. For low value of the debonding length, the model is not able to capture the actual internal distribution of the interlaminar stresses and the corresponding large scale and thus an overestimation of the first debonding load is achieved. Contrarily, as far as the debonding length increases, an accurate description of the process zone is achieved and the model tends with a convergent behaviour to the solution.

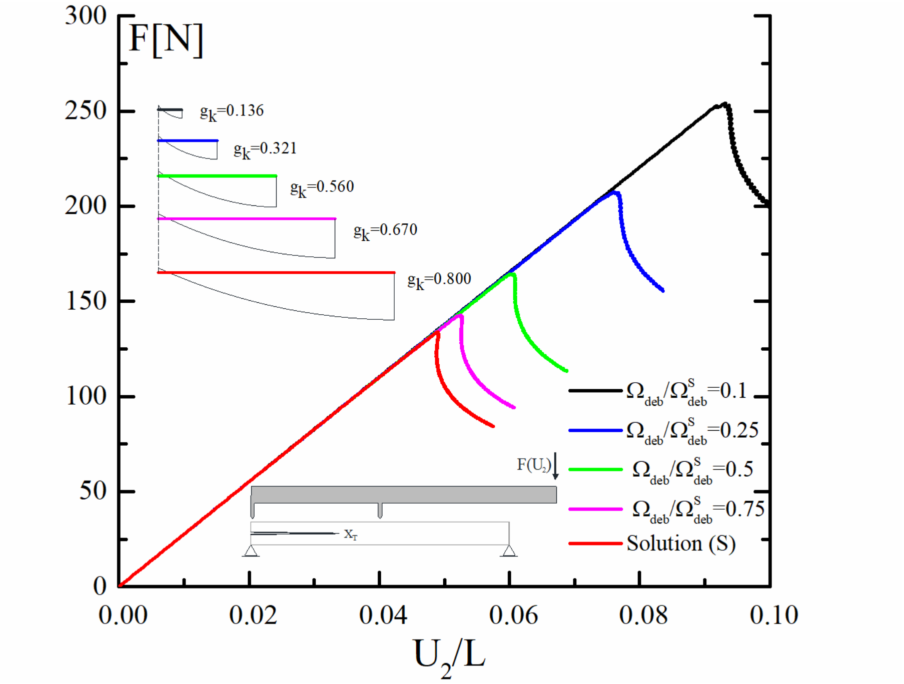

Fig. 2.11: MMB configuration: influence of the debonding length parameter (Ω_{deb}) on the loading curve (F-U_2/L) and dimensionless crack tip position (X_T/L).

2.4.1.2 Dynamic framework

Previous results are developed essentially in the framework of a static analysis, in which time dependent effects concerning loading rate and inertial forces are supposed to be negligible. The extension in dynamics is developed taking into account the generalization of the TSL of the cohesive elements, introducing rate dependent contributions arising from inertial effects of the structure and those involved, intrinsically, in the debonding process. Material parameters involved in the TSL constitutive relationships, reported in Tab. 2.2, are assumed consistently with the values suggested in the literature [83, 88]. The load history is idealized as a linear ramp curve in the prescribed velocity until the time has reached value t_0, after that the velocity remains constant. In the analyses, the quantity t_0 is assumed to be proportional to the first period of observation T_1 with a time sufficiently small to obtain a rapid crack growth and to avoid a highly fluctuating behaviour in the crack advance, i.e. $t_0=0.5T_1$ [89]. The analyses are reported in Fig. 2.12, in which resistance curves for different loading rates are compared with the solution arising from the static case. Moreover, the crack growth is investigated also in terms of measured crack tip speed normalized on the shear wave speed (V_S) of the material and kinetic energy (E_K) produced during the debonding mechanics (Fig. 2.13). The results show that high loading rates modify the static prediction in terms of resistance curve, since larger values of the first debonding load are expected. Such behaviour is quite consistent with several experimental observations, which have shown how in fast crack propagation, the process zone affects an enlarged damage zone with more dissipated energy, leading to large values and some oscillations in the resistance curve [90].

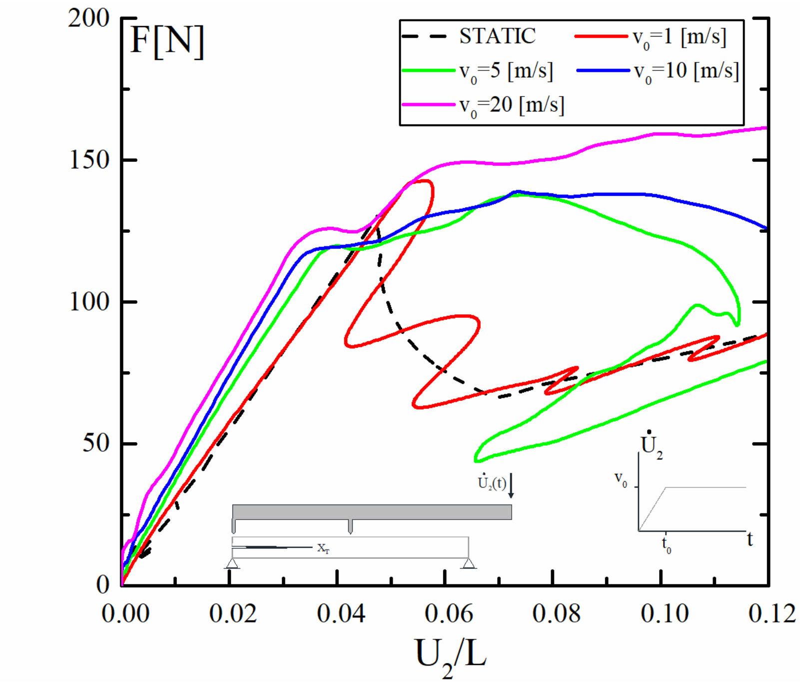

Fig. 2.12: MMB configuration: influence of the loading rate in terms of load-displacement curve.

The crack tip speeds are much larger in the initiation phase, in which high strain rates activate large amount of kinetic energy (Fig. 2.13). Subsequently, the crack tip proceeds with low speeds and definitively it is affected by crack arrest phenomena, which are mainly produced by flexural oscillations of the specimen and the reflection of high frequency waves in the desired range of the crack speeds. This behaviour is quite evident from the results obtained in Fig. 2.12, in which for low loading rates, the resistance curve oscillates close to the static solution.

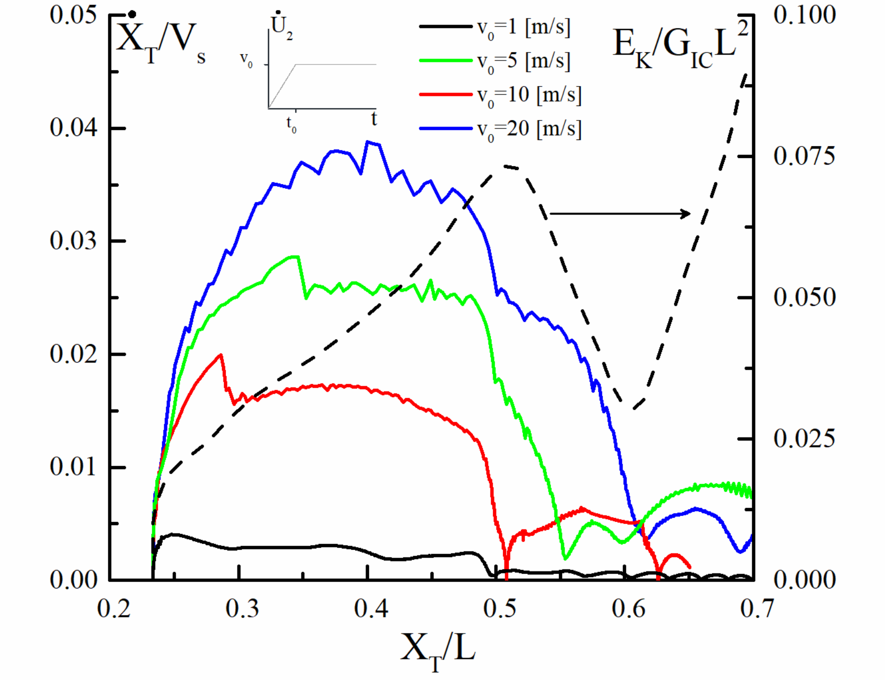

Fig. 2.13: MMB configuration: influence of the loading rate in terms of crack tip speed.

2.4.2 Multiple delaminations in unidirectional laminates

2.4.2.1 Static framework

In order to validate the proposed model, a case involving multiple delaminations is considered. The geometrical model is reported schematically in Fig. 2.14, whereas the material data are given in Tab. 2.3 and Tab. 2.4. The structure is affected by edge and internal initial cracks of different lengths.

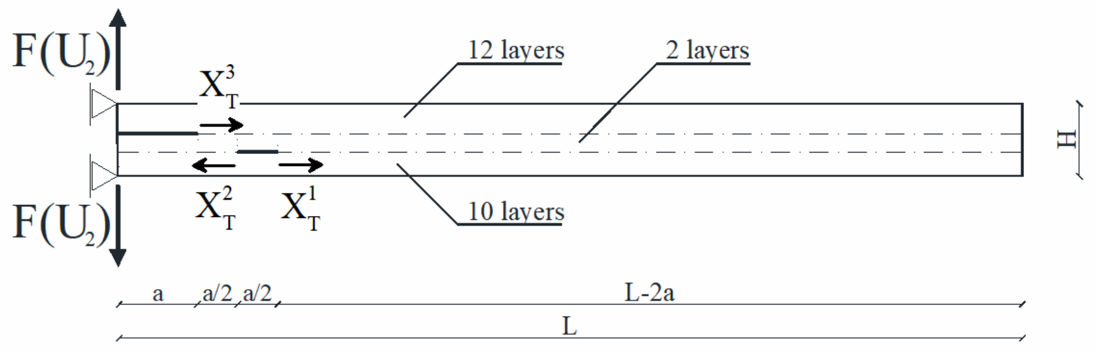

Fig. 2.14: Laminate configuration and loading scheme: Multiple Delamination Scheme (MDS).

$E_1\left[\text{GPa}\right]$	$E_2 = E_3\left[\text{GPa}\right]$	$G_{12}\left[\text{GPa}\right]$	ν	$\rho\left[\text{kg m}^{-1}\right]$
126	8.5	4.5	0.29	1500
$L\left[\text{mm}\right]$	$B\left[\text{mm}\right]$	$a\left[\text{mm}\right]$	$H\left[\text{mm}\right]$	-
200	20	40	3.18	-

Tab. 2.3: Mechanical and geometrical properties of the laminates (multiple delamination).

$T_n^c\left[\text{MPa}\right]$	$\Delta_n^0\left[\text{mm}\right]$	$\Delta_n^c\left[\text{mm}\right]$	$\bar{\dot{\Delta}}_n^c\left[\text{m s}^{-1}\right]$	-
3.3	0.02	0.2	2.5	-
$T_t^c\left[\text{MPa}\right]$	$\Delta_t^0\left[\text{mm}\right]$	$\Delta_t^c\left[\text{mm}\right]$	$\bar{\dot{\Delta}}_t^c\left[\text{m s}^{-1}\right]$	m
7.7	0.02078	0.2078	2.5	1

Tab. 2.4: Interface properties of the laminates (multiple delamination).

As a consequence, three potential process zones are able to produce debonding phenomena, namely $X_T^{1,2,3}$. The numerical model is discretized along the thickness by using one mathematical layer for each sublaminate, whereas, for the interfaces, three ALE elements are introduced between the sublayers adjoining the delaminations. In the analysis, the debonding length, in which cohesive elements are introduced, is assumed to be equal to 1/40 of the total length of the laminate. Moreover, the mesh discretization of the numerical model is based on a uniform distribution with an element length of $\Delta D / L = 0.2 / 200$ in the laminate, whereas for each debonding region a refinement of the mesh involving 10 subdivisions is utilized. Comparisons, with results arising from XFEM modeling [86], pure cohesive approach [91] and experimental data [92] are developed. In addition, in order to verify coupling effects between debonding mechanisms, the following idealized configurations are considered:

- Upper Defect (UD) only;
- Upper and Lower Defects with Lower Delamination Fixed (UD-LF).
- Upper and Lower Defects with both Delaminations Fixed (UD-UF).

In Fig. 2.15 and Fig. 2.16 and , resistance curve and crack tip location as function applied displacements (F-U_2/L) are analysed. In both figures, comparisons with results available from the literature are reported. Moreover, in Fig. 2.17, comparisons in terms of loading curve for the idealized configurations are proposed. The analysis in terms of loading curve denotes that the proposed model matches exactly the predictions provided by the numerical formulations and slightly differs from the experimental data.

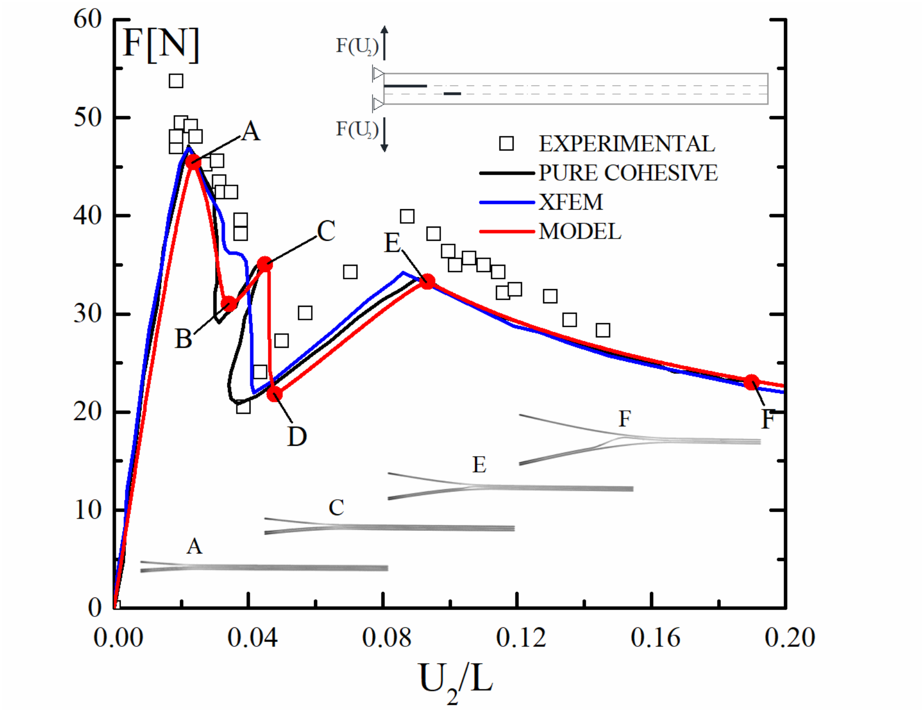

Fig. 2.15: MDS configuration: comparisons in terms of loading curve (F-U_2/L) with numerical results and experimental data

Moreover, the results show that, at first, crack growth is possible in the upper sublaminate, whose effect in the loading curve is to produce a reduction of the current stiffness similarly to the cases affected by a single delamination. This behaviour is noted also from the results reported in Fig. 2.17, in which the UD modelling presents a decreasing monotonic resistance curve once the debonding load is reached. Subsequently, the loading curve is modified from the classical evolution, since an extra local limit point is observed (Point C, Fig. 2.15). This behaviour is mainly produced by the presence of lower debonding length, that, at this stage, remaining fixed, is able to produce instability phenomena in the crack growth. As far as the upper crack reaches the midpoint of the initial lower crack, multiple delaminations affect the structure.

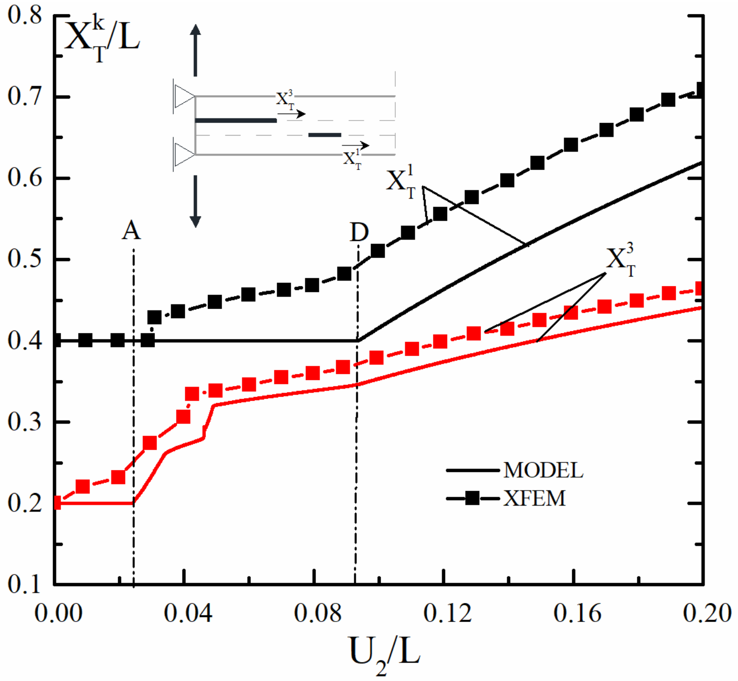

Fig. 2.16: MDS configuration: comparisons in terms of crack tip position (X_T/L) with others numerical data.

In particular, the debonding phenomena are observed also in the lower sublaminate mainly to the right direction, whereas the left tip remains basically fixed. When the upper crack is located over the Crack Tip-2, multiple delaminations affect the structure. Form C to D, the Crack Tip-3 advances over the Crack Tip-2, which moves slightly. Subsequently, when the upper crack reaches the midpoint of the initial lower crack, the crack Tip-1 is activated (point E, Fig. 2.15). The motion of upper and lower cracks at this stage is responsible of the second softening branch in the loading curve (point E, Fig. 2.15). Comparisons in terms of crack tip displacements, in lack of data, are developed only with results obtained by the XFEM methodology [86]. In particular, the results are quite in agreement for the crack tip displacements of the upper laminate, whereas different predictions are observed for the evolution of the lower delamination. In particular, the proposed model predicts the crack growth in the lower sublaminate when the upper crack has reached its midpoint initial length; contrarily by using XFEM methodology, a simultaneous crack growth of both delaminations is predicted once the debonding lengths are just overlapped. Such discrepancies can be explained by the intrinsic characteristics of XFEM and cohesive approaches. As a matter of fact, the proposed model is in agreement with the analyses reported in [91], in which the Authors clearly state that only the upper crack propagates until the second limit point, i.e. E of Fig. 2.15 is reached. Such result is also consistent with the one reported in Fig. 2.17, in which the solution related to model UD-LF is practically coincident with the one of proposed model until point D, after that, in lacking of a possible growth in the lower sublaminate, the curve proceeds with a linear branch.

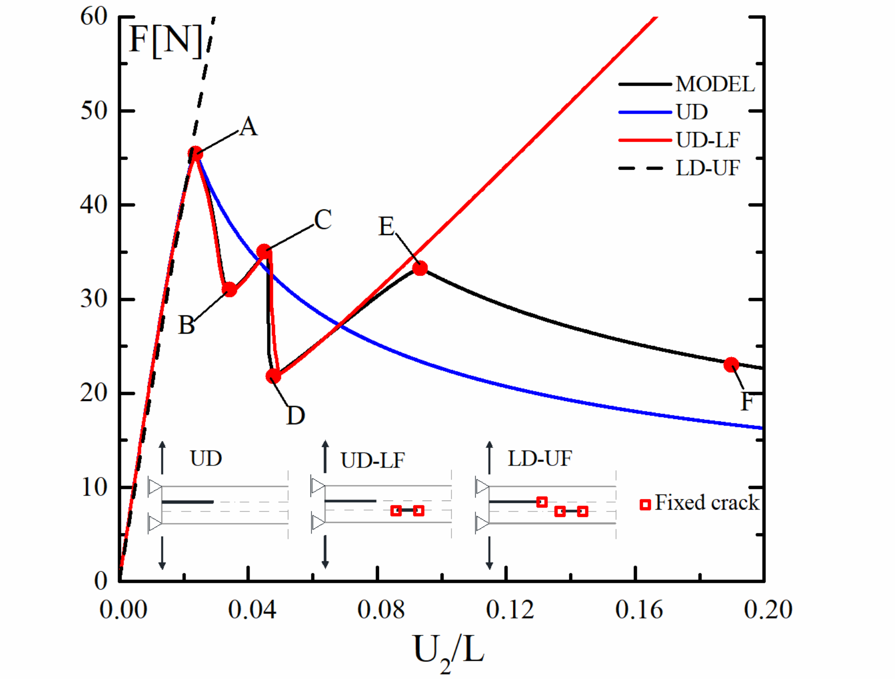

Fig. 2.17: MDS configuration: comparisons in terms of loading curve (F-U₂/L) with numerical results and experimental data.

2.4.2.2 Dynamic framework

Previous results, developed in the framework of a static analysis, are now discussed in dynamics. The main aim of the proposed comparisons is to verify how the static solution is modified, when loading rate and inertial effects affect the crack growth. The data concerning material characteristics, reported in Tab. 2.3 and Tab. 2.4, are chosen on the basis of the similar assumptions made for the case involving a single delamination. The loading history is assumed to be governed by an applied velocity with ramp curve with a constant speed at the time t_0. In Fig. 2.18 and Fig. 2.19, results in terms of loading curve and crack tip speeds for different loading rates are presented. The comparison with the static solution denotes that loading curve is strongly modified in the prediction of the first debonding load and, subsequently, when debonding phenomena are activated. For low loading rates the curve presents low oscillations around the quasi-static solution. In spite of quasistatic condition, the instability phenomena associated to the local limit point, namely point B, are not observed, since the loading curve jumps dynamically from the two equilibrium configuration relate to point A and D. This behaviour is in agreement with the experimental data, which do not predict any limit points and denote a discontinuous evolution from the two points. For increasing loading rates, dynamic effects are able to modify the static curve, introducing large values of resistance. As far as the debonding phenomena are triggered in the lower laminate, the debonding curves are affected by an abrupt change in the resistance curve and an oscillatory evolution.

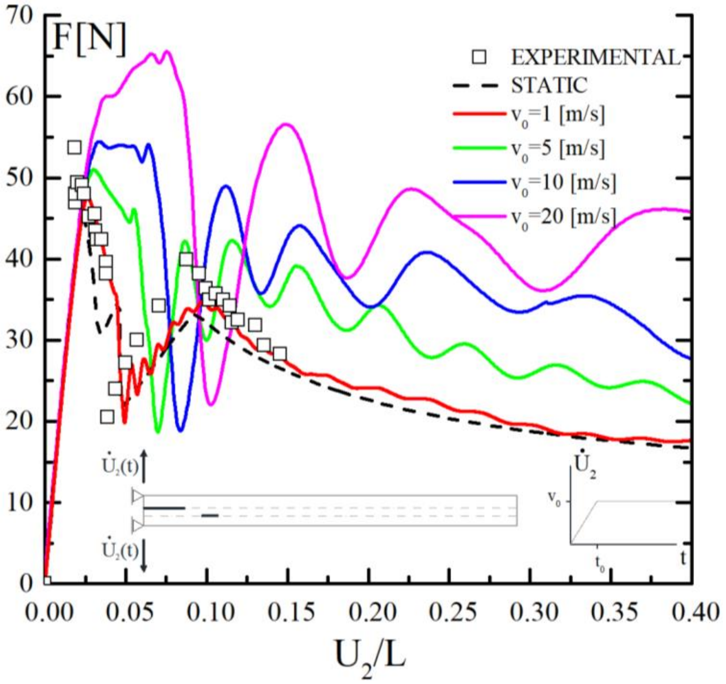

Fig. 2.18: MDS configuration: influence of the loading rate in terms of load-displacement curve.

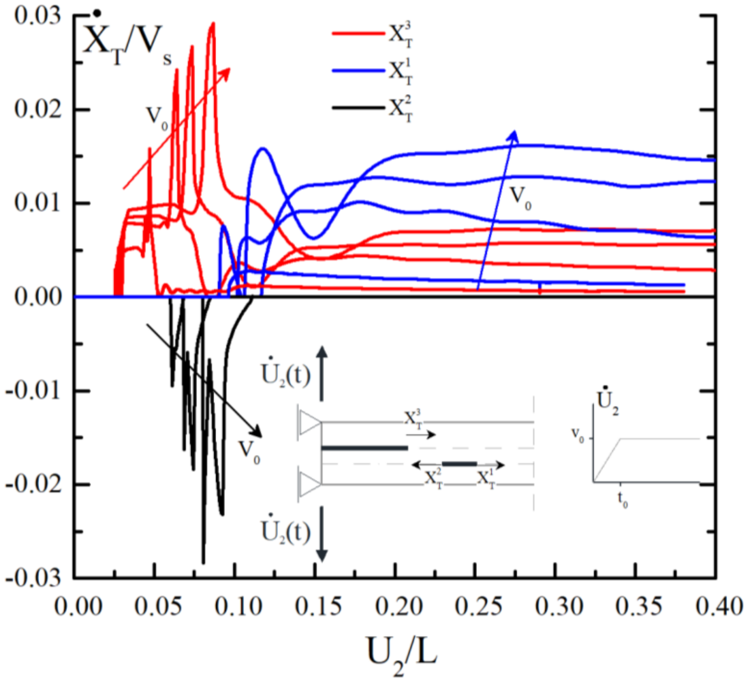

Fig. 2.19: MDS configuration: influence of the loading rate in terms of crack tip speed.

Such behaviour can be explained by the results reported in terms of time histories of the crack tip speeds. The crack tip speed of the upper sublaminate is affected by high amplifications when the crack advances in proximity of the lower delamination, leading to jumps in the time histories. At this stage, in spite the static case, crack growth is also possible in the lower left-hand side crack, which, even if for a reduced time step, is affected by large crack tip speed, comparable to the ones observed for the upper one. Finally, as far as the crack growth in the right-hand side lower delamination is possible, crack arrest phenomena or steady state crack propagation are observed at low or high loading rates, respectively.

2.4.3 Single delamination in unidirectional laminates reinforced with z-pins

In this section, results of laminate structures reinforced by z- pins are discussed. The validation scheme is developed with the purpose to verify the consistency and the reliability of the proposed approach with respect to loading schemes based on classical DCB and MMB tests taken from the literature [33, 93, 94]. In particular, the material specimen is formed by 24 plies of unidirectional prepreg of IMS/924, resulting in total 3 mm the nominal thickness of the laminate, whereas the z-pins are made of pultruded T300/BMI. The values of mechanical properties and cohesive zone model, assumed for the laminate scheme, are reported in Tab. 2.5, whereas those concerning z-pin characteristics are reported in Tab. 2.6.

$E_1\left[\text{GPa}\right]$	$E_2=E_3\left[\text{GPa}\right]$	$G_{12}\left[\text{GPa}\right]$	ν	$\rho\left[\text{kg m}^{-1}\right]$	-
138	11	4.4	0.34	1500	-
$T_n^c\left[\text{MPa}\right]$	$\Delta_n^0\left[\text{mm}\right]$	$\Delta_n^c\left[\text{mm}\right]$	$T_t^c\left[\text{MPa}\right]$	$\Delta_t^0\left[\text{mm}\right]$	$\Delta_t^c\left[\text{mm}\right]$
24.15	$9.66\ 10^{-3}$	$2.23\ 10^{-2}$	15	$6.00\ 10^{-3}$	$9.33\ 10^{-2}$

Tab. 2.5: Mechanical and Interface properties of the laminates (single delamination).

$P_{np}^c\left[\text{N}\right]$	$\Delta_{np}^0\left[\text{mm}\right]$	$\Delta_{np}^c\left[\text{mm}\right]$	$P_{tp}^c\left[\text{N}\right]$	$\Delta_{tp}^0\left[\text{mm}\right]$	$\Delta_{tp}^c\left[mm\right]$
34.5	0.0086	0.88	45	0.011	1.2

Tab. 2.6: Properties of the single nonlinear spring (z-pin T300/BMI).

2.4.3.1 Static framework

At first, analyses are developed in static framework, in which inertial effects are not taking into account. Classical DBC with opening forces, involving pure mode I loading condition is investigated. The loading, boundary conditions and geometry of the specimen are illustrated in Fig. 2.20.

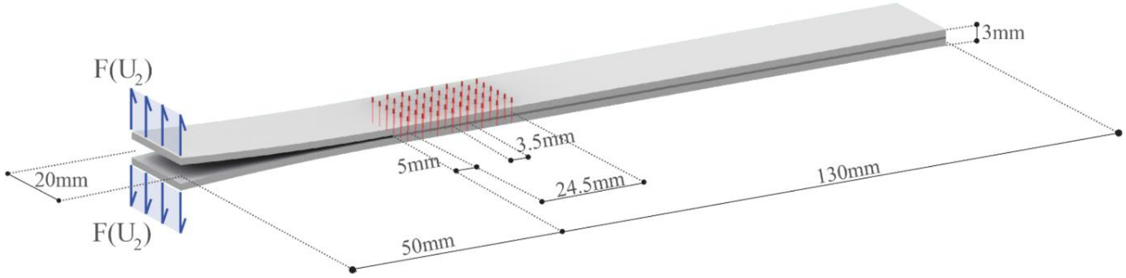

Fig. 2.20: DBC scheme reinforced by z-pins.

The numerical model is discretized along the thickness by using one mathematical element for each sublaminate, whereas, for the interfaces, an ALE element is introduced between each sublayer, in which a pre-existing crack length equal to 50 mm is assumed. It is worth noting that as shown in [95-97], a refined discretization obtained introducing more layers in classical mode I DBC scheme, does not improve the accuracy in the prediction of fracture variables. The analysis is developed under a displacement control mode, to ensure a stable crack propagation. The numerical discretization is based on a non-uniform mesh enrichment in the debonding region, i.e. $\Delta_M / L = 0.1/180$ on $\Omega / L = 1/180$, and a uniform coarse discretization in the remaining region, i.e. $\Delta_M / L = 0.5/180$. The nominal crack tip is defined as the position in which the interlaminar fracture function $\left(g_f\right)$ is equal with a relatively accuracy to zero. The results, reported in Fig. 2.21 and Fig. 2.22, are presented in terms of load or crack tip position as a function of opening end displacement, in which experimental data obtained from [93], numerical data taken from [33] and [94] are also reported. Moreover, in order to verify the improvement effects provided by the interlaminar reinforcements, the solution without z-pins is shown.

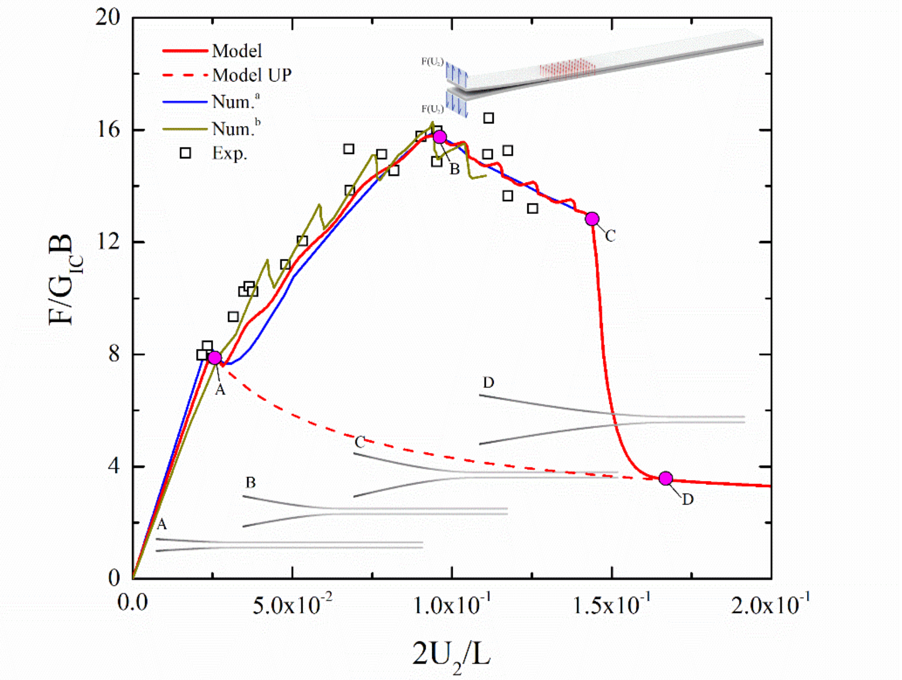

Fig. 2.21: Comparisons in terms of loading curve with experimental data [93] and numerical results [33, 94].

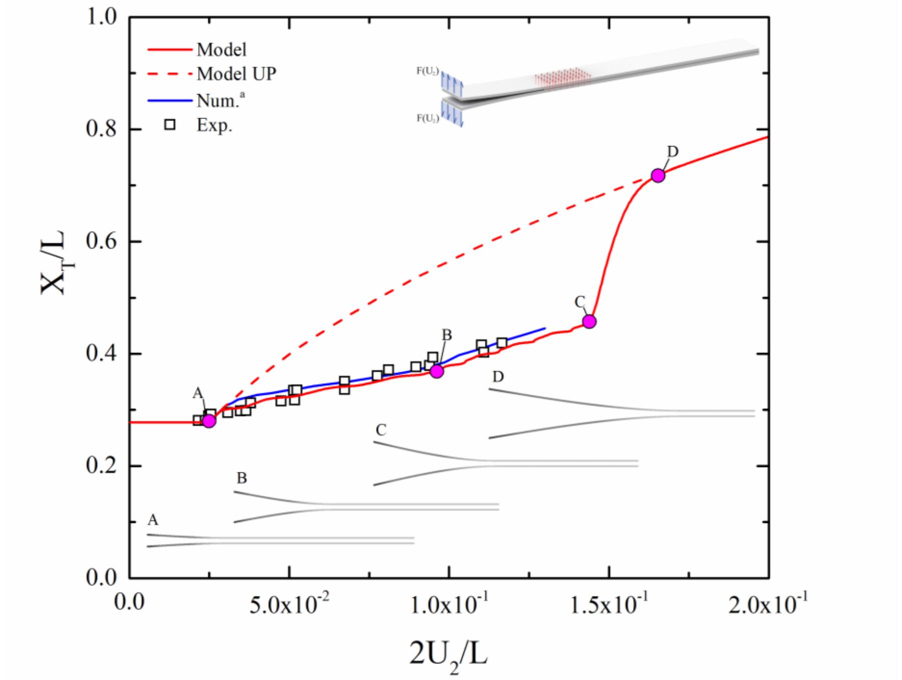

Fig. 2.22: Comparisons in terms of nominal crack tip position with experimental data [93] and numerical result [94].

Finally, in Fig. 2.23, the damage distribution in the z-pins and the interlaminar fracture function g_f are monitored at representative points of the loading curve. The results show that, from point 0 to point A, the behaviour of Pinned (P) model and Un-Pinned (UP) model is basically coincident. This is confirmed by the results obtained in Fig. 2.21, which shows how up to point A, the interlaminar fracture function g_f is lower than zero and thus the contribution of the z-pins practically negligible. From point A to point B the interaction between debonding mechanisms and z-pin traction forces produces, with respect to the UP solution, an increment in both stiffness and strength. Similarly, the slope in the crack-tip displacement curve is decreased, denoting how, at the same applied displacement, the UP configuration presents crack displacements much larger than those observed in the strengthened configuration. The maximum strength is observed, when the nominal crack tip reaches approximately the midspan of the z-pin region. At this stage the first three z-pins are completed damaged (Fig. 2.23Fig. 2.21b), whereas the central ones are partially debonded and the remaining ones are undamaged. Subsequently, the strength curve denotes a softening branch, i.e. path BC, in which the z-pins partially contribute to the total strength of the laminate. As far as the nominal crack tip goes over the strengthened region, the remaining z-pins proceed from the partial to the complete failure. This behaviour is mostly observed in the loading path, which goes from C to D, in which the laminate becomes unstable presenting a softening behaviour with no snap-back phenomena. The loading curve as well as the crack-tip displacement at the final point D match exactly with the ones of the UP configuration (Fig. 2.23e). Such behaviour is quite reasonable since the analysis is performed under a quasi-static loading scheme, but, as will be shown subsequently, the behaviour in dynamics is different since inertial effects may influence the current solution. The results obtained by the proposed model are in agreement with the experimental [93] and numerical [33, 94] data available from the literature. However, the solution presented in [94] refers to a cohesive model in which distributed interface elements are utilized. As a consequence, the loading curve is smoother than the one obtained experimentally, in which jumps due the presence of the z-pin failure occur. Numerical results reported in [33] simulate the presence of z-pins with discrete cohesive elements, reproducing in the loading curve the discontinuities due to the presence of z-pin mechanisms. The proposed model, despite the numerical solutions, is able to reproduce correctly the presence of the z-pins, since oscillations in the loading curve are properly simulated. Moreover, numerical instability problems, typically observed in debonding processes, are circumvented by the use of ALE cohesive model, since, as shown in Fig. 2.21 and Fig. 2.22, the solution is easily determined in wide large ranges of crack tip and applied displacements.

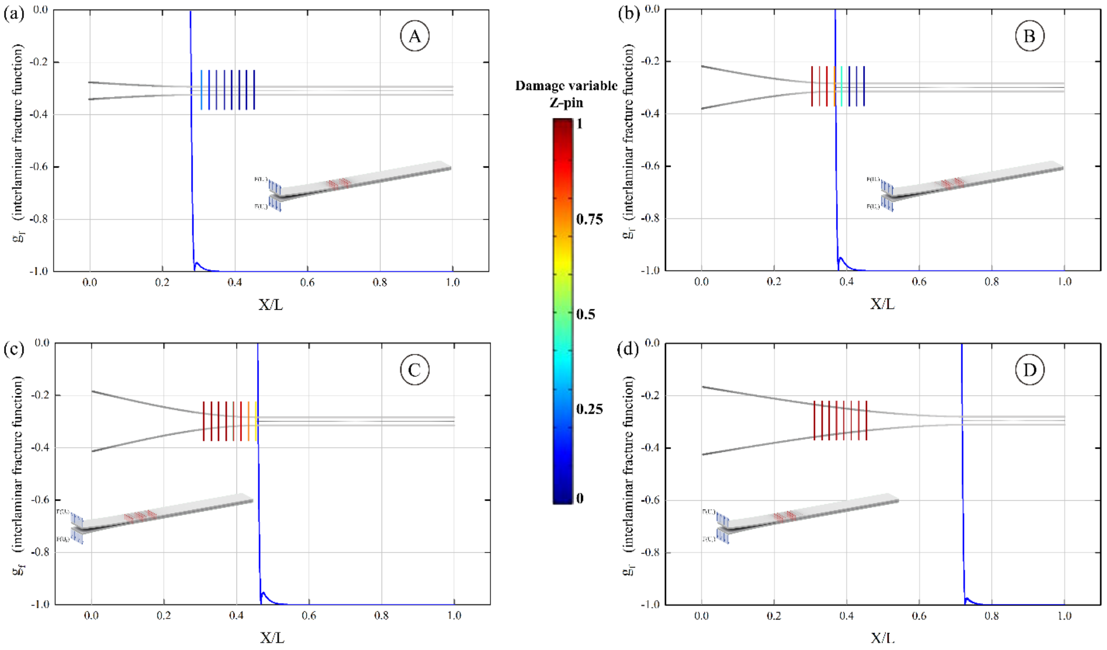

Fig. 2.23: Damage distribution in the z-pins and interlaminar fracture function at representative points of the loading curve.

The numerical methodology is validated by means of additional comparisons with existing formulations, which describe accurately the behaviour of z-pinned composite laminates. The analysis, reported in [33, 93], refers to loading schemes based on classical MMB test with G_{II} / G_T equal to 20%. The loading, the boundary conditions and the geometry are illustrated in Fig. 2.24. The values of mechanical properties assumed for the laminate scheme, those concerning the cohesive zone model and z-pin characteristics are reported in Tab. 2.5 and Tab. 2.6 respectively.

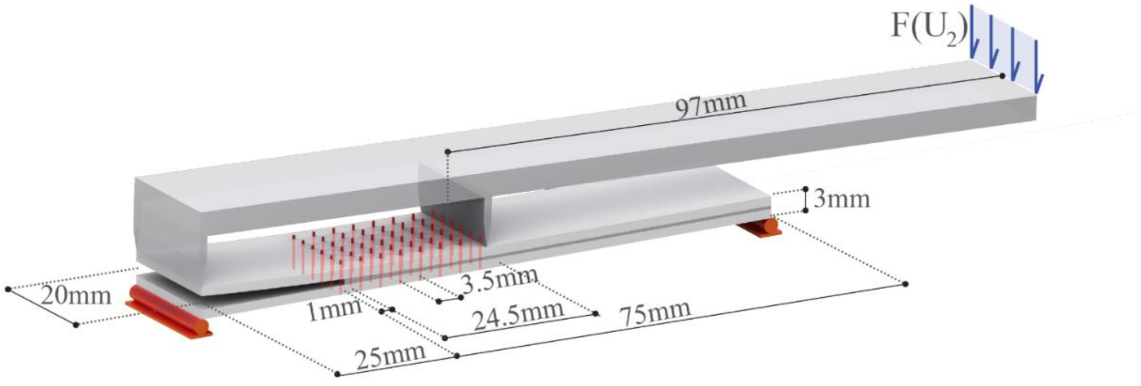

Fig. 2.24: MMB scheme reinforced by z-pins.

The numerical model is discretized along the thickness by using one mathematical layer for each sublaminate, whereas, for the interfaces, an ALE element is introduced between the sublayers adjoining the delamination. The mesh discretization of the numerical model is based on a uniform distribution with an element length of $\Delta_M / L = 0.5/100$ in the laminate, whereas for the debonding region a refinement of the mesh, i.e $\Delta_M / L = 0.1/100$ is utilized. In Fig. 2.25 , loading curves are reported with respect to different scenarios, in which P or UP configurations are analysed. In addition, numerical [33] and experimental [93] results are reported to validate the proposed formulation. Moreover, the relationship between nominal crack tip and applied displacements are reported in Fig. 2.26. The results show that, despite the case involving pure mode I loading condition, the first debonding load is influenced from the presence of z-pin distribution in the process zone, since a larger value than that of the UP configuration is observed. This behaviour is mainly produced by the position of the z-pins with respect to the initial delamination length, which is larger than the case in mode I configuration and lower in the mixed mode loading configuration. The loading curve as well as the crack tip displacement evolution present similar trends analysed in previous results concerning DCB scheme, except for the path C-D, in which the softening branch is affected by snap-back phenomenon. Finally, the comparisons with numerical and experimental data are quite in agreement with the results obtained by using the proposed model.

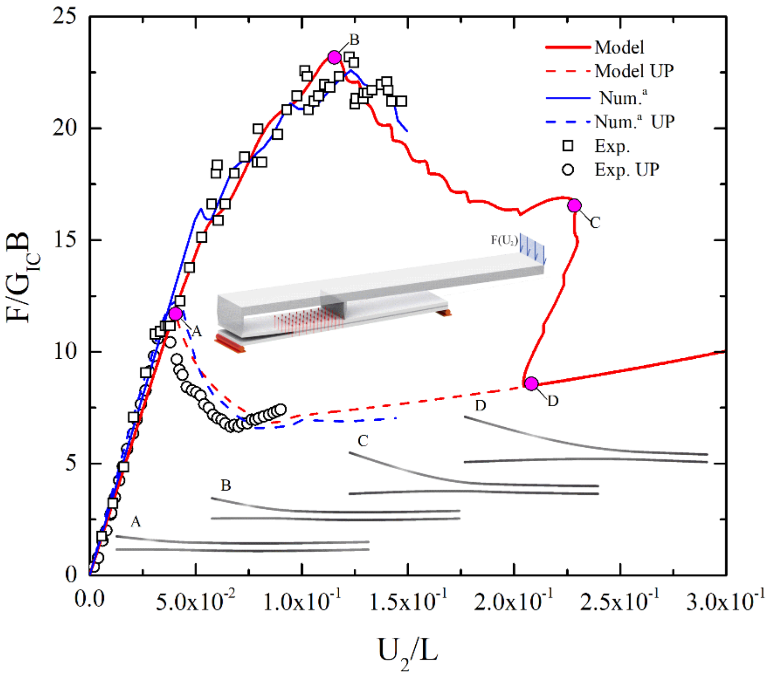

Fig. 2.25: Comparisons in terms of loading curve (F/G_{IC} B-U_2/L) with experimental data [93] and numerical result [33].

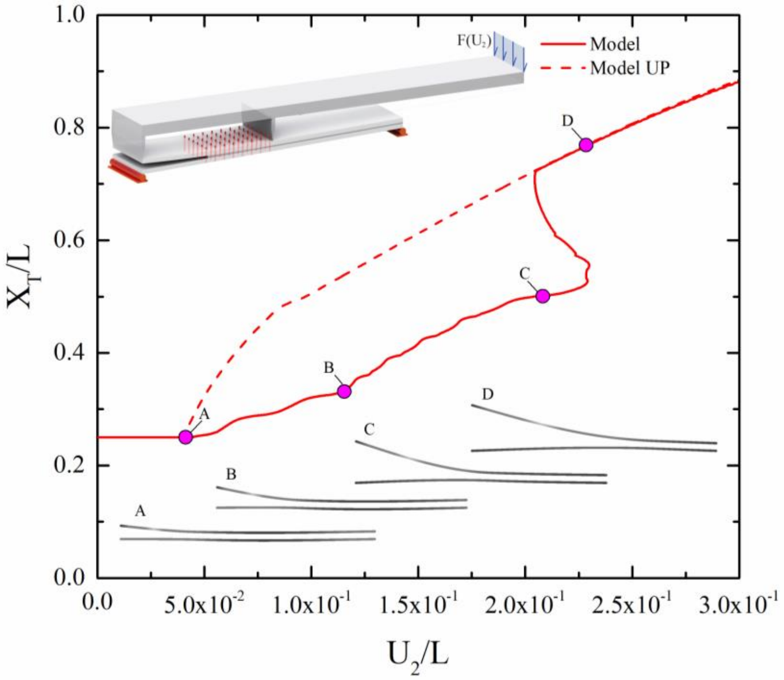

Fig. 2.26: Comparisons in terms of nominal crack tip position (X_T/L-U_2/L) with UP configuration.

2.4.3.2 Dynamic framework

Previous results are developed essentially in the framework of a static analysis, in which time dependent effects produced by the loading rate and inertial forces are supposed to be negligible. The extension in dynamics is developed taking into account rate dependent contributions arising from inertial effects of the structure. Without loss of generality, the constitutive laws of the z-pins, are supposed to be similar to the ones utilized for the static framework. The load process is assumed to be governed by an applied velocity with ramp curve and a constant speed (v_0) at the time t_0, which is assumed to be proportional to the first period of vibration of the structure ($t_0 = 0.5T_1 = 6.246\times10^{-4}$ [s]). The analyses are reported in Fig. 2.27, in which resistance curves for different loading rates are compared with the solution arising from the static case. The results show that, at low loading rate, i.e. $v_0 = 1$ [m/s], the solution oscillates around the static one. In particular, pre-debonding phase, maximum strength and softening region are practically unaffected by the inertial effects. However, as far as the applied speed is increased the solution becomes quite unstable. Such differences are mainly produced by the inertial effects of the loading rate and their interaction with the z-pin failure, especially when the debonding mechanism overpasses the z-pin region.

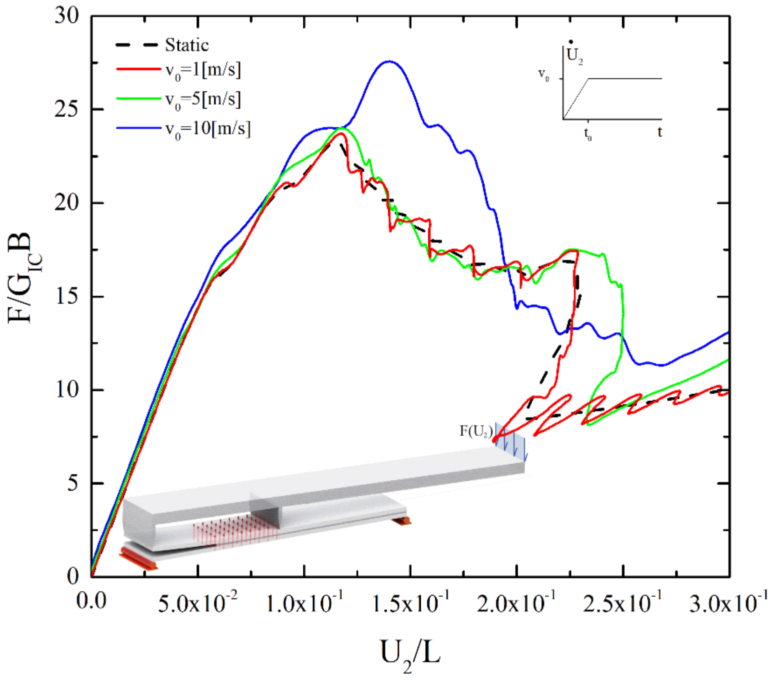

Fig. 2.27: Influence of the loading rate in terms of loading curve (F/G_{IC} B-U_2/L)..

In order to verify this phenomenon, results expressed in terms of measured crack tip speeds, normalized on the shear wave speed (V_s) of the material, as a function of the nominal crack position X / L are reported in Fig. 2.28 In the same figure the position of the z-pins is also reported.

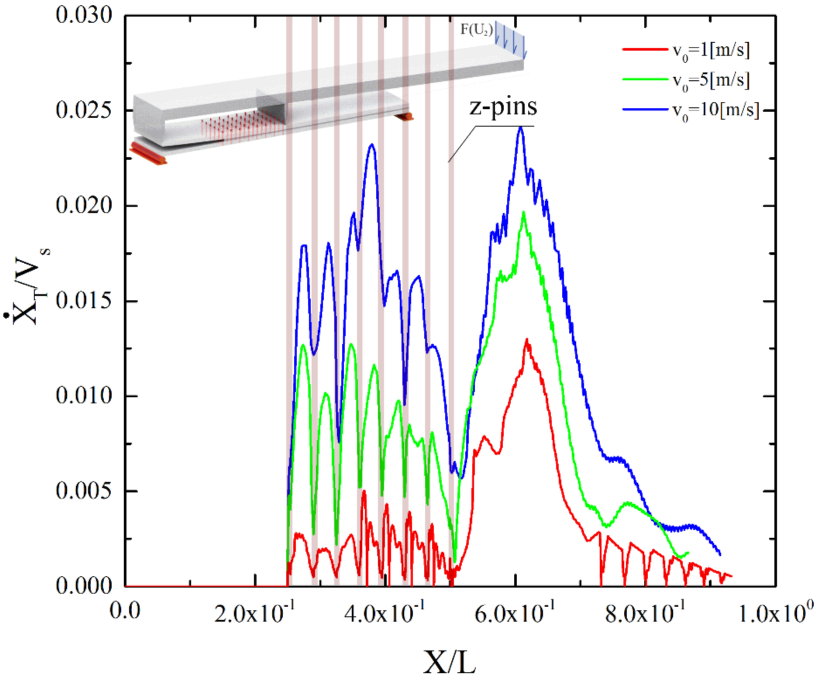

Fig. 2.28: Influence of the loading rate in terms of nominal crack tip speed .

The results show that during this transition at low loading rates, the crack tip speed in the crack initiation phase tends to be damped from the presence of z-pins, leading to crack arrest phenomena along the strengthened region. Subsequently, the observed crack tip speed is amplified with values much larger than the previous ones, because of the failure of the z-pins. Finally, the nominal crack tip tends to large values due to the presence of boundary conditions. However, at high loading rates, the inertial effects introduced by the external loads are able to produce a relevant amount of kinetic energy and thus the observed speeds in both strengthened and strengthened regions are comparable.

Chapter 3 Initiation and coalescence phenomena

The present chapter extends previous analyses in which a pre-existing defect is assumed "a priori" in the structure, taking into account the effects of crack onset. In particular, a numerical methodology based on a moving mesh technique and a multilayer formulation is developed with the purpose to predict crack onset, evolution and coalescence of interlaminar damage mechanisms. The outline of the Chapter is as follows. Section 3.1 presents the formulation of the governing equations for the ALE and interface approaches, whereas in Section 3.2 the numerical implementation is reported. Finally, comparisons and parametric results to investigate static and dynamic behaviour of the debonding phenomena are proposed in Section 3.3.

Part of analyses and results presented and discussed in this chapter were already published by the following papers:

- *Funari, M.F., Lonetti, P., Initiation and evolution of debonding phenomena in layered structures, Theoretical and Applied Fracture Mechanics, In press, corrected proof, Available online 29 May 2017.*
- *Funari, M.F., Greco, F., Lonetti, P., A coupled ALE-Cohesive formulation for layered structural systems, Structural Integrity Procedia, 2017, 3, 362-369*
- *Funari, M.F., Greco, F., Lonetti, P., Luciano, R., Penna, R., An interface approach based on moving mesh and cohesive modelling in Z-pinned composite laminates, Composites Part B: Engineering, 2018, 135, 207-217.*
- *Funari, M.F., Greco, F., Lonetti, P., Dynamic debonding in layered structures: A coupled ALE-cohesive approach, Fracture and Structural Integrity, 2017, 41, 524-535.*

3.1 Theoretical Formulation

The proposed model is based on the numerical formulation described in the previous Chapter, in which the structure is composed by the combination of beams and interfaces [36, 82]. Each layer is connected to the adjoining ones by means ALE-cohesive interfaces without pre-existing defects, in which debonding phenomena may affect the adhesion between layers introducing material discontinuities and traction forces along normal or sliding directions. In order to simulate debonding phenomena, a fundamental task to be achieved is to identify the position, in which the onset of interfacial mechanisms is produced and subsequently to simulate the evolution of the cracked length. In the proposed model, two steps, referred to different numerical models and geometries, are considered in the analysis, which will be presented, separately, in the following subsections. A synoptic representation of the model is reported in Fig. 3.1, whereas the steps involved in the proposed procedure are reported in Fig. 3.2.

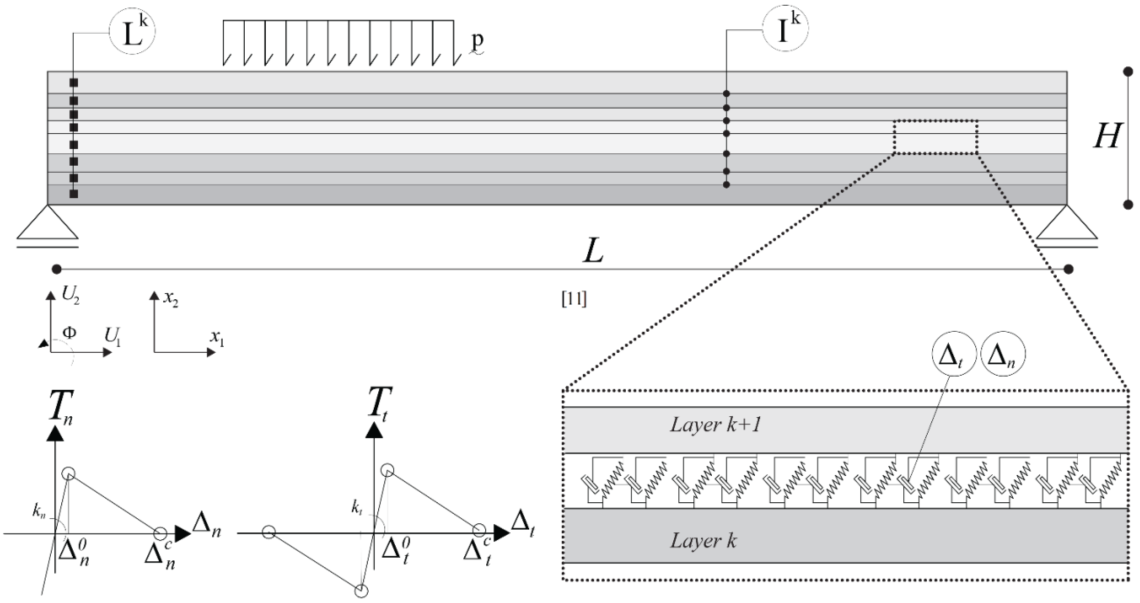

Fig. 3.1: Multilayered laminate structure: geometry, interfaces and TSL.

3.1.1 Formulation of the crack onset modelling

At this stage, it is only required to identify the positions in which the onset conditions are satisfied. Without of loss of generality, the crack onset definition is described by means of a mixed crack growth criterion, which is a function of the fracture variables, coinciding with the ratio between ERR mode components and corresponding critical values, as follows:

$$g_f^k\left(X_1^k\right)=\left(\frac{G_I\left(X_1^k\right)}{G_{IC}}\right)^{\frac{r}{2}}+\left(\frac{G_{II}\left(X_1^k\right)}{G_{IIC}}\right)^{\frac{r}{2}}-1 \tag{3.1}$$

where k represents the generic k-th interface in which debonding phenomena may occur, r is the constant utilized to describe fracture in different materials, $\left(G_{IC}, G_{IIC}\right)$ are the total area under the traction separation law and $\left(G_I, G_{II}\right)$ are the individual energy release rates calculated as $G_I=\int_0^{\Delta_n^c} T_n\left(\Delta_n\right) d\Delta_n$ and $G_{II}=\int_0^{\Delta_t^c} T_t\left(\Delta_t\right) d\Delta_t$.

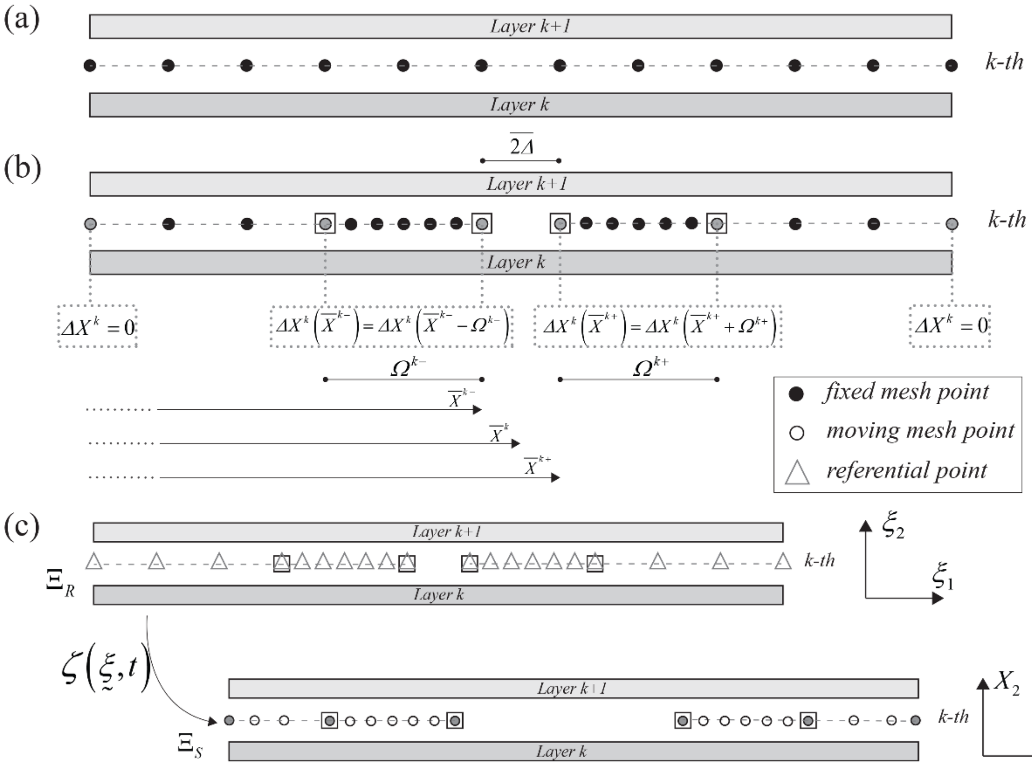

Fig. 3.2: Representation of the coordinate systems employed: Before crack initiation (a), After crack initiation, material and moving coordinates system are coincident (b), ALE formulation: referential and moving configuration introduced to describe debonding phenomena (c).

According to previous Chapter, the TSL are expressed by Eq. (2.7). However, the proposed model is quite general to include other existing cohesive formulations based on a different TSL or stress based initiation criteria, just by modifying the analytical expressions defined in Eq.(3.1)-(2.7). It is worth noting that since the main purpose of this preliminary step is to identify the position of the onset crack, the numerical model should be described by means of a relatively coarse mesh discretization, in which at the k-th interface the position of each numeric mesh points is described by the horizontal axis X_1 (Fig. 3.2a). At this stage, since the ALE equations are not activated, the position of the computational mesh points is expressed in the Fixed Material (M) Frame (M), Ξ_M identified by the x_1-x_2 coordinates (Fig. 3.2), which coincides, at this stage, with the Moving (M) Frame, Ξ_S, described in the following subsection, i.e. X_1-X_2. The location, in which the crack growth is achieved, are identified by means of those values $\overline{X}_1^k$, which set to zero Eq.(3.1). Such quantities are evaluated by enforcing in the region in which the *k*-th interface is concerned the following condition:

$$g_f^k\left(\overline{X}_{1,i}^k\right) = 0 \quad with\ 0 \le \overline{X}_{1,i}^k \le L, i = 1, \mathrm{N}_d^k \tag{3.2}$$

with the index *i* represent the number of the *i*-th debonding mechanism potentially activated at the *k*-th interface and N_d^k is the number of material discontinuities activated at the *k*-th interface.

3.1.2 Crack evolution mechanism

Once the positions of the crack are determined, the numerical model is subjected to a mesh enrichment by means of the application of a remeshing procedure, which ensures accuracy in the prediction of fracture variables in proximity of the crack onset position. At this point of the numerical procedure, the proposed model is coincident with the one developed in the previous Chapter, where only the delamination phenomena has been investigated. Without loss of generality and for conciseness, the case of an internal debonding mechanism is now considered. However, the model is quite general to include multiple crack onset and debonding conditions. Starting from the onset coordinate $\overline{X}_1^k$ at the *k*-th interface obtained by solving Eq.(3.2), two independent debonding mechanisms depart, i.e. along right and left direction. In order to reproduce the crack growth, the ALE strategy is implemented to prescribe the crack motion by modifying the geometrical positions of the computational points. In particular, at each interfaces, moving or spatial system, Ξ_S, described in terms of the geometrical positions $\underset{\sim}{X}$, is modified with the purpose to reproduce moving traction forces acting at the layers adjoining the interface (Fig. 3.2b). The mathematical description of the moving mesh modelling is defined by a mapping operator Φ, which relies a particle in a fixed Referential (R) Frame, and the one in current moving coordinate system, namely Ξ_R and Ξ_S, as follows:

$$\underset{\sim}{X} = \Phi\left(\underset{\sim}{\xi},t\right) \qquad \text{with} \qquad \Phi : \Xi_R \rightarrow \Xi_S \tag{3.3}$$

The mesh motion in terms of displacement field is described as the difference between moving and the referential coordinates:

$$\Delta X_1^k = X_1^k\left(t\right) - \xi^k\left(t\ \right) = \Phi^k\left(\xi,t\right) - \xi^k\left(t\right) \qquad on \quad \Omega^k \tag{3.4}$$

where $\Omega^k = B \times h^k$ represent the region in which the debonding mechanisms are produced. In order to reduce mesh distortions, produced by the mesh movements, rezoning or smoothing equations are introduced to simulate the grid motion. In the present study, a Laplace based equation is assumed, which is, in the case of one dimensional domain for both Static (S) and Dynamic (D) analyses, defined on the basis of the following relationships [98]:

$$\Delta X^k_{,\xi\xi} = \frac{\partial^2 \Phi^k\left(\xi,t\right)}{\partial \xi^2} \qquad \text{(S)} \qquad \Delta \dot{X}^k_{,\xi\xi} = \frac{\partial^3 \Phi^k\left(\xi,t\right)}{\partial t \partial \xi^2} \qquad \text{(D)} \tag{3.5}$$

Eqs. (3.5) should be completed by means of boundary equations to reproduce the crack tip motion on the basis of the assumed crack growth criterion, namely g_f^k. In particular, for a fixed position in which the crack initiation occurs, different boundary conditions should be introduced to enforce internal or external debonding mechanisms. Differently to previous numerical implementation explained in Chapter 2, once the position of the crack onset is determined, i.e.at $X_1 = \overline{X}_1^k$, a geometrical debonding with length equal to $\overline{2\Delta}$ is introduced in the numerical model, producing two potential finite crack tips in which debonding phenomena can be triggered (Fig. 3.2b). The evolution of debonding phenomena is considered by introducing the following boundary equations, corresponding to the Kuhn–Tucker optimality conditions concerning the crack growth:

$$\begin{aligned} &\left|\Delta \dot{X}_T^k\right|^+ \geq 0, g_f^k \leq 0 \ \text{ with } \left|\Delta \dot{X}_T^k\right|^+ \cdot g_f^k = \left|\Delta \dot{X}_T^k\right|^+ \cdot \dot{g}_f^k = 0, \ \ at \ \left(\overline{X}_1^k\right)^+ = \overline{X}_T^k + \overline{\Delta} \\ &\left|\Delta \dot{X}_T^k\right|^- \geq 0, g_f^k \leq 0 \ \text{ with } \left|\Delta \dot{X}_T^k\right|^- \cdot g_f^k = \left|\Delta \dot{X}_T^k\right|^- \cdot \dot{g}_f^k = 0, \ \ at \ \left(\overline{X}_1^k\right)^- = \overline{X}_T^k - \overline{\Delta} \end{aligned} \tag{3.6}$$

where ΔX_T^k indicates the displacement of the crack tip front of the *k*-th debonded interface, g_f^k is the fracture function defined in Eq. (3.1) and $(\bullet)^{+/-}$ represents the value of the $(\bullet)$ variable evaluated at left (-) or right (+) crack tip position. However, additional relationships are required for the ALE formulation to reproduce the crack tip motion and boundary conditions. In particular, the displacements of the computational nodes are assumed to be zero at the boundaries of the structure, whereas small portions, close to the crack tip for the left and right debonding mechanisms, namely Ω^{k-} and Ω^{k+}, are assumed to be moved rigidly, enforcing the computational nodes at the extremities to have the same displacements. This choice ensures that the NL involved in the debonding mechanisms are constrained to a small portion containing the process zone, reducing the total complexities of the model. Consequently, the following boundary conditions should be considered in the analysis (Fig. 3.2b):

$$\begin{aligned} &\Delta X_1^k = 0, \quad at \quad X_1^k = (0, L), \\ &\Delta X_1^k\left(\overline{X}_1^{k+}\right) = \Delta X_1^k\left(\overline{X}_1^{k+} + \Omega^{k+}\right) \\ &\Delta X_1^k\left(\overline{X}_1^{k-}\right) = \Delta X_1^k\left(\overline{X}_1^{k-} - \Omega^{k-}\right) \end{aligned} \tag{3.7}$$

The boundary value problem, given by the set of Eqs. (3.5)-(3.7) is solved by using a variational approach. In particular, taking into account the transformation rules defined by Eq.(3.4) and introducing mesh displacement conditions on internal and external boundaries, reported in Eq.(3.7), the following expression regulates in the referential configuration the crack growth:

$$\begin{aligned} \int_{\Omega^k} \Phi^k_{,\xi}\delta\Phi^k_{,\xi} d\xi + \left[\lambda_T^k \delta\Phi^k + \delta\lambda_T^k\left(\Phi^k - \overline{\Phi}^{k+} - \overline{\Delta X}^{k+}\right)\right]_{\xi=\overline{\xi}^{k+},\overline{\xi}^{k+}+\Omega^{k+}} + \\ + \left[\lambda_T^k \delta\Phi^k + \delta\lambda_T^k\left(\Phi^k - \overline{\Phi}^{k-} - \overline{\Delta X}^{k-}\right)\right]_{\xi=\overline{\xi}^{k-},\overline{\xi}^{k-}-\Omega^{k-}} = 0 \end{aligned} \tag{3.8}$$

where $\xi_T^{k(\pm)}$ are the positions in the referential system of the debonding length extremities, $\left(\Omega^{k+}, \Omega^{k-}\right)$ represent the entities of the debonding region for the left or right crack path, λ_T^k is the Lagrange's multiplier introduced to consider the internal boundary conditions. It is worth noting that $\left(\Omega^{k+}, \Omega^{k-}\right)$ can be considered as variable quantities for each crack path, that should be determined during the crack evolution. In particular, from the physical point of view, they represent the portion in which the traction separation laws defined by Eq. (2.7) are distributed. Since those regions are assumed to be moved rigidly, by means of the ALE strategy, the nonlinearities involved by the traction forces may be reduced to a small region close to the crack tip, avoiding as a result spurious and oscillatory effects typically documented in pure CZMs. From the numerical point of view, displacements of the debonding regions are determined according to Eq. (2.21). Furthermore, As mentioned earlier, starting from the crack onset position two independent debonding mechanisms depart, furthermore the Eq. (2.21) has been modified to describe displacements of the debonding for both side i.e left and rigth (Fig. 3.3):

$$\overline{\Delta X}_T^{k\pm}=0 \quad g_f^{k\pm}\le 0,\quad \overline{\Delta X}_T^{k\pm}=\frac{g_f^k\left(\overline{X}_1^{k\pm}\right)+toll}{g_f^k\left(\overline{X}_1^{k\pm}\right)+toll\pm g_f^k\left(\overline{X}_1^{k\pm}\pm\Omega^{k\pm}\right)}\Omega^{k\pm}\quad g_f^{k\pm}=0 \qquad (3.9)$$

It is worth noting that a enriched Cohesive Model is not utilized along the entire interface, but only on a small region containing the process zone and thus the characteristic length of fracture, namely $\Omega^{k\pm}$. Moreover, in the remaining regions, a coarse mesh should be utilized since it is required to reproduce perfect adhesion phenomena or the onset of other debonding mechanisms.

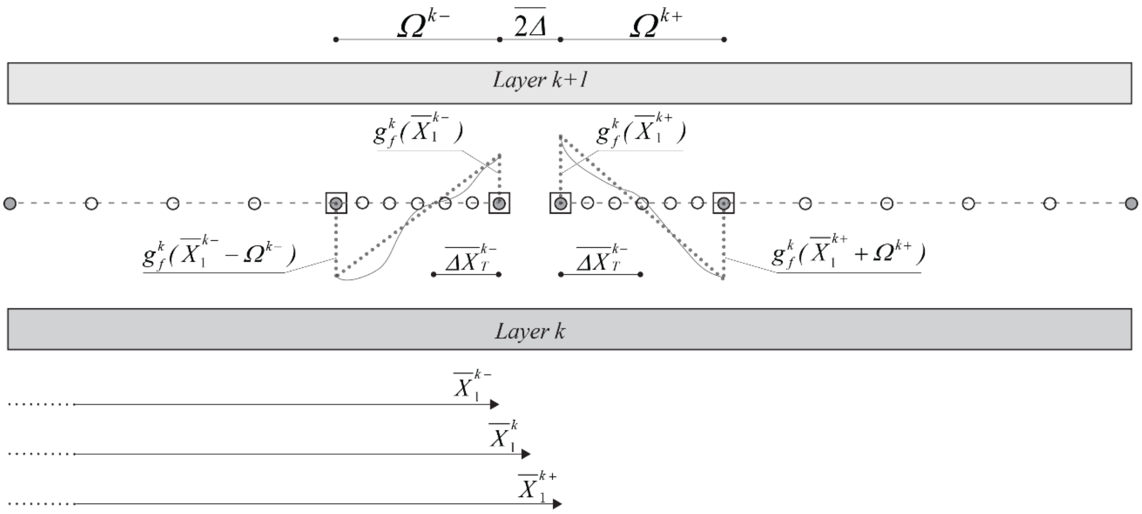

Fig. 3.3: Strategy to describe debonding phenomena by means ALE interface elements: description of the iterative procedure.

3.2 Numerical implementation

The numerical implementation of the proposed model is developed by using a finite element approach, in which the layered structure is modelled by the combination of shear deformable beam elements connected through the moving mesh interfaces. The former is utilized to simulate layer deformability by using classical Timoshenko beam formulation, whereas the latter is implemented by means of ALE approach. In particular, at the generic interface, mesh displacements and speeds of the computational nodes are defined by means of quadratic interpolation functions in terms of nodal components:

$$\left(\underset{\sim}{X}, \underset{\sim}{\dot{X}}\right).\; X\left(\xi\right) = \underset{\sim}{N}\left(\xi\right)\underset{\sim}{X}, \qquad \dot{X}\left(\xi\right) = \underset{\sim}{N}\left(\xi\right)\underset{\sim}{\dot{X}} \tag{3.10}$$

At first, the analysis is developed to identify the positions in which interfacial cracks are triggered by checking crack criterion defined in Eq.(3.1). Such task is carried out by using a relatively coarse numerical mesh, which is verified, in the next substep, by enriching the mesh utilizing remeshing procedure (Fig. 3.4a). The identification of the onset interfacial crack position is performed by introducing an operator, i.e. $\underset{\sim}{G}^k$, which collects, at each loading steps and computational nodes, the values fracture function:

$$\underset{\sim}{G}^k = \Psi^k\left(\underset{\sim}{\Delta}^k, \underset{\sim}{X}^k\right) \tag{3.11}$$

where $\underset{\sim}{\Psi}^k$ is the operator vector expressed in terms of interfacial displacement vector and geometrical position vector of the computational nodes, i.e. $\underset{\sim}{\Delta}^k$ and $\underset{\sim}{X}^k$ respectively. From the numerical point of view, the dimension of the numerical mesh should be small enough to guarantee accuracy in the prediction of the interlaminar stresses. The position, in which a finite crack length is produced, namely $\overline{X}_1^k$, is determined by solving those values which set to zero within a numerical accuracy (*toll*) Eq.(3.11):

$$\Psi^k\left(\underset{\sim}{\Delta}^k, \overline{X}_1^k\right) \geq toll \tag{3.12}$$

Once the point in which material discontinuity is produced, the continuity condition is removed introducing a physical disconnection between the adjoining layers at the *k*-th interface (Fig. 3.4b). As a consequence, the internal crack may evolve differently along the Right (R) or the Left (L) sense. From the geometrical point of view, the material discontinuity is reproduced by means of a small length $\overline{2\Delta}$, which is introduced at the position obtained by solving Eq.(3.12), i.e. $\overline{X}_1^k$. The extremities of this region consist of the two crack tip points, namely $\left(\overline{X}_1^{k+}, \overline{X}_1^{k-}\right)$ with $\left(\overline{X}_1^{k+} = \overline{X}_1^k + \overline{\Delta}, \overline{X}_1^{k-} = \overline{X}_1^k - \overline{\Delta}\right)$which may evolve due to debonding mechanisms. However, at this stage, the remaining internal points are not affected by material discontinuities, since the presence of the geometrical discontinuity produces local effects close to the onset position.

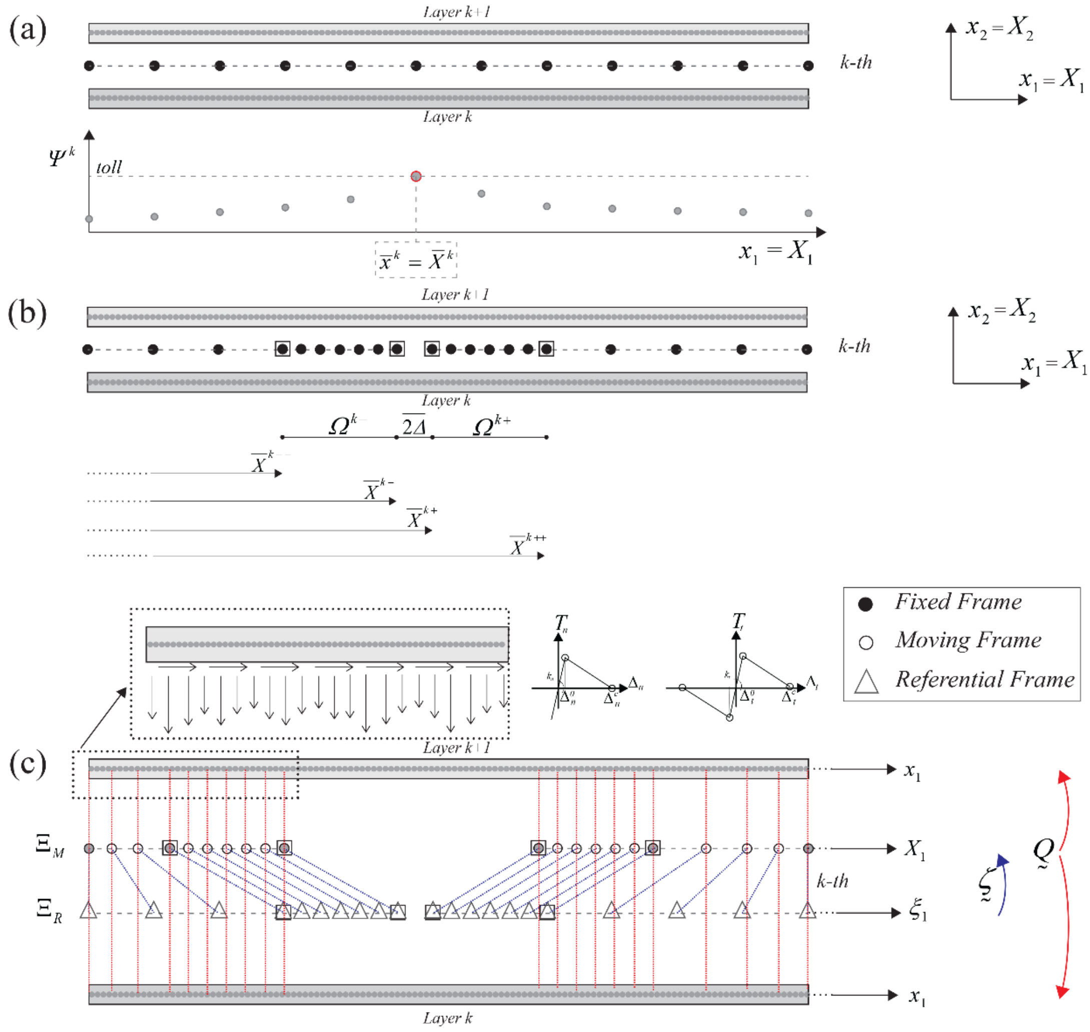

Fig. 3.4: Synoptic representation of the Numerical implementation: Searching of the crack onset condition and itself position (a), Process of changing geometry and mesh refinement (b), description of the debonding phenomena by means ALE elements (c).

Subsequently, the R or L debonding regions $\left(\Omega^{k+}, \Omega^{k-}\right)$ are identified starting from the crack tip points, by searching those nodes, whose extremities, i.e. $\left(X^{k++}, X^{k--}\right)$, present a value of the fracture function g_f^k negative within a relative tolerance criterion:

$$\Omega^{k+} = X_1^{k+} - X_1^{k++} \quad \text{with} \quad g_f^k\left(X_1^{k++}\right) < toll \tag{3.13}$$

$$\Omega^{k-} = X_1^{k-} - X_1^{k--} \quad \text{with} \quad g_f^k\left(X_1^{k--}\right) < toll \tag{3.14}$$

where the *toll* is assumed to be a quantity small enough to ensure a finite displacement of the debonding region. It is worth noting that Ω^{k+} and Ω^{k-} are assumed to be variable quantities to be identified in the computation procedure, since they are predicted on the basis of current values at the crack tip positions and those of the fracture function close to the corresponding debonding regions. From the numerical point of view, in such portions, the traction forces evolve in a NL way, whereas in the remaining ones perfect adhesion should be represented introducing proper boundary conditions on the interfacial displacements. To this end, an enrichment of the numerical mesh is performed, only in the debonding regions, by means of classical remeshing techniques [99] with the purpose to verify the prescribed accuracy in the definition of the TSL evolution.

Subsequently, the analysis is carried out by solving the governing equations arising from ALE modelling, enforcing, the extremities of each debonding regions to have the same displacements. In order to avoid distortions in these regions produced by the mesh motion, which may introduce loss of accuracy in the prediction of fracture variables, a rigid displacement of the debonding lengths is enforced by using the Lagrange's multiplier method. In particular, the discrete equations are derived by substituting Eq.(3.10) into Eq.(3.8), prescribing Eq. (3.7), in which unknown quantities are represented by the position of the computational nodes $\overline{\underset{\sim}{X}}$:

$$\underset{\sim}{W}\,\overline{\underset{\sim}{X}} + \underset{\sim}{N}\,\overline{\underset{\sim}{\Gamma}} = 0,\quad \underset{\sim}{N}\left(\overline{\underset{\sim}{X}} - \overline{\underset{\sim}{\xi}} - \underset{\sim}{I}\Delta X_T^-\right) = 0\ ,\ \underset{\sim}{N}\left(\overline{\underset{\sim}{X}} - \overline{\underset{\sim}{\xi}} - \underset{\sim}{I}\Delta X_T^+\right) = 0 \tag{3.15}$$

where $\underset{\sim}{W}$ is the ALE discretization matrix $\overline{\underset{\sim}{\Gamma}}$ is the Lagrange multiplier vector concerning the ALE formulation, $\overline{\underset{\sim}{\xi}}$ is the position of the mesh point in the referential coordinate system, $\underset{\sim}{N}$ is the allocation matrix and $\underset{\sim}{I}$ is the unity allocation vector which expresses the constraint conditions concerning the right or the left debonding displacements, i.e. ΔX_T^- and ΔX_T^+ respectively. In order to identify the current displacement of the debonding mechanisms it is required to solve the growth condition expressed in terms of Eq.(3.9) and values of the crack growth criterion at the debonding length extremities. The ALE formulation is coupled with the structural problem by means of the cohesive traction forces, whose distribution on the adjoining layers is expressed in terms of moving reference system. In particular, the traction force vector $\underset{\sim}{T}$ is defined on the basis of the relative displacement vector $\underset{\sim}{\Delta}$, by mean of the constitutive relationship operator $\underset{\sim}{C}$ expressed as a function of Eq. (2.7). As shown in Fig. 3.4c, the displacement vector is defined in terms of the ALE coordinates by means of a projection operator $\underset{\sim}{Q}$ with $\underset{\sim}{Q}:\Xi_S \rightarrow \Xi_M$ which connects moving material points on the ALE configuration Ξ_S and fixed material points Ξ_M of the adjoining layers (Fig. 3.4c). Therefore, the interface traction force vector is expressed as follows:

$$\underset{\sim}{T} = \underset{\sim}{C}\underset{\sim}{\Delta} \quad \textit{with} \quad \underset{\sim}{\Delta} = \underset{\sim}{\Pi}\left[\underset{\sim}{X}\right] = \underset{\sim}{\Pi}\left[\underset{\sim}{\Phi}\underset{\sim}{\xi}\right] \tag{3.16}$$

where $\underset{\sim}{T}$ is the traction force vector, $\underset{\sim}{C}$ defined the relative stiffness on the basis of Eq. (2.7), $\underset{\sim}{\Delta}$ contains the relative horizontal and vertical displacements expressed as a function of the $\underset{\sim}{\Pi}$ operator at the generic coordinate system $\underset{\sim}{X}$. The proposed approach is implemented by means of a customized version of the finite element package Comsol Multiphysics [85]. In particular, proper script files are carried out to manage the steps involved in the procedure, regarding the geometry variation due to the crack onset, the debonding length definition and the mesh enrichment in the process zone. The model can be solved in both static and dynamic frameworks, taking into account time dependent effects produced by the inertial characteristics of the structure and the boundary motion involved by debonding phenomena. In both cases, the governing equations are integrated by means of proper stop and restart conditions, to modify the computational mesh due to the onset of debonding phenomena. In the case of static analysis, the resulting equations are solved by using a nonlinear methodology based on Newton-Raphson or Arch length integration procedures, whereas in dynamics, the algebraic equations are solved by using an implicit time integration scheme based on a variable step-size backward differentiation formula (BDF). A synoptic representation of the numerical procedure as well as the computational algorithm implemented in the FE environmental program are reported in Fig. 3.5 and Tab. 3.1.

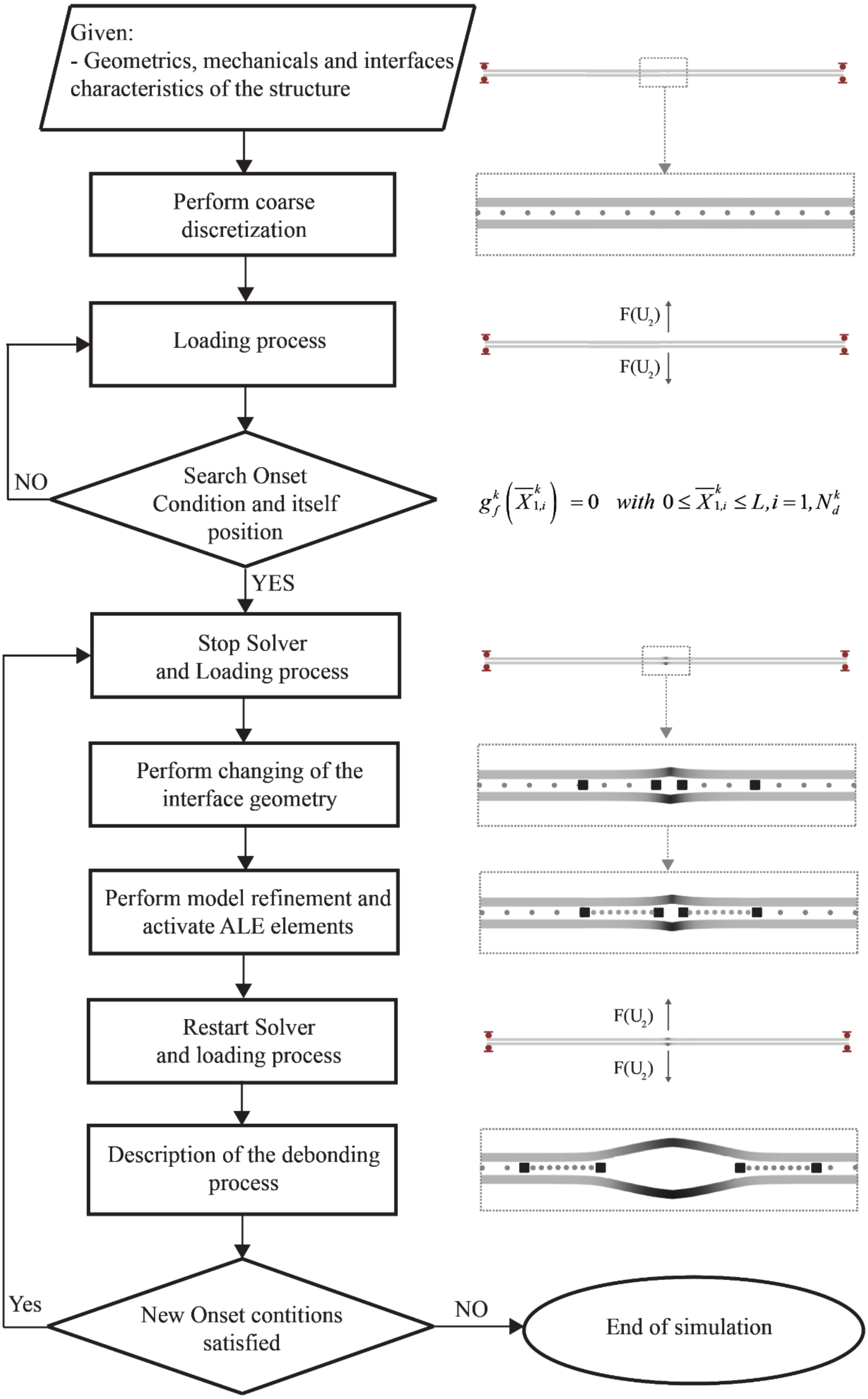

Fig. 3.5: Schematic representation of the algorithm for layered structure, crack initiation and evolution.

```
START
0. Read the input data: geometry, material and interface characteristics
1. Loop for model coarse iteration
    1.1. Initialize the nodal displacement vector
    1.2. Loop for load increment
        1.2.1. Determine the external force vector $\underset{\sim}{f}$ , stiffness, mass and ALE (in case of onset
               condition) matrixes $\left(\underset{\sim}{K},\underset{\sim}{M},\underset{\sim}{W}\right)$
        1.2.2. Solve and compute nodal vector variables
        1.2.3. Compute stress and strains for each element and evaluate the damage variable of the
               interfaces
            1.2.3.1. Update the load increment counter; if crack onset condition is not satisfied go back
                     to step 1.2 to solve current solution
            1.2.3.2. If crack onset condition is satisfied $g_f^k\left(\overline{X}_{1,i}^k\right)=0 \quad with \ 0 \le \overline{X}_{1,i}^k \le L, \ i=1,\mathrm{N}_d^k$ ,
                     perform STOP Solver condition
            1.2.3.3. In the $\overline{X}_1^k$ coordinate insert the debonding length $\left(\Omega^+,\Omega^-\right)$ by modifying the
                     interfacial geometry
            1.2.3.4. Perform model refinement and transfer the interfaces damage variables to the new
                     mesh by means of remeshing procedure
            1.2.3.5. Activate interface ALE elements concerning the current debonding process
            1.2.3.6. Prediction of the crack growth
END
```

Tab. 3.1: Incremental-iterative procedure of the proposed algorithm.

3.3 Results

The proposed formulation is verified by means of several comparisons with numerical and experimental data. The first step in the validation scheme is developed with the purpose to analyse the improvements provided by the proposed formulation with respect to available approaches based on classical CZM. At first the analyses are developed in static framework. Subsequently, in order to validate the proposed model to identify the interfacial crack tip speed dynamic simulation are presented. Finally, static and dynamic behaviour of laminate reinforced with z-pins is shown.

The analyses are developed with reference several loading schemes. At first numerical investigation to define the best discretization of the structural elements, then analysed to define the computational efficiency of the model are reported.

3.3.1 Multi-layered structures, crack onset, propagation and coalescence: Static framework

The layered structure consists of a multilayered composite beam, which presents six mathematical layers and five intact interfaces. The structural scheme, reported in Fig. 3.6**Errore. L'origine riferimento non è stata trovata.**, is based on clamped end conditions and concentrated midspan opening forces. Moreover, the mechanical properties assumed for the laminate and the interfaces as well as the ones required by the cohesive zone constitutive model are reported in Tab. 3.2 and Tab. 3.3.

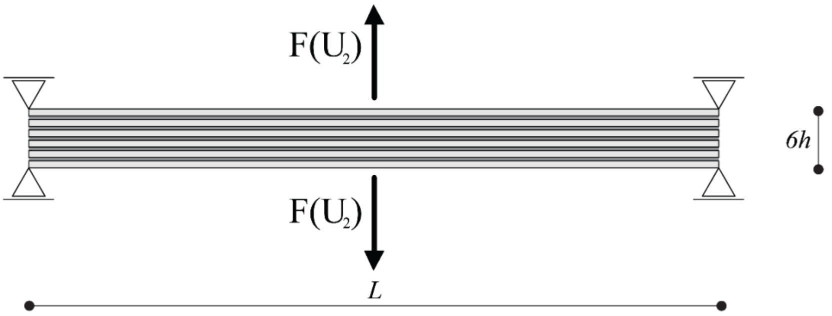

Fig. 3.6: Layered configuration formed by six structural layers.

$E_1\left[\text{GPa}\right]$	$G_{12}\left[\text{GPa}\right]$	$\rho\left[\text{kg m}^{-1}\right]$	-	-
130	*6*	*1500*	-	-
$L\left[\text{mm}\right]$	$B\left[\text{mm}\right]$	$a\left[\text{mm}\right]$	$h\left[\text{mm}\right]$	$d\left[\text{mm}\right]$
200	*20*	*20*	*2*	*5*

Tab. 3.2: Mechanical and geometrical properties of the layered structures reported in Fig. 3.6

$G_{IC}\left[\text{N mm}^{-1}\right]$	$T_n^c\left[\text{MPa}\right]$	$\Delta_n^0\left[\text{mm}\right]$	$\Delta_n^c\left[\text{mm}\right]$
0.26	30	0.00173	0.0173
$G_{IC}\left[\text{N mm}^{-1}\right]$	$T_n^c\left[\text{MPa}\right]$	$\Delta_n^0\left[\text{mm}\right]$	$\Delta_n^c\left[\text{mm}\right]$

1.02	60	0.00334	0.0334

Tab. 3.3: interface properties of the layered structures reported in Fig. 3.6.

The numerical model is discretized along the thickness by using one mathematical element for each layer, whereas, for the interfaces, five ALE elements are introduced between the sublayers, in which the crack initiation could be potentially activated. The analysis is developed under a displacement control mode, to ensure a stable crack propagation. Comparisons with existing formulations based on cohesive zone model are proposed, in which the interface regions are discretized by means of classical interface elements. In order to verify stability accuracy of the solution, several mesh discretization lengths (Δ_M), ranging from a uniform to a refined one with mesh enrichment localized along the process zone only, are considered. In particular, for the proposed model, the following numerical cases are analysed:

- uniform discretization of the mesh with a characteristic element mesh equal to $\Delta_M / L = 1/200$ with 4623 DOFs (M1) or equal to $\Delta_M / L = 3/200$ with 1504 DOFs (M2);
- non uniform discretization with mesh enrichment in the debonding region , i.e. $\Delta_M / L = 1/200$, and a uniform coarse discretization in the remaining region, i.e. $\Delta_M / L = 1/40$ with 2859 DOFs (M3) .

In addition, as a comparison, pure CZMs are developed, in which the following uniform mesh discretizations are implemented:

- uniform discretization of the mesh with element mesh length equal $\Delta_M / L = 0.2/200$ with 18018 DOFs(PC1);
- uniform discretization of the mesh with a characteristic element mesh equal $\Delta_M / L = 1/200$ with 3618 DOFs(PC2);

At first, the analysis is carried out with the purpose to identify the position, where crack onset criterion is possible. This is achieved with a coarse uniform mesh with size equal to $\Delta_M / L = 1/200$. Once the position of the crack is known, an internal discontinuity with size equal to $2\bar{\Delta} / L = 0.001/200$ is introduced, thus modifying the geometry of the numerical modeling. It is worth nothing that the size of such cracked length is chosen to be very small. However, sensitivity studies, presented subsequently, are developed to verify the influence of such parameter on the crack onset prediction.

The results, reported in Fig. 3.7, are expressed in the terms of resistance curve, in which the predictions provided by the proposed model (M1-M2-M3) assumed with different mesh discretizations and classical CZM (PC1-PC2) are investigated. The analyses show that as far as the mesh size increases the proposed solution is affected by a loss of accuracy in the prediction of the resistance values, involving some oscillations with respect to the reference solution. However, also in the case of a very low element number in the mesh discretization, the prediction obtained by the proposed model is not affected by a divergent behaviour but it is always very close to enriched one, namely PC1. The improvements provided by the proposed model should be analysed in terms of variables involved in the numerical models, since it requires a very low number of elements to reproduce the actual solution. This is also confirmed by the solution arising from the M3 discretization, which presents a smart use of the mesh elements in the numerical model. In particular, the proposed approach requires a mesh enrichment in the process zone only and a very coarse mesh in the remaining regions, in which perfect adhesion should be reproduced by means a penalty approach. Pure cohesive zone models require typically a uniform discretization along the entire interface, leading to large computational costs and mesh dependent effects in the numerical solution. This is confirmed by the analyses reported in Fig. 3.8, in which the evolution between crack tip and applied displacement is reported. The results show how the proposed model is quite stable in any mesh configuration, since the solution coincides with that of the PC1 modelling. However, in the case of a low discretization, cohesive zone model is affected by errors and a divergent trend. In order to quantify numerically the discrepancies in the prediction of the actual solution and the performance analysis of the computational procedure, a comparison in terms of number of total DOFs involved in the numerical model and CPU time between proposed model and cohesive approach is reported in Fig. 3.9. The results show how the proposed model despite existing formulation based on pure cohesive approaches, strongly reduces the computational costs within percentage values equal to 76% and 85% for the CTP time and DOFs, respectively.

Finally, in order to verify the influence of initial crack length on the actual solution, a parametric study is developed in terms of load-displacement curve. From the theoretical point of view, such value should be small enough to reproduce the multiscale variation from the macro to the micro scale modelling. However, from the results reported in Fig.

3.10, it transpires that values lower than $2\bar{\Delta}/L = 0.001/200$ do not influence the actual solution.

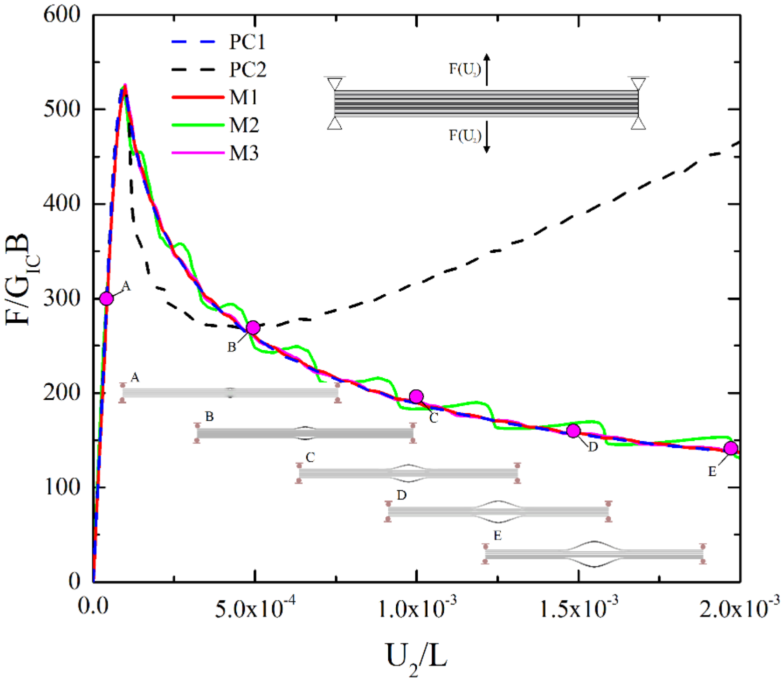

Fig. 3.7: Laminate structure: influence of the mesh discretization on the loading curve ($F/G_{IC}B$-U_2/L) and comparisons between proposed model (M1-M2-M3) with classical Cohesive approaches (PC1-PC2).

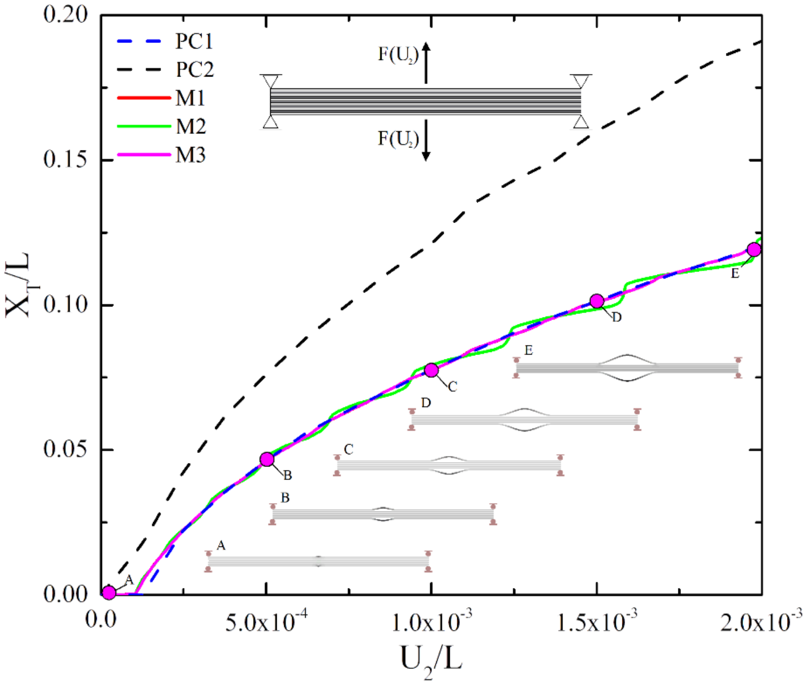

Fig. 3.8: Laminate structure: influence of the mesh discretization on the crack tip position (X_T/L-U_2/L) and comparisons between proposed model (M1-M2-M3) with classical Cohesive approaches (PC1-PC2).

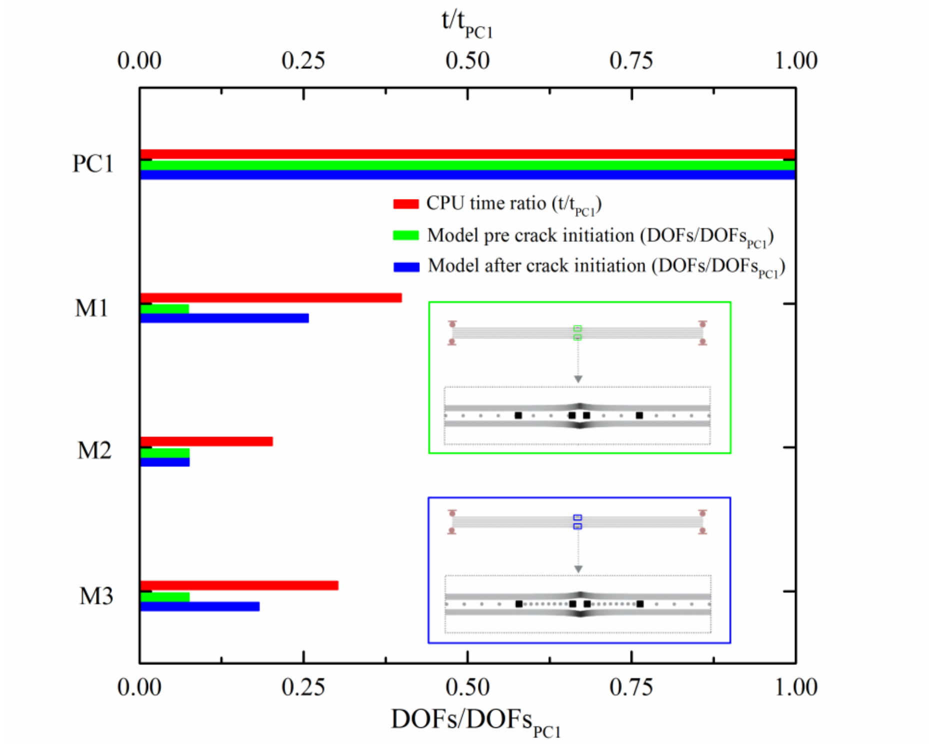

Fig. 3.9: Number of the total DOFs and CPU time ratio for the numerical simulation performed by using proposed modelling (M1-M2-M3) and classical cohesive approach (PC1).

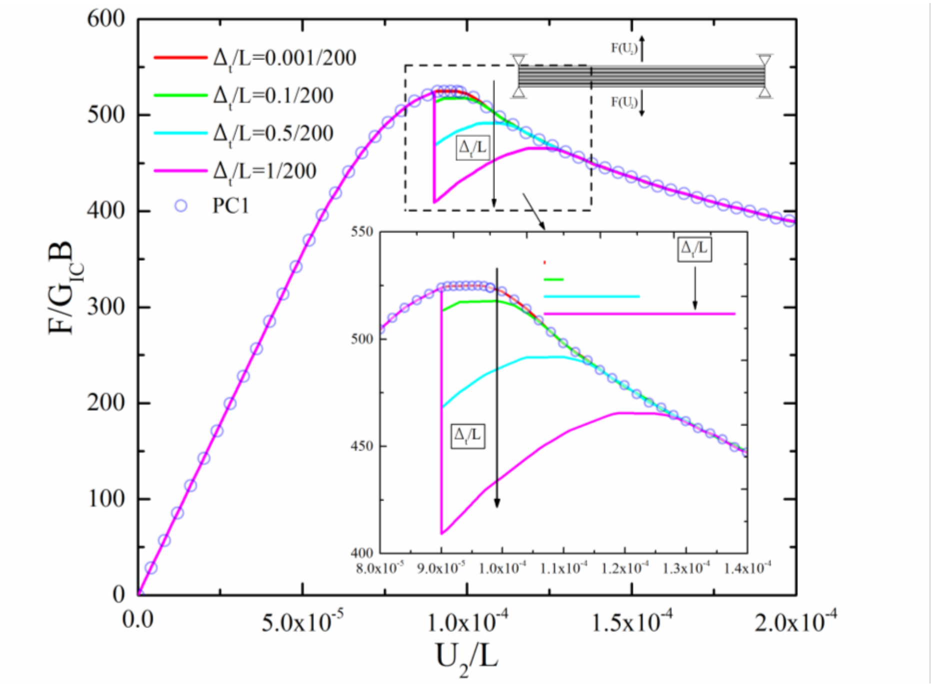

Fig. 3.10: Laminate structure: influence of the material discontinuity length on the loading curve (F/G_{IC} B-U_2/L).

The proposed model is validated by means of additional comparisons with existing formulations, which accurately predict initiation and evolution of interfacial debonding phenomena. The analysis reported in [100] refers to a four point bending test scheme, in which an edge debonding crack is produced in a two layered scheme. The geometrical and mechanical characteristics are reported in Fig. 3.11 and Tab. 3.4 and Tab. 3.5, respectively.

The approaches available from the literature refer to classical CZM and Finite Fracture Mechanics (FFM) formulations. The former assumes between each layer a traction separation bilinear law with respect to normal and tangential interfacial stresses to reproduce the debonding mechanisms. Contrarily, the latter is based on a coupled criterion based on finite crack extension which combines stress and energy conditions.

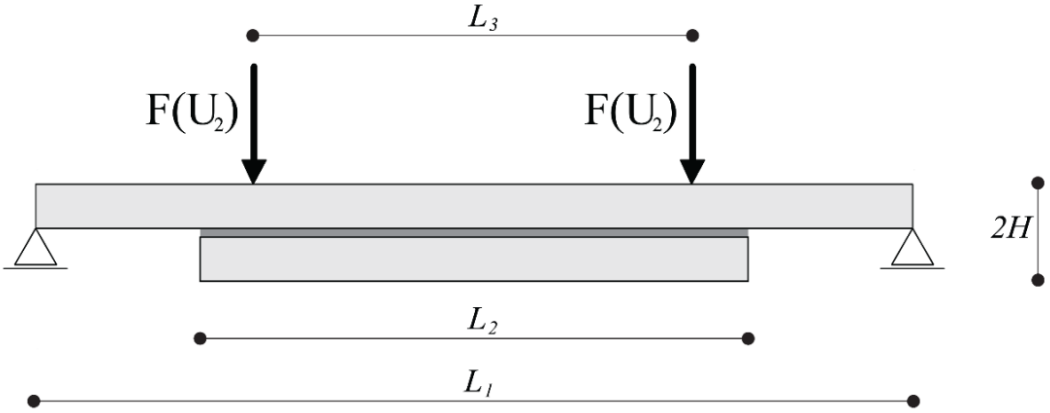

Fig. 3.11: Layered configuration submitted to a four-point bending test.

$E_1\,[\mathrm{GPa}]$	ν	$L_1\,[\mathrm{mm}]$	$L_1\,[\mathrm{mm}]$	$L_3\,[\mathrm{mm}]$	$H\,[\mathrm{mm}]$
400	0.26	40	25	20	2

Tab. 3.4: Mechanical and geometrical properties of the layered structures reported in Fig. 3.11

Interface	$G_C\,[\mathrm{N\,mm^{-1}}]$	$T^c\,[\mathrm{MPa}]$	$\Delta^0\,[\mathrm{mm}]$	$\Delta^c\,[\mathrm{mm}]$	$k\,[\mathrm{MPa\,mm^{-1}}]$
$G_C = 0.050$	0.05	100	0.0001	0.001	1E6

Interface	$G_C\,[\mathrm{N\,mm^{-1}}]$	$T^c\,[\mathrm{MPa}]$	$\Delta^0\,[\mathrm{mm}]$	$\Delta^c\,[\mathrm{mm}]$	$k\,[\mathrm{MPa\,mm^{-1}}]$
$G_C = 0.50$	0.050	100	0.0001	0.01	1E6

Tab. 3.5: Interface properties of the layered structures reported in Fig. 3.11.

The comparisons, reported in Fig. 3.12 and Fig. 3.13, are presented in terms of load-displacement curve and crack tip and applied displacement for two different values of the critical ERR (Tab. 3.5). The proposed model is described by using several mesh sizes to check the stability of the solution. To this end, the debonding length presents in all cases a mesh discretization equal to $\Delta_M / L_2 = 0.05/25$, whereas in the remaining regions the mesh is changed with $\Delta_M / L_2 = 0.1/25$ (M1), $\Delta_M / L_2 = 0.5/25$ (M2), $\Delta_M / L_2 = 1/25$ (M3). The comparisons with the results obtained from the literature are quite in agreement also assuming a very large mesh description.

However, the extrapolation for large values of crack extension, not reported in the data taken from the literature, show that also in these ranges stability and convergence of the solution are achieved. It is worth noting that the presence of a coarse mesh in the configurations utilized to identify the crack initiation and growth, do not affect the accuracy of the solution, which is achieved by means of the localized mesh enrichment in the process zone only, reducing the total computation cost of the numerical model.

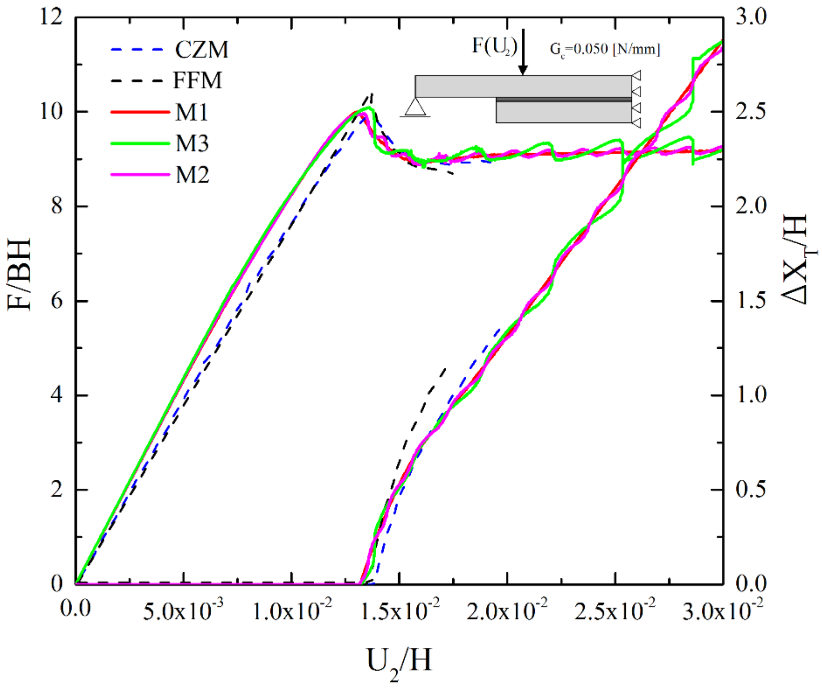

Fig. 3.12: Four-point bending test scheme: (G_c=0.050) influence of the mesh discretization on the loading curve   and crack tip displacement , comparisons with CZM [100] and FFM [100].

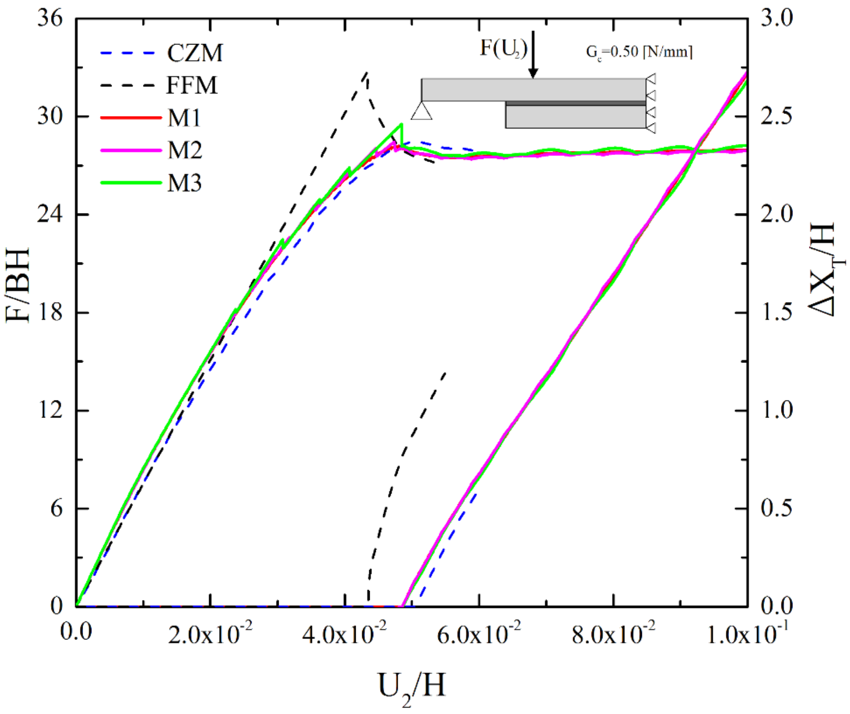

Fig. 3.13: Four-point bending test scheme: (G_c=0.50) influence of the mesh discretization on the loading curve and crack tip displacement, comparisons with CZM [100] and FFM [100].

3.3.2 Multi-layered structures, crack onset, propagation and coalescence: Dynamic framework

The analysis is extended to a dynamic debonding example, in which initiation, evolution and coalescence of pre-existing material discontinuities are discussed. The purpose of the present study is to verify the capabilities of the proposed model to reproduce multiple debonding mechanisms. As shown in Fig. 3.14, the structural scheme refers to a layered structure with fixed ends, loaded by symmetric vertical opening forces, in which a pre-existing internal discontinuity along the same delamination path is assumed.

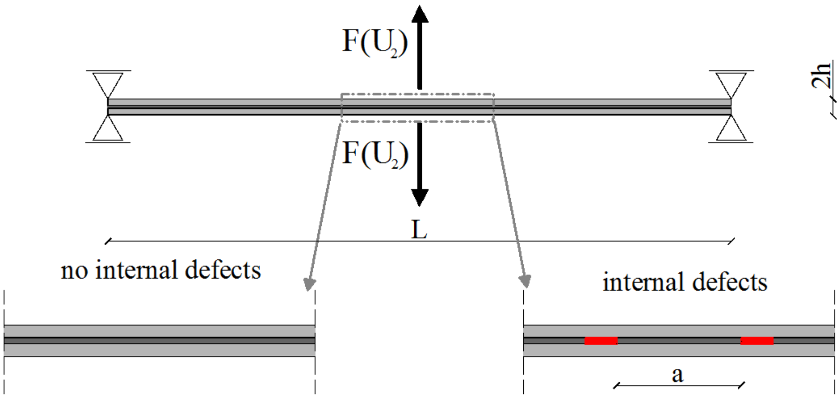

Fig. 3.14: Layered configuration formed by two structural layers.

As a consequence, two different configurations are investigated in which the interface is affected by Perfect (P) or Imperfect (IP) interfaces. The initial geometrical discontinuity in the IP configuration along the interface is assumed to be equal to $d / L = 5/200$. The data concerning material characteristics, fracture functions, CZMs are reported in Tab.1, whereas the loading history is assumed to be governed by an applied velocity with ramp curve and a constant speed (v_0) at the time t_0, which is assumed to be proportional to the first period of vibration of the structure ($t_0 = 0.5T_1 = 5.95\ 10^{-4}\ [\mathrm{s}]$). The results, presented in Fig. 3.15 and Fig. 3.16, are expressed in terms of normalized resistance curves, in which both static and dynamic analyses are developed for the cases of P and IP cases, respectively. In both cases, debonding phenomena start from the midspan cross-section, in which opening concentrated forces are applied, producing high values of interfacial normal stresses. The mesh size at this stage is assumed to be equal to $\Delta_M / L = 1/200$ of the total length of the laminate. Once the onset criterion is satisfied, a physical internal geometric discontinuity with length equal to $2\bar{\Delta} / L = 0.001/200$ and a fine mesh discretization along the debonding lengths are introduced ($\Delta_M / L = 0.2/200$). Such task is performed by means of a stop condition, remeshing and restart procedures from the last converged substep. Subsequently, the numerical procedure predicts crack evolution towards the external region, which produces a macroscopic loss of stiffness of the structure as shown in the loading curve (AB, Fig. 3.15and Fig. 3.16). In presence of a pre-existing debonding length, the resistance curve is affected by a discontinuity in the evolution curve. Such behaviour is quite clear, when the crack tip reaches the unbounded region (BC, Fig. 3.16). The analyses, developed in dynamic, reported in Fig. 3.15 and Fig. 3.16, denote a different evolution in the case of P and IP configurations with notable influence of the loading rates, especially in presence of a pre-existing debonding length. As a matter of fact, in the case of P interface, static and dynamic solutions are quite similar, except in the evolving phase in which the resistance curve present larger values for increasing loading rate (Fig. 3.15). Contrarily, for the IP configuration, despite to the static case or to the dynamic case, an oscillating behaviour is observed, which increases with the loading rate (Fig. 3.16). In particular, once the crack tip overpasses the undebonded region, the resistance curve is affected by the inertial effects produced by the material discontinuity and thus notable discrepancies with respect to the static solution are observed.

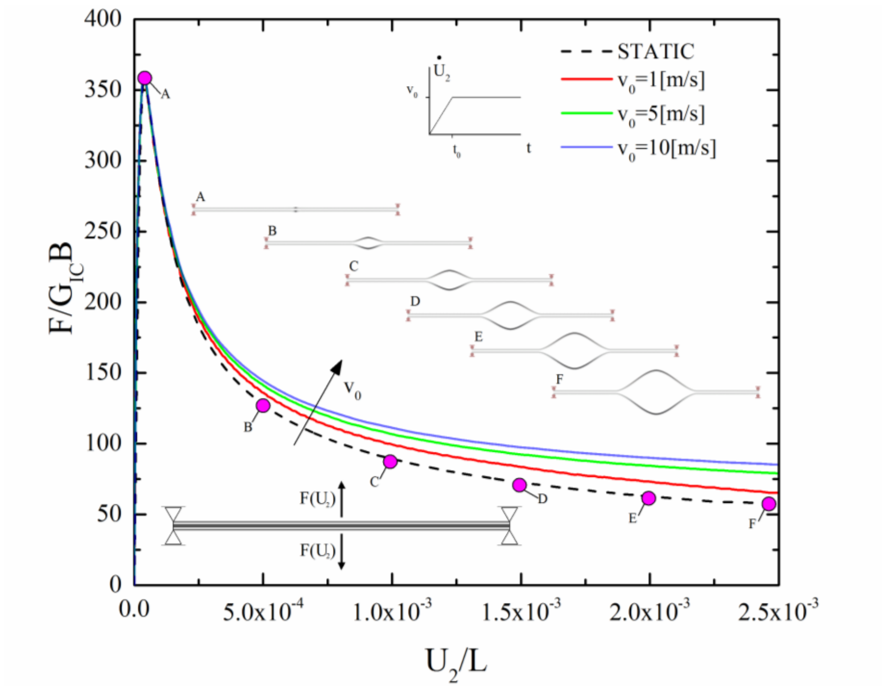

Fig. 3.15: Perfect interface debonding (P): comparison in terms of loading curve ($F/G_{IC}B$-U_2/L) between static and dynamic cases for different loading rate.

In order to investigate such phenomena, in Fig. 3.17 the time histories of the crack tip speeds are reported as a function of the loading rate. The analysis is presented only for the configuration with a pre-existing defect (Fig. 3.14 with internal defects). At crack initiation, the measured speeds tend to increase very rapidly reaching a constant value, whose entity strictly depends from the applied loading rate. However, when coalescence is produced, the debonding mechanisms jump from one extremity to the other one of the debonded region. During this transition, the crack growth is quite dependent from the applied loading rate. As matter of fact, at low loading rates, the crack tip speeds are comparable to the ones observed in the crack initiation phase, whereas large values are observed for increasing loading rate. Such behaviour can be explained by the evolution of the kinetic to strain energy ratio reported in Fig. 3.17, which presents peak value when the crack reach the pre-existing debonding length. However, when the crack tip reaches the undebonding region, the kinetic energy is at first reduced and subsequently due to crack tip motion tends to increase.

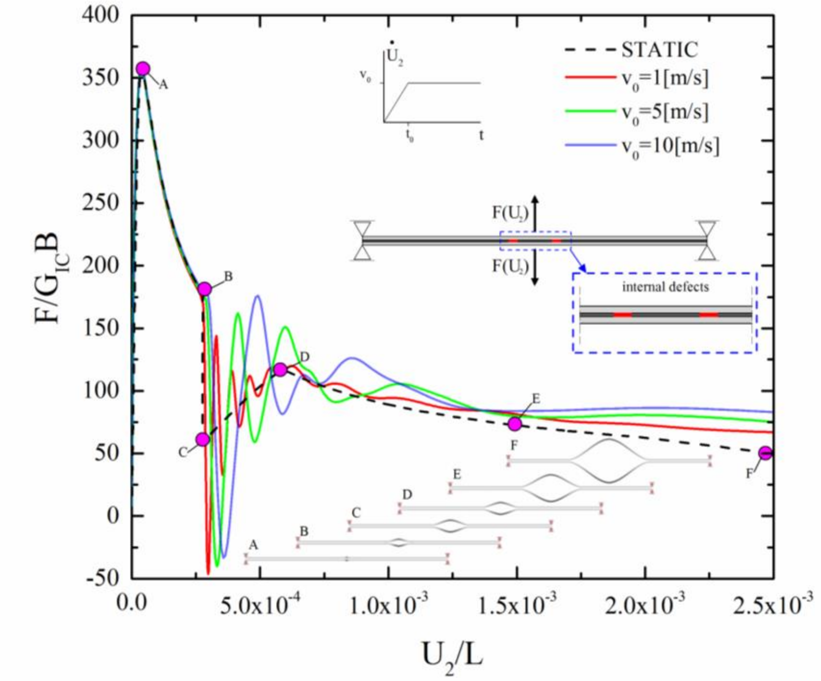

Fig. 3.16: Imperfect interface debonding (IP): comparison in terms of loading curve ($F/G_{IC}B$-U_2/L) between static and dynamic cases for different loading rate.

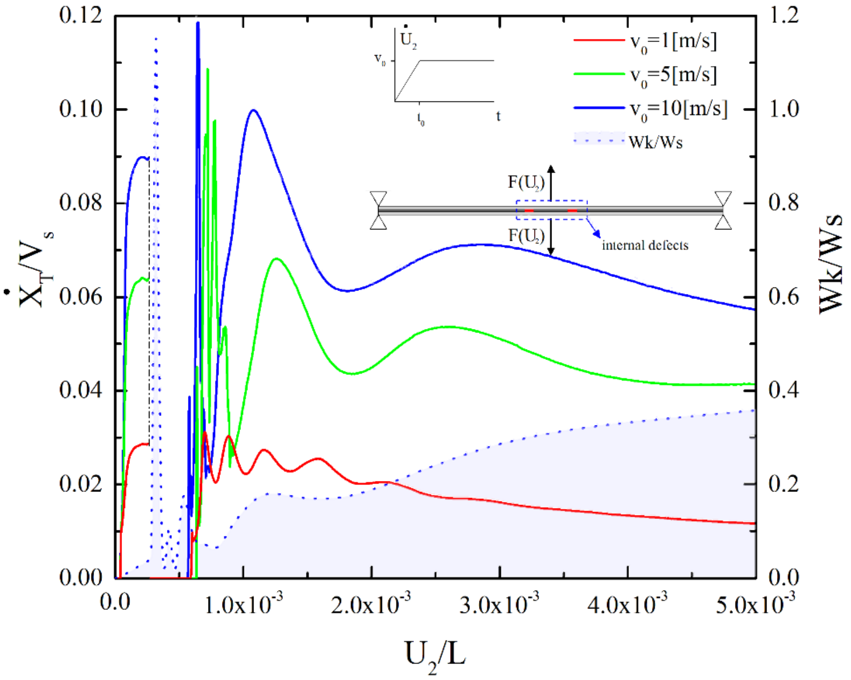

Fig. 3.17: Imperfect interface debonding (IP): evolution of the crack tip speed normalized to the shear wave speed of the material and kinetic to strain energy ratio as function of the normalized applied displacement.

In order to validate the procedure to describe the crack front speed, the results obtained using the proposed algorithm has been compared dynamic with numerical results arising from literature [21]. The analyses are developed with reference to loading schemes based on the 4-point bending, in which the dynamic effects are considered from both onset and evolution mechanisms. The loading, the boundary conditions and the geometry are illustrated in in Fig. 3.18, whereas the mechanical properties assumed for the steel, the adhesive, the FRP strip and those concerning the potential cohesive zone model are reported in Tab. 3.6, Tab. 3.7, Tab. 3.8 and Tab. 3.9, respectively.

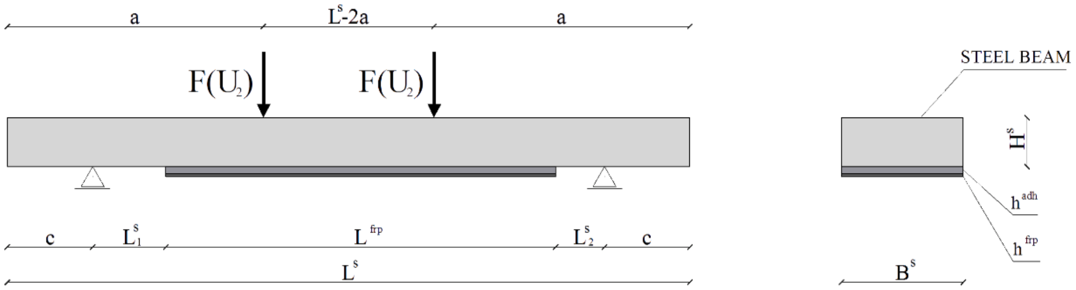

Fig. 3.18: Steel beam configuration and loading scheme.

$E_1^s\,[\mathrm{GPa}]$	$G_{12}^{adh}\,[\mathrm{GPa}]$	$\rho^s\,[\mathrm{kg\ m^{-1}}]$	$L^s\,[\mathrm{mm}]$	$L_1^s\,[\mathrm{mm}]$
190	79.3	7500	280	30
$L_2^s\,[\mathrm{mm}]$	$B\,[\mathrm{mm}]$	$a\,[\mathrm{mm}]$	$H^s\,[\mathrm{mm}]$	$c\,[\mathrm{mm}]$
20	50	105	20	35

Tab. 3.6: Geometrical and mechanical properties of the steel beam [21].

$E_1^{adh}\,[\mathrm{GPa}]$	$G_{12}^{adh}\,[\mathrm{GPa}]$	$\rho^{adh}\,[\mathrm{kg\ m^{-1}}]$	$L^{adh}\,[\mathrm{mm}]$	$B^{adh}\,[\mathrm{mm}]$	$h^{adh}\,[\mathrm{mm}]$
5	0.350	2000	160	50	3

Tab. 3.7: Geometrical and mechanical properties of the adhesive layer.

$E_1^{frp}\,[\mathrm{GPa}]$	$G_{12}^{frp}\,[\mathrm{GPa}]$	$\rho^{frp}\,[\mathrm{kg\ m^{-1}}]$	$L^{frp}\,[\mathrm{mm}]$	$B^{frp}\,[\mathrm{mm}]$	$h^{frp}\,[\mathrm{mm}]$
165	60	2000	160	50	1.2

Tab. 3.8: Geometrical and mechanical properties of the FRP strip [21].

$G_c\left[\mathrm{N\ mm}^{-1}\right]$	$\Delta_n\left[\mathrm{mm}\right]$
0.350	0.01

Tab. 3.9: Interfaces parameters of the Adhesive-Steel interface and Adhesive-Frp interface [21].

In the present case study, comparisons with results arising from the literature [18, 19] are developed. The main model refers to a steel beam, strengthened with FRP strip elements. The model is based on two cohesive interface elements, which are introduced between adhesive-steel and adhesive-FRP strip elements. As a consequence, debonding phenomena may affect the layered structures at two different interface levels. The interface law utilized to reproduce the debonding process is consistent with the model proposed by [20]. In order to obtain a stable crack propagation, the structure is loaded under a displacement control mode. In particular, to avoid the dynamic effects due to the external load, a very small loading rate equal to 1 mm/s is assumed. However, time steps are modified during the computation from 1E-3 to 1E-7 sec, before and after the activation of the debonding phenomena, to capture accurately the effects produced by crack growth. In Fig. 3.19 and Fig. 3.20, results in terms of resistance curve and crack speed time histories for different thickness of the FRP strips are reported. At first, the structure presents a linear, stable and quasi-static behaviour. Subsequently, when the crack growth criterion is satisfied in the adhesive-steel interface, the ALE interface is activated to reproduce the debonding phenomena. During the activation of debonding mechanisms, the resistance curve presents an oscillatory and variable behaviour which varies very fast. In the same figure, a detail of the resistance curve at the point in which the crack onset is activated is also reported. This trend is quite in agreement with similar experimental results available from the literature [21], which show the importance of the dynamic effects during the crack growth.

It is worth nothing that the resistance curves are quite dependent from the thickness properties of FRP strip. In particular, an increase of the FRP strip thickness reveals a similar impact on the critical displacement and load at the onset of the dynamic process (Fig. 3.19 and Fig. 3.20). Increasing the thickness of the FRP strip, the edge debonding strength of the beam is reduced (Fig. 3.19). This effect is attributed to the increased amount of energy that is accumulated in the stiffened FRP layer and the corresponding increment of the edge stresses. Once the dynamic process is activated, the influence of the FRP strip thickness produces an increase of the crack speeds, which leads to more severe failure mechanisms. Contrarily to the properties of the FRP layer, which are well documented in the literature, the influence of the adhesive on the debonding phenomena is not completely investigated. To this end, in Fig. 3.21 and Fig. 3.22, results in terms of resistance curves and crack speed time histories for different values of the thicknesses of the adhesive layer are presented

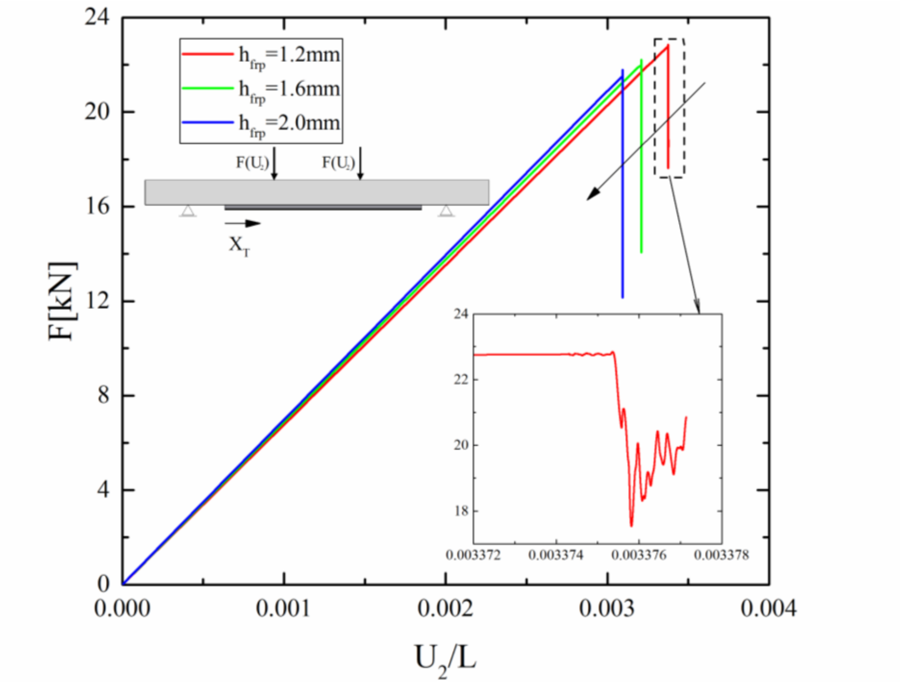

Fig. 3.19: Comparisons in terms of loading curve for different thickness of the FRP strip.

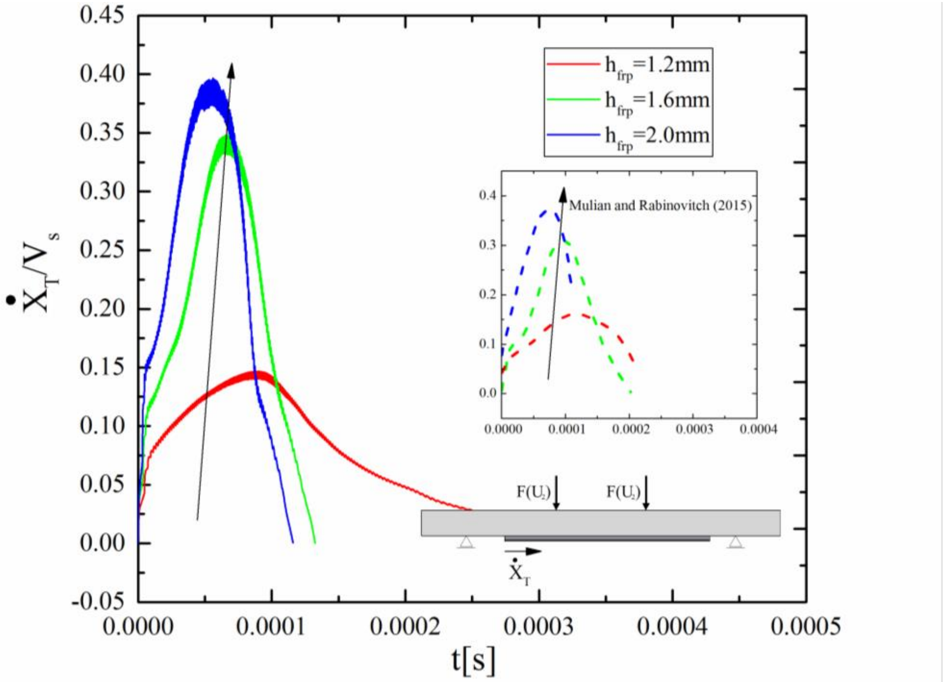

Fig. 3.20: Comparisons in terms of time histories of the debonding front speed for different thickness of the FRP strip.

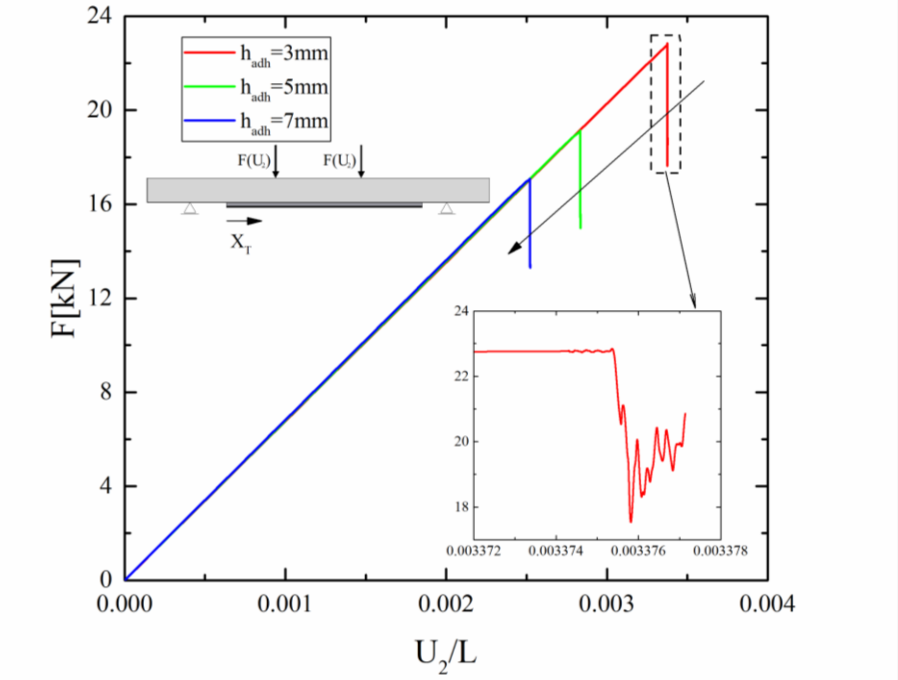

Fig. 3.21: Comparisons in terms of loading curve for different thicknesses of the adhesive layer.

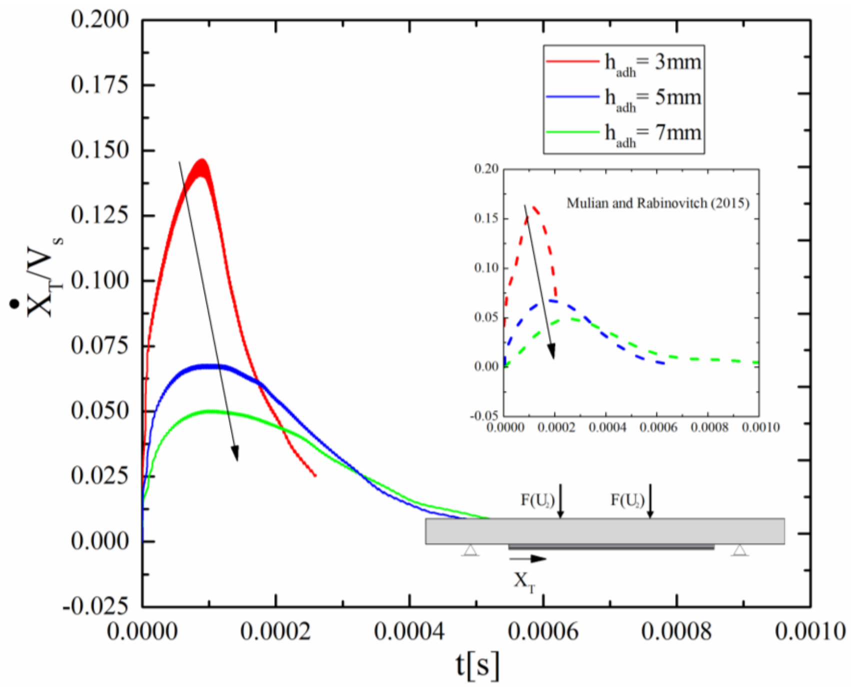

Fig. 3.22: Comparisons in terms of time histories of the debonding front speed for different thickness of the adhesive layer.

In particular, an increment of the adhesive thickness reveals a different impact with respect the previous analyses in terms of FRP strip characteristics. As a matter of fact, the results show how by using thin adhesive layers, an increase of the dynamic debonding strength is observed (Fig. 3.21) leading the structure to be affected to a more severe dynamic state

(Fig. 3.22), since the observed crack tip speeds tend to be increased. From the results reported in Fig. 3.19, Fig. 3.20, Fig. 3.21 and Fig. 3.22, a good agreement with the data available from the literature is also observed [18].

In Fig. 3.23 the interfacial tractions across the two cohesive interfaces, i.e. Adhesive-Steel (*as*) and Adhesive-Frp (*af*), for different time steps of the delamination process, are reported. At first, in Fig. 3.23a, the distribution of the interfacial traction forces is presented for the status A of the zoom reported in Fig. 3.19 and Fig. 3.21, which basically corresponds to the peak load of the quasi-static branch. It represents the stage just before the initiation of the debonding process, in which all layers are still bonded together.

However, at the point A, the non-linear response of the cohesive adhesive-steel interface shows how the interfacial normal and tangential tractions tend to zero. This reflects the initiation of the dynamic debonding failure. In Fig. 3.23b-d, the representation of the evolution of the dynamic debonding, in terms of interfacial traction, has been reported for different lengths of the debondend region. In particular, the results are referred to the points B, C, D of the zoom reported in Fig. 3.19 and Fig. 3.21, in which the debonding lengths of adhesive-steel region are equal to 25, 50 and 75mm, respectively. It is worth noting that the *af* does not debond but it is able to provide interfacial tractions between the mathematical layers. Finally, the consistency of the proposed model has been investigated also in terms of computational efforts. In particular, in order to satisfy the solution accuracy, the numerical model arising from [18] is based on a discretization with 560 and 320 elements for the steel and FRP strip layer, respectively. Moreover, the discretization of the 2D adhesive layer presents a uniform length equal to 0.5. As a consequence, the total number of DOFs is approximately 7100. Contrarily, by using the proposed approach, in which also the adhesive layer is simulated by means the shear deformable beam elements, the number of variables is strongly reduced. In particular, the proposed model has been discretized by means a uniform mesh length equal to 1 mm for the laminate and 1 mm for the interface involving 3018 DOFs. Therefore, a computational saving approximately equal to 60% is achieved.

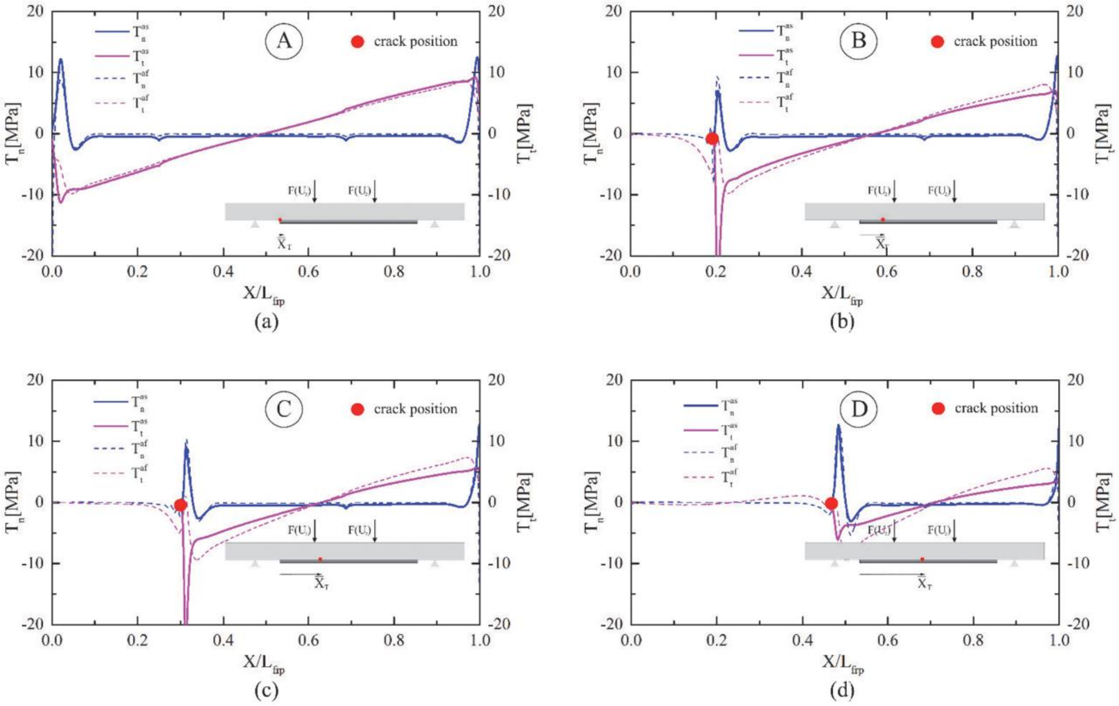

Fig. 3.23: Comparisons in terms of interfacial tractions across the two cohesive interfaces for different positions of debonding front.

3.3.3 Multi-layered structures with inter-laminar reinforced with z-pins

Once the proposed methodology is validated, a layer configuration involving multiple delaminations, crack onset and z-pin interlaminar reinforcement is considered. As shown in Fig. 3.24, the structural scheme refers to a layered structure with fixed ends, loaded by symmetric vertical opening forces, in which a pre-existing internal discontinuity along the same delamination path is assumed. Mechanical properties of the laminate and the interfaces are reported in Tab. 3.2 and Tab. 3.3, whereas those concerning the cohesive zone model and z-pin characteristics are defined in Tab. 2.6. The main purpose of the analysis is to investigate how crack initiation and evolution interact with the z-pin debonding phenomena. To this end, the following configurations are investigated:

UP with two pre-existing debonding regions;

- 10 columns of z-pins uniformly distributed along both initiation and pre-existing lengths (C1);
- 4 columns of z-pins for each side overlapped on the pre-existing delamination lengths (C2);

- 4 columns of z-pins for each side overlapped behind the pre-existing delamination lengths (C3).

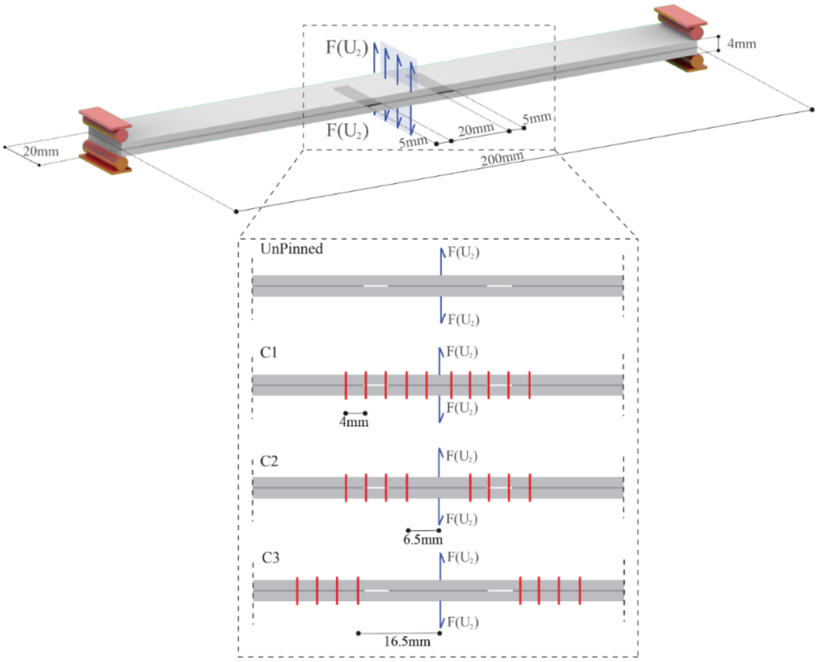

Fig. 3.24: Layered configuration with two structural layers and two material discontinuities: UP configuration, C1 configuration, C2 - C3 configurations.

In each configuration, the mesh discretization of the numerical model is based on a uniform distribution with an element length of $\Delta_M / L = 0.5/200$ in the laminate, whereas for the debonding region a refinement of the mesh, i.e $\Delta_M / L = 0.1/200$, is utilized. The analyses, reported in Fig. 3.25, are presented in terms of load-displacement curves. The results in the first loading path, i.e. 0A, are basically coincident, since the main mechanism is the one associated to the crack initiation. Subsequently, the solution appears to be quite influence by the presence of z-pins. As a matter of fact, when the z-pins are distributed in the region, in which the crack initiation occurs, they modify the loading curve from the UP configuration without producing increments of the debonding load. The presence of the z-pins, at this stage, determines a local stress distribution, which is activated as far as the nominal crack tip reaches the z-pin position. This is confirmed by the path AB of C1-C2 configurations, which strongly differ from the UP scheme. However, as far as the z-pins are located far from the onset position the differences between UP and P solutions tend to be annihilated. All curves present a jump, when the nominal crack tip reaches the internal material discontinuity. However, the snap, observed during such transition, is quite influenced by the presence of the z-pins, which are able to reduce the loss of strength (BC).

At this stage, the nominal crack tip is jumped through the debonding region and, in order to produce crack tip advance, a larger applied displacement is required. This is confirmed by the presence of a linear branch in the loading curve, i.e. path CD. At point D, the motion of the nominal crack tip is activated and a decreasing behaviour is observed in the loading curve, whose characteristics depend from the number of z-pins not completely broken. The coincidence of C1-C2 in the loading curve, at large applied displacements, proves such remark. Finally, when the z-pins are located far from the crack onset position, the effects of the interlaminar reinforcement is observed only when the crack tip reaches the z-pin region and thus the loading curves are coincident before it happens.

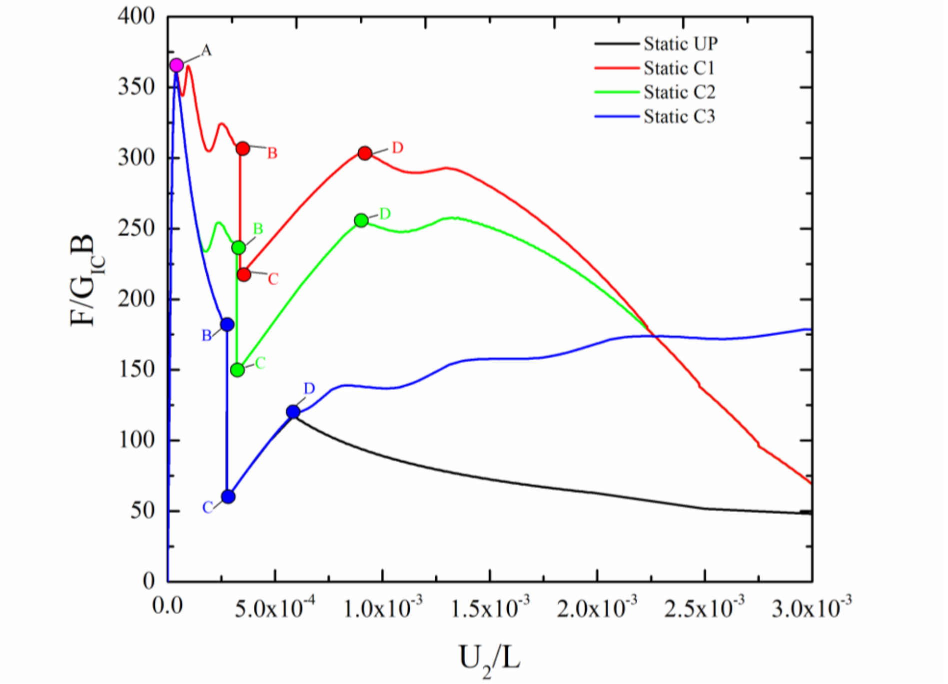

Fig. 3.25: Comparisons of the different pinned configurations in terms of loading curve ($F/G_{IC}B$-U_2/L) with the UP solution [101].

Previous results are extended in dynamics, introducing a time dependent law for the applied displacement. In particular, an applied velocity with ramp curve and constant speed (v_0) at the time t_0, assumed to be proportional to the first period of vibration of the structure ($t_0 = 0.5 T_1 = 5.95\ 10^{-4}\ [\mathrm{s}]$), are supposed. The analyses, developed in dynamics, reported in Fig. 3.26, denote a different evolution in the case of P and UP configurations with notable influence of the loading rates, especially in presence of a pre-existing debonding length. As a matter of fact, in the case of UP interface, static and dynamic solutions are quite similar, except in the evolving phase, in which the debonding length reaches the pre-existing material discontinuity (Fig. 3.26). The presence of the z-pins modifies loading curves observed in the static case, since the curves present larger strength values and an oscillatory behaviour is produced by the interaction between debonding phenomena and z-pin failure. Finally, in Fig. 3.27 the time histories of the crack tip speeds are reported as a function of the loading rate for all configurations. The results show that at crack initiation, the measured speeds tend to increase very rapidly reaching a constant value, whose entity strictly depends from the applied loading rate. However, when coalescence is produced, the debonding mechanisms jump from one extremity to the other one of the debonded region, leading to amplifications in the measured crack tip speed. However, in presence of z-pins, the crack tip evolution denotes an oscillatory evolution, in which the traction forces constrain the debonding mechanisms enforcing crack arrest phenomena.

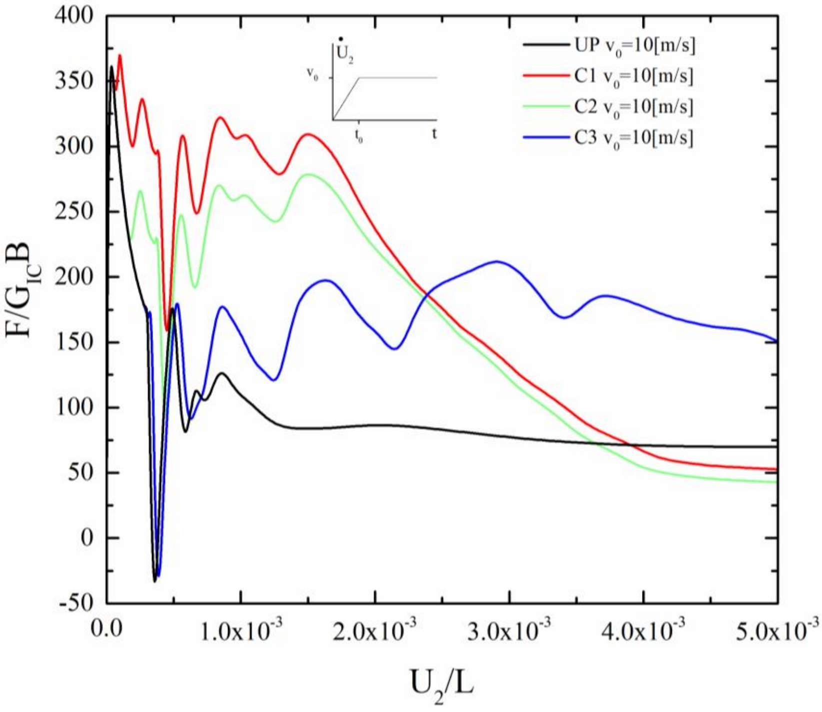

Fig. 3.26: Influence of the inertial effects (v_0=10 [m/s]): comparisons of the different pinned configurations in terms of loading curve ($F/G_{IC}\,B$-U_2/L) with the UP solution [101].

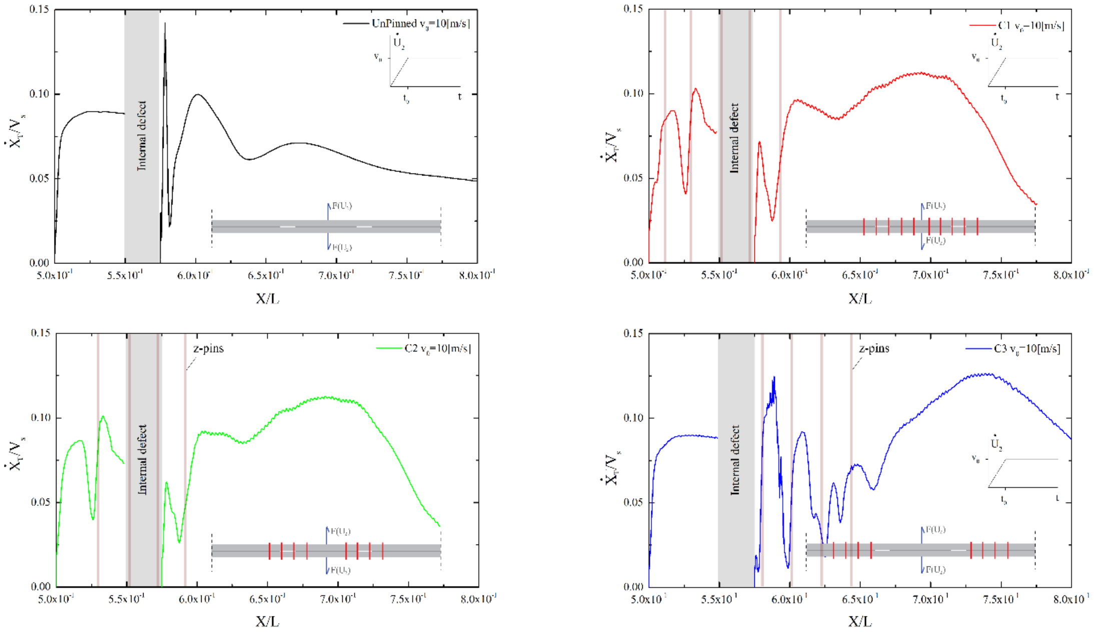

Fig. 3.27: Comparisons in terms of nominal crack tip speed: UP configuration [101] (a), C1 configuration (b), C2 configuration (c) and C3 configuration (d).

Chapter 4 **Sandwich structures**

In this Chapter sandwich structure failure modes are investigated. From physical and mathematical viewpoints, two main issues are demanding a detailed understanding of the mechanical behaviour of sandwich panels: the propagation of internal macro-cracks in the core and the delamination at skin/core interfaces. In section 4.1, in order to described skin/core decohesion, previous numerical strategy, already used in the framework of composite laminates, was generalized simply by modifying the relative displacement between skin (shear deformable beam) and core (2D plane stress formulation). Then, To concern the evolution of defects inside the core a new numerical methodology based on moving mesh methodology will be proposed in in Section 4.2. Finally, in Section 4.3 will be described the experimental test performed to detect the fracture parameters of a typical semi-rigid PVC foam used like core in the sandwich panels (Divinycell H100, H130, H200).

Part of analyses and results presented and discussed in this chapter were already published by the following papers:

- *Funari, M.F., Greco, F., Lonetti, P., Sandwich panels under interfacial debonding mechanisms, Composite Structures, 2018, 203, 310-320.*
- *Funari, M.F., Greco, F., Lonetti, P., A coupled ALE-Cohesive formulation for interfacial debonding propagation in sandwich structures, Structural Integrity Procedia, 2018, 9, 92-100.*
- *Funari, M.F., Greco, F., Lonetti, P., Spadea, S., A numerical model based on ALE formulation to predict crack propagation in sandwich structures, Fracture and Structural Integrity, 2018, Accepted for publication.*
- *Funari, M.F., Lonetti, P., Spadea, S., A crack growth strategy based on moving mesh method and fracture mechanics, Theoretical and Applied Fracture Mechanics, 2018, Submitted.*

4.1 Generalization of the ALE interface model to describe skin core debonding

The numerical model developed in Chapter 2 and Chapter 3 is here generalized with the propose to describe delamination phenomena along the skin/core interfaces in the framework of a two-dimensional idealization of a sandwich structure. The numerical model consists of an internal core, modelled by means of a plane stress formulation, and two external skins, following a Timoshenko beam kinematic. The formulation is able to predict crack growth of material discontinuities, which may affect the skin/core interfaces and the core. This is achieved by the use of interface elements based on moving mesh technique, which ensures an accurate description of the fracture variables and the application of cohesive interlaminar stresses in the process zone. Without loss of generality and for the sake of clarity, a sandwich structure is analysed, in which fracture phenomena affect the upper skin/core interface only, producing two debonding lengths departing from right (R) or left (L) directions. A schematic representation of the model is reported in Fig. 4.1.

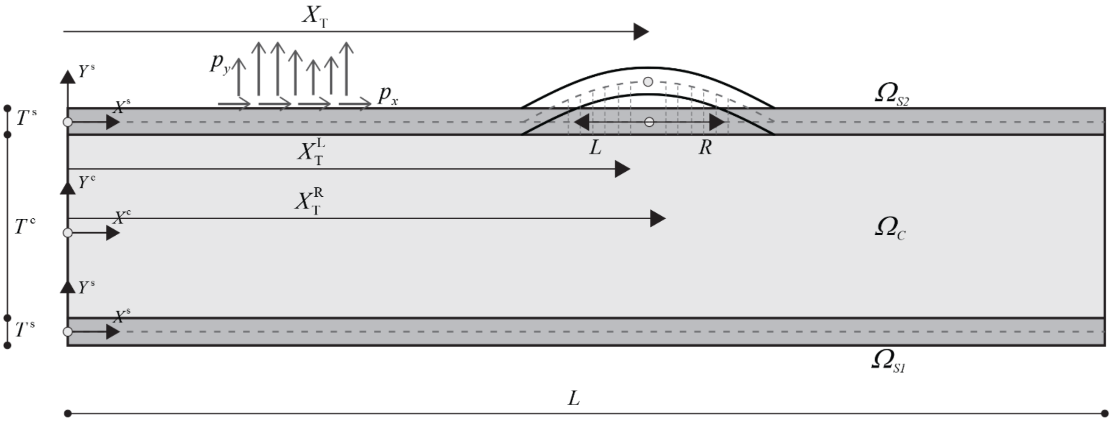

Fig. 4.1: Synoptic representation of the sandwich structure.

Moving interface elements between core and skins are introduced to simulate onset and evolution of debonding phenomena. In particular, the crack growth is expressed as a function of two coordinate systems, i.e. referential and moving, which parametrize the motion of the process zone from onset to crack advance (Fig. 4.1). Without going into too much details, the ALE interface formulation shows the same equations reported in the previous Chapters, which are not repeated here. As shows Fig. 4.2 and Fig. 4.3, ALE interface elements are incorporated in the sandwich structure at the lines in which debonding phenomena may occur.

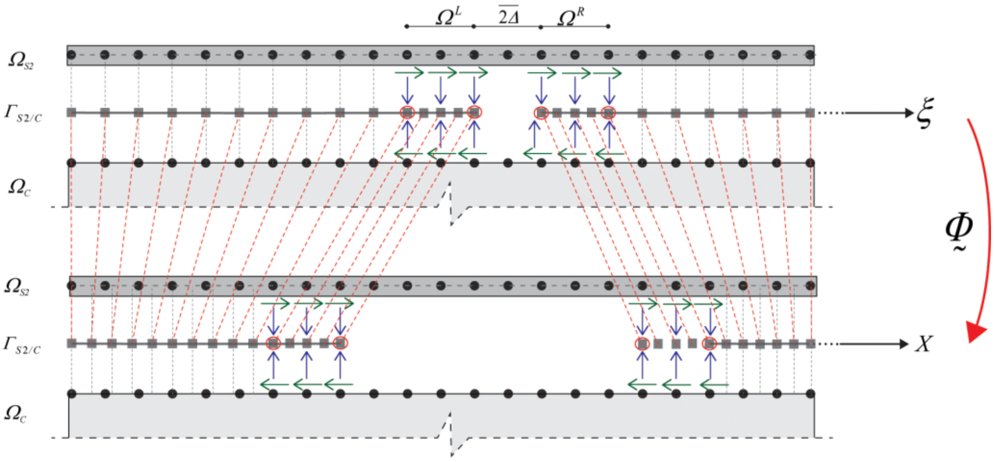

Fig. 4.2: Moving and referential coordinate systems in the ALE description.

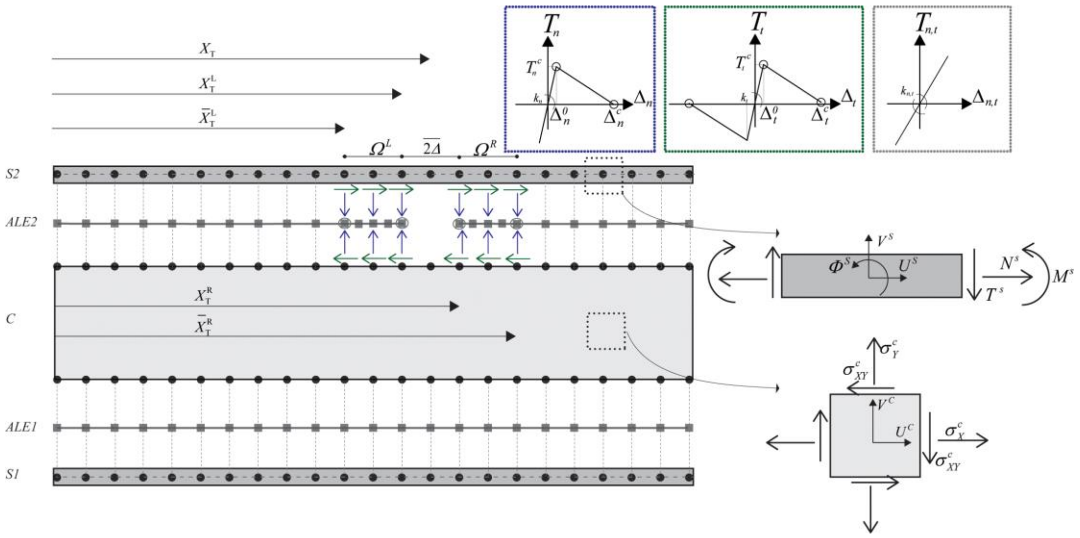

Fig. 4.3: Moving mesh interface elements, process zone and crack onset.

However, at first, the interfaces are assumed to be perfectly bonded to both upper and lower skin/core lines and thus moving coordinates match with the referential or material ones. In this framework, dynamic equations of motion can be expressed by introducing equilibrium conditions along the horizontal and vertical directions and flexural rotation (counterclockwise) as follows:

$$\begin{aligned}
&\mu\ddot{U}_2^k-\left[EAU_{2,X}^k\right]_{,X}+F_X\left(X\right)+p_x\left(X\right)=0,\\
&\mu\ddot{V}_2^k-\left[GA^*\left(V_{2,X}^k-\Phi_2^k\right)\right]_{,X}+F_Y\left(X\right)+p_y\left(X\right)=0,\quad \text{on}\quad (\Omega_{S_1},\Omega_{S_2})\\
&I_0\ddot{\Phi}_2^k-EI\Phi_{2.XX}^k-\left[GA^*\left(V_{2,X}^k-\Phi_2^k\right)\right]+m\left(X\right)=0,
\end{aligned} \tag{4.1}$$

$$div\left[\underset{\sim}{E}\nabla\underset{\sim}{U}\right]+\underset{\sim}{f}-\mu\ddot{\underset{\sim}{U}}=0,\qquad \text{on}\qquad (\Omega_C) \tag{4.2}$$

$$\begin{aligned} & E_{33}\left(U_{,Y}^{C}+V_{,X}^{C}\right)=F_{X}\left(X\right) \\ & \left(E_{12}U_{,X}^{C}+E_{22}V_{,Y}^{C}\right)=F_{Y}\left(X\right) \end{aligned} \qquad \text{on} \quad \left(\Gamma_{S_1/C}.\Gamma_{S_2/C}\right) \tag{4.3}$$

where, as shown in Fig. 4.3, the superscript *k* with *k*=S1,S2, here and in the following, refers to the lower (S1) or upper skins (S2), $\left(\Omega_{X},\Gamma_{X/Y}\right)$are the domain of the *X* or the boundary between *X* and *Y* (with *X,Y=S1, S2, C, ALE1, ALE2*), $\left(I_0,\mu\right)$ are the per unit length inertial rotation and mass of the skin, $\left(EI,GA^{*}\right)$are the flexural and shear stiffnesses, $\left(p_x,p_y,m\right)$ are the axial, vertical and flexural external loads applied to the skins, the notation $\left(\dot{X}\right)=\dfrac{d\left(X\right)}{dt}$indicates the time derivative of the function *X*, E_{ij} with *i,j=1,2,3* is the 2D plane stress elastic matrix, $\underset{\sim}{U}$ with $\underset{\sim}{U}^{T}=\left[U^{C} \quad V^{C}\right]$ is the vector containing the horizontal and vertical displacements of the core, $\underset{\sim}{f}$ is the per unit volume vector force. Moreover, the interlaminar stresses are defined on the basis of moving mesh coordinates and interlaminar relative displacements as follows:

$$\begin{aligned} & F_{X}\left(X_1^{k}\right)=T_{n}\left[\Delta_{n}^{k}\left(X_1^{k}\right)\right] \\ & F_{Y}\left(X_1^{k}\right)=T_{s}\left[\Delta_{s}^{k}\left(X_1^{k}\right)\right] \end{aligned}, \qquad \text{on} \quad \Gamma_{S_1/\mathrm{C}} \text{ and } \Gamma_{S_2/\mathrm{C}} \tag{4.4}$$

with

$$\begin{aligned} & \Delta_{n}^{S_1}\left(X\right)=V^{C}\left(X,-0.5T^{C}\right)-V^{S_1}\left(X\right), \\ & \Delta_{n}^{S_2}\left(X\right)=V^{S_2}\left(X\right)-V^{C}\left(X,0.5T^{C}\right), \\ & \Delta_{t}^{S_1}\left(X_1^{R}\right)=U^{C}\left(X,-0.5T^{C}\right)-\left[U^{S_1}\left(X_1^{R}\right)-\Phi^{S_1}\left(X_1^{R}\right)\left(T^{S}/2\right)\right]' \\ & \Delta_{t}^{S_s}\left(X_1^{R}\right)=\left[U^{S_2}\left(X_1^{R}\right)+\Phi^{S_2}\left(X_1^{R}\right)\left(T^{S}/2\right)-U^{C}\left(X,0.5T^{C}\right)\right] \end{aligned} \tag{4.5}$$

where T^{S} and T^{C} are the thickness of the skin and core, respectively. Previous equations, i.e. Eq.(4.1), should be considered in those cases, in which the interfaces are not affected by debonding phenomena. However, once crack initiation condition is satisfied, at the position $X=X_T$ debonding phenomena should be simulated from the right and left directions. In particular, two different positions are introduced, which identify fictitious crack tips for the right and left debonding lengths, i.e. $X=\left(X_T^{L},X_T^{R}\right)$. Such quantities differ from the internal length $2\overline{\Delta}$, which refers to the initial defect predicted by the crack growth criterion and from the numerical point of view, it is taken to be very small in the numerical model to simulate the presence of an initial defect. For more details, the influence of such parameter was investigated in [53]. Therefore, the governing equations are expressed as follows:

$$\begin{aligned} &\mu \ddot{U}_2^k - \left[EAU_{2,X}^k \right],_X + F_X\left(X^R\right) + F_X\left(X^L\right) + p_x\left(X\right) = 0, \\ &\mu \ddot{V}_2^k - \left[GA^*\left(V_{2,X}^k - \Phi_2^k\right)\right],_X + F_Y\left(X^R\right) + F_Y\left(X^L\right) + p_y\left(X\right) = 0, \qquad \Omega_{S_2} \\ &I_0 \ddot{\Phi}_2^k - EI\Phi_{2.XX}^k - \left[GA^*\left(V_{2,X}^k - \Phi_2^k\right)\right] + m\left(X\right) = 0, \end{aligned} \tag{4.6}$$

where the superscript k is $k=S_2$, $\left(X^R, X^L\right)$ are the effective moving coordinates for the left (L) and right (R) directions measured on the material domain. Moreover, the governing equations of the core, i.e. field and initial conditions, refer to a classical 2D plane stress modelling, which, for the sake of brevity, is not reported in detail. However, boundary conditions concerning the interface regions between core and skins are defined by the following expressions:

$$\begin{aligned} &E_{33}\left(U_{,Y} + V_{,X}\right) = F_X\left(X^R\right) + F_X\left(X^L\right) \\ &\left(E_{12}U_{,X} + E_{22}V_{,Y}\right) = F_Y\left(X^R\right) + F_Y\left(X^L\right) \end{aligned} \qquad \text{on } \Gamma_{S_2/C} \tag{4.7}$$

It is worth noting that interface traction forces are expressed in terms of the moving coordinate systems, i.e. $\left(X^R, X^L\right)$, for the right and left debonding phenomena, leaving unaltered, with respect to the standard material formulation, the governing equations of the structural elements [102].

4.1.1 Results

In this section, the proposed model is verified by means of comparisons with numerical and experimental data. The first step is developed with the purpose to analyse the consistency of the proposed formulation under mode I and mode II loading conditions. In particular, according to standard experimental methods, the static behaviour of interfacial cracks for several sandwich debonding configurations is investigated. The main aim of the comparisons is to validate the proposed model and to examine its ability to describe debonding failure mechanisms in sandwich configurations. The structural behaviour is investigated in both static and dynamic frameworks to identify the influence of inertial effects on the crack growth phenomena, produced by different levels of the loading rate.

4.1.1.1 Mode I DCB loading scheme

At first, analyses are developed with reference to a classical DCB loading involving a pure mode I fracture analysis. The loading, boundary conditions and geometry of the specimen are illustrated in Fig. 4.4, whereas, according to data recovered in [103, 104], mechanical properties assumed for the laminate, core and interfaces as well as the ones required by the cohesive elements, are summarized in Tab. 4.1. The crack evolves in the interface region between core and face sheet (namely at $\Gamma_{S_2/C}$). In particular, a pre-existing delaminated length is assumed in the upper interface, whereas the lower interface is considered as perfectly bonded. The numerical model is discretized by means of shear deformable beam elements with cubic interpolation functions for each face sheet, whereas the core is modelled by quadratic interpolation functions with linear elastic material behaviour. Moreover, ALE elements with linear interpolation functions are introduced between each sheet-core interfaces to predict crack onset or debonding advance. The analysis is developed under a displacement control mode to ensure a stable crack propagation. Cohesive constitutive relationships are based on exponential laws, with smooth decay branches according to [105]. The numerical discretization utilized for the face sheet is assumed to be generally uniform with a length equal to $\Delta_M / L = 1/30$, with Δ_M the element length. The core has been discretized by means plane stress quadrilateral elements with maximum element length equal to $\Delta_M / L = 1/30$. At the interfaces a coarse discretization is adopted, except at the process zone ($\Omega^{R,L}$) where a mesh enrichment is considered, i.e. $\Delta_M / L = 1/300$.

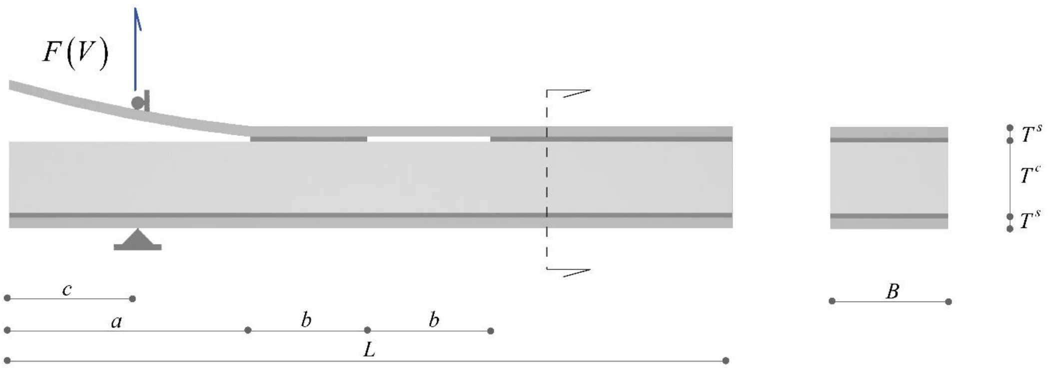

Fig. 4.4: Loading schemes and geometrical configuration for mode I analysis. Definition of the internal debonding geometry.

Face - sheet aluminium	$E_1^s\left[\text{GPa}\right]$	$G_{12}^s\left[\text{GPa}\right]$	ν^s	$\rho^s\left[\text{kg m}^{-1}\right]$	-	-
	70	26	0.33	2700	-	-
Core - PMI AIRES R 90.400	$E_1^s\left[\text{GPa}\right]$	$G_{12}^s\left[\text{GPa}\right]$	ν^s	$\rho^s\left[\text{kg m}^{-1}\right]$	-	-
	0.42	0.22	0.25	400	-	-
Geometrical properties	$L\left[\text{mm}\right]$	$B\left[\text{mm}\right]$	$a\left[\text{mm}\right]$	$a\left[\text{mm}\right]$	$T^s\left[\text{mm}\right]$	$T^c\left[\text{mm}\right]$
	152.4	25.4	50.8	27.1	2.2	15
Interface properties	$G_C\left[\text{N mm}^{-1}\right]$	$\Delta_0\left[\text{mm}\right]$				
	0.550	0.12				

Tab. 4.1: Geometrical, mechanical and interface properties.

In Fig. 4.5, comparisons in terms of loading curves as a function of opening end displacements, for two different core thickness configurations, i.e. T^c=15,20 mm, are reported. The results show that the proposed approach is able to reproduce correctly the behaviour of the structure, since the loading curves are quite in agreement with experimental [104] and analytical data available in [103].

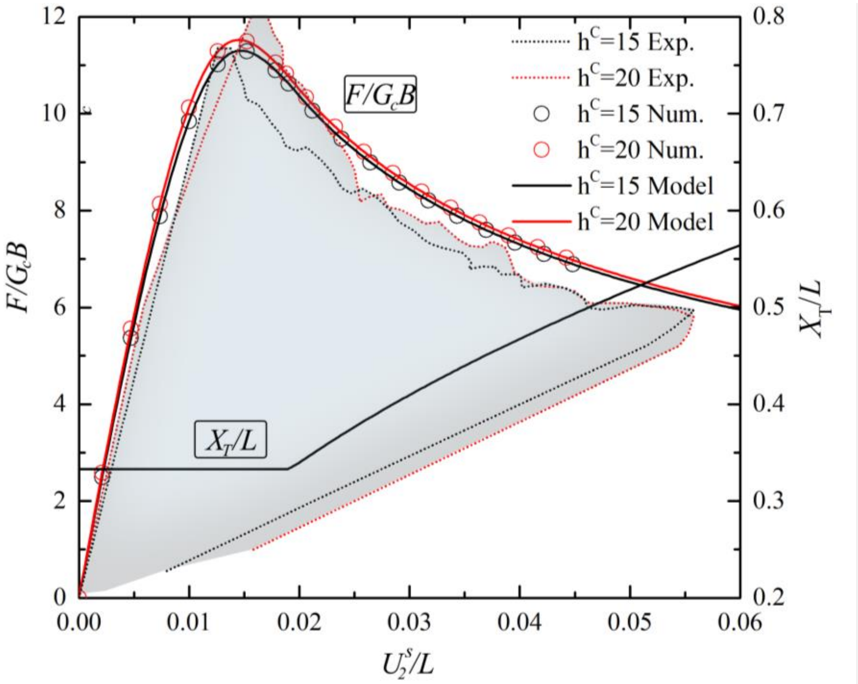

Fig. 4.5: Mode I analysis, normalized loading vs opening displacement: comparisons with numerical [103] and experimental [104] data in terms of normalized loading curve and opening displacement.

The results show that an increment in the core thickness does not produce improvements in the loading curves, which are basically coincident in terms of stiffness, displacements except for a small variation of the peak load. Previous analyses developed essentially in statics are extended in a dynamic framework. The main aim is to investigate the influence of the loading rate on both resistance curve and crack tip speed evolution. In addition, the effect of an internal pre-existing delamination region is also considered to verify the dynamic amplifications produced during the crack growth and their interaction with an external debonding length. The structure is subjected to an applied speed with a ramp curve until the time (t_0), which is assumed proportional to the first period of vibration of the structure ($t_0=0.5T_1$); subsequently a fixed velocity is prescribed to the end displacement (v_0). In Fig. 4.6, comparisons in terms of resistance curve between static and dynamic results are developed, obtained by means several prescribed opening speeds with refers to low or high ranges. Moreover, the following configurations are considered in the analyses:

- external debonding length only with b=0 (C_1);
- internal and external discontinuities with different geometric lengths, i.e. b/a=0.2 (C_2) or b/a=0.5 (C_3).

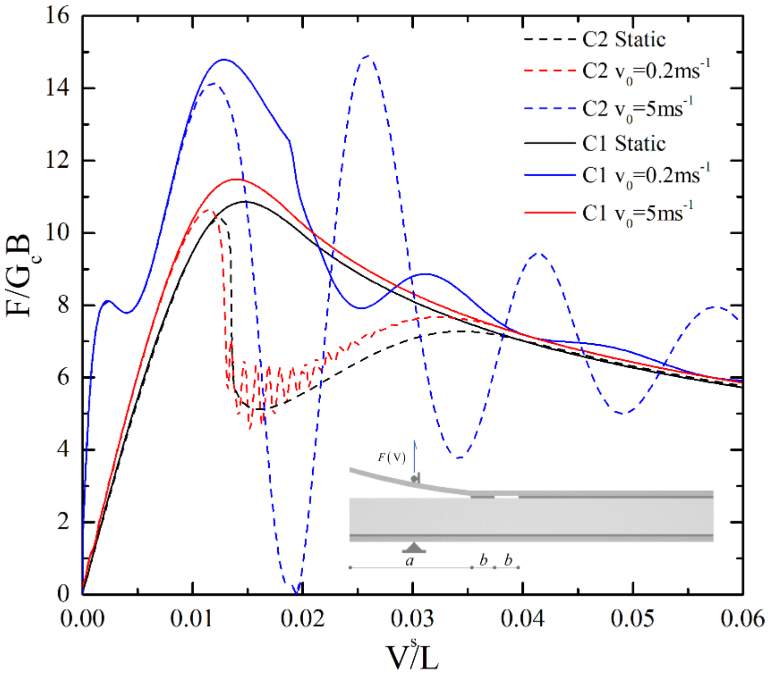

Fig. 4.6: Mode I analysis, normalized loading vs opening displacement: effect of the loading rate on the resistance curve: comparisons between static and dynamic loading curves.

The results show that under static loading the presence of an internal debonding length modifies load-displacement curves, increasing system instability during the crack growth and leading large oscillations with respect to the static case. The presence of an internal debonding, at low speeds, does not modify the evolution curve, which, apart little oscillations in the unstable path, is quite coincident with the C_1 configuration. However, at large speeds, the dynamic effects modify the crack growth behaviour, since C_1 and C_2 denote notable oscillations, which tend to be reduced, for increasing values of the opening displacements, leading to same predictions of the static solution.

In Fig. 4.7, the influence of an internal discontinuity on the dynamic behaviour of debonding phenomena is discussed. In particular, for a fixed loading rate, comparisons in terms of loading curve are proposed for the C_1, C_2 and C_3 configurations. The results show how the presence of an internal discontinuity modifies the equilibrium path, introducing a marked span-back phenomenon in the loading curve. However, once the crack tip overcomes the internal debonding length, the curves for the configurations with internal debonding lengths, i.e. C_2 and C_3, tend to the same prediction.

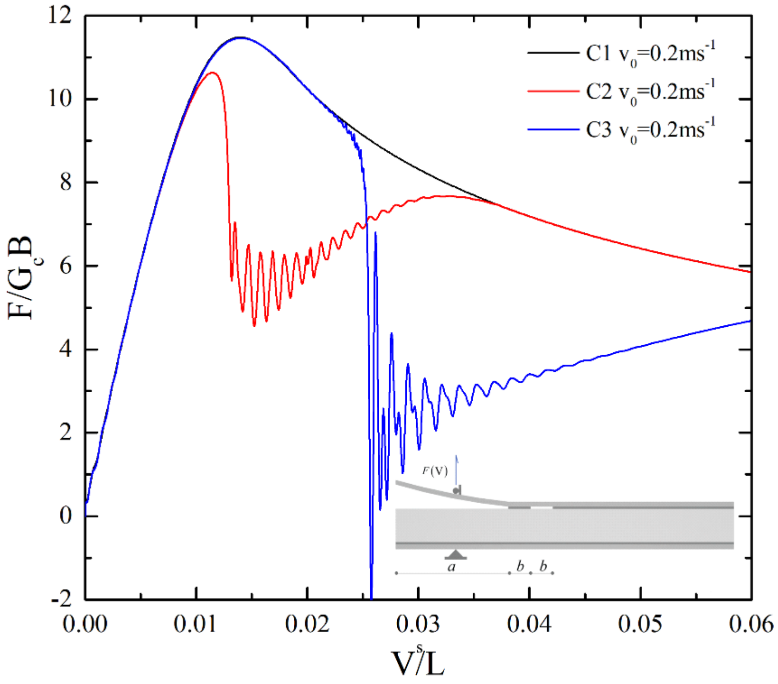

Fig. 4.7: Mode I analysis, normalized loading vs opening displacement: Effect of the internal debonding length: comparisons between static and dynamic loading curves.

.

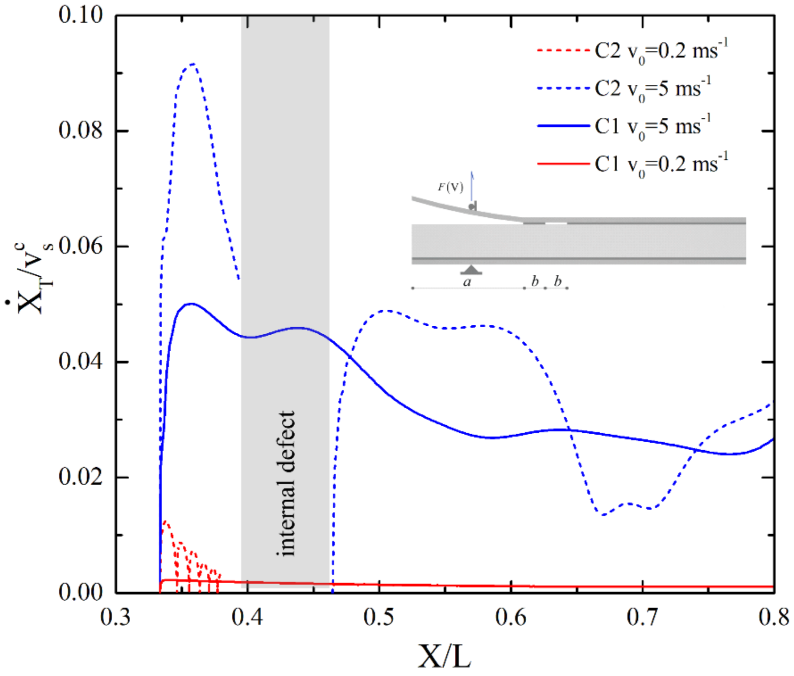

Fig. 4.8: Mode I analyses: crack tip speed vs crack displacement as a function of the loading rate and the internal debonding length for C1 and C2 configurations.

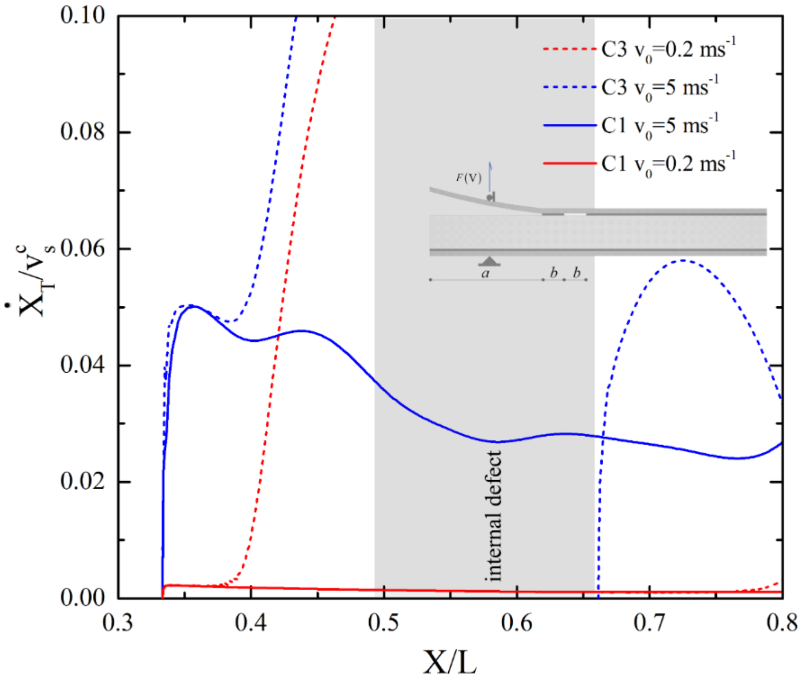

Fig. 4.9: Mode I analyses: *crack tip speed vs crack displacement as a function of the loading rate and the internal debonding length for* C1 and *C2 configuration*s.

Additional results are presented Fig. 4.8 and Fig. 4.9, in which the relationship between speed and position of the crack tip is investigated. The analyses show that during the crack onset, the tip is affected by large accelerations, which tend to be reduced as far as the crack tip speed grows. However, at low loading rates, after a maximum value is reached, the crack tends to a steady state advance, since a constant speed is observed. In presence of an internal debonding region, the crack is affected by an oscillating behaviour and, especially at low loading rates, crack arrest phenomena are observed. This phenomenon is mainly produced by the presence of the internal debonded region, which produces a local distribution of contact forces with respect to the case of perfectly debonded region. Large amplifications in the crack tip speeds are observed, especially, during the transition regions from the adhesive to the delaminated length

4.1.1.2 Mode II CSB loading scheme

The analyses are extended to a loading scheme involving a mode II loading condition. Comparisons with numerical data are reported for a sandwich configuration based on a three-point bending loading scheme. As shown in Fig. 4.10, the initial crack is located in the upper interface between the face-sheet and the core, whereas geometrical and mechanical characteristics are reported in Tab. 4.2 The numerical discretization utilized for the face sheet is assumed to be generally uniform with a length equal to $\Delta_M / L = 1/55$. The core has been discretized by means plane stress quadrilateral elements with maximum element length equal to $\Delta_M / L = 1/55$. At the interfaces a coarse discretization is adopted, except at the process zone ($\Omega^{R,L}$) where a mesh enrichment is considered, i.e. $\Delta_M / L = 1/550$. The following configurations are considered in the analyses:

- external debonding length, i.e. b=0, (C_1);
- internal and external discontinuities with b/a=0.5 (C_2).

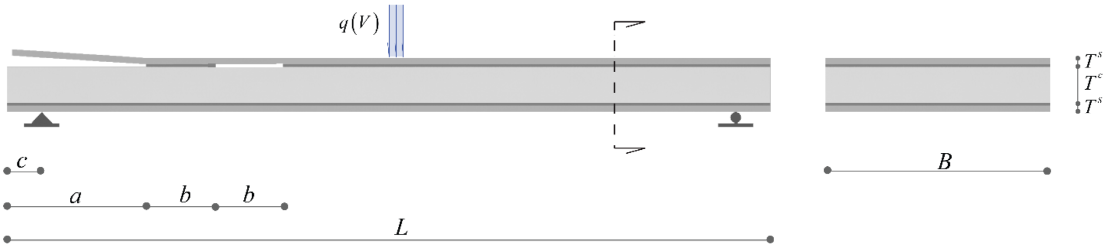

Fig. 4.10: Loading schemes and geometrical configuration for Mode II analysis. Definition of the internal debonding geometry.

Face - CFRP	$E_{11}^{s}\left[\text{GPa}\right]$	$E_{22}^{s}\left[\text{GPa}\right]$	$G_{12}^{s}\left[\text{GPa}\right]$	ν^{s}	$\rho^{s}\left[\text{kg m}^{-1}\right]$	-
	135	9.75	9.75	0.28	1800	-
Core - PMI RHOACELL 71RIST	$E_{1}^{s}\left[\text{GPa}\right]$	$G_{12}^{s}\left[\text{GPa}\right]$	ν^{s}	$\rho^{s}\left[\text{kg m}^{-1}\right]$	-	-
	0.105	0.042	0.25	75	-	-
Geometrical properties	$L\left[\text{mm}\right]$	$B\left[\text{mm}\right]$	$a\left[\text{mm}\right]$	$a\left[\text{mm}\right]$	$T^{s}\left[\text{mm}\right]$	$T^{c}\left[\text{mm}\right]$
	550	250	100	25	2.25	25.7
Interface properties	$G_{C}\left[\text{N mm}^{-1}\right]$	$\Delta_{0}\left[\text{mm}\right]$				
	0.385	0.20				

Tab. 4.2: Geometrical, mechanical and interface properties..

Comparisons in terms of applied loads as a function of mid-span vertical displacement for two different pre-existing crack length configurations are reported. In both cases, results obtained by the proposed model are in agreement with the ones obtained by analytical approach based on pure cohesive model [103](Fig. 4.11). Moreover, in Fig. 4.12, comparisons are developed to verify the consistency of the solution with respect to the local distribution of interfacial stresses. Despite numerical data reported in the literature, the proposed model is able to reproduce the crack growth also for more extended tip displacements. The results point out in the load-displacement curves the presence of a knee once the position of the crack tip overcomes the one of the applied loads. The accuracy of the solutions is guaranteed also locally in terms of stress distribution. Good agreement with the values obtained by using a pure cohesive modelling, in which an accurate description in terms of mesh element length is required along all the interface regions is found. Contrarily in the proposed model, based on ALE approach, the mesh refinement is introduced along the process zone only, leading to a reduction of the computational costs involved in the analysis.

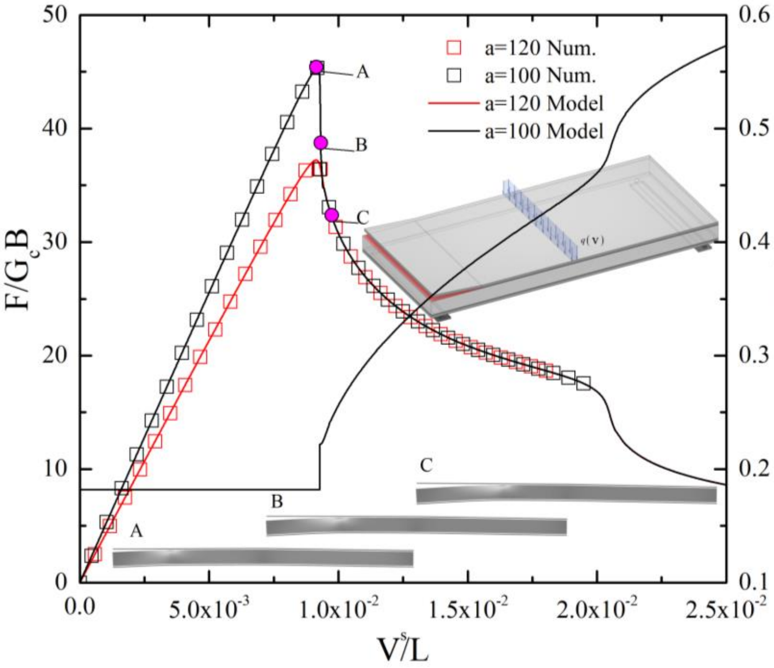

Fig. 4.11: Mode II analysis, normalized loading vs opening displacement: comparisons with numerical [103] in terms of normalized loading curve and opening displacement.

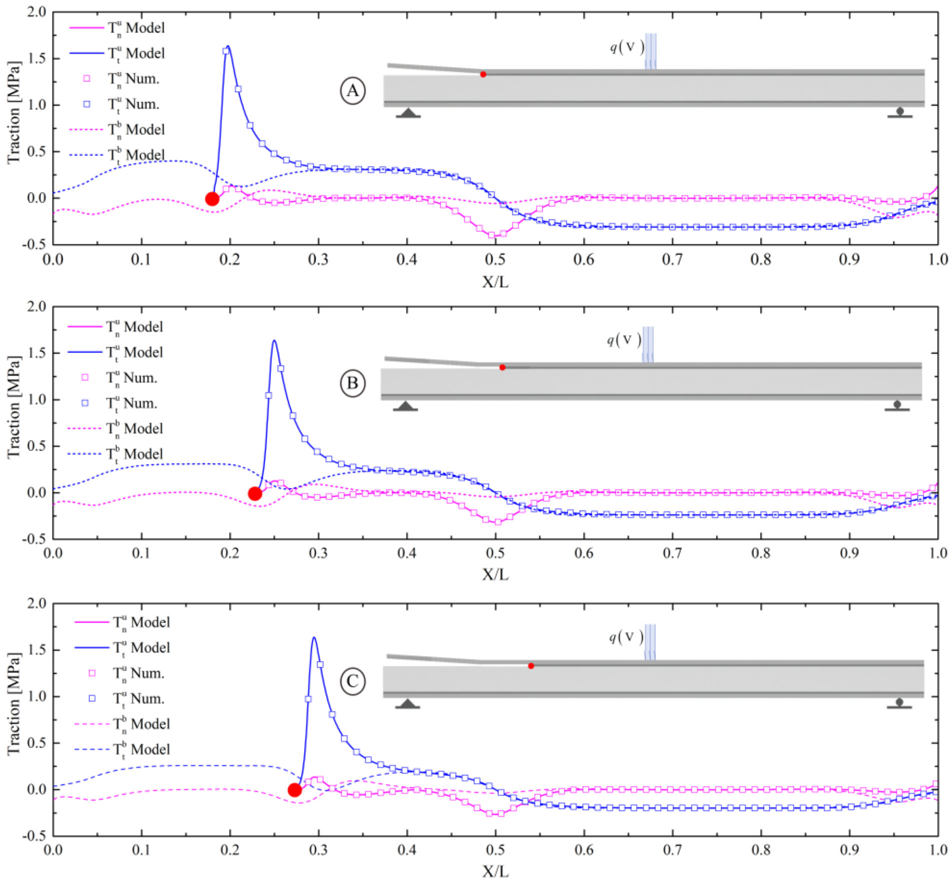

Fig. 4.12: Mode II analysis: comparisons with numerical data arising from [103] in terms of traction forces for lower and upper interfaces.

Previous results developed essentially in statics are extended in a dynamic framework, in which applied speeds based on a ramp curve with different loading rates are considered. Resistance curves are reported in Fig. 4.13 and Fig. 4.14, which refer to configurations with or without an internal debonding length, i.e. C_1 and C_2, respectively. The results show that, at high loading rates, large oscillations and amplifications with respect to the static solution are observed. Similarly, to results obtained under pure mode I loading scheme, Mode II configuration is also affected by the presence of an internal discontinuity, since an instable behaviour in the loading curve with small oscillations is observed with respect to the static equilibrium path. The stress distributions for two different structural scenarios related to C_1 and C_2 configurations are reported in Fig. 4.15. The results show that, in presence of an internal debonding length, the traction forces present a discontinuous behaviour at the extremity points, leading to singular values of the interfacial stresses. In Fig. 4.16, comparisons in terms of crack tip speeds, denote how the presence of an internal discontinuity produces an amplifications of the tip speed also for low loading rates, leading to jumps of crack speeds once the tip reaches the debonded length. Moreover, as far as the crack tip overcomes the delaminate length; the crack tip speed oscillates leading to crack arrest phenomena during the crack evolution.

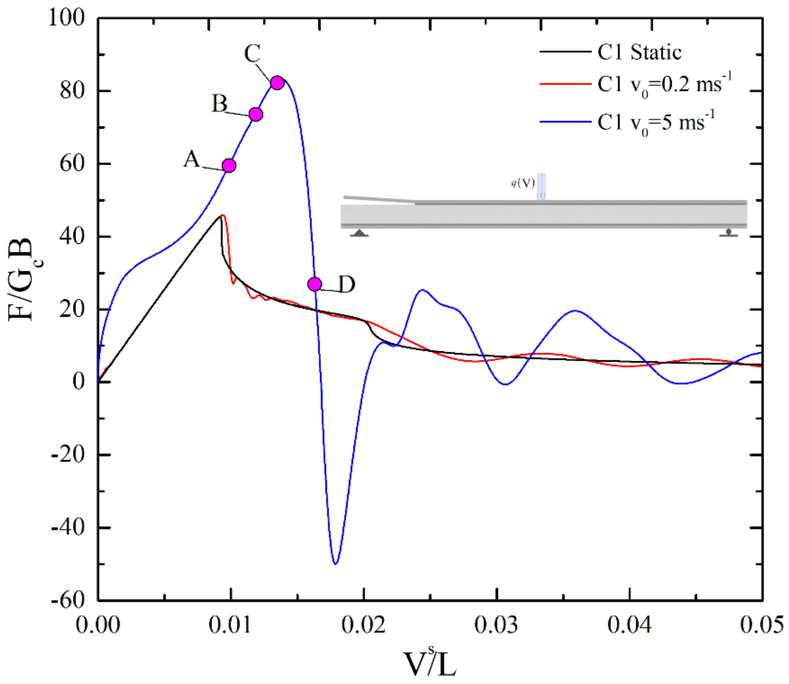

Fig. 4.13: Mode II analysis, normalized loading vs opening displacement: comparisons between static and dynamic loading curves for C1 configuration.

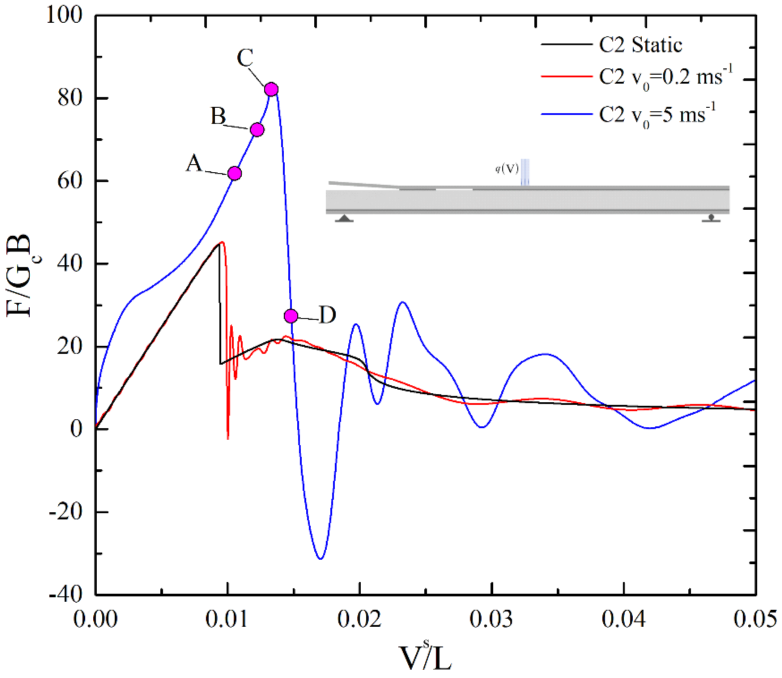

Fig. 4.14: Mode II analysis, normalized loading vs opening displacement: comparisons between static and dynamic loading curves for C2 configuration.

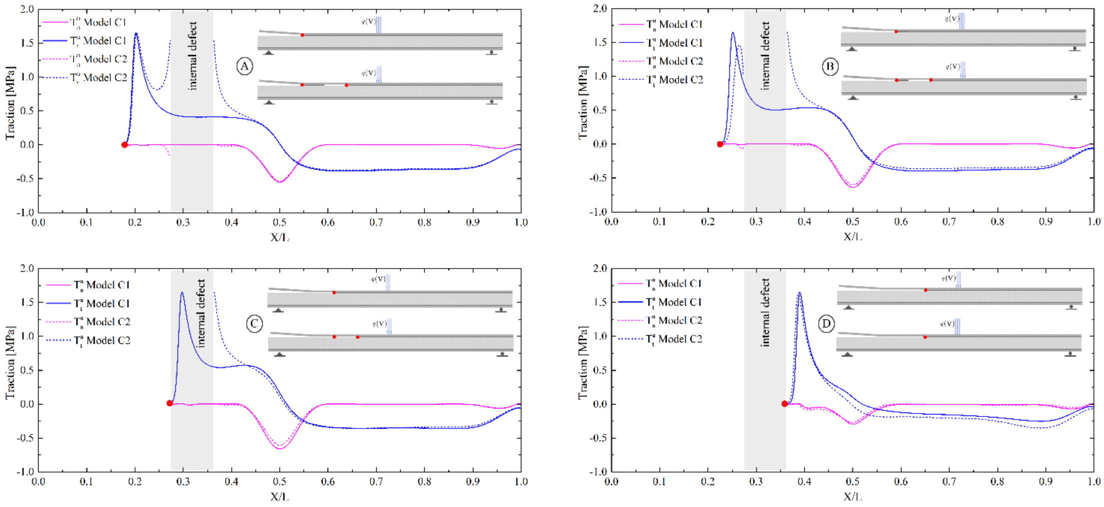

Fig. 4.15: Mode II analysis: comparisons in terms of traction forces for different position of the debonding front

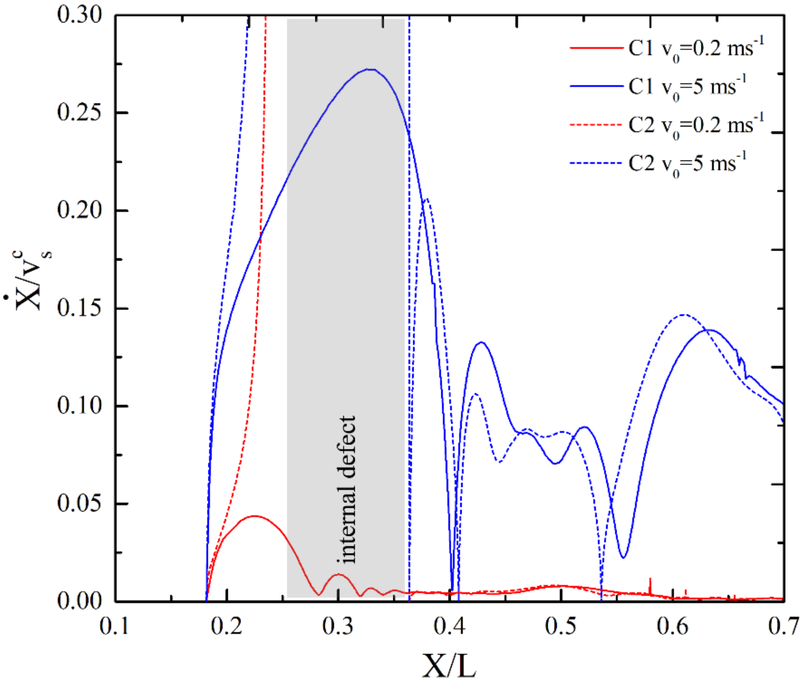

Fig. 4.16: Mode II analysis: comparisons in terms of the crack tip speed for different internal debonding lengths.

4.2 Model based on ALE to describe crack propagation 2D solids

The evolution of pre-existing cracks in the core is simulated by the generalization of the formulation developed in previous subsection to a two-dimensional domain. Two configurations are introduced to describe the mesh motion defined as referential or material ones. The latter is modified by the geometry variations produced by the crack advance, whereas the former is basically fixed or at least re-meshed in those cases in which large distortions occur.

4.2.1 Theoretical formulation of the model

The proposed approach is presented for a 2D continuum model, based on plane-stress or plane strain assumptions, in which an initial material discontinuity is assumed in the material. As shown in Fig. 4.17, the governing equations of the structural model are defined by a classical formulation related to a 2D problem, with essential and natural boundary conditions on $S_u = S_u \cup S_p$, as follows:

$$div\left[\underset{\sim}{E}\ \nabla\underset{\sim}{u}\right]+\underset{\sim}{f}=\underset{\sim}{0}\ \text{ in } V \qquad \underset{\sim}{u}=\underset{\sim}{u}_c\ \ (S_c), \qquad \left[\underset{\sim}{E}\nabla\underset{\sim}{u}\right]\underset{\sim}{n}=\underset{\sim}{p}\ \ (S_p) \tag{4.8}$$

where, V , S_p , S_c and h *with* $V = S_p \bigcup S_c \times h$ are the volume, load and displacement boundary surfaces, loading and thickness of the structure, $\underset{\sim}{u}^T = \left[u \quad v \right]$ is the displacement vector function, $\underset{\sim}{E}$ with $\underset{\sim}{E} = \underset{\sim}{E}^T$ is the elastic matrix defined differently for plane strain/stress, $\underset{\sim}{f}$ is the per unit volume force vector, $\underset{\sim}{u}_c$ is the prescribed vector function and $\underset{\sim}{p}$ is the per unit surface force vector. Eq.s (4.8) are completed by the crack growth conditions, which will be introduced, subsequently, in terms of Fracture Mechanics variables.

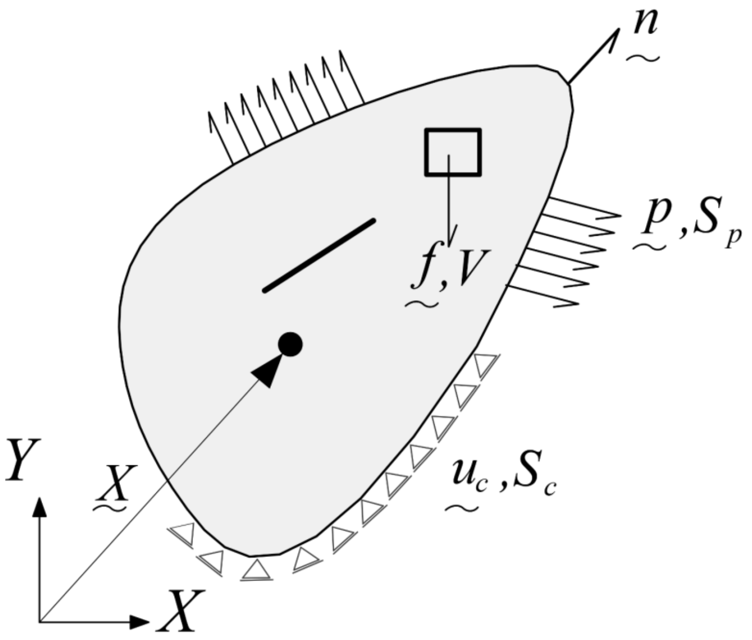

Fig. 4.17: Schematic representation of a 2D problem including a macro-discontinuity.

It is worth noting that in this context the evolution of an initial material discontinuity is simulated by the use of ALE approach, which is introduced to take into account of a geometry variation of the structural boundaries. As a consequence, previous equations should be reformulated in terms of moving coordinates, introducing proper relationships between initial and current geometrical configurations. Consistently to ALE formulation, two coordinate systems are introduced, known as Referential (R) and Moving (M) ones (Fig. 4.18), which identify, for each mesh point, the mapping between the current and fixed nodes:

$$\underset{\sim}{X}_M = \underset{\sim}{\Phi}\left(\underset{\sim}{X}_R\right) \qquad\qquad \underset{\sim}{X}_R = \underset{\sim}{\Phi}^{-1}\left(\underset{\sim}{X}_M\right) \qquad (4.9)$$

where $\underset{\sim}{\Phi}: C_R \rightarrow C_M$ with $\underset{\sim}{\Phi}^T = \begin{bmatrix} \Phi_X & \Phi_Y \end{bmatrix}$ is assumed to be invertible with continuous inverse. In order to take into account of geometry variation produced by the crack propagation phenomena, Jacobian matrix of the ALE mapping is required, by which gradient operators can be expressed by means of the following relationships:

$$\nabla_M(\bullet) = \underset{\sim}{J}^{-1} \cdot \nabla_R(\bullet) \quad div_M(\bullet) = \underset{\sim}{J} \cdot \nabla_M(\bullet) \quad \text{with} \quad \underset{\sim}{J} = \begin{bmatrix} \dfrac{\partial \Phi_X}{\partial X_R} & \dfrac{\partial \Phi_Y}{\partial X_R} \\ \dfrac{\partial \Phi_X}{\partial X_R} & \dfrac{\partial \Phi_Y}{\partial Y_R} \end{bmatrix} \tag{4.10}$$

Therefore, the governing equations of the structural problem are defined by substituting Eq.(4.10) into Eq.(4.8), as follows:

$$div_M \left[\underset{\sim}{E}\left(\underset{\sim}{X}_M\right) \; \left(\underset{\sim}{\nabla}\underset{\sim}{u}\left(\underset{\sim}{X}_R\right) \cdot J\right)\right] + \underset{\sim}{f}\left(\underset{\sim}{X}_M\right) = 0 \text{ in V in V}$$

(4.11)

$$\underset{\sim}{u}\left(\underset{\sim}{X}_M\right) = \underset{\sim}{u}_c \text{, (Sc),} \quad \left[\underset{\sim}{E}\left(\underset{\sim}{\nabla}\underset{\sim}{u}\left(\underset{\sim}{X}_R\right) \bullet J\right)\right]\underset{\sim}{n} = \underset{\sim}{p} \text{ ,(Sp)} \tag{4.12}$$

Eq.s(4.11)-(4.12) evaluate the elasto-static problem and are completed by the relationships to identify the crack propagation.

In particular, introducing the fracture function fF defined on the basis of material characteristics, the crack growth displacement at the generic point of the tip contour, can be obtained by means of the following incremental relationships:

$$f_F \dot{\lambda}_F = 0, \quad \dot{\lambda}_F \geq 0, \quad f_F \leq 0, \quad \dot{\delta}_F = \dot{\lambda}_F \frac{\partial f_F}{\partial G} \text{ on } S_F \tag{4.13}$$

where S_F is the fracture domain shown in Fig.1, $\dot{\lambda}_F$ is the fracture multiplier, $\dot{\delta}_F$ is the incremental crack tip displacement vector along normal direction, G is the energy release rate associated to the crack area extension.

In order to describe the shape variation produced by the cracked surface, specific boundary conditions and field equations are required. Introducing the nodal mesh displacement vector function, defined as $\Delta\underset{\sim}{X} = \underset{\sim}{X}_M - \underset{\sim}{X}_R$, boundary conditions should be introduced along the crack tip contour to enforce normal crack tip displacements according to Eq.(4.13), as follows:

$$\Delta\underset{\sim}{X} \cdot \underset{\sim}{n} = \dot{\delta}_F \quad \text{on} \quad S_F \tag{4.14}$$

where $\underset{\sim}{n}$ is the normal vector at generic point of the cracked surface and $\dot{\Omega}$ is the incremental displacement obtained by solving Eq.(4.13).

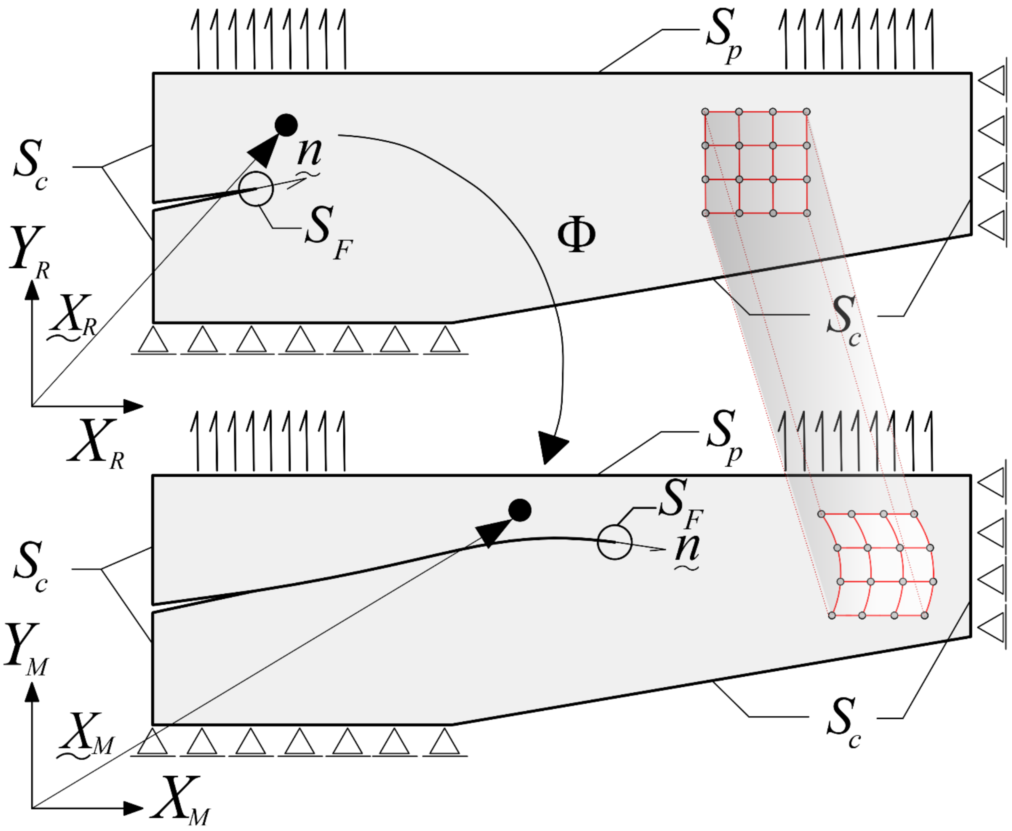

Fig. 4.18: Referential and Moving coordinate systems for a 2D problem

In addition, rezoning equations as well proper boundary conditions are required to redistribute the material points adjoining the cracked surface. Without loss of generality, a Laplace regularization technique is utilized to reduce mesh element distortion. Moreover, additional boundary conditions are required on the external contour to constraint the displacements of the mesh points. As a consequence, the governing equations of the ALE problem are defined by means of the following expressions:

$$\underset{\sim}{\nabla}^2\Phi_X = 0 \qquad \underset{\sim}{\nabla}^2\Phi_Y = 0 \qquad \text{in} \qquad V \tag{4.15}$$

$$\Delta\underset{\sim}{X} = \underset{\sim}{0}, \qquad on \quad S_U \tag{4.16}$$

where $\underset{\sim}{\nabla}^2$ is square nabla operator and S_M is with $S_M = S_U \cup S_F$ *with* $S_M \cap S_F = \varnothing$ is the external contour of the structural system.

4.2.2 Numerical implementation of the model

Previous equations are implemented, numerically, by using a finite element formulation based on Galerkin approximation method. At first, the following sets of kinematic and weighing functions are defined as follows:

$$U=\left\{\underset{\sim}{u}\,\middle|\,\underset{\sim}{u}\in H^{1}(V),\underset{\sim}{u}(X_{M})=u_{c}\ on\ V\right\} \tag{4.17}$$

$$W=\left\{\left(\underset{\sim}{w}_{u}\right)\middle|\,\underset{\sim}{w}_{u}\in H^{1}\left(\underset{\sim}{w}_{u}\right),\underset{\sim}{w}_{u}(X_{M})=0\ on\ V\right\} \tag{4.18}$$

where H^1 denote the Sobolev space, $\underset{\sim}{w}_u$ is the weighting function vector related to displacement fields. Starting from Eq.(4.11)-(4.12) and introducing Eq.(4.10), the following expression represents the weak form for the structural problem:

$$\begin{gathered}\int_{V_R}\left[\,\underset{\sim}{\nabla}_{R}\underset{\sim}{W}_{u}\left(\underset{\sim}{X}_{R}\right)J\,\right]:\underset{\sim}{E}\left(\underset{\sim}{X}_{M}\right):\left[\,\underset{\sim}{\nabla}\underset{\sim}{u}\left(\underset{\sim}{X}_{R}\right)\cdot J\,\right]\overline{J}dV+\\-\int_{V_R}\underset{\sim}{f}\left(\underset{\sim}{X}_{M}\right)\underset{\sim}{W}_{u}\,\overline{J}dV-\int_{S_R}\underset{\sim}{p}\left(\underset{\sim}{X}_{M}\right)\underset{\sim}{W}_{u}\,\overline{J_{A}}dA=0\end{gathered} \tag{4.19}$$

where V_R or S_R are the volume or the boundary surface of the structural system in the referential configuration, $\overline{J}$ or $\overline{J_A}$ are the jacobians related to the volume or area, respectively. Similarly, for the moving mesh equations, the corresponding weak form is derived starting from Eq.(4.14)-(4.16), the following sets are introduced to describe mesh displacements and weight functions:

$$X=\left\{\underset{\sim}{X}_{M}\,|\,\underset{\sim}{X}_{M}\in H^{1}(S_{M}),\underset{\sim}{X}_{M}=X_{R}\ on\ S_{M}\right\} \tag{4.20}$$

$$W=\left\{\left(\underset{\sim}{w}_{X}\right)\middle|\,\underset{\sim}{w}_{X}\in H^{1}(S_{M}),\underset{\sim}{w}_{X}=0\ on\ S_{M}\right\} \tag{4.21}$$

Constraint conditions are introduced to prescribe crack tip displacements, defined according to Eq.(4.13). In particular, implicit boundary conditions at the crack tip front, are simulated by means of Lagrange Multiplier Method (LMM) enforcing Energy Release Rate (ERR), extension and angle orientation to verify Eq.s (4.13). The fracture function is consistent to a Griffith’s local law of propagation. Moreover, the crack direction may be predicted in terms of existing criteria available from the literature based on local fields at crack tip such as maximum circumferential stress [106] or [107] or global energy variables such as maximum strain energy density [108]. Crack tip displacements are predicted by the ALE approach by solving Eq.(4.15) with explicit and implicit boundary conditions defined by Eq.(4.16) and Eq.s (4.13)-(4.14),respectively. In particular, the following weak form is determined:

$$\int_{V_R} \underset{\sim}{\nabla}\underset{\sim}{\Phi} : \underset{\sim}{\nabla}\underset{\sim}{W}_{\Phi} dV - \int_{S_F} \left(\underset{\sim}{\Delta}\underset{\sim}{X}\underset{\sim}{n} - \dot{\Omega} \right) \underset{\sim}{W}_{\lambda}\, dA - \int_{S_F} \underset{\sim}{W}_{\Phi}\underset{\sim}{n}\underset{\sim}{\lambda} dA = 0 \tag{4.22}$$

where $\underset{\sim}{\lambda}$ is the LMM vector and W_{λ} is the corresponding weak function. Eq.(4.19) and Eq.(4.22) are solved by using Galerkin's approximation, by using a proper discretization of the geometric domain into N_e elements and the use of isoparametric elements defined by the following set of structural and ALE variables:

$$\underset{\sim}{u} = \sum_{I=1}^{N_e} \underset{\sim}{N}_I \underset{\sim}{U}_I, \quad \underset{\sim}{X}_M = \sum_{I=1}^{N_e} \underset{\sim}{N}_{MI} \underset{\sim}{X}_{MI}, \quad \underset{\sim}{\lambda} = \sum_{I=1}^{N_e} \underset{\sim}{N}_{\lambda I} \underset{\sim}{\Lambda}_I \tag{4.23}$$

where N_e represents the number of elements utilized and $\left(\underset{\sim}{N}, \underset{\sim}{N}_M, \underset{\sim}{N}_{\lambda} \right)$ are the matrix interpolation functions and $\left(\underset{\sim}{U}, \underset{\sim}{X}_M, \Lambda_I \right)$ are the nodal vector functions. Introducing Eq.(4.23) into Eq.(4.19) and Eq.(4.22), the following discrete equations are derived:

$$\underset{\sim}{K}\underset{\sim}{U} = \underset{\sim}{F}, \quad \underset{\sim}{A}\underset{\sim}{X}_M + \underset{\sim}{R}\underset{\sim}{\Lambda}_I = 0, \quad \underset{\sim}{R}\underset{\sim}{X}_M - \underset{\sim}{C}_1 = 0 \tag{4.24}$$

where $\underset{\sim}{K}$, $\underset{\sim}{U}$, $\underset{\sim}{F}$ are the global stiffness matrix, displacement and load vector, $\left(\underset{\sim}{A}, \underset{\sim}{R} \right)$ are the ALE matrix and vector respectively. Moreover, $\underset{\sim}{C}_1$ represents the vector containing the positions of the crack tip front obtained by solving Eq.(4.13). Explicit expressions of the ALE and structural problems are reported in Appendix A.

4.2.3 Computational procedure and implementation algorithm

In this section, computational procedure and implementation steps, involved in the advancing crack scheme, are presented. In order to facilitate the readability of the paper, some practical and general assumptions regarding the choice of the fracture function and crack propagation angle criterion have been made. The crack growth conditions are enforced by using a remapping mesh algorithm, which takes into account of geometry variation on the basis of Eq.(4.13). With reference to Fig. 4.19, in which a straight crack path is considered, the fracture function is based on local-Griffith approach criterion expressed as a function of the ERR and critical values. ERR is evaluated by using *J*-integral based approach with respect to a path surrounding the crack tip and a coordinate system aligned with respect to the direction of propagation (ξ) :

$$J = \int_{\Gamma} \left(W n_{\xi} - \underset{\sim}{\sigma} \frac{\partial \underset{\sim}{u}}{\partial \xi} \underset{\sim}{n} \right) dA \tag{4.25}$$

where Γ is the contour enclosing the crack tip, W is per unit volume strain energy, $\underset{\sim}{n}$ is the normal to contour Γ, n_{ξ} is the component of the normal vector along the crack propagation direction. Without loss of generality, the crack propagation angle is defined on the basis of Maximum Energy release rate criterion expressed in terms of as *J*-integral components as follows:

$$\theta = \arctan\left(\frac{J_2}{J_1} \right) \tag{4.26}$$

where J_2 and J_1 are the components of the *J* integral along normal (e_1) and tangential (e_2) directions, i.e. $J_2 = J \cdot e_2$ and $J_1 = J \cdot e_1$. With reference to Fig. 4.19, a suitable procedure to predict kinking angle and crack advance is performed, which is based on the crack angle criterion tolerance.

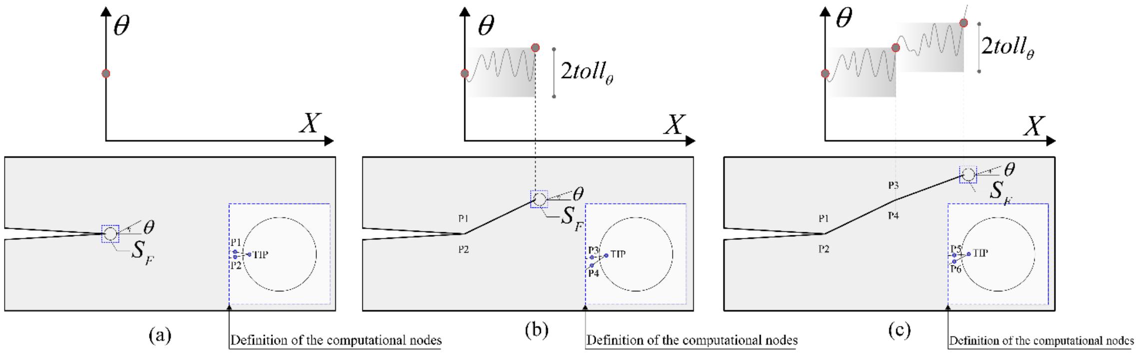

Fig. 4.19: Schematic representation of the proposed algorithm: (a) crack onset condition satisfied, evaluation of θ; (b) crack propagation in θ direction until the angle variation predicted is lower than $toll_Q$; (c) tolerance condition is satisfied, new definition of the computational nodes (P3 and P4).

In particular, it is supposed that at the crack tip front, a surrounding region is introduced to predict fracture variables by using *J*-integral expression defined in Fig.(4.25). In such region a large number of mesh points are introduced, which are moved rigidly to achieve an accurate evaluation of the fracture variables. The current solution is obtained by solving at the current iteration step, Eq.(4.25)-(4.26) and by prescribing the movements of the surrounding crack region by means of the following relationships:

$$\Delta \dot{X}_T = \cos\left[\theta\right]\dot{\delta}_F, \qquad \Delta \dot{Y}_T = \sin\left[\theta\right]\dot{\delta}_F, \tag{4.27}$$

where $\left[\theta\right]$ is the angle of propagation predicted at the current step and $\dot{\delta}_T$ is the incremental scalar quantity related to the crack advance. Moreover, additional constraint conditions are required to do not change the shape of pre-existing crack, whose positions are basically governed by displacements values obtained by solving the structural problem. This task is achieved by introducing two nodes close to the region adjoining the crack tip, which are stretched as far as the angle variation predicted by Eq.(4.26) is lower than a fixed tolerance value ($toll_\theta$). Once tolerance condition is satisfied a new definition of the computational nodes is required, which are driven, eventually, by the new value of crack propagation angle. It is worth noting that during the crack growth, mesh movements of the computational nodes produce mesh distortions, which require the use of a remeshing algorithm to reconstruct a new regular mesh discretization, transferring the nodal variables from the distorted to the new computational points. This procedure is recalled by means of a mesh quality parameter, which control the allowable distortion in each element. However, consistently to the ALE formulation, the use of rezoning or regularization methods strongly reduces the use of remeshing algorithm. Previous steps are implemented by using an external subroutine that interacts with a COMSOL MULTIPHYSICS FE software [109]. In particular, the algorithm was developed by means of proper customized script files, which manage the parameters and the results required by the iterative procedure. The computational procedure is presented, synoptically, in Fig. 4.20, and in Tab. 4.3 the steps involved in the user-subroutine are reported.

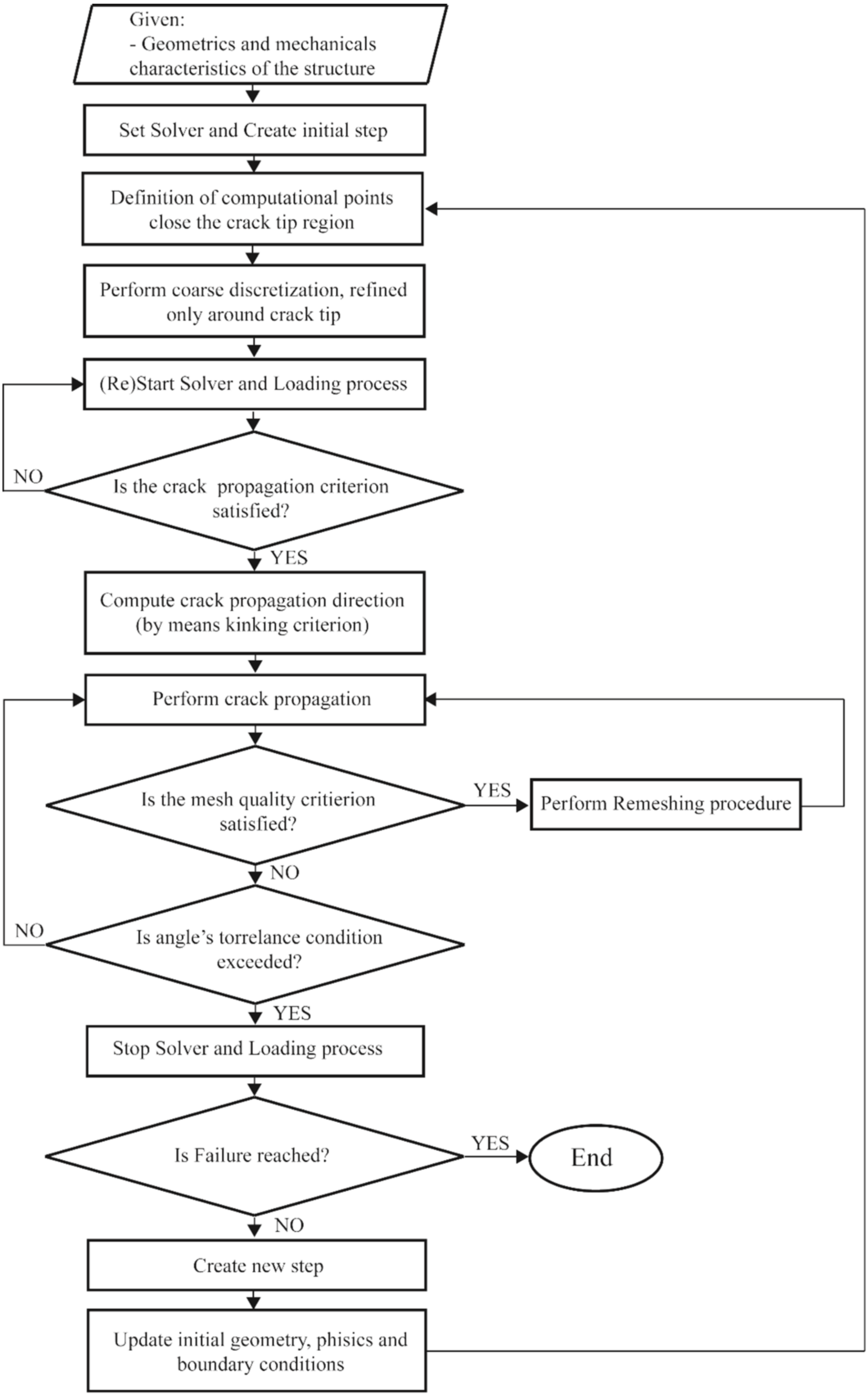

Fig. 4.20: Schematic representation of the algorithm for crack propagation in 2D solids.

```
START
0. Read the input data: geometry, material, mesh discretization and load configuration.
1. Loop for each load increment
      1.1 Determine the external force vector, stiffness, mass and ALE  matrixes (Eq.(4.24));
      1.2 Evaluate fracture variables (Eq.(4.13), Eq.(4.25))
   1.2  Check crack growth conditions as well as fracture variable (Eq.(4.13), Eq.(4.25))
   1.3  Loop to predict crack tip displacements if 1.2 is satisfied;
      1.3.1      Solve incremental Structural and ALE problem;
      1.3.2      Identify crack tip displacement and crack tip angle;
      1.3.3      Solve incremental problem to predict crack tip position
      1.3.4      Check tolerance conditions for the angle variation or mesh quality;
      1.3.5      If angle variation or mesh quality tolerances are satisfied
      1.3.5.1 Perform point node refinement at crack tip and modify the current mesh on the predicted moving geometry
      ELSE
      Continue
    End Loop 1.3
 End Loop 1.
 END
```

Tab. 4.3: Incremental-iterative procedure of the proposed algorithm.

4.2.4 Results and validation

In this section, the proposed algorithm is verified by means of a number of case study that are compared to numerical and experimental results available from literature. The first step, in the validation scheme, involves a single edge cracked cantilever plate subject to either mode I or mixed-mode loading. Finally, a polymethyl methacrylate (PMMA) continuum with different initial defects is investigated under a three-point bending loading scheme.

4.2.4.1 Single edge cracked cantilever plate

The first case study is aimed at verifying the computational performance of the proposed model. In this view, two rectangular plates fixed at the bottom edge, with an initial crack located at the plate mid-length, and alternatively subject to in-plane crack opening or shear unit loading at the upper edge, are taken into consideration. The loading, boundary conditions and geometry considered are illustrated in Fig. 4.21a-b whereas dimensionless mechanical properties are taken as elastic modulus E = 3 10^7 and Poisson's ratio ν = 0.3, all in accordance with the data provided in [110].

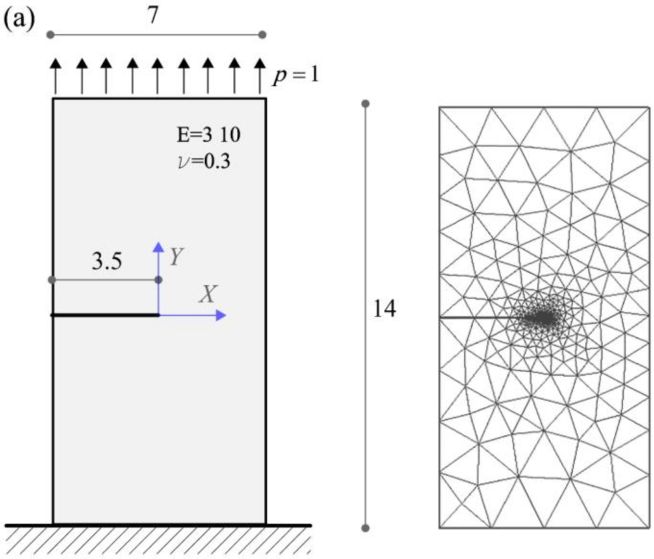

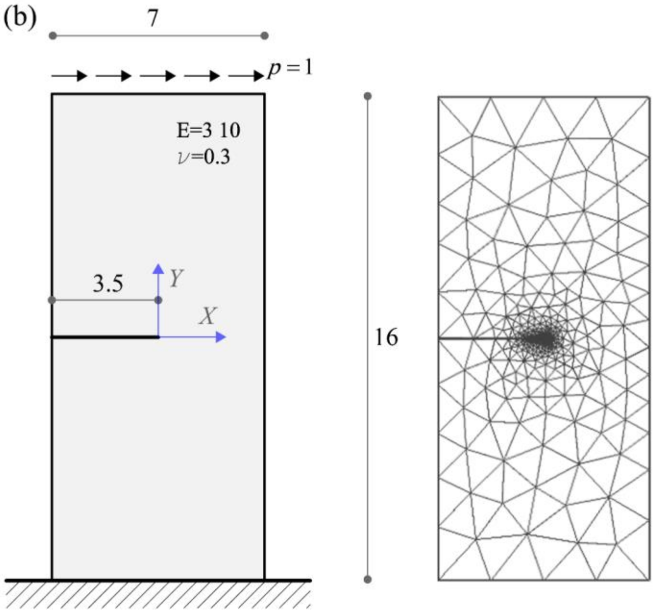

Fig. 4.21: Geometrical, loading and mesh configuration: (a) Model A involving in pure mode I; (b) Model B involving in Mixed Mode.

The loading scheme involve a pure Mode I crack propagation with a very low value of the ERR mode component ratio (Fig. 4.21a) or a mixed Mode I/Mode II crack propagation with prevalent mode I fracture component (Fig. 4.21b). Mode partition is verified by the results reported in Fig. 4.22, in which the ERR ratio, for both loading case, is expressed as a function of normalized crack length and synoptically in term of the maps of contour of the maximum principal stress. In both cases, the prediction of the crack tip variables is guaranteed by using *J*-integral concept on a region close to the crack tip front, in which a uniform mesh is utilized. In the remaining region, a coarse mesh is utilized to achieve the required accuracy in the prediction of the field variables.

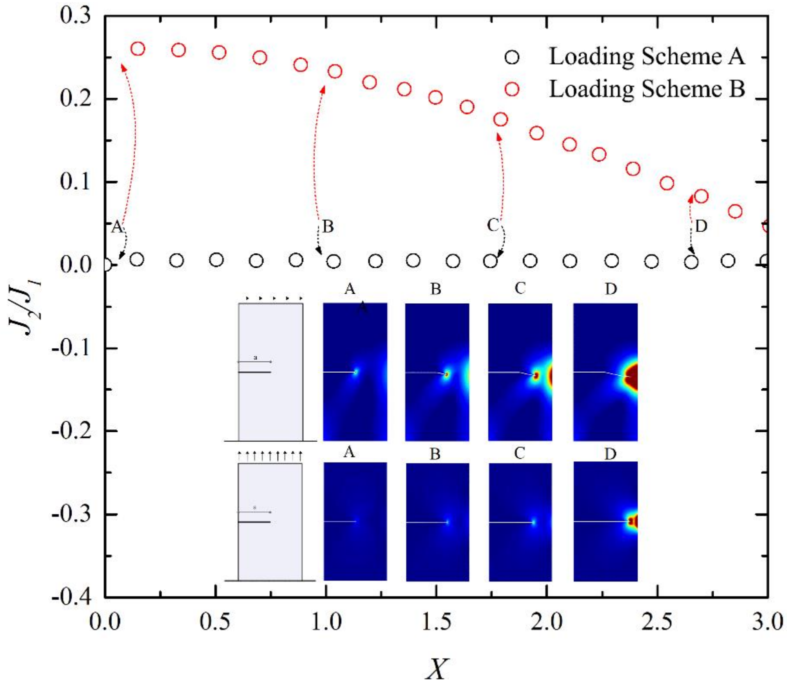

Fig. 4.22: Influence of the loading condition in the J_2/J_1*-X, comparisons between loading scheme A and B.*

In order to verify the prediction of the proposed model, in Fig. 4.23 , comparisons in terms of Mode I Stress Intensity Factor (SIF) (K_1) as a function of the crack length extension are reported for the case shown in Fig. 5a. The mesh discretization length at the crack tip region is equal to $\Delta D / R = 1/4$, whereas in the remaining region a coarse mesh with a total number of elements equal to 1047 s utilized. In the case of pure mode I, the mesh discretization does not influence the prediction of the fracture variables [46] and thus a coarse mesh is utilized. As expected, the crack growth proceeds along a straight path, with a zero propagation angle, because of the pure Mode I loading condition. The value of K_1, obtained by the proposed model, seems to be in good agreement with the data arising from [111], producing a low relative error between the curves, as shown also by means of Person’s coefficient of correlation, whose maximum value is equal to 0.998 .

The second example is referred to the loading scheme reported in Fig. 4.21b, in which due to the mode mix crack growth the propagation angle is not zero. Fig. 4.22 shows that in this case a higher value of the J_2 / J_1 ratio results in a mixed mode crack propagation. The initial mesh configuration used for the analyses is generally coarse in the region externally located to the crack tip region. As shown in Fig. 4.21b the tip region $\left(S_F\right)$ is discretized by means triangular plane stress elements with length equal to $\Delta D / R = 1/4$, whereas in the remaining part of the structure a transition mesh with maximum length equal to $\Delta D / R = 20/1$, involving in total 12506 DOFs.

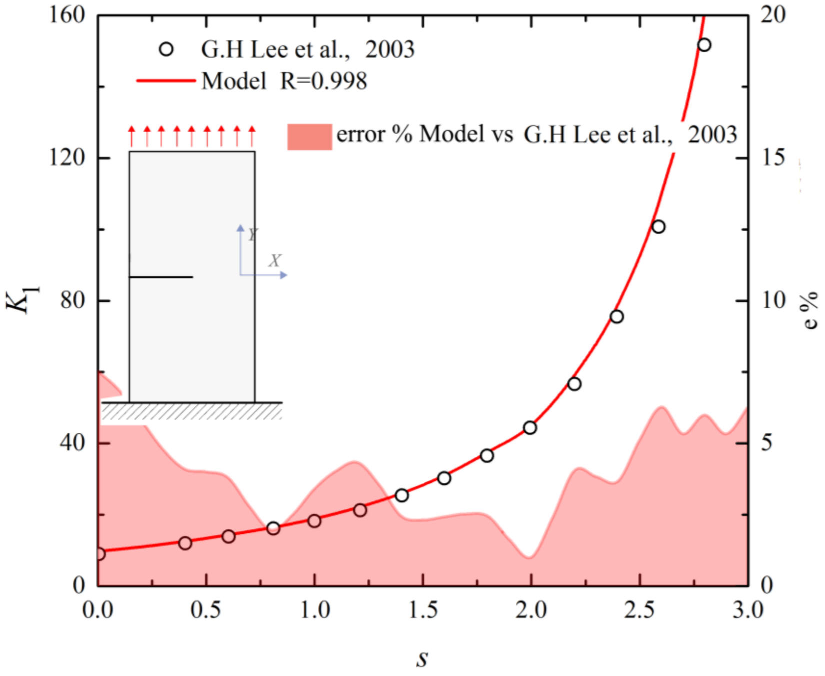

Fig. 4.23: Loading scheme: mode I SIF in terms of the crack propagation length, comparisons with numerical data arising from [111]. In the legend is reported the Pearson's correlation coefficient (R=0.998).

In Fig. 4.24 the crack tip coordinates predicted by means of the proposed model are compared with the ones obtained using a numerical strategy based on a meshless formulation [110]. In the proposed model, a crack tolerance angle equal to $\Delta\theta = 1°$ is assumed, to predict the crack direction. The two models are in good agreement within each other's. The accuracy of the solution is also confirmed by the low value of the relative error and by the Pearson's coefficient of correlation, which is very close to the unity.

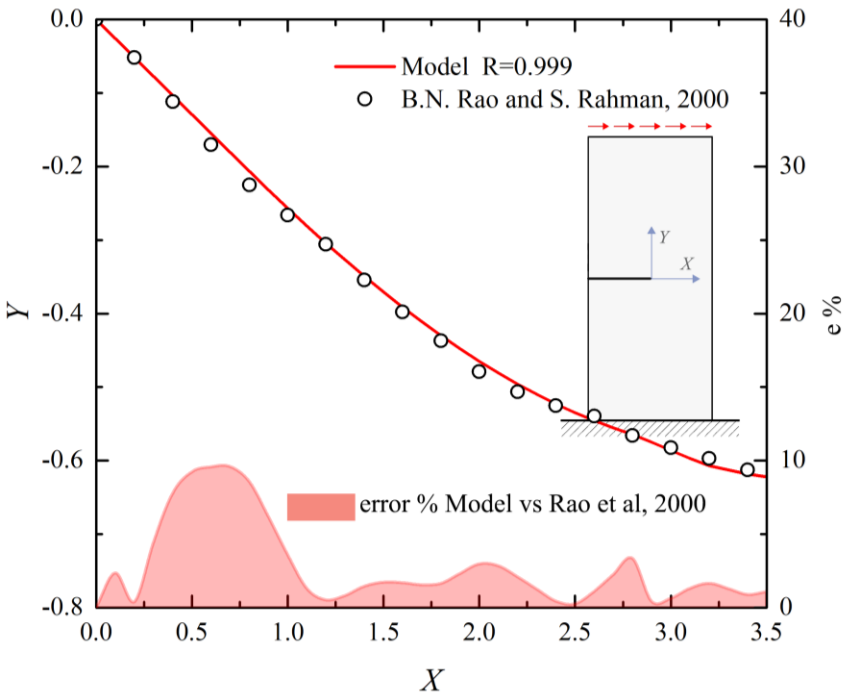

Fig. 4.24: Loading scheme: crack tip coordinates Y-X, comparison with numerical data arising from [110]. In the legend is reported the Pearson's correlation coefficient (R=0.999).

In Fig. 4.25 , a synoptic representation of the mesh motion during the crack propagation is reported. In particular, the evolution of the mesh discretization during the crack propagation at four different crack propagation steps is reported. It is worth noting that a high number of computational points are condensed around the crack tip region to ensure a good prediction of the fracture variables. However, a coarse discretization is adopted in the remaining parts of the structure during the entire simulation process. For the same four crack propagation steps mentioned earlier, the Von Mises stress maps based on the proposed model are compared with the ones arising from the meshless approach proposed by [110]. The comparisons reported in Fig. 9b-c show a good correlation between the stress maps and therefore confirm the accuracy of the proposed model.

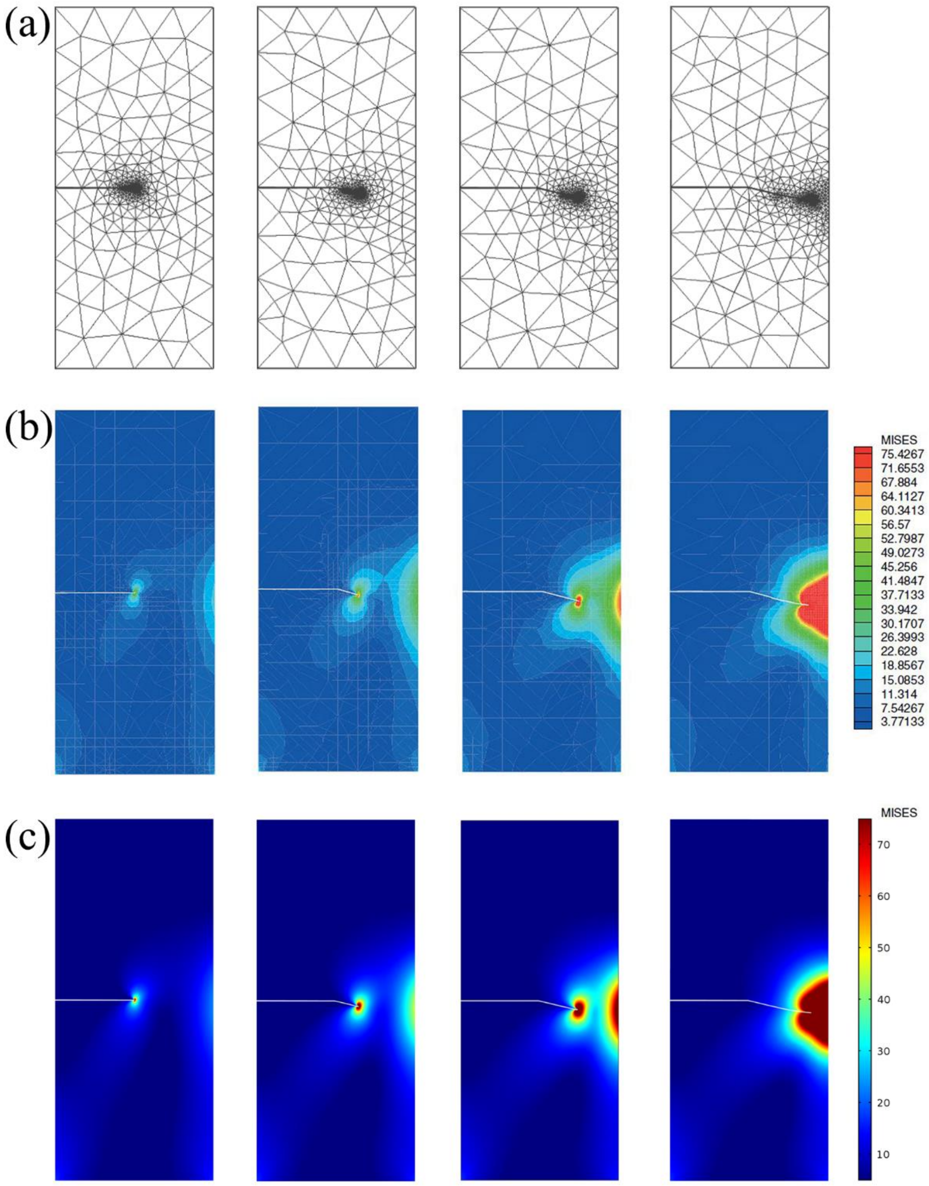

Fig. 4.25: Synoptic representation of the mesh motion during the crack propagation; (b) Von Mises stress maps for four crack propagation steps arising from[108]; (c) Von Mises stress maps for four crack propagation steps arising from the proposed model.

As shown in Fig. 4.26, an increase of the parameter $toll_\theta$ produces a loss of accuracy in the prediction of the crack tip coordinates. In detail, the relative error between the refined (C1) and (C3) configurations is equal to 0% in the initiation phase, while tending to 12%, i.e with larger accuracy, at the start of the crack propagation. However, in all the investigated cases the analyses do not show divergence or convergence problems, leading prediction of the crack path quite reasonable from an engineering point of view.

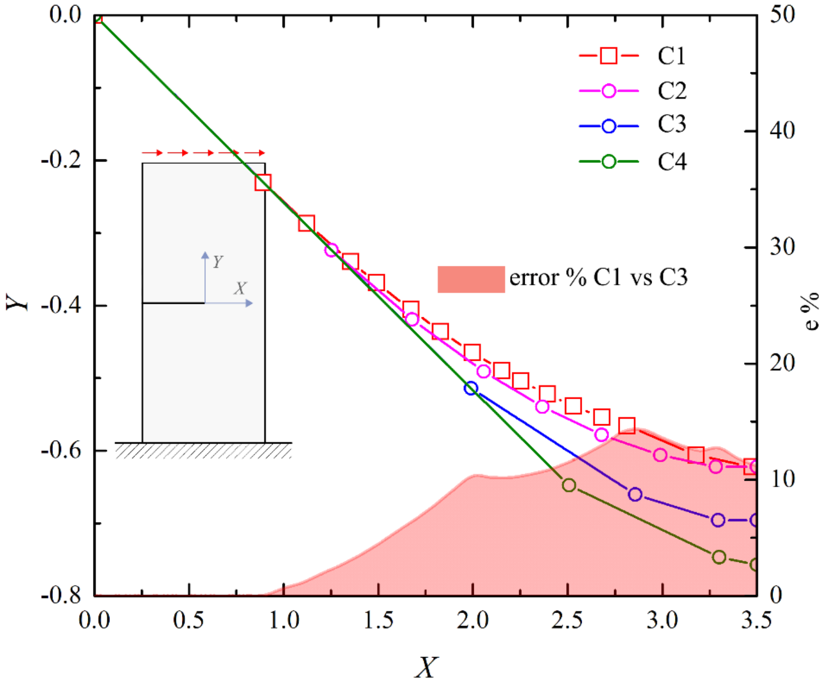

Fig. 4.26: Loading scheme Fig.5b: influence of the algorithm parameter $toll_{Q}$ *in the prediction of the crack path. The symbols on the graph represent the remeshing events. On each curve the presence of the symbol denotes a remeshing event*

In order to quantify the efficiency of the proposed model with respect to the effects produced by $toll_{\theta}$, in Fig. 4.27 a comparison in terms CPU time and number of remeshing events is proposed. For all investigated configurations, the same number of mesh elements as well as the setup required by the NL solving procedure are assumed. Three different configurations, with a different limit angle tolerance value, are assumed. The configuration C1 is based on a small limit value of angle tolerance, i.e. $toll_{\theta} = 1^{\circ}$, which, although it provides an accurate description of the crack path, it makes the use of a large number of mesh variations, leading to a notable increase of computational complexities and CPU time. In addition, C2, C3 and C4 configurations are based on larger values of limit angle tolerance, ranging from 2 to 7.5 degree. These cases provide less accuracy in the prediction of the crack growth, but a lower computational time is expected. Moreover, the tests were performed on a Xeon processor running on Windows 10 system. The analyses, reported in Fig. 4.27, in terms of CPU time, number of remeshing events and angle tolerance, show how the computational costs measured in terms of CPU time could be strongly reduced with respect to the C1 configuration ensuring good accuracy in the prediction of the crack path. This aspect connected with the possibility to perform a smart mesh discretization in the process zone and remaining part of the structure can be utilized, as shown in the next subsection, to produce additional benefits to reduce the computational costs of the analyses.

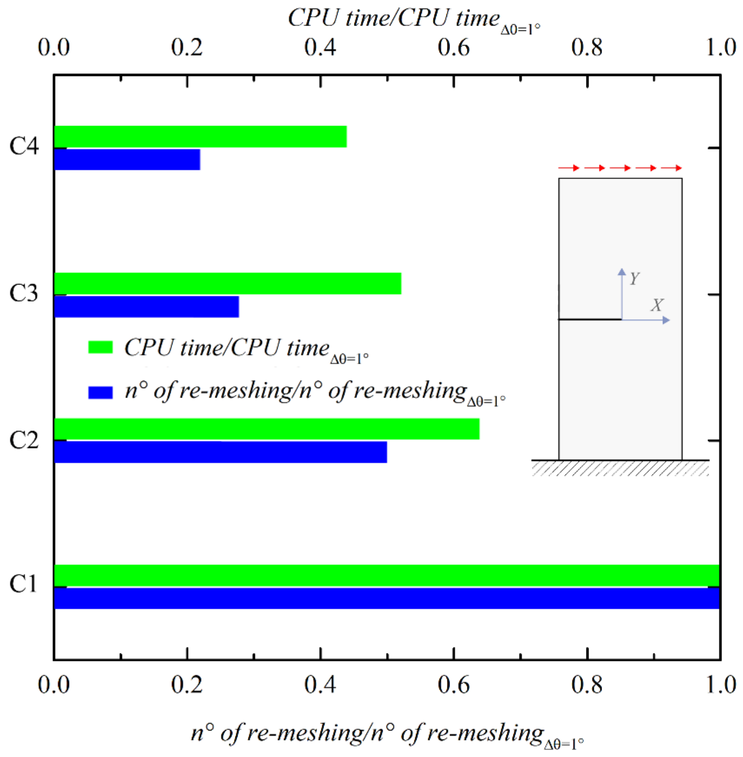

Fig. 4.27: Loading scheme B: comparisons in term CPU time and number of remeshing for the numerical simulation performed by using different idealized value of toll$_Q$ *(C1, C2, C3 and C4).*

4.2.4.2 Three-point-bending in a PMMA beam

The second case study focuses on a continuum, either provided or not, with multiple holes and different initial crack lengths and locations. A PMMA beam is therefore investigated under a three-point bending loading scheme, with the aim of testing the numerical procedure on a more complex mechanical problem. This case study has been experimentally studied by [112] and the results were subsequently analysed by several authors within the bounds of different numerical methods, such as XFEM [113], phase field method [114] e.g.

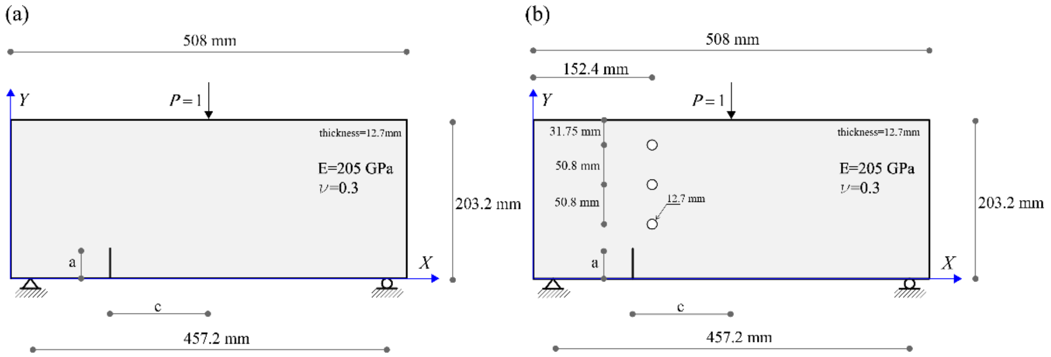

Fig. 4.28: Geometrical and loading configuration of the PMMA beam: (a) without holes, (b) with holes

As shown in Fig. 4.28, the considered beam has a clear span of 457.2mm, a width of 203.2mm and thickness of t = 12.7mm. For the first configuration (P_1, Fig. 12a, the initial crack a has a length equal to 38.1 mm and it is located at a distance c=127 mm from the mid-span of the beam. The second configuration (P_2) differs from the first one in terms of both initial crack length (a =25.4mm) and initial crack location (c=152.4mm). To concern the mechanical properties, they are taken as elastic modulus E=205GPa and Poisson's ratio ν = 0.3. Both configurations have been additionally analysed considering a set of three holes vertically aligned and located at a distance of 152.4 mm from the mid-span of the beam. According to experimental data provided from [112], the loading schemes and the elastic properties of the material are shown in Fig. 4.28, whereas a summary of the geometrical configurations considered is reported in the Tab. 4.4. Similarly to the previous analysed cases, plane stress 6 node elements featuring Lagrange quadratic interpolation functions are utilized to discretize the structure. It is worth noting that a refined mesh discretization is adopted just in the region adjoining the crack tip front $\left(S_F\right)$,whereas in the complementary part of the structure a relatively coarse mesh discretization is introduced. In particular, the initial mesh presents a number of elements equal to 149 and 911 for the S_F and remaining domains, respectively. Fig. 4.29, Fig. 4.30, Fig. 4.31 and Fig. 4.32 illustrate the crack trajectory numerically determined by means of the proposed algorithm and assuming fixed value for the crack advance and tolerance limit value equal to $\dot{\delta}_F = 0.1\,\text{mm}$ and $toll_\theta = 2^\circ$, respectively.

In Fig. 4.29 and Fig. 4.30, the results obtained assuming, respectively, the P_1 and P_1-holes configurations are compared with existing experimental [112] and numerical [113] data. In P1-holes configuration, the first hole attracts the crack trajectory due to the vicinity of initial crack. However, the crack is able to bypasses it whilst stopping his run in the middle hole.

In Fig. 4.31 and Fig. 4.32 the results of similar analyses obtained assuming, respectively, the P2 and P2-holes configurations are compared with existing experimental [112] and numerical [113] data. As shown, the proposed model is again able to reproduce accurately the crack paths.

Configuration	$c[\mathrm{mm}]$	$a[\mathrm{mm}]$
P1	127	38.1
P1-holes	127	38.1
P2	152.4	25.4
P2-holes	152.4	25.4

Tab. 4.4: PMMA Beam simulated configurations.

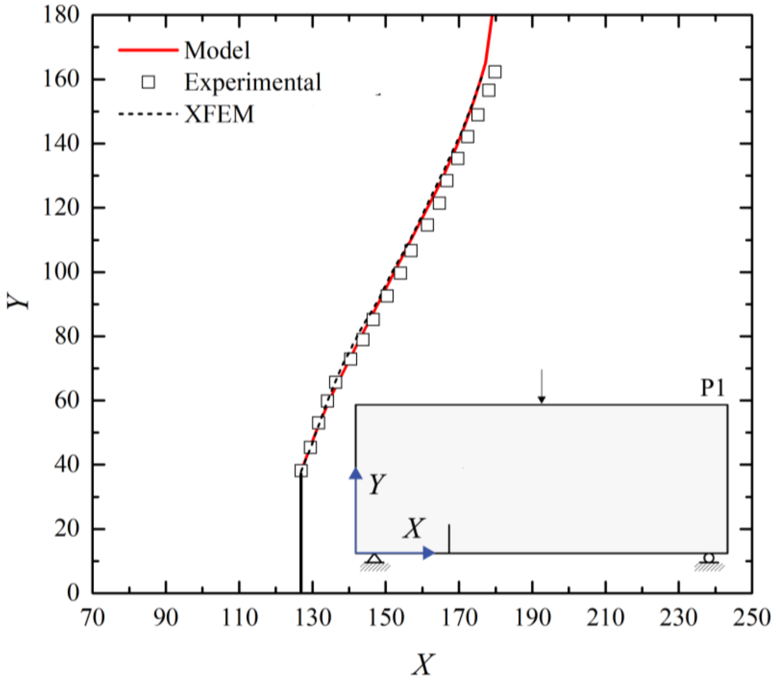

Fig. 4.29: P1 configuration: Predicted crack path, comparisons between Experimental [114] and Numerical [113] data.

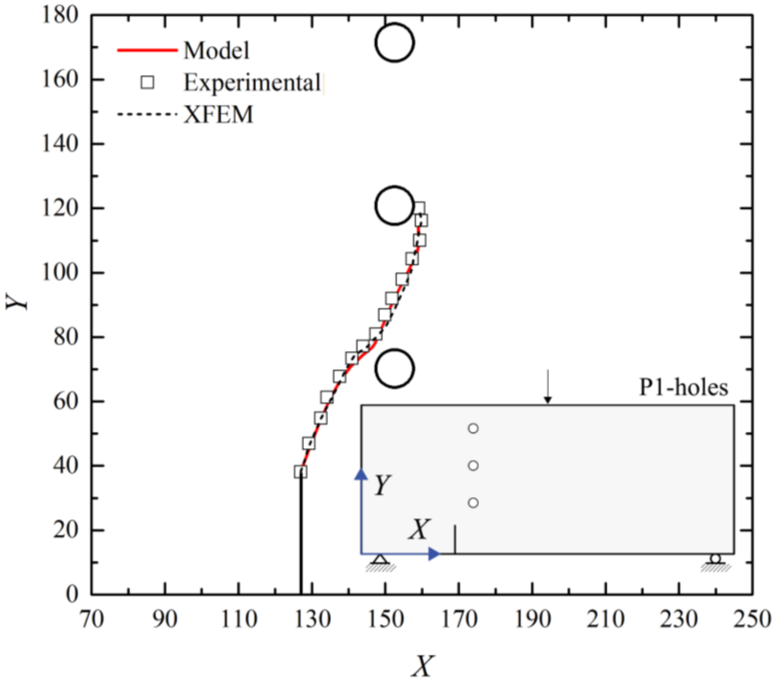

Fig. 4.30: P1-holes configuration: Predicted crack path, comparisons between experimental [114] and numerical [113] data.

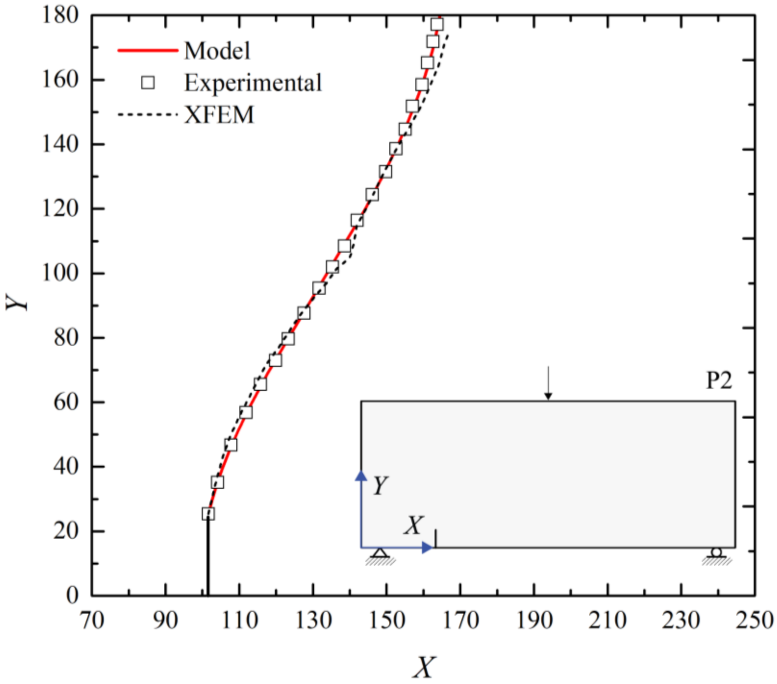

Fig. 4.31: P2 configuration: predicted crack path, comparisons between experimental [114] and numerical [113] data.

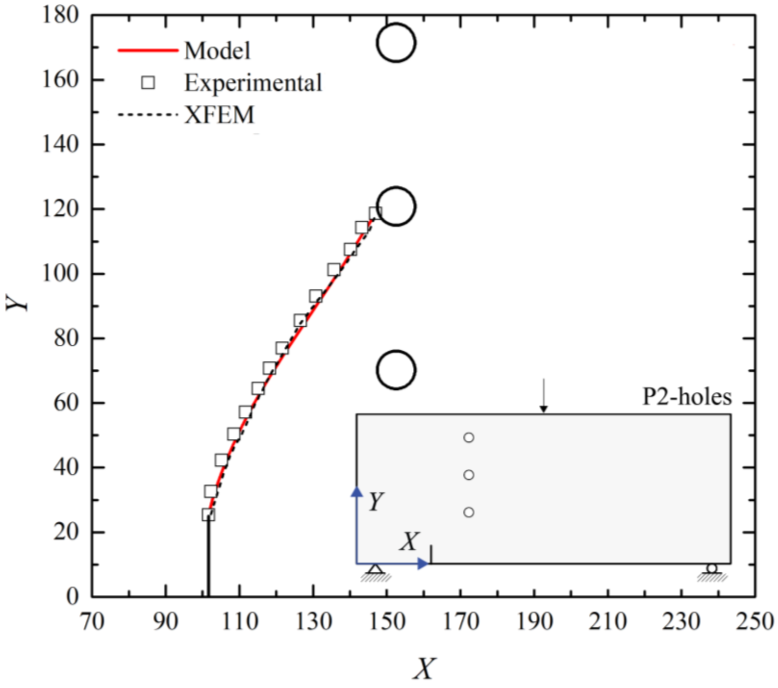

Fig. 4.32: P2-holes configuration: predicted crack path, comparisons between experimental [114] and numerical [113] data.

With particular reference to the simulation performed on the P2-holes configuration, the crack path propagates directly towards the second hole, ending its run in this location. It is worth noting that P_1-holes configuration is affected by larger computational complexities than the case by P2-holes configuration, since it presents a considerable increase in the shear stress intensity factor K_2 around the holes and a more complex crack pattern.

Finally, in order to verify the influence of the initial mesh discretization on the accuracy of the solution, a parametric analysis is performed. To this end, comparisons expressed in terms of crack paths and ERR mixed mode ratio J_2 / J_1 as a function of the crack length occurred are computed by assuming three different mesh sizes. It is worth noting that the numeric model presents different mesh discretizations of the geometry with lower characteristic length in the crack tip region and a larger one with transition mesh in the remaining part. The relative discretization in terms of total and relative number of DOF involved in both region is discussed. The investigation is performed on the P2 configuration with respect to the following mesh discretizations

- enrichment at the crack tip region $\left(S_F\right)$ with element mesh length equal to $\Delta_M / R = 1/3$ and transition mesh in the remaining part of the structure with maximum length equal to $\Delta_M / R = 40/1$, involving in total 6342 DOFs (M1);
- enrichment at the crack tip region $\left(S_F\right)$ with element mesh length equal to $\Delta_M / R = 1/5$ and transition mesh in the remaining part of the structure with maximum length equal to $\Delta_M / R = 20/1$, involving in total 12548 DOFs (M2);
- enrichment at the crack tip region $\left(S_F\right)$ with element mesh length equal to $\Delta_M / R = 1/8$ and transition mesh in the remaining part of the structure with maximum length equal to $\Delta_M / R = 7/1$, involving in total 26746 DOFs (M3);

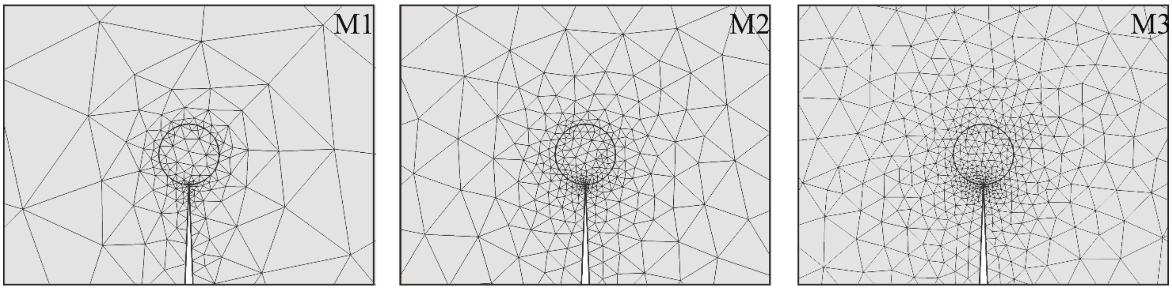

Fig. 4.33: Mesh discretization detail around the crack tip for M1, M2 and M3 configurations.

It is worth noting that M_1 discretization is based on a low number of mesh elements, since mesh enrichment is introduced only in the region adjoining the crack tip front, in which accuracy is required to predict fracture mechanics variable. In the remaining region, it is only necessary to reproduce the mesh motion and thus a low element order is required. Fig. 4.33 illustrates a zoom view of the detail around the crack tip for each mesh discretization adopted in the analysis.

In Fig. 4.34comparisons in terms of crack tip coordinates for each mesh discretization are reported. The crack paths are almost perfectly overlapped, denoting a low dependence of the results from the mesh refinement. This result is also confirmed by the comparisons in terms of J_2 / J_1 as a function of the crack length occurred. In particular, Fig. 4.35 shows that the use of a relatively coarse mesh discretization does not produce significant loss of accuracy or divergence phenomena and, thus, it is able to identify with good accuracy ERR mixed mode ratio. This is confirmed also by the results reported in Fig. 4.36, in which a comparison in terms of CPU time and number of mesh elements introduced at the crack tip and remaining region is proposed. In particular, the results show that a smart mesh discretization, i.e. M1, can be useful to reduce the computational costs, since the crack path prediction does not show a high dependency from the degree of refinement of the discretization. Moreover, the results show that the use of a coarse or a relatively coarse mesh discretization, i.e. M1 or M2, allows to reduce the computational cost of the analysis by 67% or 48% with respect to M3 configuration, respectively. Finally, the evolution of the mesh motion is presented in Fig. 4.37 for M1 configuration, in which mesh discretizations before and after remeshing procedure are reported for several steps of the analysis. The results show that, according to the ALE methodology, the mesh movements of the crack tip region is enforced rigidly, ensuring the required accuracy in the prediction of the fracture variables. The elements of the remaining regions are stretched due to the rezoning or regularization requirements, leading to a consistent transition mesh discretization in the structure and a strong reduction of the computational complexity of the model.

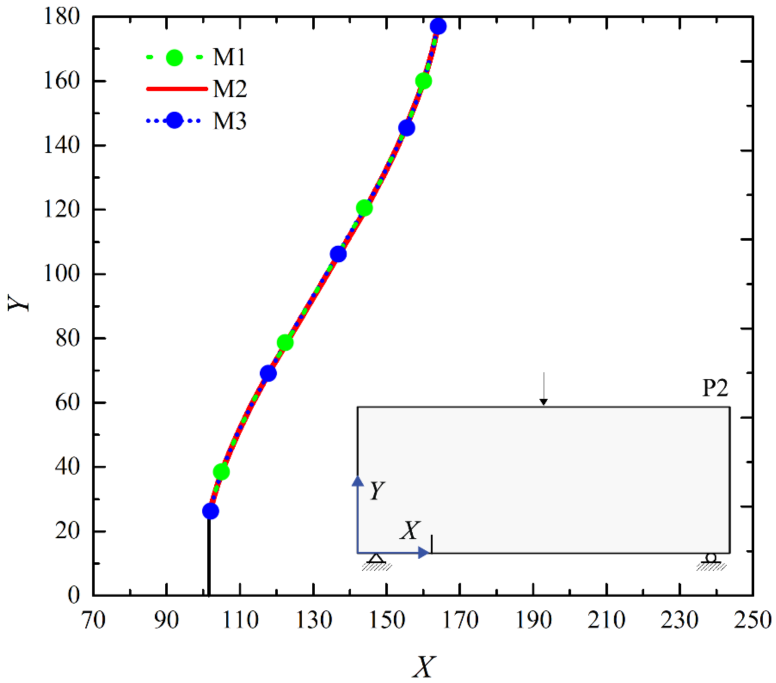

Fig. 4.34: P2 configuration: influence of the mesh discretization on the prediction of the crack path.

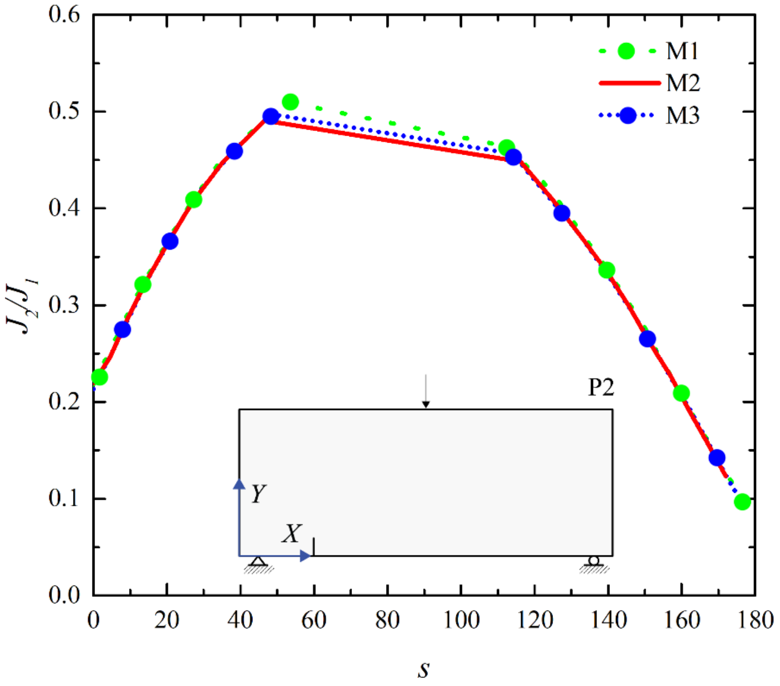

Fig. 4.35: configuration: influence of the mesh discretization on the prediction of the ERR mode ratio

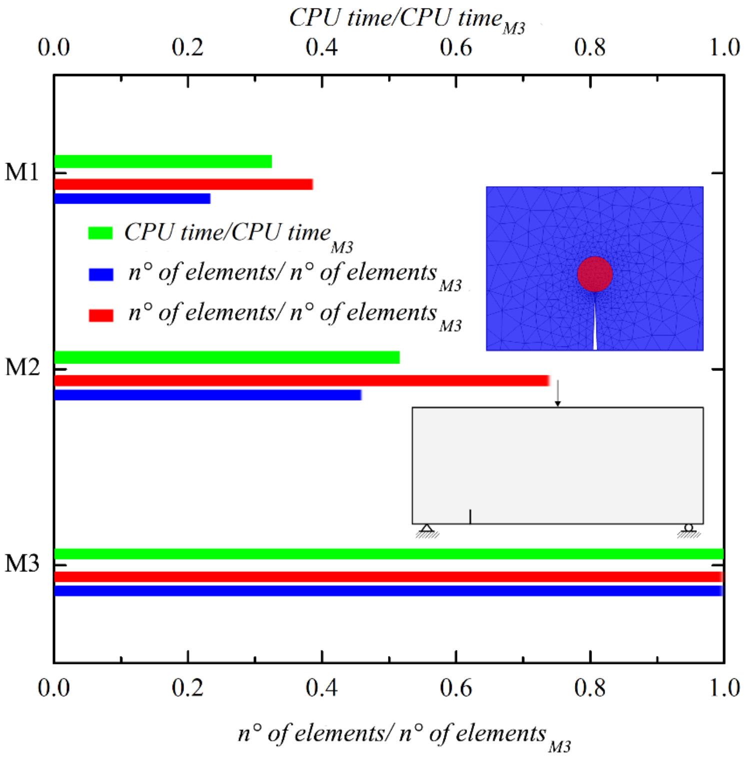

Fig. 4.36: P2 configuration: comparisons in term CPU time and number of elements for the numerical simulation performed by using different mesh discretizations (M1, M2 and M3).

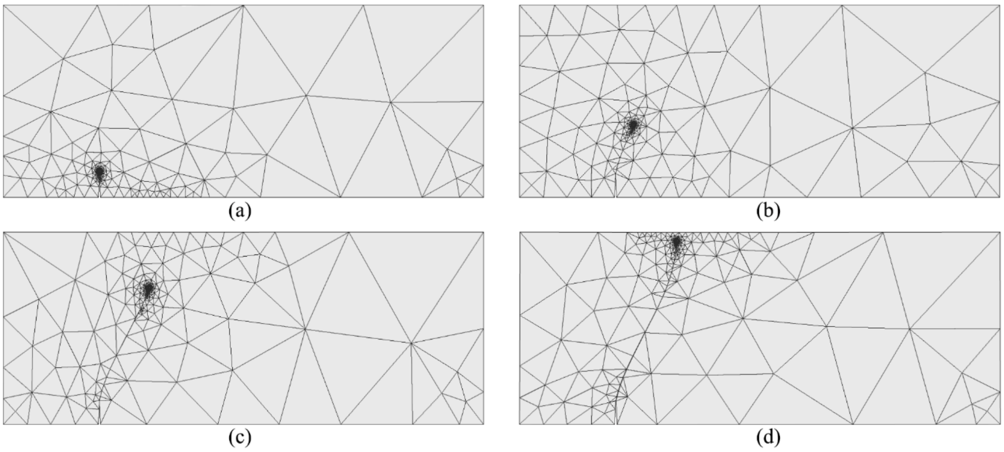
(a) (b) (c) (d)

Fig. 4.37: M1 configuration: synoptic representation of the mesh motion during the crack propagation.

4.3 Experimental Campaign

In this section, the fracture toughness of a commercially available semi-rigid PVC foam under mode I is evaluated by three-point bending tests on Semi-Circular Bending (SCB) specimens. Mode II and Mixed Mode are analysed on Asymmetric Semi-Circular Bend (ASCB) specimens. Ayatollahi et al. [115] proved that the ASCB loading scheme is able to generate all range of mixed fracture modes in fragile construction materials, including a pure mode II fracture condition. The method was used by Marsavina et al. [72, 73] for PVC foams.

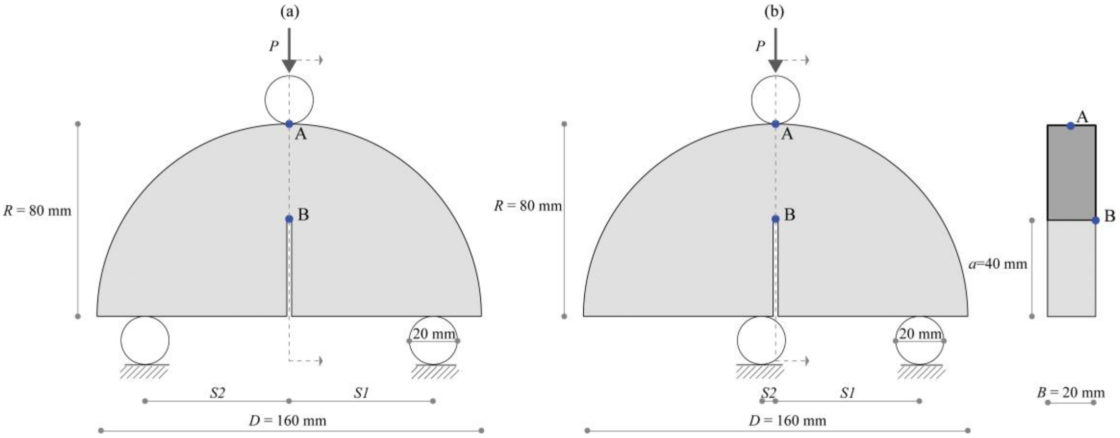

Fig. 4.38: Experimental Setup: (a) SCB specimen; (b) ASCB specimen.

All specimens were cut from 20 mm Divinycell H100, H130 and H200 panels in the two main directions using a Denford CNC router with a 0.1 mm resolution equipped with a 3 mm drill bit (Fig. 4.39). Although the numerical cutting procedure included the mid-span sample notching, the natural crack was initiated using a fresh razor blade, which was tapped to sharpen and extend the pre-notched tip to a final nominal length of 40 mm. The samples were uniformly sprayed with several coats of white paint. Subsequently a stream of black paint was applied as to obtain a random b/w speckle pattern, the ideal reference system for Digital Image Correlation (DIC) purpose [116].

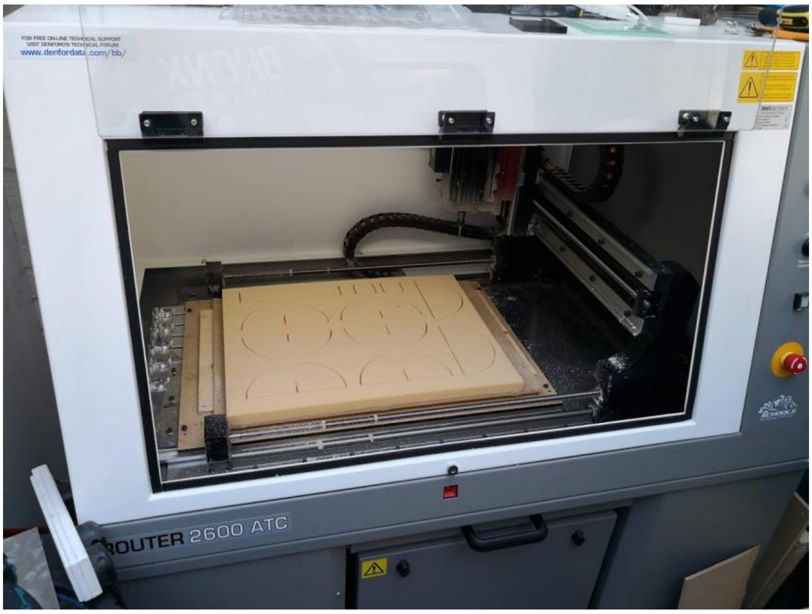

Fig. 4.39: Cutting samples by using Denford CNC router.

In order to check the density declared from the Divinycell®, the density of the foams was determined according with ASTM D 1622-08, using cubic specimens of 15x15x15 mm, an electronic balance Sartorius LA230S for weighting and a digital caliper for dimension determination.

Fig. 4.38 shows the load conditions taken in consideration. Three samples were tested according to each scheme, accounting for a total of eighteen specimens for each density typology. All samples had identical geometrical properties: the radius, *R*, of the semi-circular samples was 80 mm, whereas the length of the notch, *a*, was 40 mm.

The SCB loading scheme consisted of a point load centred on the top edge of the half-disc, which was spanned at 120 mm $\left(S_1 = S_2 = 60 \text{ mm}\right)$. In the ASCB (mixed mode) loading scheme the left supports was moved to a 5.5 mm, 8 mm 12 mm, 16mm, 24mm, $\left(S_2\right)$ distance from the specimen mid span, with the second supports remaining at a 60 mm$\left(S_1\right)$ distance from midspan.

All tests were performed in displacement control, at 2 mm/min rate. Load and displacement data were continuously recorded using the testing machine built-in sensors and data acquisition system (Fig. 4.40). Additionally, fixed focal lens camera shots were taken every 5 second to digitally monitor the specimen change of configuration under the applied loads.

Fig. 4.40: Experimental Setup: Load machine, digital camera and high speed led lights.

Fig. 4.41 and Fig. 4.42 show the average force vs mid-span vertical displacement relations, exhibited by the SCB $\left(S_2 = 5.5\ \text{mm}\right)$ and ASCB $\left(S_1 = S_2 = 60\ \text{mm}\right)$ specimens, respectively, as well as the ε_{xx} strain maps retrieved by means of the DIC processing referred to H100.

The black curves refer to the specimen displacement measured at the top point A, using the machine built-in transducer. These values are affected by the loading-pin penetration, as evidenced by the heavy non-linear behaviour of the curve. An additional measure of the experimental displacement at the crack mouth (point B) was retrieved from the correlation of the digital images collected, each corresponding to a known load step. The DIC processing was performed using the freeware Matlab script Ncorr, developed by Blaber et al. [117]. The red curve obtained in this manner is a more realistic representation of the flexural deflection of the specimen, being only affected by minor local compressions occurring at the specimen supporting pins.

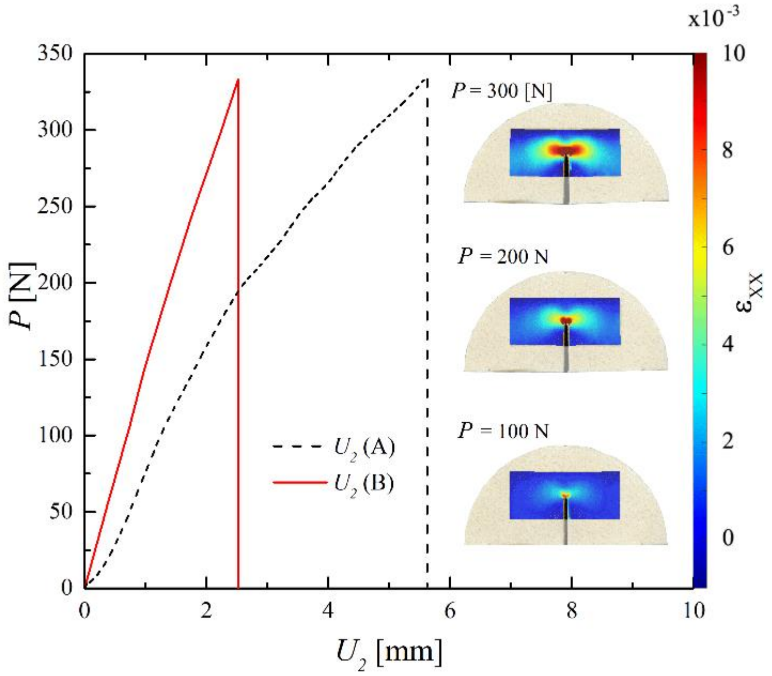

Fig. 4.41: Load – midspan vertical displacement relationship and DIC strain maps: (a) SCB specimen.

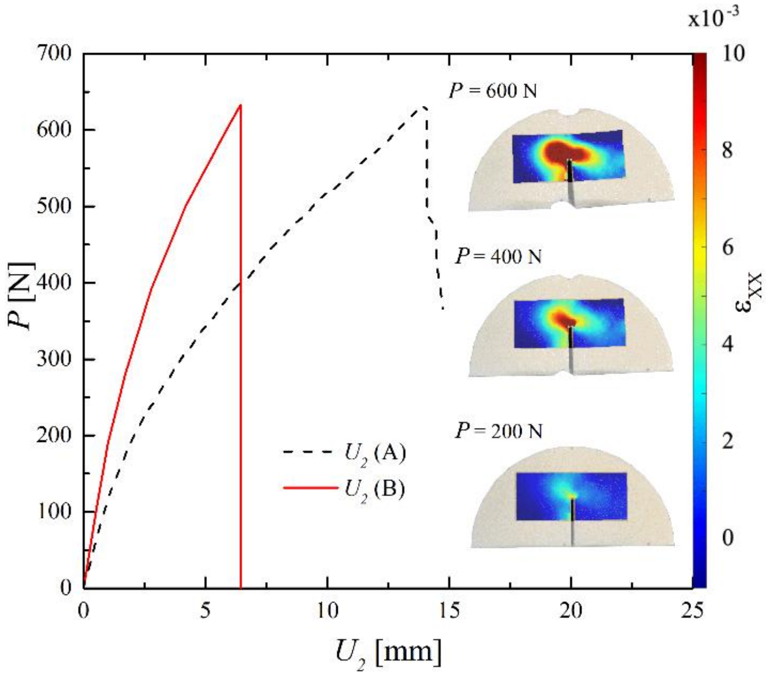

Fig. 4.42: Load – midspan vertical displacement relationship and DIC strain maps: ASCB specimen (S_2=5.5 mm) .

The average values of maximum forces detected in the experimental tests, as detailed in Tab. 4.5, were employed for the calculation of the Stress Intensity Factors (SIFs).

The SIFs for mode I, K_{1c}, and mode II K_{2c}, were computed according to the following expression, proposed by Ayatollah et al. [115]:

$$K_{ic} = \frac{P_{\max}}{2Rt}\sqrt{\pi a_i}Y_i\left(a/R, S_1/R, S_2/R\right), \quad i = 1,2 \tag{28}$$

where $P_{\max}$ is the average value of the maximum load experimentally measured either on SCB or ASCB specimens, and the functions $Y_i\left(a/R, S_1/R, S_2/R\right)$ are given by Marsavina et al. [72, 73]:

$$\begin{aligned} &Y_1\left(S_2/R\right) = 6.235\left(S_2/R\right)^3 - 15.069\left(S_2/R\right)^2 + 17.229\left(S_2/R\right) - 1.062 \\ &Y_2\left(S_2/R\right) = 1.884\left(S_2/R\right)^5 - 7.309\left(S_2/R\right)^4 + 5.037\left(S_2/R\right)^3 + 2.77\left(S_2/R\right)^2 - 5.075\left(S_2/R\right) + 1.983 \end{aligned} \tag{29}$$

Computed values of SIFs with reference to the two set of tests are listed in Tab. 4.5.

Core-Divinycell H100	K_{1c} [MPa m$^{0.5}$]	K_{2c} [MPa m$^{0.5}$]	P^1_{max} [N]	P^2_{max} [N]
	0.222±0.001	0.116±0.002	334±1	628±5
Core-Divinycell H130	K_{1c} [MPa m$^{0.5}$]	K_{2c} [MPa m$^{0.5}$]	P^1_{max} [N]	P^2_{max} [N]
	0.303±0.001	0.177±0.005	456±6	970±3
Core-Divinycell H200	K_{1c} [MPa m$^{0.5}$]	K_{2c} [MPa m$^{0.5}$]	P^1_{max} [N]	P^2_{max} [N]
	0.599±0.004	0.337±0.002	901±5	1847±5

Tab. 4.5: Experimental results in terms SIFs and maximum load reached.

4.3.1 Preliminary results

In this set of numerical results aims to validate the capability of model to describe the crack propagation in 2D solids. With this purpose, a sandwich structure fixed at bottom skin with an initial horizontal crack is taken into consideration as reference case study (Fig. 4.43a).

Although the proposed model is able to describe both the skin/core interface delamination and the crack propagation in the core, the aim of these simulations is specifically to describe the crack path occurred in the core of the sandwich structures and verify its effects on the interfacial traction forces.

The reference specimen has a 150 mm length and width equal to 35 mm. The core and skin thickness are 75 mm and 2 mm, respectively. The initial crack has a length to 25 mm and it is located at the core mid-depth.

Two different loading conditions are investigated:

- a uniformly distributed opening force applied along the upper skin of the panel (Fig. 4.43a).
- a point opening force applied at the cracked edge of the panel (Fig. 4.43b)

The idealized sandwich structure presents glass/polyester skins and a Divinycell H100 foam core, therefore the material and interface properties are the same as the ones listed in Tab. 4.6 with reference to the MMB test. The fracture parameters and experimentally determined Divinycell H100 foams, as detailed in the experimental section of this Chapter, are employed in this analysis.

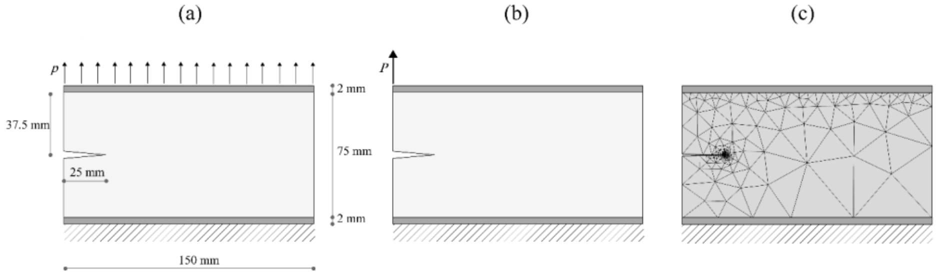

Fig. 4.43: (a) uniformly distributed opening force applied along the upper skin of the panel; (b) point opening force applied at the cracked edge of the panel (b); detail of the mesh discretization in the core (c).

Face-sheet glass/polyester	$E_{11}^{s}\left[\text{GPa}\right]$	$G_{12}^{s}\left[\text{GPa}\right]$	ν^{s}	$\rho^{s}\left[\text{kg m}^{-1}\right]$
	16.4	2.7	0.17	1500
Core-Divinycell H100	$E_{1}^{s}\left[\text{GPa}\right]$	$G_{12}^{s}\left[\text{GPa}\right]$	ν^{s}	$\rho^{s}\left[\text{kg m}^{-1}\right]$
	0.135	0.035	0.32	100
Interface properties	$G_{C}\left[\text{N mm}^{-1}\right]$	$\Delta_{0}\left[\text{mm}\right]$		
	0.800	0.12		

Tab. 4.6: Mechanical and interface properties of the structures reported in Fig. 4.43.

The 2D model involves a discretization of each face sheet by means of shear deformable beam elements, whereas the foam core is modelled by plane stress triangular elements. Both skin and core elements features cubic interpolation functions and a linear elastic constitutive behaviour of the materials. ALE equations are introduced at each skin/core interfaces, in view of possible debonding phenomena, and in the core, to predict the propagation of the pre-existing crack length. Linear interpolation functions are assumed for the ALE variables. The numerical discretization used for the face sheet is assumed to be generally uniform with an element length ΔD equal to 5mm. A coarse discretization is adopted at the interface, in absence of any pre-existing interfacial defects. With reference to the core modelling, a high number of computational points is condensed around the crack tip region, whereas a coarse discretization is adopted in the remaining domain (Fig. 4.43a). The analysis is developed in displacement control mode, with the aim to ensure a stable crack propagation. Fig. 4.44 and Fig. 4.45 show the load / opening displacement curves numerically obtained with reference to both the schemes here considered. As shown, the constitutive behaviour shown is initially linear and stable. Once the crack function criterion is satisfied, the curves show a sudden descending trend. A clearly different trend can be observed in the two descending branches: the point loading causes a snap-back, a phenomenon that is not evidenced when a uniformly distributed opening load is applied to the structure.In Fig. 4.46 and Fig. 4.47, the Von Mises stress maps at four subsequent load steps are shown together with crack propagation pattern for both loading configurations. Although in both cases a mixed mode fracture arises, the crack propagation paths exhibited by the two specimens are visibly distinguishable. Whereas the point load activates a mode II dominated fracture process, the distributed load tends to cause a mode I dominated fracture mode.

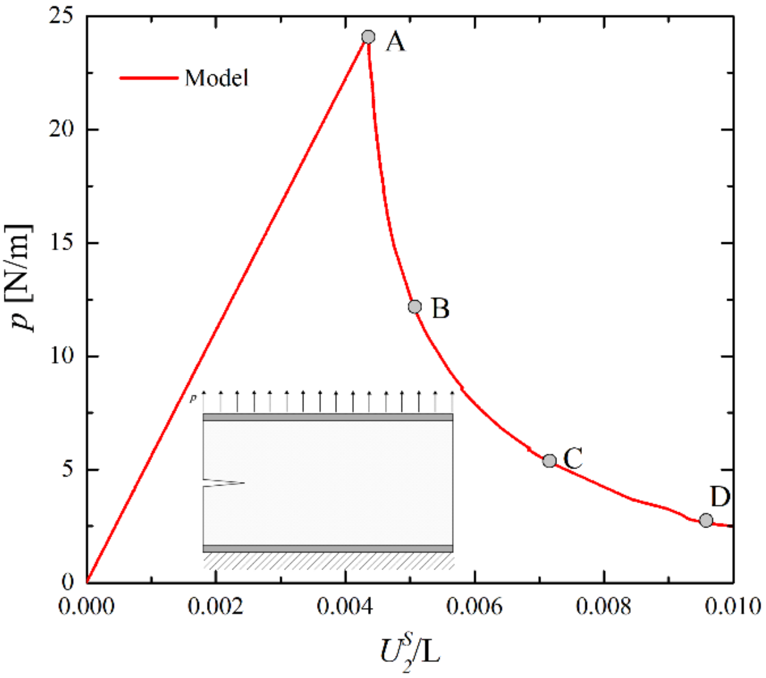

Fig. 4.44: Load-displacement response: uniformly distributed opening force.

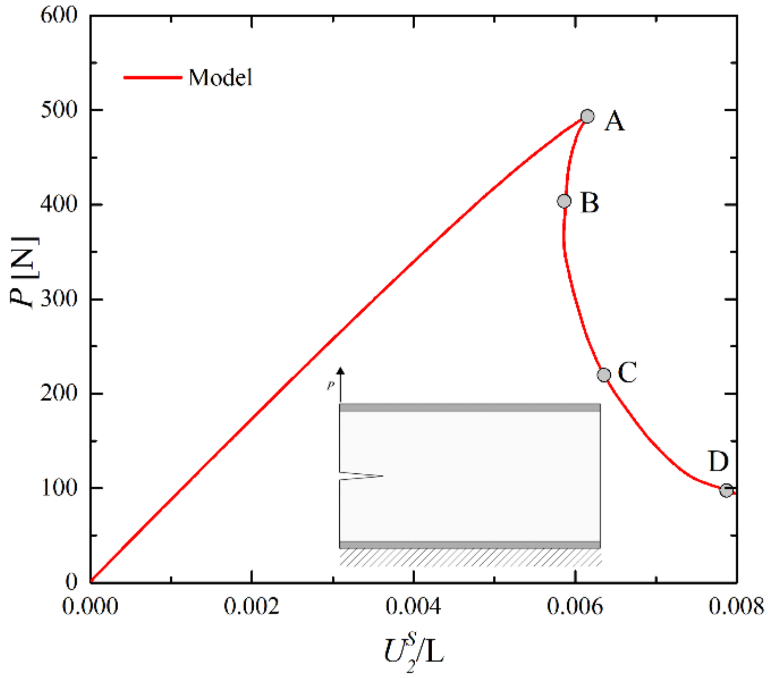

Fig. 4.45: Load-displacement response: point opening force.

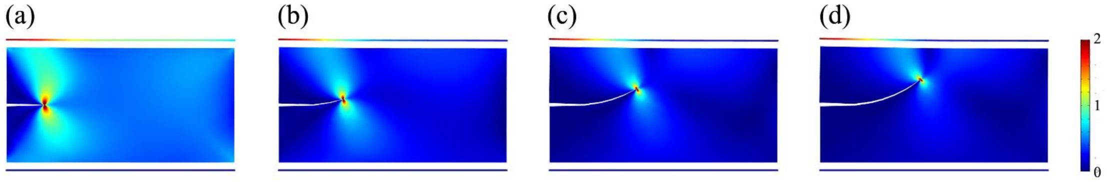

Fig. 4.46: Uniformly distributed opening force: Von Mises contour plots and crack evolution for different loading steps.

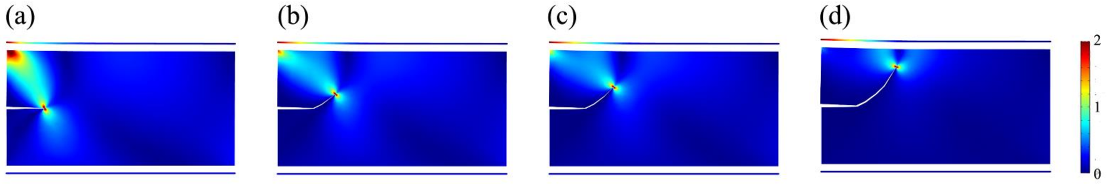

Fig. 4.47: Point opening force: Von Mises contour plots and crack evolution for different loading steps.

In sandwich structures, loads are typically applied to the face-sheets and these are transmitted to the core by the adhesive interface. The core behaviour and its sensitivity to crack propagation is, therefore, strongly affected by the interfacial stress, which are, in turn, related to the external loads, the materials stiffness's, and the cohesive law.

In this view, the interfacial traction forces detected at the upper skin-to-core interface are shown in Fig. 4.48 and Fig. 4.49 for both load configurations analysed.

Fig. 4.48a depicts the distribution of the interfacial forces corresponding to the peak load of the linear elastic branch (A) in the distributed load case. The distribution of stresses is quite uniform, which suggest the cohesive interface is not threatened by any possible debonding phenomenon. The propagation of the crack in the core is able to slightly affect the distribution of the interfacial traction forces (Fig. 4.48 (b), (c), and (d)), whilst it does not substantially modify the quality of interface response.

A similar analysis is illustrated in Fig. 4.49(a-d) with reference to the point opening force scheme. As shown in Fig. 4.49 (a), high values of the interfacial traction arises at the sandwich panel edge, in correspondence of the applied load. The onset condition could have been easily activated at the interface region but it is prevented, in this case, by the crack propagation in the core. This phenomenon tremendously affects the interfacial stresses, whose peak tends to move congruently with the crack tip position. However, a more even distribution of stresses suggests that an interface debonding is unluckily to occur at this stage.

The results show how the interfacial stresses distribution can affect the crack propagation in the core and highlights the usefulness of a numerical model able to couple the two effects in an effective manner.

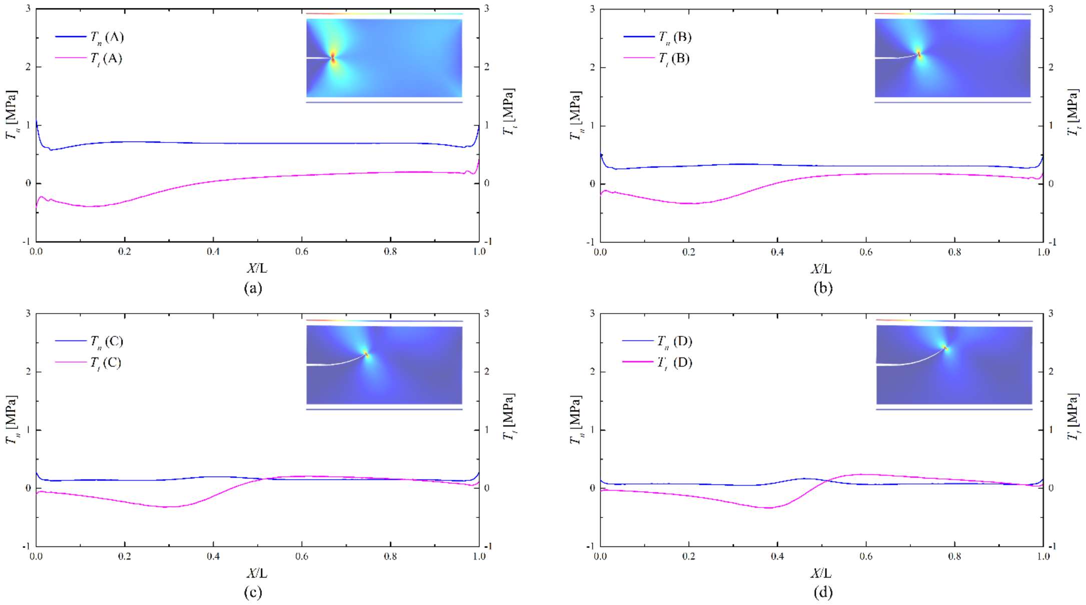

Fig. 4.48: Uniformly distributed opening force: interfacial stresses across the upper cohesive interfaces at different value of core's crack tip positions.

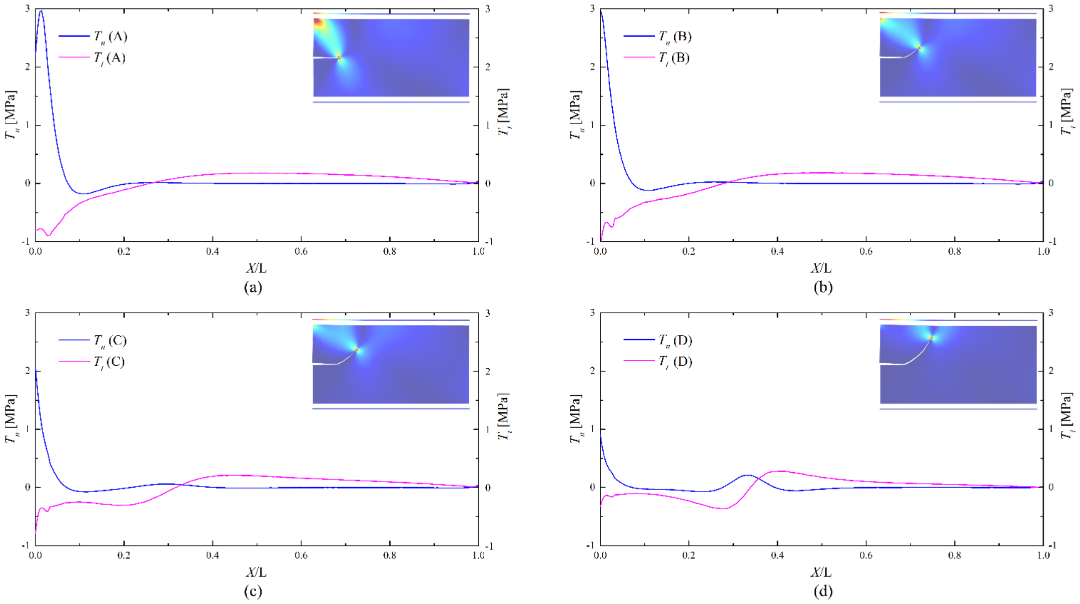

(a) (b) (c) (d)

Fig. 4.49: point opening force: interfacial stresses across the upper cohesive interfaces at different value of core's crack tip positions.

Chapter 5 **Conclusions**

In this chapter the conclusions and the future works are discussed. Some critical considerations about the features of the developed numerical models are analysed.

5.1 Conclusions

At first, the aim of the presented thesis was the investigation of the interface crack propagation phenomena in multilayered structures simulated by using shear deformable beam elements. The theoretical formulation was based on Arbitrary Lagrangian and Eulerian (ALE) methodology and cohesive interface elements, in which weak based moving connections are implemented by using a finite element formulation. In this framework, only the nodes of the computational mesh of the interface region are moved on the basis of the predicted fracture variables, reducing mesh distortions by using continuous rezoning procedures.

The following conclusions can be drawn in respect of the obtained numerical results:

- ALE interface formulation are introduced with the purpose to simulate the evolution of crack growth phenomena, avoiding to modify the governing equations of the structural problem.
- Despite of existing formulations, available in the literature, this model gives the possibility to introduce nonlinear interface elements in a small region containing the crack tip front, whereas in the remaining one, linear constrain equations are introduced to simulate perfect adhesion.
- The computational efforts and numerical complexities arising from classical debonding approaches were avoided.
- The proposed model is quite general to be implemented in several existing FE software, since it leaves basically unaltered the governing equations of the structural problem.
- In order to validate the proposed approach several comparisons are proposed with existing formulations, for cases involving single or multiple delaminations.
- The robustness of the solution is verified by means of sensitivity analyses in terms of mesh characteristics and parameters involved in the numerical model.
- The parametric study in dynamics has shown how debonding phenomena are much influenced by inertial forces and loading rates, since instability phenomena, jumps and amplifications in both resistance curve and crack tip speeds are observed.

Along the way the proposed model has been generalized with the purpose to simulate also onset and coalescence which typically affect layered structures. The proposed strategy is based on two different stages solved simultaneously, which are devoted to identify onset crack position along the interfaces and the corresponding evolution.

The following definitive conclusions are drawn based on numerical simulations:

- The numerical approach is quite general since it does not depend from TSL or the structural formulation and can be easily implemented in conventional FE software.
- The validation procedure is developed by means of comparisons in the framework of both static and dynamic analyses, with existing results arising from literature.
- The layered structures involving crack onset, growth and coalescence phenomena are proposed and discussed to verify the applicability of the proposed approach to complex debonding configurations.
- The results denote how debonding phenomena are quite influence by the presence of internal material discontinuities, which produce strong oscillations in the loading curve, amplifications of the total kinetic energy and large crack tip speeds.

Finally, the research project has been focused on the study of the sandwich structure failure modes. From physical and mathematical viewpoints, two main issues are demanding a detailed understanding of the mechanical behaviour of sandwich panels: the propagation of internal macro-cracks in the core and the delamination at skin/core interfaces. To concern the delamination between skin and core, the previous numerical strategy, already used in the framework of composite laminate, was generalized simply by modifying the relative displacement between skin (shear deformable beam) and core (2D plane stress formulation). Moreover, crack growth in the core has been described by a 2D moving mesh approach, in which a proper fracture criterion and mesh refitting procedure were introduced to predict crack tip front direction and displacement. Based on the results obtained, the following conclusions can be drawn:

- The results show the capabilities of the proposed model to reproduce correctly the behavior in both static and dynamic frameworks.
- The parametric study denotes how debonding phenomena are quite influenced by the presence of internal material discontinuities, which produce strong oscillations and instabilities in the resistance curve and high speeds during the crack evolution.

- This study could be very useful for developing modeling strategies to understand debonding phenomena in sandwich composites subject to low-velocity impact.
- The proposed model is able to simulate both micro-cracks at core and skin interfaces, which can proceed independently during the crack advance.
- The use of proper regularization or rezoning methods, which adapt the mesh motion reducing mesh distortions during the transition procedure and ensuring consistency in the mesh topology.
- The model is validated with several comparisons with numerical and experimental data, in which complex structures also in presence of holes/inclusions are considered.

References

1. de Borst, R., et al., *Discrete vs smeared crack models for concrete fracture: Bridging the gap.* International Journal for Numerical and Analytical Methods in Geomechanics, 2004. **28**(7-8): p. 583-607.
2. Camacho, G.T. and M. Ortiz, *Computational modelling of impact damage in brittle materials.* International Journal of Solids and Structures, 1996. **33**(20-22): p. 2899-2938.
3. Zhang, C. and A. Savaidis, *Time-domain BEM for dynamic crack analysis.* Mathematics and Computers in Simulation, 1999. **50**(1-4): p. 351-362.
4. Mobasher, M.E. and H. Waisman, *Adaptive modeling of damage growth using a coupled FEM/BEM approach.* International Journal for Numerical Methods in Engineering, 2016. **105**(8): p. 599-619.
5. Mantič, V. and F. París, *Relation between SIF and ERR based measures of fracture mode mixity in interface cracks.* International Journal of Fracture, 2004. **130**(2): p. 557-569.
6. Leguillon, D. and K. Siruguet, *Finite fracture mechanics - Application to the onset of a crack at a bimaterial corner.* Iutam Symposium on Analytical and Computational Fracture Mechanics of Non-Homogeneous Materials, Proceedings, 2002. **97**: p. 11-18.
7. Martin, E. and D. Leguillon, *A strain energy density criterion for the initiation of edge debonding.* Theoretical and Applied Fracture Mechanics, 2015. **79**: p. 58-61.
8. Rabinovitch, O., *Cohesive interface modeling of debonding failure in FRP strengthened beams.* Journal of Engineering Mechanics-Asce, 2008. **134**(7): p. 578-588.
9. Park, K. and G.H. Paulino, *Cohesive Zone Models: A Critical Review of Traction-Separation Relationships Across Fracture Surfaces.* Applied Mechanics Reviews, 2011. **64**(6).
10. Sørensen, B.F. and T.K. Jacobsen, *Determination of cohesive laws by the J integral approach.* Engineering Fracture Mechanics, 2003. **70**(14): p. 1841-1858.
11. Slowik, V., et al., *Computational aspects of inverse analyses for determining softening curves of concrete.* Computer Methods in Applied Mechanics and Engineering, 2006. **195**(52): p. 7223-7236.
12. Kwon, S.H., Z. Zhao, and S.P. Shah, *Effect of specimen size on fracture energy and softening curve of concrete: Part II. Inverse analysis and softening curve.* Cement and Concrete Research, 2008. **38**(8): p. 1061-1069.
13. Abanto-Bueno, J. and J. Lambros, *Experimental determination of cohesive failure properties of a photodegradable copolymer.* Experimental Mechanics, 2005. **45**(2): p. 144-152.
14. Kulkarni, M.G., P.H. Geubelle, and K. Matouš, *Multi-scale modeling of heterogeneous adhesives: Effect of particle decohesion.* Mechanics of Materials, 2009. **41**(5): p. 573-583.
15. Greco, F., et al., *An adaptive multiscale strategy for the damage analysis of masonry modeled as a composite material.* Composite Structures, 2016. **153**: p. 972-988.
16. Tvergaard, V., *Effect of fibre debonding in a whisker-reinforced metal.* Materials Science and Engineering: A, 1990. **125**(2): p. 203-213.

17. Tvergaard, V. and J.W. Hutchinson, *The influence of plasticity on mixed mode interface toughness.* Journal of the Mechanics and Physics of Solids, 1993. **41**(6): p. 1119-1135.
18. Scheider, I. and W. Brocks, *Simulation of cup–cone fracture using the cohesive model.* Engineering Fracture Mechanics, 2003. **70**(14): p. 1943-1961.
19. Ortiz, M. and A. Pandolfi, *Finite-deformation irreversible cohesive elements for three-dimensional crack-propagation analysis.* International Journal for Numerical Methods in Engineering, 1999. **44**(9): p. 1267-1282.
20. Wittmann, F.H., et al., *Fracture energy and strain softening of concrete as determined by means of compact tension specimens.* Materials and Structures, 1988. **21**(1): p. 21-32.
21. de Borst, R., J.J.C. Remmers, and A. Needleman, *Mesh-independent discrete numerical representations of cohesive-zone models.* Engineering Fracture Mechanics, 2006. **73**(2): p. 160-177.
22. Carvelli, V., et al., *Advances in damage mechanics of polymer composites.* Composites Part B-Engineering, 2014. **65**: p. 1-1.
23. Ben, S.D., et al., *The interface strength and debonding for composite structures: Review and recent developments.* Composite Structures, 2015. **129**: p. 8-26.
24. Caporale, A., et al., *Debonding of FRP in multi-span masonry arch structures via limit analysis.* Composite Structures, 2014. **108**: p. 856-865.
25. Caporale, A., R. Luciano, and L. Rosati, *Limit analysis of masonry arches with externally bonded FRP reinforcements.* Computer Methods in Applied Mechanics and Engineering, 2006. **196**(1-3): p. 247-260.
26. Cavalagli, N., V. Gusella, and L. Severini, *Lateral loads carrying capacity and minimum thickness of circular and pointed masonry arches.* International Journal of Mechanical Sciences, 2016. **115**: p. 645-656.
27. Mouritz, A.P., *Review of z-pinned composite laminates.* Composites Part A: Applied Science and Manufacturing, 2007. **38**(12): p. 2383-2397.
28. Singh, R., et al., *Experimental investigations for mechanical and metallurgical properties of friction stir welded recycled dissimilar polymer materials with metal powder reinforcement.* Composites Part B: Engineering, 2016. **103**: p. 90-97.
29. Yasaee, M., et al., *Experimental characterisation of mixed mode traction-displacement relationships for a single carbon composite Z-pin.* Composites Science and Technology, 2014. **94**: p. 123-131.
30. Dantuluri, V., et al., *Cohesive modeling of delamination in Z-pin reinforced composite laminates.* Composites Science and Technology, 2007. **67**(3-4): p. 616-631.
31. Robinson, P. and S. Das, *Mode I DCB testing of composite laminates reinforced with z-direction pins: A simple model for the investigation of data reduction strategies.* Engineering Fracture Mechanics, 2004. **71**(3): p. 345-364.
32. Yan, W.Y., H.Y. Liu, and Y.W. Mai, *Mode II delamination toughness of z-pinned laminates\\.* Composites Science and Technology, 2004. **64**(13-14): p. 1937-1945.
33. Cui, H., et al., *Mixed mode cohesive law for Z-pinned composite analyses.* Computational Materials Science, 2013. **75**: p. 60-68.
34. Allegri, G., et al., *A novel model of delamination bridging via Z-pins in composite laminates.* International Journal of Solids and Structures, 2014. **51**(19-20): p. 3314-3332.

35. Bruno, D., F. Greco, and P. Lonetti, *A fracture-ALE formulation to predict dynamic debonding in FRP strengthened concrete beams.* Composites Part B-Engineering, 2013. **46**: p. 46-60.
36. Funari, M.F., F. Greco, and P. Lonetti, *A moving interface finite element formulation for layered structures.* Composites Part B-Engineering, 2016. **96**: p. 325-337.
37. Funari, M.F., F. Greco, and P. Lonetti, *A cohesive finite element model based ALE formulation for z-pins reinforced multilayered composite beams.* Procedia Structural Integrity, 2016. **2**: p. 452-459.
38. Funari, M.F., F. Greco, and P. Lonetti, *A coupled ALE-Cohesive formulation for layered structural systems.* Procedia Structural Integrity, 2017. **3**: p. 362–369.
39. Feo, L., et al., *Mixed-mode fracture in lightweight aggregate concrete by using a moving mesh approach within a multiscale framework.* Composite Structures, 2015. **123**: p. 88-97.
40. Funari, M.F., F. Greco, and P. Lonetti, *Dynamic debonding in layered structures: a coupled ALE-cohesive approach.* Fracture and Structural Integrity, 2017. **41**: p. 524-535.
41. Barretta, R., et al., *Functionally graded Timoshenko nanobeams: A novel nonlocal gradient formulation.* Composites Part B: Engineering, 2016. **100**: p. 208-219.
42. de Borst, R. and J.J.C. Remmers, *Computational Methods for Debonding in Composites.* Mechanical Response of Composites, 2008. **10**: p. 1-25.
43. Tarantino, A.M., et al., *Structural modelling at the Micro-, Meso-, and Nanoscales.* Modelling and Simulation in Engineering, 2017. **2017**.
44. Greco, F., P. Lonetti, and R. Zinno, *An analytical delamination model for laminated plates including bridging effects.* International Journal of Solids and Structures, 2002. **39**(9): p. 2435-2463.
45. Ben Dror, E. and O. Rabinovitch, *Size effect in the debonding failure of FRP strengthened beams.* Engineering Fracture Mechanics, 2016. **156**: p. 161-181.
46. Bruno, D., F. Greco, and P. Lonetti, *Dynamic Mode I and Mode II Crack Propagation in Fiber Reinforced Composites.* Mechanics of Advanced Materials and Structures, 2009. **16**(6): p. 442-455.
47. Carlsson, L.A. and G.A. Kardomateas, *Structural and Failure Mechanics of Sandwich Composites*. SOLID MECHANICS AND ITS APPLICATIONS, ed. S.D.H.L.N. York. Vol. 121. 2011, Springer Dordrecht Heidelberg London New York: Springer.
48. Mortas, N., P.N.B. Reis, and J.A.M. Ferreira, *Impact response of balsa core sandwiches.* Frattura ed Integrita Strutturale, 2014. **30**: p. 403-408.
49. Morada, G., A. Vadean, and R. Boukhili, *Failure mechanisms of a sandwich beam with an ATH/epoxy core under static and dynamic three-point bending.* Composite Structures, 2017. **176**: p. 281-293.
50. Tumino, D., et al., *Mechanical behavior of a sandwich with corrugated GRP core: Numerical modeling and experimental validation.* Frattura ed Integrita Strutturale, 2014. **30**: p. 317-326.
51. Triantafillou, T.C. and L.J. Gibson, *Failure Mode Maps for Foam Core Sandwich Beams.* Materials Science and Engineering, 1987. **95**: p. 37-53.
52. Stylianou, V. and A. Ivankovic, *Finite volume analysis of dynamic fracture phenomena I: A node release methodology.* International Journal of Fracture, 2002. **113**(2): p. 107-123.

53. Funari, M.F. and P. Lonetti, *Initiation and evolution of debonding phenomena in layered structures.* Theoretical and Applied Fracture Mechanics, 2017. **92**: p. 133-145.
54. Funari, M.F., et al., *An interface approach based on moving mesh and cohesive modeling in Z-pinned composite laminates.* Composites Part B-Engineering, 2018. **135**: p. 207- 217.
55. Ingraffea, A.R., in *Computational Fracture Mechanics*. 2007.
56. Murotani, K., G. Yagawa, and J.B. Choi, *Adaptive finite elements using hierarchical mesh and its application to crack propagation analysis.* Computer Methods in Applied Mechanics and Engineering, 2013. **253**: p. 1- 14.
57. Rashid, M.M., *The arbitrary local mesh replacement method: An alternative to remeshing for crack propagation analysis.* Computer Methods in Applied Mechanics and Engineering, 1998. **154**(1): p. 133-150.
58. Mi, Y. and M.H. Aliabadi, *Three-dimensional crack growth simulation using BEM.* Computers & Structures, 1994. **52**(5): p. 871-878.
59. Belytschko, T., et al., *Meshless methods: An overview and recent developments.* Computer Methods in Applied Mechanics and Engineering, 1996. **139**(1-4): p. 3-47.
60. Barbero, E. and P. Lonetti, *An Inelastic Damage Model for Fiber Reinforced Laminates.* Journal of Composite Materials, 2002. **36**: p. 941-962.
61. Dong, Y., et al., *Analysis of concrete fracture using a novel cohesive crack method.* Applied Mathematical Modelling, 2010. **34**(12): p. 4219-4231.
62. Li, F. and D. Xingwen, *Mesh-dependence of Material with Softening Behavior.* Chinese Journal of Aeronautics, 2010. **23**(1): p. 46-53.
63. Xu, X.P. and A. Needleman, *Numerical simulations of fast crack growth in brittle solids.* Journal of the Mechanics and Physics of Solids, 1994. **42**(9): p. 1397-1434.
64. Xu, D.D., et al., *Modeling of dynamic crack branching by enhanced extended finite element method.* Computational Mechanics, 2014. **54**(2): p. 489-502.
65. Menouillard, T. and T. Belytschko, *Smoothed nodal forces for improved dynamic crack propagation modeling in XFEM.* International Journal for Numerical Methods in Engineering, 2010. **84**(1): p. 47-72.
66. Ciantia, M.O., et al., *A numerical investigation of the incremental behavior of crushable granular soils.* International Journal for Numerical and Analytical Methods in Geomechanics, 2016. **40**(13): p. 1773-1798.
67. Mohammadi, S., D.R.J. Owen, and D. Peric, *A combined finite/discrete element algorithm for delamination analysis of composites.* Finite Elements in Analysis and Design, 1998. **28**(4): p. 321-336.
68. Nguyen, N.H.T., et al., *A discrete element modelling approach for fatigue damage growth in cemented materials.* International Journal of Plasticity, 2019. **112**: p. 68-88.
69. Daxini, S.D. and J.M. Prajapati, *A review on recent contribution of meshfree methods to structure and fracture mechanics applications.* The Scientific World Journal, 2014. **2014**.
70. Hyun Moo, K., L. Hae Sung, and J. Un Yong, *An incremental formulation of the moving-grid finite element method for the prediction of dynamic crack propagation.* Nuclear Engineering and Design, 1995. **158**(2): p. 295-309.
71. Gibson, L.J. and M.F. Ashby, *Cellular Solids: Structure and Properties*. 2 ed. Cambridge Solid State Science Series. 1997, Cambridge: Cambridge University Press.

72. Marsavina, L., et al., *Refinements on fracture toughness of PUR foams.* Engineering Fracture Mechanics, 2014. **129**: p. 54-66.
73. Marsavina, L., et al., *On the crack path under mixed mode loading on PUR foams.* Frattura ed Integrita Strutturale, 2015. **9**(34): p. 387-396.
74. Viana, G.M. and L.A. Carlsson, *Mechanical Properties and Fracture Characterization of Cross-Linked PVC Foams.* Journal of Sandwich Structures & Materials, 2002. **4**(2): p. 99-113.
75. Saenz, E.E., L.A. Carlsson, and A. Karlsson, *Characterization of fracture toughness (Gc) of PVC and PES foams.* Journal of Materials Science, 2011. **46**(9): p. 3207-3215.
76. Danielsson, M., *Toughened rigid foam core material for use in sandwich constructions.* Cellular Polymers, 1996. **15**(6): p. 417-435.
77. Kabir, M.E., M.C. Saha, and S. Jeelani, *Tensile and fracture behavior of polymer foams.* Materials Science and Engineering: A, 2006. **429**(1): p. 225-235.
78. 14, A., *Standard Test Methods for Plane-Strain Fracture Toughness and Strain Energy Release Rate of Plastic Materials*. 2014.
79. Hallström, S. and J.L. Grenestedt, *Mixed Mode Fracture of Cracks and Wedge Shaped Notches in Expanded PVC Foam.* International Journal of Fracture, 1997. **88**(4): p. 343-358.
80. Marsavina, L., et al., *Experimental and numerical crack paths in PUR foams.* Engineering Fracture Mechanics, 2016. **167**: p. 68-83.
81. Greco, F. and P. Lonetti, *Mixed mode dynamic delamination in fiber reinforced composites.* Composites Part B-Engineering, 2009. **40**(5): p. 379-392.
82. Bruno, D., F. Greco, and P. Lonetti, *A coupled interface-multilayer approach for mixed mode delamination and contact analysis in laminated composites.* International Journal of Solids and Structures, 2003. **40**(26): p. 7245-7268.
83. Zhou, F.H., J.F. Molinari, and T. Shioya, *A rate-dependent cohesive model for simulating dynamic crack propagation in brittle materials.* Engineering Fracture Mechanics, 2005. **72**(9): p. 1383-1410.
84. Seagraves A, R.R., *Advances in Cohesive Zone Modeling of Dynamic Fracture* Springer New York Dordrecht Heidelberg London ed, ed. D.F.o.M.a. Structure. 2010.
85. COMSOL, *Multiphysics Reference Guide.* 2014.
86. Zhao, L.B., et al., *XFEM simulation of delamination in composite laminates.* Composites Part a-Applied Science and Manufacturing, 2016. **80**: p. 61-71.
87. Reeder, J.R., K. Demarco, and K.S. Whitley, *The use of doubler reinforcement in delamination toughness testing.* Composites Part a-Applied Science and Manufacturing, 2004. **35**(11): p. 1337-1344.
88. Rosa, A.L., et al., *A loading rate dependent cohesive model for concrete fracture.* Engineering Fracture Mechanics, 2012. **82**: p. 195-208.
89. Lundsgaard-Larsen, C., R. Massabo, and B.N. Cox, *On acquiring data for large-scale crack bridging at high strain rates.* Journal of Composite Materials, 2012. **46**(8): p. 949-971.
90. Greco, F., L. Leonetti, and P. Lonetti, *A novel approach based on ALE and delamination fracture mechanics for multilayered composite beams.* Composites Part B-Engineering, 2015. **78**: p. 447-458.
91. Alfano, G. and M.A. Crisfield, *Finite element interface models for the delamination analysis of laminated composites: Mechanical and computational*

issues. International Journal for Numerical Methods in Engineering, 2001. **50**(7): p. 1701-1736.

92. Robinson, P. and D.Q. Song, *A Modified Dcb Specimen for Mode-I Testing of Multidirectional Laminates.* Journal of Composite Materials, 1992. **26**(11): p. 1554-1577.
93. Cartié, D.D.R., *Effect of Z-Fibres on the Delamination Behaviour of Carbon Fibre I Epoxy Laminates*. 2000.
94. Bianchi, F. and X. Zhang, *A cohesive zone model for predicting delamination suppression in z-pinned laminates.* Composites Science and Technology, 2011. **71**(16): p. 1898-1907.
95. Bruno, D., F. Greco, and P. Lonetti, *Computation of energy release rate and mode separation in delaminated composite plates by using plate and interface variables.* Mechanics of Advanced Materials and Structures, 2005. **12**(4): p. 285-304.
96. Bruno, D., F. Greco, and P. Lonetti, *Interaction between interlaminar and intralaminar damage in fiber-reinforced composite laminates.* International Journal of Computational Methods in Engineering Science and Mechanics, 2008. **9**(6): p. 358-373.
97. Greco, F. and P. Lonetti, *Mixed mode dynamic delamination in fiber reinforced composites.* Composites Part B: Engineering, 2009. **40**(5): p. 379-392.
98. Lonetti, P., *Dynamic propagation phenomena of multiple delaminations in composite structures.* Computational Materials Science, 2010. **48**(3): p. 563-575.
99. Alliez, P., et al., *Recent Advances in Remeshing of Surfaces*, in *Shape Analysis and Structuring*, L. De Floriani and M. Spagnuolo, Editors. 2008, Springer Berlin Heidelberg: Berlin, Heidelberg. p. 53-82.
100. Martin, E., et al., *Initiation of edge debonding: coupled criterion versus cohesive zone model.* International Journal of Fracture, 2016.
101. Funari, M.F. and P. Lonetti, *Initiation and evolution of debonding phenomena in layered structures.* Theoretical and Applied Fracture Mechanics, 2017. **https://doi.org/10.1016/j.tafmec.2017.05.030**.
102. Funari, M.F., F. Greco, and P. Lonetti, *A moving interface finite element formulation for layered structures.* Composites Part B: Engineering, 2016. **96**: p. 325-337.
103. Odessa, I., Y. Frostig, and O. Rabinovitch, *Modeling of interfacial debonding propagation in sandwich panels.* International Journal of Solids and Structures, 2017 (in press).
104. Prasad, S. and L.A. Carlsson, *Debonding and Crack Kinking in Foam Core Sandwich Beams .2. Experimental Investigation.* Engineering Fracture Mechanics, 1994. **47**(6): p. 825-841.
105. Volokh, K.Y. and A. Needleman, *Buckling of sandwich beams with compliant interfaces.* Computers & Structures, 2002. **80**(14-15): p. 1329-1335.
106. Erdogan, F. and G.C. Sih, *On the Crack Extension in Plates Under Plane Loading and Transverse Shear.* Journal of Basic Engineering, 1963. **85**(4): p. 519-525.
107. Maiti, S.K. and R.A. Smith, *Comparison of the criteria for mixed mode brittle fracture based on the preinstability stress-strain field Part I: Slit and elliptical cracks under uniaxial tensile loading.* International Journal of Fracture, 1983. **23**(4): p. 281-295.
108. Yishu, Z., *A strain energy criterion for mixed mode crack propagation.* Engineering Fracture Mechanics, 1987. **26**(4): p. 533-539.

109. COMSOL, *COMSOL Multiphysics® v. 5.2, www.comsol.com*. 2015: COMSOL AB, Stockholm, Sweden.
110. Rao, B.N. and S. Rahman, *An efficient meshless method for fracture analysis of cracks*. Computational Mechanics, 2000. **26**(4): p. 398-408.
111. Lee, G.H., H.J. Chung, and C.K. Choi, *Adaptive crack propagation analysis with the element-free Galerkin method*. International Journal for Numerical Methods in Engineering, 2003. **56**(3): p. 331-350.
112. Ingraffea, A.R. and M. Grigoriu, *Probabilistic fracture mechanics: A validation of predictive capability*. 1990, CORNELL UNIV ITHACA NY DEPT OF STRUCTURAL ENGINEERING.
113. Dirik, H. and T. Yalçinkaya, *Crack path and life prediction under mixed mode cyclic variable amplitude loading through XFEM*. International Journal of Fatigue, 2018. **114**: p. 34-50.
114. Miehe, C., M. Hofacker, and F. Welschinger, *A phase field model for rate-independent crack propagation: Robust algorithmic implementation based on operator splits*. Computer Methods in Applied Mechanics and Engineering, 2010. **199**(45-48): p. 2765-2778.
115. Ayatollahi, M.R., M.R.M. Aliha, and H. Saghafi, *An improved semi-circular bend specimen for investigating mixed mode brittle fracture*. Engineering Fracture Mechanics, 2011. **78**(1): p. 110-123.
116. Spadea, S., et al., *Wound FRP Shear Reinforcement for Concrete Structures*. Journal of Composites for Construction, 2017. **21**(5).
117. Blaber, J., B. Adair, and A. Antoniou, *Ncorr: Open-Source 2D Digital Image Correlation Matlab Software*. Experimental Mechanics, 2015. **55**(6): p. 1105-1122.

Appendices

Publications in international Peer-reviewed journals

1 Funari, M.F., Lonetti, P., Spadea, S., A crack growth strategy based on moving mesh method and fracture mechanics, Theoretical and Applied Fracture Mechanics, 2018, Accepted for publication.

2 Funari, M.F., Greco, F., Lonetti, P., Spadea, S., A numerical model based on ALE formulation to predict crack propagation in sandwich structures, Fracture and Structural Integrity, 2018, Accepted for publication.

3 Funari, M.F., Lonetti, P., Pascuzzo, A., A Moving Cohesive Mesh Formulation to predict Debonding Phenomena in Layered Structures, CEPM Journal, 2018, 1(2), 16-26.

4 Funari, M.F., Greco, F., Lonetti, P., A coupled ALE-Cohesive formulation for interfacial debonding propagation in sandwich structures, Structural Integrity Procedia, 2018, 9, 92-100.

5 Funari, M.F., Greco, F., Lonetti, P., Sandwich panels under interfacial debonding mechanisms, Composite Structures, 2018, 203, 310-320.

6 Funari, M.F., Greco, F., Lonetti, P., Luciano, R., Penna, R., An interface approach based on moving mesh and cohesive modeling in Z-pinned composite laminates, Composites Part B: Engineering, 2018, 135, 207-217.

7 Funari, M.F., Greco, F., Lonetti, P., Dynamic debonding in layered structures: A coupled ALE-cohesive approach, Fracture and Structural Integrity, 2017, 41, 524-535.

8 Funari, M.F., Lonetti, P., Initiation and evolution of debonding phenomena in layered structures, Theoretical and Applied Fracture Mechanics, In press, corrected proof, Available online 29 May 2017.

9 Funari, M.F., Greco, F., Lonetti, P., A coupled ALE-Cohesive formulation for layered structural systems, Structural Integrity Procedia, 2017, 3, 362-369

10 Fortunato G., Funari, M.F., Lonetti, P., Survey and seismic vulnerability assessment of the Baptistery of San Giovanni in Tumba (Italy), Journal of Cultural Heritage, 26, 2017, 64-78.

11 Funari, M.F., Greco, F., Lonetti, P., A cohesive finite element model based ALE formulation for z-pins reinforced multilayered composite beams, Structural Integrity Procedia, 2016, 2, 452-459.

12 Funari, M.F., Greco, F., Lonetti, P., A moving interface finite element formulation for layered structures, Composites Part B: Engineering, 2016, 96, 325-337

Publications in national and international Conference Proceedings

1 Bruno, D., Funari, M.F., Lonetti, P., Pascuzzo, A., Instability design analysis in network arch bridges, RECENTI SVILUPPI NELL'INGEGNERIA STRUTTURALE, Maratea (PZ), September 27-28 2017.

2 Bruno, D., Funari, M.F., Lonetti, P., Pranno, A., Debonding phenomena in Z-pin reinforced composite laminates, 25° International Conference on Composites/Nano Engineering (ICCE-25), Rome, July 16-22 2017.

3 Bruno, D., Funari, M.F., Greco, F., Lonetti, P., Dynamic debonding phenomena in Z-pin reinforced composite laminates, AIMETA 2017, Salerno, September 4-7 2017, 4, 1719-1727

4 Fortunato G., Funari, M.F., Lonetti, P., Seismic assessment of a masonry historic building: 3D survey, modelling and structural analysis, IX Congresso Nazionale AIAr Arcavacata di Rende, 9-11 Marzo 2016

Acknowledgements

I am especially grateful to my supervisor, **Professor Paolo Lonetti**, for giving me the opportunity to work at University of Calabria for this PhD. His advice, support and guidance throughout this work were immeasurable and I am both grateful and proud to have studied under his supervision. Special thanks go to **Professor Fabrizio Greco,** who leads the lab of Engineering Material and Structures at University of Calabria, for his insightful advice.

I would like to thank my family and all my friends, for their patience, understanding and support.

Finally, I would like to thank the reviewers for their detailed comments and suggestions for my thesis.